MODELLING EL NIÑO-SOUTHERN OSCILLATION: THE UTILITY OF CONTEMPORARY DIAGNOSTIC FRAMEWORKS

by

Felicity Susan Graham, B.A. B.Sc., (Hons B.Sc.)

Submitted in partial fulfilment of the requirements for the Degree of
Doctor of Philosophy in Quantitative Marine Sciences

Institute for Marine and Antarctic Studies/CSIRO
University of Tasmania
April, 2015

I declare that this thesis contains no material which has been accepted for a degree or diploma by the University or any other institution, except by way of background information and duly acknowledged in the thesis, and that, to the best of my knowledge and belief, this thesis contains no material previously published or written by another person, except where due acknowledgement is made in the text of the thesis, nor does the thesis contain any material that infringes copyright.

Signed: _____
Felicity Susan Graham

Date: _____

Signed: _____
Felicity Susan Graham

Date: _____

Abstract

The development and application of process-based diagnostics is fundamental in improving our understanding of the simulation of El Niño-Southern Oscillation (ENSO) behaviours by coupled general circulation models (CGCMs). Several theoretical frameworks have potential utility as diagnostics; however, their accuracy in describing the dynamics governing ENSO evolution has not yet been systematically evaluated. This thesis presents a comprehensive analysis of a number of theoretical frameworks - the unified oscillator, Bjerknes stability index, and heat budget equation - to assess their representation of ENSO dynamics and capacity to diagnose ENSO behaviours in CGCMs.

The unified oscillator description of ENSO was first investigated for its accuracy in replicating the ENSO cycle simulated by flux-forced output from the Australian Community Climate and Earth System Simulator ocean model (ACCESS-OM). The unified oscillator equations for anomalous sea surface temperature, thermocline depth, and zonal wind stress tendencies were unable to capture the structure, amplitude, and period of the corresponding tendencies in ACCESS-OM. Furthermore, the unified oscillator was considerably less effective than the simple delayed oscillator model in replicating the simulated ENSO cycle. It was concluded that the overly simplified formulation of the unified oscillator limits its power as a diagnostic of ENSO behaviours.

This thesis also evaluated the effectiveness of the Bjerknes stability index in representing ENSO ocean feedbacks. Output from ACCESS-OM was used to calculate the Bjerknes stability index feedbacks, which were compared with the corresponding heat budget equation feedbacks. Due to the assumption of linearity in its derivation and an oversimplification of the relationship between ENSO variables, the Bjerknes stability index feedbacks correlated poorly with the original heat budget feedbacks. Therefore, the Bjerknes stability index could not necessarily be relied upon to accurately quantify ENSO dynamics. It follows that in its current form, and compared with the heat budget equation, the Bjerknes stability index has limited utility as a diagnostic tool, particularly

in the context of intercomparisons between models that are inherently nonlinear.

Finally, the heat budget equation was employed to diagnose the realism of El Niño evolution simulated by an ACCESS coupled model (ACCESS-CM1.3). The heat budget equation for the tropical Pacific was calculated in ACCESS-CM1.3 and the ocean feedbacks benchmarked against the corresponding terms calculated in ACCESS-OM. Instead of simulating the central Pacific El Niño type, the ACCESS-CM1.3 captured a double peaked event with warming centres evolving concurrently in the eastern and western Pacific. The separation between the two peaks arose due to a westward bias in the dynamic warm pool edge. Coupling biases in ACCESS-CM1.3 also modified the magnitude, location, and timing of the heat budget dynamics during El Niño evolution relative to ACCESS-OM. Finally, some double peaked events in ACCESS-CM1.3 were erroneously categorised as central Pacific El Niños by standard SST metrics.

This thesis highlights the importance of considering multiple diagnostics, including those that inherently account for spatial and temporal variability such as the tropical Pacific heat budget equation, when evaluating ENSO behaviours in CGCMs.

Acknowledgements

I'm sure someone once said "It takes a village to raise a PhD candidate." And, I have certainly had the support and encouragement from a very special community of advisors, colleagues, and friends to make this thesis possible.

Foremost, I thank my supervisors: Jaci Brown, Neil Holbrook and Andrew Wittenberg. I am incredibly fortunate to have had such a supervisory team. Their scientific knowledge, generosity of time, and gentleness with manuscript corrections and suggestions have been invaluable.

Jaci's openness and availability to discuss science problems and her motivating drive were fundamental in bringing this project to its conclusion. Her inspiration of the big picture often helped me out of details-land.

Neil's constructive comments and suggestions, guidance, and patience in reading several iterations of long manuscripts, were invaluable. His advice and feedback during the final months of the project were extremely helpful.

I have appreciated immensely Andrew's commitment to scientific integrity, honesty, and rigour, and am fortunate to have had his advice and input over my candidature. I would also like to thank Andrew for allowing me to visit GFDL twice during my candidature, and for the opportunities these experiences afforded in meeting, and discussing science with, the overseas ENSO community.

During my candidature IMAS/UTAS, CSIRO, WHOI, and Monash University contributed time, assistance, and money towards providing me with a well-rounded, international experience of the field of oceanography.

A huge thank you to my family, friends, and housemates - who have become like family - for laughter, music, and cups of tea, especially during the Melbourne experience.

Finally, to Dylan. I appreciate beyond measure your companionship, love, and support over the last 3 and a half years. Thank you.

Statement of Co-Authorship

The following people contributed to work undertaken as part of this thesis:

- **Felicity S. Graham, Institute for Marine and Antarctic Studies (IMAS), CSIRO = Author 1 (Candidate)**
- Dr Jaclyn N. Brown, CSIRO, Oceans and Atmosphere Flagship = Author 2
- Assoc. Prof. Neil J. Holbrook, IMAS, ARC Centre of Excellence for Climate System Science = Author 3
- Dr Andrew T. Wittenberg, NOAA Geophysical Fluid Dynamics Laboratory = Author 4
- Dr Simon J. Marsland, CSIRO, Oceans and Atmosphere Flagship = Author 5
- Dr Clothilde Langlais, CSIRO, Oceans and Atmosphere Flagship = Author 6

Paper 1/Chapter 2, accepted (*El Niño, La Niña, and the Southern Oscillation*):

- **Felicity S. Graham (95%)**
- Jaclyn N. Brown (5%)

Paper 2/Chapter 3, submitted (*Reassessing conceptual models of ENSO*):

- **Felicity S. Graham (85%)**
- Jaclyn N. Brown (5%)
- Andrew T. Wittenberg (5%)
- Neil J. Holbrook (5%)

Paper 3/Chapter 4, published (*Effectiveness of the Bjerknes Stability Index in representing ocean dynamics*):

- **Felicity S. Graham (85%)**
- Jaclyn N. Brown (3%)
- Clothilde Langlais (3%)
- Simon J. Marsland (3%)
- Andrew T. Wittenberg (3%)
- Neil J. Holbrook (3%)

Paper 4/Chapter 5, submitted (*How coupled models alter El Niño dynamics: a case study using ACCESS coupled model*):

- **Felicity S. Graham (86%)**
- Jaclyn N. Brown (5%)
- Andrew T. Wittenberg (3%)
- Simon J. Marsland (3%)
- Neil J. Holbrook (3%)

Details of the author's roles:

Felicity S. Graham designed and implemented most of the code, performed data analysis and manuscript writing. Jaclyn N. Brown, Neil J. Holbrook, and Andrew T. Wittenberg contributed with project development and refinement, technical and conceptual discussion, and manuscript preparation. Simon J. Marsland contributed with technical assistance and manuscript discussion in Chapters 4 and 5. Clothilde Langlais contributed with conceptual discussion in Chapter 4.

We, the undersigned, agree with the above stated proportion of work undertaken for each of the above published (or submitted) peer-reviewed manuscripts contributing to this thesis:

Signed: _____
Assoc. Prof. Neil J. Holbrook
Supervisor
Institute for Marine and Antarctic Studies, University of Tasmania

Date: _____

Signed: _____
Dr Jaclyn N. Brown
Supervisor
CSIRO, Oceans and Atmosphere Flagship

Date: _____

Signed: _____
Prof. Nathan Bindoff
Deputy Director
Institute for Marine and Antarctic Studies, University of Tasmania

Date: _____

Table of Contents

List of Tables

LIST OF TABLES

List of Figures

Chapter 1

Introduction

El Niño-Southern Oscillation (ENSO) is the dominant mode of interannual global climate variability, arising from ocean-atmosphere interactions in the tropical Pacific Ocean. At the simplest level, ENSO can be understood as an oscillation between two complementary phases. One phase, denoted El Niño, involves warm sea surface temperature (SST) anomalies in the central-eastern equatorial Pacific Ocean. The other phase, La Niña, involves cool SST anomalies in the central-eastern equatorial Pacific. Changes in SST during ENSO events feedback to modify the Southern Oscillation - an east-west seesaw of sea level surface pressure across the equatorial Pacific.

Through atmospheric and oceanic teleconnections, ENSO impacts climate and weather across the globe, including ocean, atmosphere, and land temperatures, patterns of precipitation (Ropelewski and Halpert, 1987; Dai and Wigley, 2000; Taschetto and England, 2009), and the occurrence of tropical cyclones (Wu and Lau, 1992). The ensuing human impacts can be devastating. For example, La Niña-induced cooling in the Northern Hemisphere during 1918, combined with the failure of the Indian Monsoon during the subsequent El Niño, have been linked to the catastrophic 1918 influenza pandemic that killed over 25 million people worldwide (Johnson and Mueller, 2002; Giese et al., 2010; Shaman and Lipsitch, 2013). The 1997-98 El Niño was the strongest event on record and was linked to droughts, bushfires, and severe weather worldwide, leading to an estimated 32 000 deaths and displacing up to 300 million people (Trenberth, 1999). A Worldwatch Institute and Munich Re report estimated total losses associated with the 1997-98 El Niño event to be up to $92 billion USD (Munich Re, 1999). More recently, flooding in the Australian state of Queensland precipitated by the 2010-11 La Niña, which oc-

curred in concert with anomalously high SSTs around northern Australia (Evans and Boyer-Souchet, 2012), resulted in the loss of 36 lives and more than $5 billion AUD (Queensland Government, 2011).

Such extreme events as the 1997-98 El Niño and the 2010-11 La Niña have triggered further research into the ocean-atmosphere interactions associated with ENSO, including through observational, theoretical, and modelling studies. One outcome has been the advancement of coupled general circulation models (CGCMs) that combine highly complex oceanic and atmospheric general circulation models (OGCMs and AGCMs, respectively; Delecluse et al., 1998). CGCMs are costly to run and their ENSO behaviours may be difficult to diagnose due to the complexity of coupling procedures and physical parameterisations; yet, CGCMs are crucial in developing our understanding of, and ability to forecast, ENSO.

Despite recent progress in the CGCM representation of ENSO behaviours, issues pertaining to the simulation of dynamics, development, and predictability remain unresolved (Guilyardi et al., 2009). This is in part due to a relatively limited observational record with which to constrain the balance of processes contributing to ENSO evolution. However, there is also considerable need for the development and application of process-based diagnostic tools to aid in improving our understanding of the realism of CGCM ENSO behaviours. This thesis assesses a number of such diagnostic frameworks for their capacity to identify and describe ENSO-related processes and dynamics in CGCMs.

1.1 Modelling historical and future ENSO behaviours

The simulation of ENSO-related anomalies by CGCMs has improved markedly over recent decades (Delecluse et al., 1998; Latif et al., 2001; van Oldenborgh et al., 2005; AchutaRao and Sperber, 2006; Wittenberg et al., 2006; Kug et al., 2012; Bellenger et al., 2014). Advances have been achieved via improvements in physical parameterisations, grid resolution, and the mean state of the tropical Pacific, including the seasonal cycle (Guilyardi et al., 2004; Roberts et al., 2009), as well as in the theoretical understanding of ENSO behaviours and dynamics (Neelin et al., 1998; Jin et al., 2006). As a result, many models now perform reasonably well at simulating some of the salient features of

ENSO, such as its periodicity and the spatial patterns of SST anomalies in the eastern Pacific (AchutaRao and Sperber, 2006). Effort is also being made to understand how ENSO will change in the future, evidenced by the participation of 20 modelling centres in the Coupled Model Intercomparison Project phase 5 (CMIP5), which underpins the Fifth Assessment Report of the Intergovernmental Panel on Climate Change (IPCC; Taylor et al., 2012).

Nevertheless, significant challenges remain in our pursuit of the accurate representation of ENSO dynamics in CGCMs. Of note are the many biases in CGCM simulations of the tropical Pacific, which include (from Wittenberg et al., 2006): (i) a cool SST bias in the central-eastern equatorial Pacific - the cold-tongue bias; (ii) a westwards shift in ENSO anomalies; (iii) a warm SST bias in the eastern equatorial Pacific near the coast of South America; (iv) zonal wind stress anomalies that are meridionally confined closer to the equator; (v) an overly diffuse thermocline structure; (vi) the presence of a strong (double) Intertropical Convergence Zone (ITCZ) in the south eastern Pacific; and (vii) a weak Equatorial Undercurrent. A further complication is the diversity in the simulation of the tropical Pacific climate both within and across the current generation of CGCMs, including in the strength of the trade winds and consequent oceanic upwelling, mixing, and latent heat flux, and penetration of surface radiative heat fluxes, as well as ENSO-related features, such as period, and location, timing, and relative importance of CGCM ENSO dynamics (Capotondi et al., 2006; Guilyardi, 2006; Wittenberg et al., 2006; Guilyardi et al., 2009; Wittenberg, 2009; Collins et al., 2010; Kim and Jin, 2011b; Vecchi and Wittenberg, 2010; Guilyardi et al., 2012a; Watanabe et al., 2012; Brown et al., 2013; Choi et al., 2013; Capotondi and Wittenberg, 2013; Kim et al., 2014b).

It follows that an important consideration to be made is how faithful to observations are the behaviours and dynamics simulated by CGCMs, particularly if we are using these models to predict future changes to ENSO. Three of the possible explanations for the differences between ENSO described by CGCMs and observations of the phenomenon are (figure 1.1): i) CGCMs realistically capture historic features of ENSO, including some features that have not yet been observed in our relatively short record; ii) the ENSO events simulated by CGCMs lie outside the realm of possible ENSO events under historic

CO_2 forcings; or iii) CGCMs somewhat realistically simulate ENSO, although their representations may deviate slightly from that which is expected. [We note that there are additional possible scenarios to these three discussed here, such as the observational or reanalysis data exhibiting biases in their representation of reality, as well as the real-world variability changing due to external radiative forcings.] Based on recent studies (e.g. Wittenberg et al., 2006; Guilyardi et al., 2009; Brown et al., 2013), the current generation of CGCMs are likely to fit within the third category. That is, the CGCMs simulate a qualitatively similar ENSO to that observed, but exhibit biases, such as those mentioned above, and inherent diversity arising from differences in the underlying structure of the model, that together modify the quantitative elements of the ENSO event beyond those observed.

It has been suggested that ENSO-related biases and diversity in CGCM simulations may be reduced through a better understanding of the sensitivity of ENSO to changes in processes and feedbacks (Guilyardi et al., 2009). For this to occur, a number of factors are required. First, the balance of processes contributing to ENSO evolution in CGCMs needs to be constrained by a longer observational record. Second, greater computing power is needed to enable further refinement through increasing horizontal and vertical resolutions and through improvement of the parameterisations of small-scale physical phenomena. Finally, there is a need for the development of process-based metrics that can be used to understand both the realism of simulated ENSO dynamics and behaviours as well as the underlying reasons that lead to differences between CGCMs and observations.

There is a hierarchy of frameworks currently available to perform such a diagnosis of CGCM ENSO behaviour. In what follows we briefly review three levels of frameworks - namely, low-order conceptual models, the Bjerknes stability index, and the tropical Pacific heat budget equation - that are adopted in this thesis for the analysis of general circulation model data.

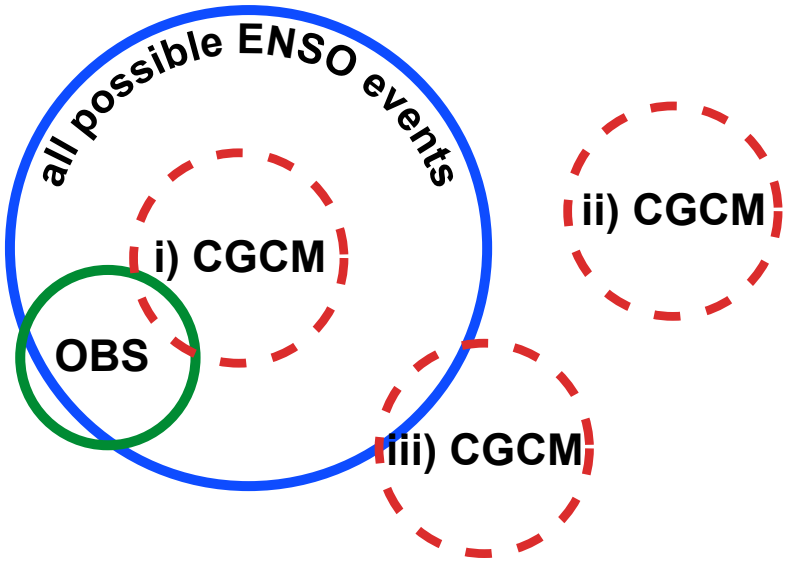

Figure 1.1: Venn diagram describing the space of all possible ENSO behaviours and dynamics (blue circle). Observed behaviours represent only a subset of all possible types (green circle). The dynamics of a particular coupled general circulation model (CGCM) may: (i) be quantitively similar to observed dynamics or within the realm of possible features under historical CO_2 forcings; (ii) lie outside the realm of possible ENSO behaviours; or (iii) be qualitatively similar to observed dynamics, but affected by biases that modify the quantitative features beyond those that are likely under historical CO_2 forcings. The green circle extends slightly outside the blue circle to represent observational errors, such as in measurement or reconstruction. We also note that the blue circle is itself evolving on decadal to centennial timescales due to natural internal variability, as well as due to external radiative forcings.

1.1.1 Low-order conceptual models

There are two main explanations given for the oscillatory nature of ENSO: in one, ENSO can be understood as a self-sustaining oscillation; in the other, ENSO is a damped mode triggered by external noise forcing (Wang and Picaut, 2004). Most conceptual models are based on the former oscillatory framework, where growth is provided by the Bjerknes feedback mechanism (Bjerknes, 1969), described as follows. During an El Niño event, an initial warm SST anomaly in the eastern equatorial Pacific decreases the zonal SST gradient along the equator and, in turn, weakens the easterly trade winds via the Walker Circulation. The resulting westerly zonal wind stress anomaly initiated in the central equatorial Pacific reduces the east-west tilt of the equatorial thermocline, reinforcing the

original warm SST anomaly in the east. For the coupled system to oscillate requires the action of one or more negative feedback mechanisms. Four leading conceptual models have been proposed over the past few decades: (i) the delayed oscillator (Suarez and Schopf, 1988; Battisti and Hirst, 1989); (ii) the recharge oscillator (Wyrtki, 1975; Cane et al., 1986; Zebiak, 1989; Jin, 1997a); (iii) the advective-reflective oscillator (Picaut et al., 1997); and (iv) the western Pacific oscillator (Weisberg and Wang, 1997). These models each incorporate one or more of four known negative feedbacks that lead to transition between ENSO phases.

Evidence suggests that each of the mechanisms described by these four leading conceptual model frameworks of the 20th century play a role in the growth of or transition between the two ENSO phases (McCreary, 1983; McCreary and Anderson, 1984; Graham and White, 1988; Picaut and Delcroix, 1995; Picaut et al., 1996; Meinen and McPhaden, 2000; Boulanger and Menkes, 2001; Boulanger et al., 2003; Hasegawa and Hanawa, 2003). However, it is likely that more than one of the mechanisms operate in concert during the transition between ENSO phases. For this reason, the four negative feedback mechanisms were recently combined in the unified oscillator conceptual model of ENSO by Wang (2001). Yet, the unified oscillator framework has not been tested to ascertain its fidelity in modelling observed ENSO dynamics, or whether it is an appropriate tool with which to diagnose observed or simulated ENSO behaviours.

While conceptual models are useful in identifying the leading mechanisms that contribute to the development and decay of ENSO events, their low-order limits their ability to describe the temporally and spatially varying balance between ENSO dynamics, and hence the realism of dynamics simulated by CGCMs.

1.1.2 The tropical Pacific heat budget equation

The heat budget equation of the tropical Pacific Ocean describes the dynamical processes governing the variability of temperature anomalies there. Being formulated in terms of 4-dimensional quantities - that is, varying with respect to longitude, latitude, depth, and time - the heat budget equation provides a convenient method of tracking the dominant balance of dynamics on various timescales: from the evolution of particular ENSO events

through to the time mean over decades and centuries.

A number of previous studies have examined and ranked the dominant terms from the heat budget equation during ENSO events in the tropical Pacific (Hirst, 1986; An et al., 1999; Jin and An, 1999; An and Wang, 2000; Wang and An, 2001; Kang et al., 2001; Huang et al., 2010; Belmadani et al., 2010). The most important terms leading to growth and termination of El Niño events are the thermocline feedback - the vertical advection of temperature anomalies by the action of the mean upwelling on the anomalous vertical temperature gradient - and the zonal advective feedback - the zonal advection of temperature anomalies by the action of the anomalous zonal current on the mean zonal temperature gradient.

To a large extent, the thermocline and zonal advective feedbacks are responsible for setting the ENSO period and patterns of evolution of temperature anomalies. A strengthening of the mean upwelling after the 1970s "regime shift" (during which easterly wind stress anomalies were strengthened) saw an increase in the thermocline feedback over the eastern equatorial Pacific (Wang and An, 2001). In turn, the volume of warm water available for discharge and recharge under the recharge oscillator mechanism increased, which led to an increase in the ENSO period and an eastwards shift in the evolution of ENSO temperature anomalies (An and Wang, 2000). The meridional extent of the thermocline feedback also plays a role in determining the structure and volume of warm water available for discharge and recharge, and hence the ENSO timescales (Capotondi et al., 2006).

In the case of the zonal advective feedback, a westwards shift in the location of maximum advection leads to a westwards shift in the temperature anomalies and a shortening of the ENSO period to 2-4 years (An and Wang, 2000). Under this regime, the zonal advective feedback also favours the transition, rather than growth, of ENSO. By contrast, an eastwards shift in the zonal advective feedback causes an eastwards shift in ENSO temperature anomalies, a lengthening of the ENSO period to 4-6 years, and the favouring of ENSO growth by the zonal advective feedback (An et al., 1999; An and Wang, 2000).

Given the importance of the thermocline and zonal advective feedbacks in determining the behaviour of ENSO, it is not surprising that biases in the CGCM simulations of

tropical features result in biases in the simulations of these two feedbacks. For instance, CGCM biases in the longitudinal maximum and meridional extent of zonal wind stress anomalies during ENSO evolution directly impact the location and magnitude of the thermocline and zonal advective feedbacks (An and Wang, 2000). Furthermore, a recent study by Belmadani et al. (2010) found a relationship between the sign and magnitude of biases in the mean circulation fields of 18 IPCC-class CGCMs and the relative contribution of the thermocline and zonal advective feedbacks to ENSO growth. Consequently, examination of the dominant balance of heat budget terms may shed light on the regime favoured by a CGCM as well as possible simulation biases that affect the growth rate of ENSO. An offshoot of the heat budget, the Bjerknes stability index, also sheds light on the dominant regime of CGCMs, by ranking the contributions of the linearised heat budget terms to the leading growth rate of ENSO.

1.1.3 The Bjerknes stability index

While the heat budget equation offers a more complete description of ENSO evolution than low-order conceptual models, the complexity of the heat budget may make it difficult to analyse and interpret. The Bjerknes stability index was proposed as a simplified alternative to the heat budget equation that approximates the dominant features leading to ENSO growth and decay.

The Bjerknes stability index (BJ index) quantifies the processes leading to growth and damping, and hence overall stability, of the leading ENSO-like mode (Jin et al., 2006; Kim and Jin, 2011a,b). It is derived by employing a series of approximations that reduce the mixed layer heat budget equation to a coupled system of equations in terms of the eastern averaged mixed layer temperature anomaly, the western Pacific averaged thermocline depth anomaly, and the basinwide average of the zonal wind stress anomaly.

The BJ index is used to parameterise growth in a system of equations that is identical in form to the recharge oscillator (a low-order conceptual model), but in this system, the remaining coefficients that set the period of oscillation are determined from the linearised dynamics of the mixed layer heat budget equation. By directly quantifying the contribution of different dynamics to the leading growth rate of the system, the BJ

index is a useful tool in understanding the dominant regime simulated in a model (i.e. whether the simulated ENSO growth is dominated by the thermocline feedback or the zonal advective feedback; Kim and Jin, 2011a). Furthermore, given its dependence on the mean state and surface wind stresses, the BJ index has been used to account for diversity between CGCMs (Kim and Jin, 2011b). Another key application of the BJ index has been in quantifying how changes to the mean state under global warming scenarios will impact the behaviour of ENSO feedbacks (Kim and Jin, 2011b; Kim et al., 2014b).

Despite the importance of the BJ index in quantifying the leading balance of dynamics contributing to ENSO growth, questions remain as to its accuracy in representing the heat budget feedbacks. Notably, deriving the BJ index requires the implementation of a number of linear assumptions each of which fail to account for ENSO nonlinearities, such as asymmetries in duration, sequencing, and amplitude (Choi et al., 2013). Furthermore, given that no two ENSO events are identical in their evolution, the utility of averaging all events, as in the BJ index, to quantify ENSO diversity within and across CGCMs is questionable. For instance, the two flavours of El Niño, the eastern Pacific and central Pacific types, are characterised by different dynamics: eastern Pacific events tend to be dominated by the thermocline feedback, while central Pacific events tend to be dominated by the zonal advective feedback (Kug et al., 2009). It follows that averaging all ENSO events over a set period might result in a misleading picture of the the balance of the heat budget feedbacks since the average would be weighted towards events of larger magnitude (for example, the two super eastern Pacific El Niño events during the period 1980-2000, which were dominated by the thermocline feedback), rather than other events of smaller magnitude.

1.2 Thesis overview

1.2.1 Aims

The three frameworks outlined above are among a proliferation of such frameworks in recent decades that have collectively advanced our theoretical understanding of ENSO. However, the utility of these frameworks in diagnosing a range of ENSO behaviours

has not necessarily been systematically evaluated, nor have we seen them methodically employed to improve CGCMs. This is in part due to the fact that many of these diagnoses are linear (when ENSO processes may involve nonlinear relationships between variables), not sufficiently versatile, or make an inappropriate set of simplifying assumptions.

Consequently, there are a number of broad research aims in the ENSO community relating to the evaluation of ENSO theories and diagnostic tools, including:

(I) How accurate are the frameworks in capturing the observed balance of processes and dynamics contributing to ENSO evolution?

(II) Can the frameworks be improved to better their performance in diagnosing simulated ENSO behaviour?

(III) Can the frameworks be used to understand and diagnose model behaviours and sensitivities?

By addressing these aims in the modification and development of existing frameworks, we can seek to address the realism of CGCM ENSO behaviours.

To this end, this thesis reviews the descriptions of ENSO provided by the unified oscillator conceptual model and the Bjerknes coupled-stability index, comparing the latter with the heat budget equation from which it was derived. The utility of these frameworks in describing observed ENSO dynamics is evaluated, along with their implied capacity for understanding and diagnosing the ENSO behaviours simulated by CGCMs. The thesis objectives can be grouped into two specific categories: (i) the evaluation of current descriptions of ENSO; and (ii) the classification of CGCM ENSO behaviours.

1.2.2 Evaluation of current descriptions of ENSO

The unified oscillator, Bjerknes stability index, and heat budget equation are systematically evaluated in the context of a realistic flux-forced model, the Australian Community Climate and Earth System Simulator Ocean Model (ACCESS-OM). The following objectives, which are related to the broad aims of ENSO research above, are specifically addressed in this thesis:

The unified oscillator

1. To what extent does the unified oscillator faithfully represent the ENSO behaviour of a realistic flux-forced OGCM? This relates directly to aim (I) above.

2. Considering that multiple mechanisms are likely to be involved in the evolution of ENSO events, does the unified oscillator offer an improvement over the simpler conceptual models that it combines (aim I)?

3. Can modifications to the formulation of the unified oscillator be made to improve the way it captures ENSO events, including its versatility in accounting for different ENSO behaviours (aim II)?

The Bjerknes stability index/heat budget

4. How faithfully does the Bjerknes stability index reproduce the key ocean dynamics important to ENSO evolution compared with the corresponding heat budget formulations (aim I)?

5. How useful is the Bjerknes stability index in the context of model intercomparisons (aim III)?

1.2.3 Classification of CGCM ENSO behaviours

Following the evaluation of the frameworks outlined above, the leading diagnostic for understanding ENSO behaviour and dynamics, namely the heat budget equation, is applied to a CGCM. The following objectives are addressed:

6. How close are the El Niño evolution heat budget dynamics in a CGCM simulation to the dynamics of a corresponding flux-forced OGCM simulation, which are comparable to observed (aim III)?

7. Are the spatial flavours that are present in the flux-forced OGCM simulation faithfully replicated in the CGCM (aim III)?

8. How do the El Niño evolution pathway/s of the CGCM compare to those of the flux-forced OGCM simulation (aim III)?

1.2.4 Structure

Each chapter in this thesis is prepared as a manuscript for peer-review and publication in a refereed journal. A summary of the background information and relevant literature is provided in the introduction to each chapter, followed by a discussion of the main results and their contribution to the overall understanding of this topic.

Chapter 2 introduces background theory on the phenomenon of ENSO and has been accepted for publication in the *Encyclopedia of Natural Resources*. Chapter 3 comprises a paper submitted to the *Journal of Climate* that reviews the unified oscillator framework relative to the individual conceptual models that it comprises, and evaluates its utility in describing the main evolution dynamics of ENSO events. Chapter 4 is in the form of a paper published in *Climate Dynamics* that evaluates the representation of the ocean dynamics described by the Bjerknes stability index in comparison with the same dynamics described by the heat budget equation. The limitations of the Bjerknes stability index are analysed and discussed. Chapter 5 comprises a paper submitted to *Climate Dynamics* that investigates the realism of the heat budget dynamics simulated by an IPCC-class CGCM. The evolution pathway of each El Niño spatial flavour in the CGCM is summarised and contrasted with those of a realistic flux-forced OGCM simulation. Finally, a discussion of the main results, their implications, and future research directions are presented in Chapter 6.

This chapter has been removed for copyright or proprietary reasons.

Chapter 2. El Niño, La Niña, and the Southern Oscillation, published with the same title in, Encyclopedia of Natural Resources Volume 2, pp. 1086, 2014

Chapter 2

El Niño, La Niña, and the Southern Oscillation

This chapter reviews the background to El Niño-Southern Oscillation, including mean state ocean-atmosphere interactions in the tropical Pacific giving rise to the phenomenon, and the evolutionary characteristics of the canonical eastern Pacific type El Niño event.

Contribution

The main text of this chapter forms an article accepted at the *Encyclopedia of Natural Resources* under the same title. All sections of the paper were written, and the review process led, by myself under the guidance of my coauthor, Dr Jaclyn N. Brown.

Chapter 3

Reassessing conceptual models of ENSO

This chapter presents an analysis of the unified oscillator conceptual model of ENSO (that is, the unified oscillator model described by Wang (2001)) and the component models that it combines. In accordance with the overall thesis aims (chapter 1), this chapter addresses the following specific objectives:

1. To what extent do the unified oscillator equations for sea surface temperature anomaly, thermocline depth anomaly, and zonal wind stress anomaly tendencies accurately diagnose the corresponding tendencies calculated directly from the flux-forced Australian Community Climate and Earth System Simulator Ocean Model (ACCESS-OM)?

2. Does the unified oscillator have greater diagnostic capabilities than the conceptual models that it combines?

3. How can the unified oscillator be improved to better capture the salient features of ENSO simulated in ACCESS-OM?

To this end, the unified oscillator system of equations are fit to the flux-forced ACCESS-OM data. The fitted curves describing the sea surface temperature anomaly, thermocline depth anomaly, and zonal wind stress anomaly tendencies from the unified oscillator are calculated, and compared with the corresponding fitted curves from each of the conceptual models combined in the unified oscillator, along with the original formulations of these models. Finally, the fitted parameter values are used to solve the unified oscillator equations numerically.

Contribution

The main text of this chapter forms a manuscript submitted to the *Journal of Climate* under the same title. The experimental design and analysis methods were discussed between my coauthors, Dr Jaclyn N. Brown, Dr Andrew T. Wittenberg, and Assoc. Prof. Neil J. Holbrook, and myself. The ACCESS-OM simulation data were supplied by Dr Simon J. Marsland. I performed the necessary coding to calculate and analyse the unified oscillator. The writing of all sections of the coauthored paper and the review process were led by myself, under the guidance of the coauthors.

3.1 Abstract

The complex and nonlinear nature of El Niño - Southern Oscillation (ENSO) is often simplified through the use of conceptual models, each of which offers a different perspective on the ocean-atmosphere feedbacks underpinning the ENSO cycle. One theory, the unified oscillator, combines a variety of well-known conceptual frameworks into a single system. The unified oscillator takes the form of a coupled system of delay differential equations, in which the coefficients are determined using theoretical arguments, and the system produces a self-sustained oscillation on interannual timescales.

While the unified oscillator is assumed to provide a more complete conceptual framework of ENSO behaviors than the models it incorporates, its formulation and performance have not been systematically assessed. This paper investigates the accuracy and utility of the unified oscillator through its ability to replicate the ENSO cycle modeled by surface flux-forced output from the Australian Community Climate and Earth System Simulator Ocean Model (ACCESS-OM). The anomalous sea surface temperature equation is found to reproduce the main features of the corresponding tendency modeled by ACCESS-OM reasonably well. However, the remaining equations - for the western equatorial thermocline depth anomaly and zonal wind stress anomalies - are unable to accurately replicate the corresponding tendencies in ACCESS-OM.

Modifications to the unified oscillator, including a diagnostic form of the zonal wind stress anomaly equations, improve its ability to emulate simulated ENSO tendencies. Despite these improvements, the unified oscillator model is less adept than the delayed oscillator model in capturing ENSO behavior in ACCESS-OM, bringing into question its utility as a unifying ENSO framework.

3.2 Introduction

Bjerknes (1969) first recognized that the growth of El Niño-Southern Oscillation (ENSO) events is due to a positive feedback mechanism resulting from ocean-atmosphere interactions in the equatorial Pacific. Specifically, during warm ENSO events, an initial positive sea surface temperature (SST) anomaly develops in the eastern equatorial Pacific, reduc-

ing the SST gradient along the equator. As a result, the atmospheric Walker circulation is weakened with weakening equatorial trade winds, leading to surface wind stress changes that reinforce the original SST anomaly - a positive feedback mechanism collectively known as the Bjerknes positive feedback. Since the seminal work of Bjerknes (1969), other important research has been undertaken to identify and describe the feedback mechanisms underpinning the decay and phase change of ENSO events, and to test their ability to represent ENSO variability (Barnett, 1977). Conceptual models have played a very valuable role in advancing our understanding of ENSO feedback mechanisms by their relatively simple representation of often complex dynamics, without replicating the entire ocean-atmosphere coupled system. These conceptual models usually combine the Bjerknes positive feedback mechanism with one or more negative feedback mechanisms, which enables them to produce oscillations on interannual timescales (approximately every 2-7 years; Wang, 2001; Wang and Picaut, 2004). The feedback mechanisms of conceptual models are often tested against observations and simulations of coupled general circulation models (CGCMs; Kessler, 1991; Picaut et al., 1996; Clarke et al., 2000; Meinen and McPhaden, 2000, 2001; Boulanger et al., 2003; Hasegawa and Hanawa, 2003; Mechoso et al., 2003; Bettio, 2007; Choi et al., 2013).

One of the earliest conceptual models of ENSO, the delayed oscillator, was instrumental in highlighting the importance of equatorial Kelvin and Rossby waves in the transition of an ENSO event (Schopf and Suarez, 1988; Suarez and Schopf, 1988; Battisti and Hirst, 1989). In the delayed oscillator, the growth of an El Niño event is driven by the Bjerknes positive feedback mechanism: westerly wind anomalies in the central Pacific incite an eastward propagating downwelling Kelvin wave that acts to increase SST in the Niño-3 region. At the same time, off-equatorial upwelling Rossby waves reflect at the western Pacific boundary as an equatorial upwelling Kelvin wave, which propagates eastwards, shoaling the equatorial thermocline and allowing cool, subsurface waters to suppress the warm SST anomaly in the eastern equatorial Pacific. Previous studies (Schneider et al., 1997) demonstrate that wave reflection at the western boundary does indeed play a role in the termination of some ENSO events; however, the damping (negative feedback) due to wave reflection alone is not always sufficient in describing the transition between

ENSO events (Li and Clarke, 1994; McPhaden and Yu, 1999).

Similar to the delayed oscillator, the western Pacific oscillator describes the effect of local wind-induced wave dynamics in the growth and termination of an ENSO event (Weisberg and Wang, 1997). During an El Niño event, an increase in off-equatorial sea level pressure in the western Pacific generates local easterly wind anomalies. These wind anomalies force an upwelling, eastward propagating Kelvin wave that shoals the thermocline in the eastern Pacific, terminating the event. Previous studies have confirmed that locally generated waves in the western Pacific do play a role in the termination of an ENSO event (McPhaden and Yu, 1999; McPhaden, 2004), most likely operating in concert with other negative feedback mechanisms (Boulanger and Menkes, 2001; Boulanger et al., 2003).

The recharge oscillator (Jin, 1997a,b) has advanced our understanding of the role of equatorial heat content in ENSO phase change. Under this framework, the termination of an El Niño event is achieved through polewards Sverdrup transport of equatorial heat content incited by changes in the wind stress curl in the central equatorial Pacific (Clarke et al., 2007; Brown and Fedorov, 2010). The Sverdrup transport leaves the equatorial Pacific thermocline anomalously shallow, allowing for the transition to a cool event (La Niña). Given the role of wave dynamics in inducing the anomalous thermocline tilts that lead to the discharge/recharge of equatorial heat content, the recharge oscillator can be loosely regarded as an integrated version of the delayed oscillator. The mechanism described by the recharge oscillator is hypothesized to have value in forecasting ENSO beyond the spring persistence barrier due to the slow adjustment time of oceanic equatorial heat content (McPhaden, 2003). To leading order, the recharge oscillator agrees well with observations of eastern Pacific (i.e. 'canonical') El Niño events, with SST anomalies peaking in the cold tongue region (Meinen and McPhaden, 2000). However, the recharge oscillator mechanism is less able to emulate observations of central Pacific (or Modoki) events with peak warming near the western Pacific warm pool edge, as the discharge and recharge of equatorial heat content plays a less important role during central Pacific El Niño events (Kug et al., 2010; McPhaden, 2012; Singh and Delcroix, 2013; Graham et al., 2014). It has also been suggested that external forcing is required

to initiate central Pacific El Niño events, and this event can be described as a damped oscillation, rather than the self-sustaining oscillation that describes the eastern Pacific El Niño events (Yeh et al., 2014).

Finally, the advective-reflective oscillator (Picaut et al., 1997) emphasizes the importance of the edge of the western Pacific warm pool in the growth and transition of an ENSO event. Development of a warm event is provided by the Bjerknes positive feedback mechanism and eastwards advection of the edge of the warm pool by anomalous zonal currents. The subsequent transition to La Niña occurs due to westwards displacement of the edge of the warm pool by two sets of zonal currents. The first set is a result of wave reflection at both boundaries of the Pacific. The second is the mean westward zonal equatorial surface current that is stronger in the eastern Pacific and has a greater influence on the westwards advection of the warm pool edge. Brown et al. (2013) have further suggested it is the gradient of the zonal current that is important in setting the decay rate. The advective-reflective oscillator generally accords well with observations, playing an important role in the growth and decay of the 1997-98 El Niño event (Picaut et al., 1996; Boulanger and Menkes, 1999). Shu and Clarke (2002) use a similar mechanism to that described by the advective-reflective oscillator in an intermediate complexity model to demonstrate that zonal advection and wave dynamics are able to reproduce the patterns of SST anomaly evolution characteristic of central and eastern Pacific ENSO events.

Wang (2001, hereafter W01) combined the four above-mentioned conceptual models in a system of delay differential equations that became known as the unified oscillator (UO). W01 argues that since it is likely that multiple mechanisms are responsible for the decay of an ENSO event, the unification of a number of conceptual models should more accurately describe the ENSO cycle than each of the mechanisms alone. Using selected parameter values, W01 demonstrates that the UO produces oscillations on ENSO timescales (every 2-7 years). The UO is an often cited theory to account for ENSO growth and transition (e.g. Guilyardi et al., 2003; Wang and Picaut, 2004; Guilyardi et al., 2009; Duan et al., 2013; Singh and Delcroix, 2013); however, the assumptions underlying the UO and its relevance have not been systematically assessed. Importantly, it

has not been established that the UO model is able to simulate a realistic ENSO period when fit to observations or model data.

In this study, we explore the value of the UO as a conceptual framework for ENSO. We apply the UO theory to the output of an ocean general circulation model (OGCM) simulation - an historical surface flux-forced simulation of the Australian Community Climate and Earth System Ocean Model (ACCESS-OM) - with the aim of determining the extent to which the UO equations for the SST anomaly, thermocline depth anomaly, and zonal wind stress anomaly tendencies can diagnose their corresponding simulated ENSO tendencies. We investigate whether the UO has greater diagnostic power than the models it combines, comparing these underpinning models with their original formulations.

3.3 Data and methods

3.3.1 ACCESS-OM

Monthly means of the analyzed variables are derived from the output of an historical air-sea flux-forced simulation using the Australian Community Climate and Earth System Simulator Ocean Model (ACCESS-OM; Bi et al., 2013a). ACCESS-OM is the ocean/sea-ice component of the ACCESS Coupled Model (ACCESS-CM), a model participant in the Coupled Model Intercomparison Project phase 5 (CMIP5; Bi et al., 2013b). ACCESS-OM draws its codebase and most of its configuration from the NOAA Geophysical Fluid Dynamics Laboratory (GFDL) MOM4 ocean model, versions of which have been used in most of GFDL's contributions to CMIP3 and CMIP5: CM2.0 and CM2.1 (Delworth et al., 2006; Gnanadesikan et al., 2006; Wittenberg et al., 2006), ESM2M (Dunne et al., 2012), CM3 (Griffies et al., 2011), CM2.5 (Delworth et al., 2012), and CM2.5-FLOR (Jia et al., 2015; Vecchi et al., 2014). ACCESS-OM has a zonal resolution of 1° and a meridional resolution of 1/3° between 10°S and 10°N, which extends to 1° between 10°S (°N) and 20°S (°N). The vertical discretization uses a z^* coordinate scheme (Adcroft and Campin, 2004) and there are 50 vertical levels with a resolution extending from 10m in the upper 200m to approximately 333m in the deep ocean. The ACCESS-OM simulation analyzed here is forced with the surface heat, freshwater, and

momentum fluxes derived from the Large and Yeager (2009) forcing and bulk-formulae. The simulation follows the protocols of the CLIVAR Working Group on Ocean Model Development interannually varying Coordinated Ocean-ice Reference Experiments version 2 (CORE-II; Griffies et al., 2012). The accuracy of the CORE-II forcing in the tropical Pacific is difficult to verify due to a sparsity of observational data; however, the incoming solar radiation is generally accurate to within 10 W m^{-2} of mooring data (Large and Yeager, 2009).

SST, thermocline depth, and wind stress anomalies are calculated by subtracting the annual cycle from the monthly values of the model outputs. Multivariate empirical orthogonal functions (EOFs) are then applied to the variables SST, thermocline depth, and zonal wind stress anomalies in the UO, to analyze their spatial patterns of variability and determine the optimal averaging regions from the ACCESS-OM simulation that correspond to the regions defined in W01 (figure 3.1). The region of maximum SST anomaly variability in the eastern Pacific is within the bounds of the standard Niño-3 region (5°S-5°N, 150-90°W); zonal wind stress anomalies are averaged in the modified Niño-4 region (5°S-5°N, 150°E-160°W), which is located 10° west of the standard region, and in the Niño-5 region (5°S-5°N, 120-140°E); and thermocline depth anomalies are averaged in the modified Niño-6 region (8-16°N, 150-170°E). While the modified Niño-6 region is relatively small, it represents a region of maximum interannual variability in thermocline depth and, as such, suffices to take account of the behavior of and variability in thermocline depth anomalies during ENSO events. In what follows, we refer to the modified regions as Niño-4* and Niño-6*, to avoid confusion with the standard versions. The depth averaged potential temperature above 300m is used as a proxy for the thermocline depth, as it is strongly correlated with the 20°C isotherm depth. That is, for variables averaged in the Niño-6* region, 89% of the variance in the 20°C isotherm depth anomaly is explained by the depth averaged temperature anomaly above 300m, for an estimated regression coefficient of 20m $°C^{-1}$.

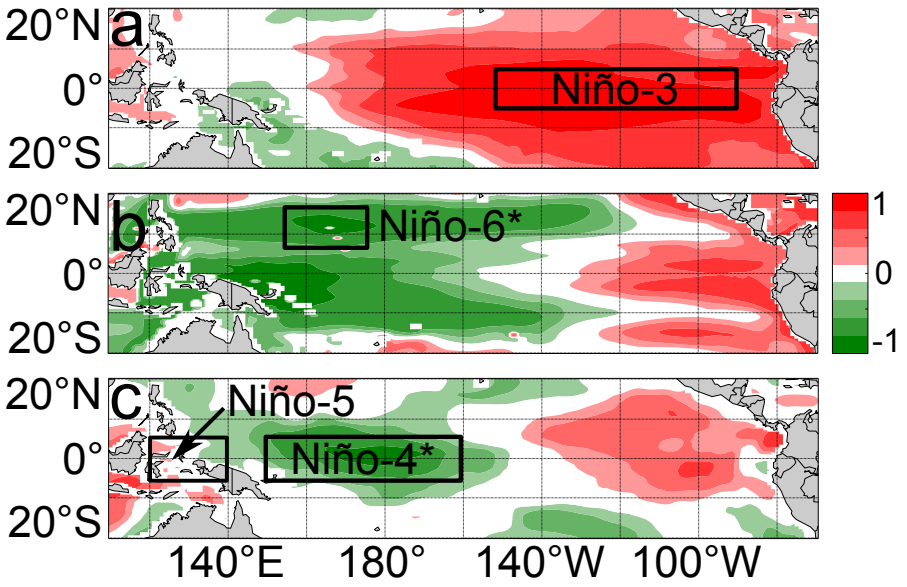

Figure 3.1: Averaging regions for the unified oscillator determined from EOF analysis of **a** SST anomalies; **b** thermocline depth anomalies; and **c** zonal wind stress anomalies. The units are normalized between -1 and 1 and the contour intervals are 0.2 units, with values between -0.2 and 0.2 in white.

3.3.2 The simulated tropical Pacific

In general, ACCESS-OM is a realistic model that reproduces historical ENSO-like variability well (Bi et al., 2013a; Graham et al., 2014), although its accuracy is uncertain to a degree since the atmospheric fluxes forcing ACCESS-OM are poorly known (Wittenberg, 2004). One limit of this study is the relatively short period of time - 60 years from 1948-2007 - over which this ACCESS-OM simulation extends. An alternative would be to use a simulation from a CGCM, although this would have introduced model biases, further complicating the interpretation of our results (Brown et al., 2012).

Surface and subsurface potential temperature data from the Australian Bureau of Meteorology Research Centre (BMRC) ocean analyses (Smith, 1994), derived predominantly from the Tropical Atmosphere Ocean/Triangle Trans-Ocean Buoy Network mooring data and ship-of-opportunity XBT data, are compared with the corresponding ACCESS-OM data. The spatial pattern of SST is similar between the two datasets, although ACCESS-OM is generally warmer in the far eastern off-equatorial Pacific and

cooler in the central-eastern equatorial Pacific (top panels in figure 3.2). Along the equator, ACCESS-OM produces a realistic pattern of subsurface potential temperature, with a deep warm pool in the western equatorial Pacific, shoaling to a thin mixed layer in the eastern equatorial Pacific (bottom panels in figure 3.2). ACCESS-OM is slightly less thermally stratified near the surface. The mean equatorial thermocline depth in ACCESS-OM compares well with the BMRC data, although it has a slightly steeper east-west slope in the central-eastern Pacific (150-120°W). The center of the western Pacific warm pool is also deeper and shifted slightly east in ACCESS-OM.

Figure 3.3 shows the difference between the climatological SST for the ACCESS-OM simulation and the BMRC data. In all seasons, the western Pacific warm pool is warmer in the far west (120-140°E) in ACCESS-OM than in the BMRC data and the equatorial SST in the central-eastern equatorial Pacific (150-100°W) is notably cooler in ACCESS-OM during boreal winter and spring. There is a warm SST bias of less than 1°C in ACCESS-OM in the far eastern off-equatorial Pacific, which is unlikely to have any significant effect on the conclusions of this study.

The unfiltered Niño-3 timeseries (5°S-5°N, 150-90°W) derived from the ACCESS-OM simulation is compared with the corresponding unfiltered timeseries derived from the BMRC dataset, the Simple Ocean Data Assimilation (SODA) version 2.2.4 (Carton and Giese, 2008), and the National Oceanic and Atmospheric Administration Extended Reconstructed SST (ERSST) version 3 dataset (provided by the NOAA/OAR/ESRL from their website at \http://www.esrl.noaa.gov/psd/; figure 3.4a). The magnitude and phase of ENSO is very similar across the four datasets, although the magnitude of ENSO events in ACCESS-OM tends to be slightly larger than the other products. Figure 3.4b compares the standard deviation of the SST anomaly at each longitude and averaged between 2°S and 2°N for the ACCESS-OM, BMRC, SODA, and ERSST datasets. For the same range of years (1980-2000), the ERSST data have a large spike in standard deviation near 100°W, while the remaining datasets display similar variability along the equator. Figures 3.4c-e illustrate the unfiltered timeseries of Niño-3 thermocline depth anomalies, Niño-4* zonal wind stress anomalies, and Niño-5 zonal wind stress anomalies, respectively, from the ACCESS-OM and SODA simulations. There is gen-

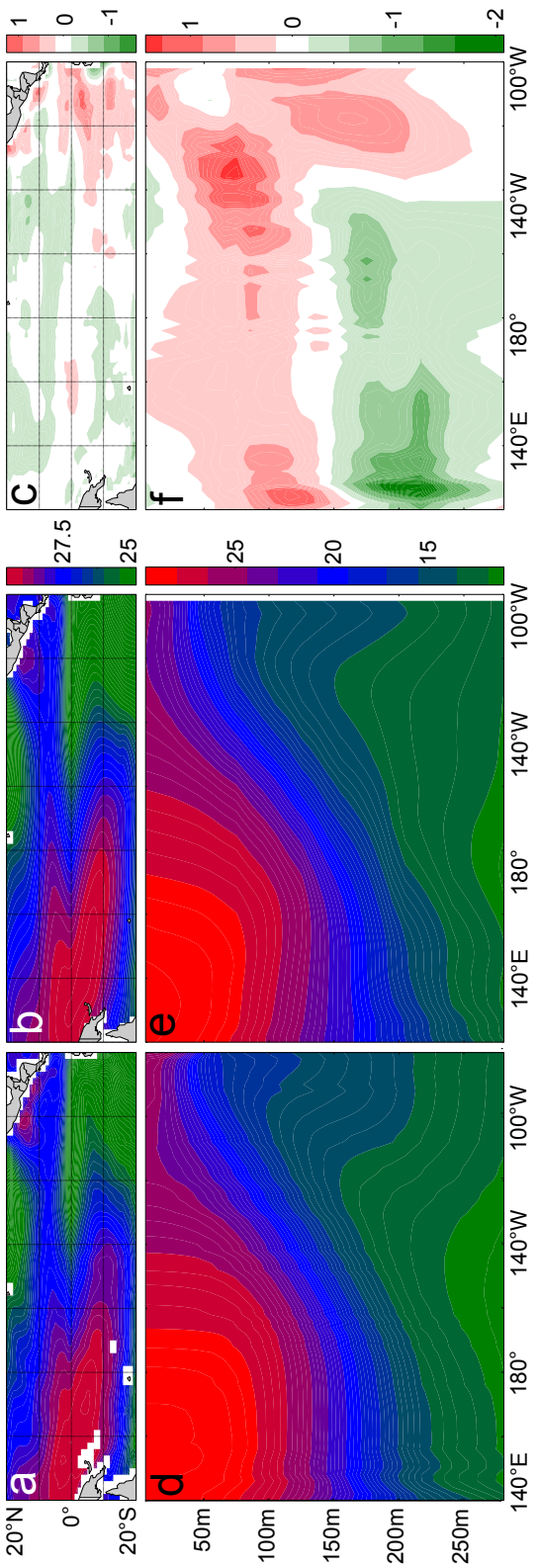

Figure 3.2: Comparison between mean surface (upper plots) and mean equatorial subsurface (lower plots) potential temperature data derived from the BMRC dataset (panels **a** and **d**) and the ACCESS-OM simulation (panels **b** and **e**; originally published as an online resource in Graham et al., 2014). The far right panels (**c** and **f**) show the difference between the ACCESS-OM and BMRC data. Data are in units of °C. The ACCESS-OM and BMRC data are averaged over the period 1980-2004.

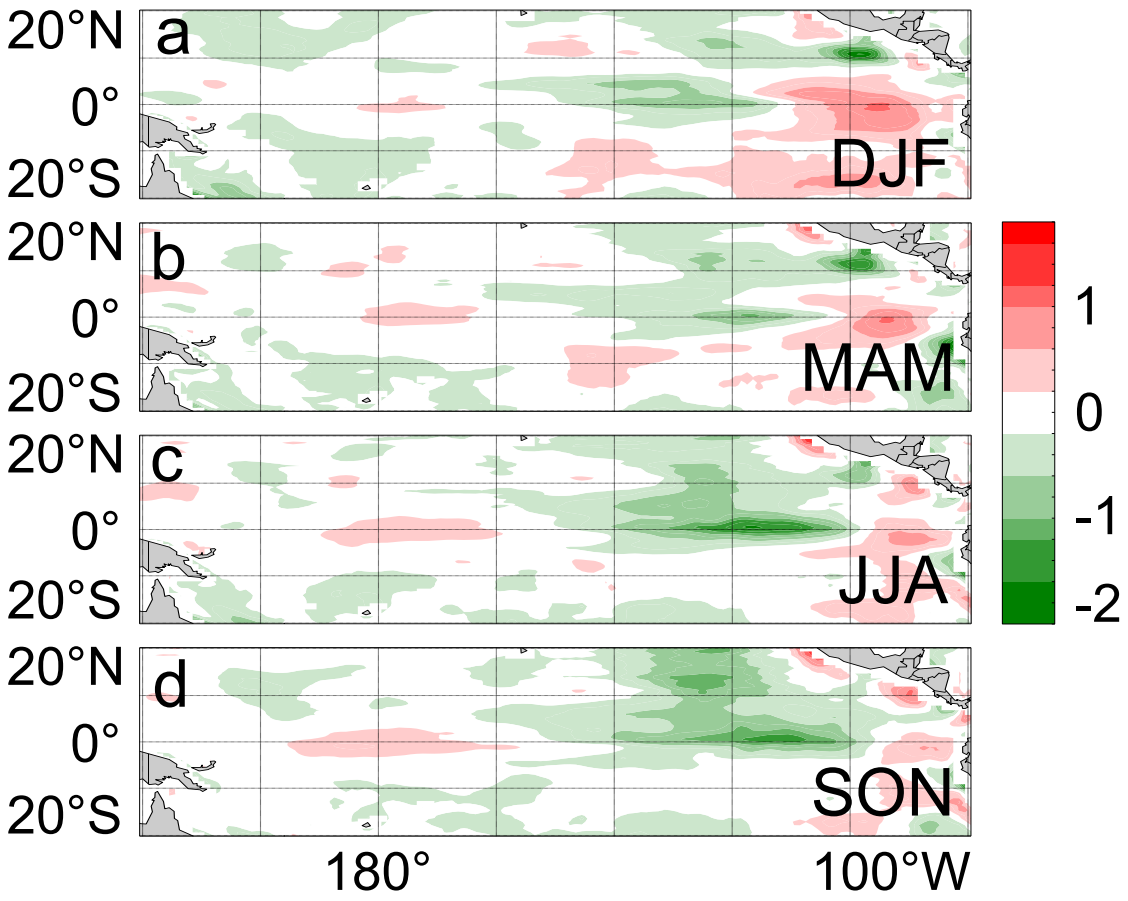

Figure 3.3: Difference between seasonal sea surface temperature (°C) derived from the ACCESS-OM simulation and the BMRC dataset (originally published as an online resource in Graham et al., 2014). The seasonal cycle is averaged over the period 1980-2004. The contour intervals are 0.2°C.

erally a high level of agreement between ACCESS-OM and SODA. Prior to 1970, the Niño-5 zonal wind stress anomalies in ACCESS-OM have a positive bias compared with those of SODA. However, as mentioned previously, the atmospheric fluxes forcing both ACCESS-OM and SODA, including the zonal wind stresses, are poorly known, such that the significance of differences between the Niño-4* and Niño-5 zonal wind stress anomalies in ACCESS-OM and SODA is difficult to accurately quantify.

Mean surface zonal currents from the Ocean Surface Current Analysis Real-time (OSCAR) and ACCESS-OM datasets are plotted in figure 3.5. The ACCESS-OM data

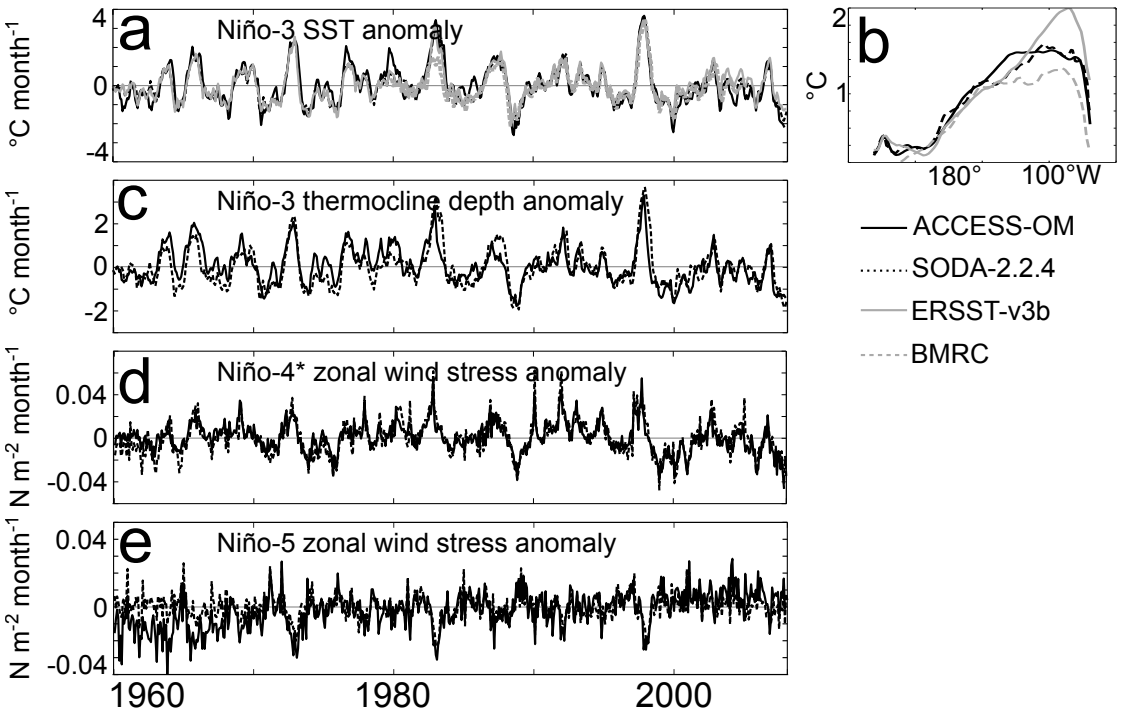

Figure 3.4: In each panel the unfiltered data derived from the ACCESS-OM simulation are illustrated by the black solid line, data from SODA v2.2.4 are illustrated by the dotted line, data derived from ERSST v3b are illustrated by the gray solid line, and data derived from the BMRC dataset are illustrated by the gray dashed line. **a** Niño-3 (5°S-5°N, 150-90°W) SST anomaly indices; **b** standard deviation over the period 1980-2000 of the SST anomalies averaged over 2°S-2°N at each longitude; **c** Niño-3 thermocline depth anomaly indices; **d** Niño-4* (5°S-5°N, 150°E-160°W) zonal wind stress anomaly indices; and **e** Niño-5 (5°S-5°N, 120-140°E) zonal wind stress anomaly indices.

display a small (<0.2m s^{-1}) westward bias in the eastern equatorial Pacific (5°S-5°N, 130-80°W) and in the western-central Pacific (2-8°N, 130°E-130°W), and an eastward bias (< 0.5m s^{-1}) across the entire basin at approximately 10°N and at the equator between 160°E-140°W. Both the ACCESS-OM and OSCAR data are averaged over the period 1993-2007 and in the top 30m.

3.3.3 Generalized least squares regression

To investigate the relative importance of the feedback mechanisms described in the UO and its underpinning conceptual models, parameter values are obtained by fitting the

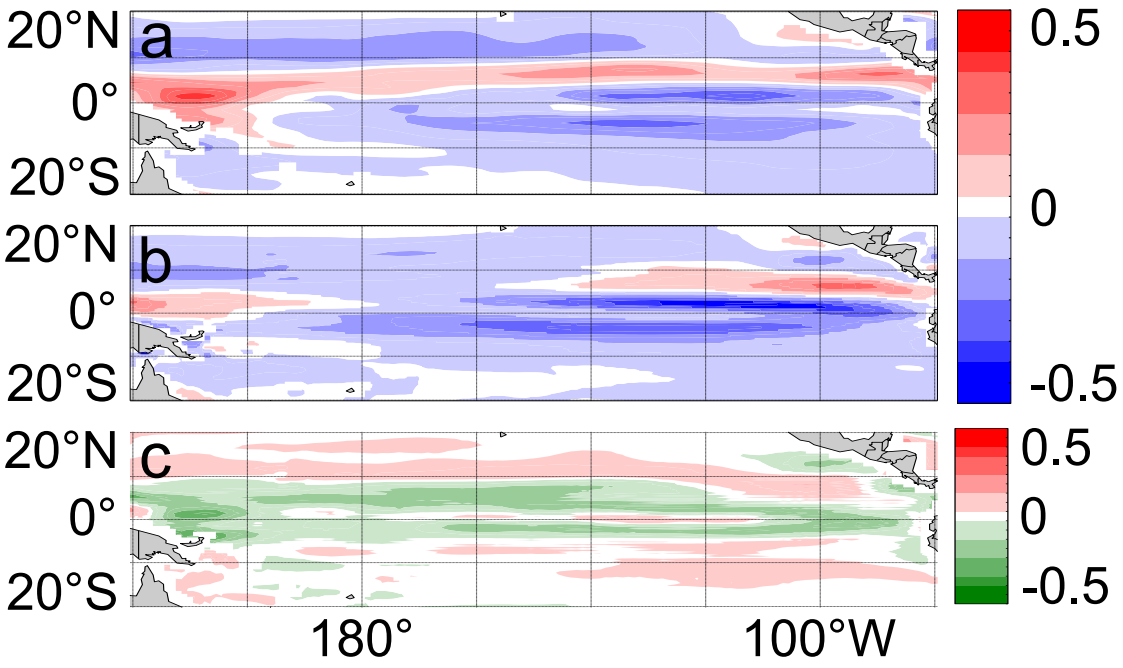

Figure 3.5: Comparison between mean surface zonal current data (m s^{-1}) derived from **a** ACCESS-OM and **b** OSCAR (originally published as an online resource in Graham et al., 2014). Panel **c** shows the difference between the ACCESS-OM and OSCAR data. The data are averaged over the period 1993-2007 in the top 30 m. The contour intervals are 0.1 m s^{-1}.

relevant model equations to the corresponding tendencies calculated directly from the ACCESS-OM simulation data (using centred differences). That is, we fit the UO and underpinning conceptual model formulations of the following equation

$$\frac{dY}{dt} = \alpha_1 X_1 + \alpha_2 X_2 + ... + \alpha_n X_n + E_t, \tag{3.1}$$

where dY/dt is the tendency obtained directly from the ACCESS-OM simulation data and $\{X_n\}$ are the independent variables, to find estimates of the coefficients $\{\alpha_n\}$ that minimize the error term E_t. However, as is often the case for climate data, we find that our data are serially correlated. It follows that ordinary least squares (OLS) regression of each of the model equations will not permit robust estimates of the standard errors and t-statistics of the fit, as evidenced in the autocorrelation (ACF) and partial autocorrelation (PACF) functions of the fitted residuals (von Storch and Zwiers, 1999). For example, the ACF and PACF estimates for the OLS fit of the delayed oscillator SST anomaly

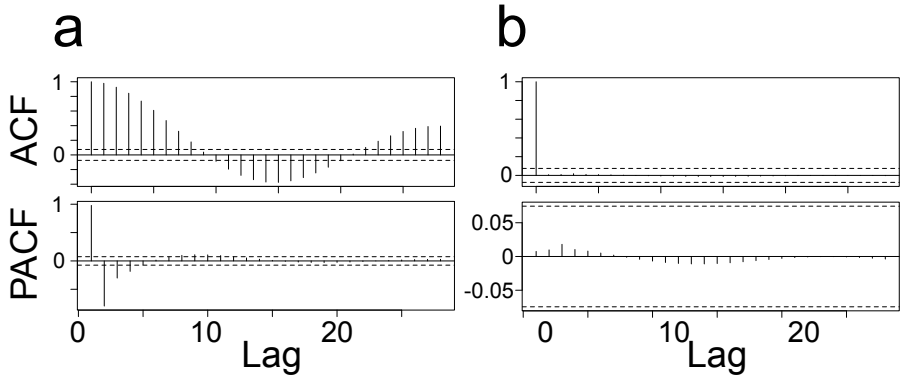

Figure 3.6: Autocorrelation (ACF; upper panels) and partial autocorrelation (PACF; lower panels) functions of the residuals from the fitting analysis of the original delayed oscillator SST anomaly Eq. (3.8). Panel **a** illustrates the results from ordinary least squares, where no error correlation structure is assumed. Panel **b** illustrates the minimization of the residuals when an AR(3) error correlation structure is assumed. The dashed lines represent the 95% confidence intervals for the null hypothesis that the autocorrelation and partial autocorrelation values are zero, for lags of one or more. Note the different scales on the y-axes of the PACFs in panels **a** and **b**.

tendency Eq. (3.8) clearly demonstrate serial correlation in the residuals (figure 3.6a).

To address the issue of serial correlation, we refit the conceptual model equations assuming a correlated error structure using generalized least squares (GLS) regression. We follow a similar procedure to that presented in Dong et al. (2008). Autoregressive processes of order p (AR(p); von Storch and Zwiers, 1999), for values of $p = 0, 1, 2$, and 3, are fit to the residuals to remove the correlation structure of the errors (e.g. figure 3.6b). Since the models AR(0), AR(1), ..., AR(3) are nested, the optimal values of p can be easily determined from a likelihood ratio test. In each fitting, the ACF and PACF estimates are used to verify that: (i) the timeseries are serially correlated; and (ii) the AR(p) model selected using the likelihood ratio test indeed minimizes the residuals from which the effect of the fitted correlation structure has been removed. The regression model is tested using a 9-fold cross-validation scheme (Hastie et al., 2001; Lima et al., 2009). The data are first divided into 9 equal samples, which ensures that the resulting sequence of approximately 60 months consists of at least one temporal degree of freedom for the ENSO system. For the kth sample, the parameters of each of the conceptual model

equations are estimated using the first $k-1$ samples. Using these parameter values, an estimate of the skill of the model is calculated using the kth sequence of withheld data. Non-zero delay parameters in the conceptual model equations are chosen to minimize the root mean square error (rmse) of the cross validated results, while yielding non-negative values for the coefficients. GLS analysis is undertaken using the open-source R statistical programming language (\http://www.r-project.org/; R Development Core Team, 2008). The anomalous data are linearly detrended and filtered prior to fitting using a 12-month parzen filter to remove variability with frequencies shorter than 12 months. When the analysis is repeated using a 3-month parzen filter prior to fitting we find that the performance of the UO and its underpinning models is generally slightly worse than when a 12-month filter is applied.

3.4 The conceptual models

The UO model equations are first introduced, followed by the delayed oscillator, recharge oscillator, and western Pacific oscillator equations that are derived from the UO. The advective-reflective oscillator equation for the SST anomaly tendency, that includes one extra term than in the corresponding UO equation describing reflection of waves at the eastern boundary, is also introduced. The UO versions of the delayed oscillator, recharge oscillator, and western Pacific oscillator models are further contrasted with their original formulations.

3.4.1 The unified oscillator

The UO is represented by the following system of delay differential equations (W01):

$$\frac{dT_3}{dt} = \underbrace{a\tau_4^x}_{[1]} - \underbrace{b_1\tau_4^x(t-\eta)}_{[2]} + \underbrace{b_2\tau_5^x(t-\delta)}_{[3]} - \underbrace{\varepsilon T_3}_{[4]}, \tag{3.2}$$

$$\frac{dh_6}{dt} = -c\tau_4^x(t-\lambda) - R_h h_6, \tag{3.3}$$

$$\frac{d\tau_4^x}{dt} = eT_3 - R_{\tau_4^x}\tau_4^x, \tag{3.4}$$

$$\frac{d\tau_5^x}{dt} = kh_6 - R_{\tau_5^x}\tau_5^x. \tag{3.5}$$

where T_3 is the Niño-3 SST anomaly, derived from the Lamont intermediate-complexity model of equatorial SST (Zebiak and Cane, 1987), and h_6 is the Niño-6* region thermocline depth anomaly, adapted from the vorticity equation for low-frequency, off-equatorial Rossby waves (Meyers, 1979; Kessler, 1990). A reduced gravity atmospheric model forced by thermodynamic heating anomalies is used in W01 to derive the zonal wind stress anomalies - namely, the Niño-4* region averaged zonal wind stress anomaly τ_4^x, and the Niño-5 region averaged zonal wind stress anomaly τ_5^x. The derivation of Eqs. (3.2) - (3.5) in W01, including the underlying balance relations, is outlined in the appendix. The terms a, b_1, b_2, c, e, k, ε, R_h, $R_{\tau_4^x}$, and $R_{\tau_5^x}$ are constants. In the original paper, W01 uses theoretical arguments and similar studies (e.g. Battisti and Hirst, 1989; Weisberg and Wang, 1997) to derive values for these coefficients and to constrain the system to ensure an oscillation on ENSO-like timescales. The suitability of the W01 parameter values to the ACCESS-OM simulation is analyzed in section 3.5.

Term [1] on the right-hand side of Eq. (3.2) is the Bjerknes positive feedback term, which describes the atmospheric response to changes in SST. Term [2] represents reflection of off-equatorial Rossby waves at the western boundary (i.e. the delayed oscillator), where η represents the time taken for the Rossby waves to reflect at the western boundary and propagate as an equatorial Kelvin wave to the eastern Pacific. Term [3] in Eq. (3.2) represents the forcing stress from easterly anomalous winds in the western Pacific generating an eastward propagating equatorial Kelvin wave (the western Pacific oscillator), where δ represents the time taken for the Kelvin wave to propagate eastwards. Term [4] in Eq. (3.2) is a damping term that takes into account processes such as advection and convection, limiting the growth of the ENSO mode. In W01 the damping term is cubic; however, in our fitting analyses we find that a linear damping term produces smaller rmses than a cubic term and is therefore adopted here.

In Eq. (3.3), the first term on the right-hand side represents the meridional transport of heat content (the recharge oscillator), where the delay parameter λ is the lag time between the basin-wide discharge-recharge mode and the anomalous zonal wind stress. The second term on the right-hand side of Eq. (3.3) represents damping from a variety of processes. Eqs. (3.4) and (3.5) close the system by relating zonal wind stress anomalies

to SST and thermocline depth anomalies. The derivative form of Eqs. (3.4) and (3.5) do not conform to the steady atmosphere used in previous studies (Battisti and Hirst, 1989; Jin, 1997a,b). Curiously, neither of Eqs. (3.4) and (3.5) include explicit noise terms, which contribute significantly to wind stresses in the Niño-4* and Niño-5 regions (Vecchi et al., 2006). We also note that Eq. (3.5) relates τ_5^x directly to thermocline depth anomalies, when in reality τ_5^x depends on h_6 through local SST anomalies, which themselves are a function of the position of the warm pool edge, variations in wind- and buoyancy-induced mixing, and barrier layer transience.

By a series of approximations, the UO reduces to modified formulations of the delayed oscillator (denoted the UDO), recharge oscillator (URO), and western Pacific oscillator (UWPO), which are discussed in the following subsections alongside their original formulations. The UO formulation of the advective-reflective oscillator (denoted the UARO), which consists of the four UO equations and an additional term describing wave reflection at the eastern boundary, is also discussed.

3.4.2 The delayed oscillator

W01 derives the delayed oscillator from the UO (i.e., the UDO) by setting $b_2 = 0$ in Eq. (3.2), decoupling the system of delay differential equations to yield the following

$$\frac{dT_3}{dt} = a\tau_4^x - b_1\tau_4^x(t-\eta) - \varepsilon T_3, \tag{3.6}$$

$$\frac{d\tau_4^x}{dt} = eT_3 - R_{\tau_4^x}\tau_4^x, \tag{3.7}$$

where a, b_1, ε, e, $R_{\tau_4^x}$, and η are identical to those coefficients in the UO Eqs. (3.2) and (3.4).

In the original delayed oscillator equation derived by Battisti and Hirst (1989), the zonal wind stress anomaly averaged in the Niño-4* region is assumed to be proportional to the SST anomaly averaged in the Niño-3 region ($\tau_4^x = eT_3/R_{\tau_4^x}$, obtained from Eq. (3.7) by setting $d\tau_4^x/dt = 0$) yielding the following single equation for the SST anomaly tendency

$$\frac{dT_3}{dt} = \frac{ae}{R_{\tau_4^x}}T_3 - \frac{b_1 e}{R_{\tau_4^x}}T_3(t-\eta), \tag{3.8}$$

where $ae/R_{\tau_4^x}$ now parameterizes the Bjerknes positive feedback process and thermodynamic damping, and $b_1 e/R_{\tau_4^x}$ is the negative feedback term corresponding to term [2] in Eq. (3.2). We highlight the lack of an explicit damping term ε in Eq. (3.8); in the formulation of Battisti and Hirst (1989), the damping term is linear in SST so we incorporate this term into the coefficient $ae/R_{\tau_4^x}$. Note also that Eq. (3.8) implicitly includes thermocline depth variability since the thermocline depth anomaly in the eastern Pacific (i.e., h_E) is proportional to the sum of the instantaneous response to equatorial wind stresses, plus a delayed response due to off-equatorial wind curl.

3.4.3 The recharge oscillator

The recharge oscillator model assumes that during an El Niño (La Niña) event, the atmosphere responds almost instantaneously to warm (cool) SST anomalies in the central-eastern equatorial Pacific and the resultant change in the wind stress curl incites discharge (recharge) of equatorial heat content (Clarke et al., 2007). Hence, in the derivation of the URO, the anomalous zonal wind stress tendencies in the Niño-4* and Niño-5 regions from Eqs. (3.4) and (3.5) are set to zero, yielding

$$\tau_4^x = \frac{e}{R_{\tau_4^x}} T_3, \qquad\qquad \tau_5^{xL} = \frac{k}{R_{\tau_5^x}} h_6, \tag{3.9}$$

where τ_5^{xL} is the low-frequency component of τ_5^x. These relations are substituted into Eqs. (3.2) and (3.3) and, setting each of the delay constants to zero, W01 derives the following coupled system of differential equations for the URO

$$\frac{dT_3}{dt} = \frac{ae - b_1 e}{R_{\tau_4^x}} T_3 + \frac{b_2 k}{R_{\tau_5^x}} h_6 - \varepsilon T_3, \tag{3.10}$$

$$\frac{dh_6}{dt} = -\frac{ce}{R_{\tau_4^x}} T_3 - R_h h_6. \tag{3.11}$$

Again, the constants a, b_1, b_2, ε, e, k, R_h, $R_{\tau_4^x}$, and $R_{\tau_5^x}$ are identical to those in Eqs. (3.2)-(3.5). The term $(ae - b_1 e)/R_{\tau_4^x}$ in Eq. (3.10) parameterizes growth by the Bjerknes positive feedback and the term $b_2 k/R_{\tau_5^x}$ parameterizes thermocline feedback processes. From Eq. (3.11), $ce/R_{\tau_4^x}$ represents Sverdrup transport north and south of the equatorial region, while R_h represents damping of thermocline depth anomalies, mediated by upwelling (Mechoso et al., 2003).

The recharge oscillator equations derived by Jin (1997a) can be written

$$\frac{dT_3}{dt} = \frac{ae - b_1 e}{R_{\tau_4^x}} T_3 + \frac{b_2 k}{R_{\tau_5^x}} h_W, \tag{3.12}$$

$$\frac{dh_W}{dt} = -\frac{ce}{R_{\tau_4^x}} T_3 - R_h h_W. \tag{3.13}$$

These equations differ from the URO Eqs. (3.10) and (3.11) with respect to the region in which the thermocline depth anomaly is defined: while h_6 in Eq. (3.10) is averaged off-equatorially in the Niño-6* region, in Eqs. (3.12) and (3.13) the thermocline depth anomaly, denoted h_W, is averaged in the western equatorial Pacific (5°S-5°N, 140°E-180°E). Similar to the original delayed oscillator equations, the damping term εT_3 from Eq. (3.10) is not explicit in Eq. (3.12).

3.4.4 The western Pacific oscillator

W01 derives the UWPO SST anomaly equation from the UO by setting b_1 in Eq. (3.2) to zero, yielding

$$\frac{dT_3}{dt} = a\tau_4^x + b_2 \tau_5^x (t - \delta) - \varepsilon T_3. \tag{3.14}$$

The remaining equations for thermocline depth and zonal wind stress anomalies are identical to the UO Eqs. (3.3)-(3.5).

By contrast with the UWPO, the original western Pacific oscillator does not explicitly take into account SST anomalies, instead including prognostic equations for thermocline depth anomalies in the eastern equatorial and western off-equatorial Pacific (Weisberg and Wang, 1997). The original model comprises a system of four delay differential equations

$$\frac{dh_3}{dt} = a^h \tau_4^x + b_2^h \tau_5^x (t - \delta) - \varepsilon^h h_3. \tag{3.15}$$

$$\frac{dh_6}{dt} = -c\tau_4^x (t - \lambda) - R_h h_6, \tag{3.16}$$

$$\frac{d\tau_4^x}{dt} = e^h h_3 - R^h_{\tau_4^x} \tau_4^x, \tag{3.17}$$

$$\frac{d\tau_5^x}{dt} = k h_6 - R_{\tau_5^x} \tau_5^x, \tag{3.18}$$

where the coefficients c, k, R_h and $R_{\tau_5^x}$ are identical to those in the UO Eqs. (3.3) and (3.5), and the remaining constants a^h, b_2^h, e^h, ε^h, and $R^h_{\tau_4^x}$ have similar physical

interpretations to their counterparts in Eqs. (3.14) and (3.4) that were parameterized in terms of T_3. The variable h_3 denotes the Niño-3 averaged equatorial thermocline depth anomaly while the variable h_6 denotes the Niño-6* off-equatorial thermocline depth anomaly. In the original formulation, the damping terms were cubic. However, the linear and cubic forms of the damping terms do not result in significantly different estimates for the coefficients, so we adopt only linear forms here.

3.4.5 The advective-reflective oscillator

While the advective-reflective oscillator was well described by Picaut et al. (1997), W01 first defined the UARO in a system of delay differential equations. In W01, the UARO model couples Eqs. (3.3) - (3.5) of the UO with the following equation for the Niño-3 SST anomaly tendency

$$\frac{dT_3}{dt} = a\tau_4^x - b_1\tau_4^x(t-\eta) + b_2\tau_5^x(t-\delta) - b_3\tau_4^x(t-\mu) - \varepsilon T_3, \tag{3.19}$$

where all but the fourth term on the right hand side of Eq. (3.19), which represents wave reflection at both the eastern and western boundaries of the Pacific, are identical to the terms in Eq. (3.2).

3.5 Analysis of the conceptual models

Table 3.1 summarizes the main results from the GLS fits of the UO and conceptual models it attempts to unify, as well as the original versions of the delayed, recharge, and western Pacific oscillators. The calculated rmse values and explained variances, ρ^2, are also reported, along with the statistical significance of each of the fitted parameters.

3.5.1 SST tendency equations

Unified oscillator and underpinning models

We first consider how well the UO equation captures the SST anomaly tendency in the ACCESS-OM simulation using: (1) the parameter values given by W01, and (2) the parameter values estimated via GLS regression to the model data.

Table 3.1: Regression coefficients obtained via GLS regression of the UO, Eqs. (3.2) - (3.5), and the original and UO versions of the delayed, recharge, western Pacific, and advective-reflective oscillators, Eqs. (3.6) - (3.19). In each case, the 'U' prefix denotes a model that has been derived from the UO. The explained variance (ρ^2) of the fitted curves to the model tendencies along with the corresponding rmse values are reported. Estimates for the parameter values significant at the 95% confidence interval ($p < 0.05$ estimated using a two-sided Student's t-test) are shown in bold. The parameters in W01 are also listed. Coefficients marked with an asterisk * are derived from the original WPO equation for Niño-3 (5°S-5°N, 150-90°W) thermocline depth and have different units to the corresponding fitted values from other models (see Eq. (3.15)). Coefficients marked with a cross $^+$ are derived from the original WPO equation for Niño-4* (5°S-5°N, 150°E-160°W) zonal wind stress, parameterized in terms of the Niño-3 thermocline depth, and have different units to the corresponding fitted values from other models (see Eq. (3.18)).

Constant	UO	UDO	DO	URO	RO	UWPO	WPO	UARO	W01
SST equations: dT_3/dt									
a, °C (N m^{-2})$^{-1}$ month^{-1}	**8.8**	**11**	-	-	-	**2.8**	0*	**23**	13
b_1, °C (N m^{-2})$^{-1}$ month^{-1}	**13**	**16**	-	-	-	-	-	4.5	21
b_2, °C (N m^{-2})$^{-1}$ month^{-1}	1.1	-	-	-	-	**1.8**	8.6*	0.34	63
b_3, °C (N m^{-2})$^{-1}$ month^{-1}	-	-	-	-	-	-	-	21	21
$ae/R_{\tau_4^x}$, month^{-1}	-	-	**0.16**	-	-	-	-	-	-
$b_1 e/R_{\tau_4^x}$, month^{-1}	-	-	**0.20**	-	-	-	-	-	-
$(a-b_1)e/R_{\tau_4^x}$, month^{-1}	-	-	-	0	**0.066**	-	-	-	-
$b_2 k/R_{\tau_5^x}$, month^{-1}	-	-	-	0.013	**0.18**	-	-	-	-
ε, month^{-1}	0	0	-	-	-	**0.025**	0*	0	0.10
η, months	6	5	5	-	-	-	-	7	5
δ, months	2	-	-	-	-	3	3*	2	1
μ, months	-	-	-	-	-	-	-	2	3
ρ^2, %	61	58	94	≈ 0	35	14	11*	67	10
Rmse, °C month^{-1}	0.062	0.052	0.052	0.10	0.076	0.093	0.070*	0.068	0.71
Thermocline equations: dh_6/dt									
c, °C (N m^{-2})$^{-1}$ month^{-1}	0	-	-	-	-	0	0	0	6.3
$ce/R_{\tau_4^x}$, month^{-1}	-	-	-	0.0034	**0.071**	-	-	-	-
R_h month^{-1},	0	-	-	**0.042**	**0.068**	0	0	0	0.42
λ, months	6	-	-	-	-	6	6	6	6
ρ^2, %	0	-	-	4.6	54	0	0	0	0.11
Rmse, °C month^{-1}	0	-	-	0.040	0.043	0	0	0	0.16
Niño-4* wind stress equations: $d\tau_4^x/dt$									
e, N m^{-2} °C^{-1} month^{-1}	0	0	-	-	-	0	**0.0015**$^+$	0	0.0030
$e/R_{\tau_4^x}$, °C^{-1} (N m^{-2})	-	-	**0.0096**	**0.0096**	**0.0096**	-	-	-	-
$R_{\tau_4^x}$, month^{-1}	0.032	0.032	-	-	-	0.032	**0.13**$^+$	0.032	0.17
ρ^2, %	0.00013	0.00013	58	58	58	0.00013	1.0$^+$	0.00013	2.9
Rmse, N m^{-2} month^{-1}	0.0010	0.0010	0.0059	0.0059	0.0059	0.0010	0.0012$^+$	0.0010	0.0020
Niño-5 wind stress equations: $d\tau_5^x/dt$									
k, N m^{-2} °C^{-1} month^{-1}	**0.00054**	-	-	-	-	**0.00054**	**0.00054**	**0.00054**	0.0050
$k/R_{\tau_5^x}$, °C^{-1} (N m^{-2})	-	-	-	**0.0098**	-	-	-	-	-
$R_{\tau_5^x}$, month^{-1}	0.0051	-	-	-	-	0.0051	0.0051	0.0051	0.17
ρ^2, %	0.0013	-	-	3.5	-	0.0013	0.0013	0.0013	0.052
Rmse, N m^{-2} month^{-1}	0.00069	-	-	0.0066	-	0.00069	0.00069	0.00069	0.0031

The W01 curve provides a poor fit to the model dT_3/dt (rmse = 0.71°C month^{-1}, $\rho^2 = 14\%$, $dt = 1$ month), generally producing stronger growth followed by large, cool events that tend to terminate quickly (note that the W01 coefficients are converted to units of months). Essentially, the W01 coefficients overestimate each of the positive and negative feedbacks in Eq. (3.2). This is particularly evident for the western Pacific oscillator negative feedback coefficient b_2, which is over 50 times the size of the GLS estimate. The W01 value for the Bjerknes positive feedback coefficient a and the delayed oscillator negative feedback coefficient b_1 are of a similar order to the fitted values (W01 derives the latter two values from Battisti and Hirst (1989)).

By contrast with the W01 curve, there is a much closer fit between the curve obtained using GLS regression analysis and the model dT_3/dt (rmse = 0.062°C month^{-1}, $\rho^2 = 61\%$; figure 3.7a). However, it is possible that the GLS analysis results in an overfitting of the UO equation. To test this hypothesis, the individual balance relations used in W01 to derive the UO Eq. (3.2) - namely Eqs. (3.25) and (3.28) from the appendix - are refit to the ACCESS-OM simulation data. The coefficients estimated from these equations, and the corresponding compiled estimates for the UO coefficients a, b_1, and b_2, are compared with the values estimated directly from Eq. (3.2) in table 3.2. The two fitting methods result in considerably different values for the coefficients, with differences of up to 4 orders of magnitude between the two estimates. The GLS analysis of Eq. (3.28) results in a value for β that is statistically indistinguishable from zero, leading to a fitted curve explaining 72% of the variance in h_3 calculated directly from ACCESS-OM (rmse=0.29°C).

Next, the UO component oscillators are fit to dT_3/dt from the ACCESS-OM simulation data using GLS regression (figure 3.8). In each case we use the formulation of the individual oscillators derived from the UO - namely the UARO, UDO, URO, and UWPO - rather than their original formulations (which are discussed in the following subsection). Compared with the UO, the UARO model provides a better fit to the model dT_3/dt ($\rho^2 = 67\%$); however, we note that this result is expected since the UARO model adds a parameter to the UO. The fit of the UDO to the ACCESS-OM simulation data is slightly worse than the UO ($\rho^2 = 64\%$), although the differences are not statistically significant

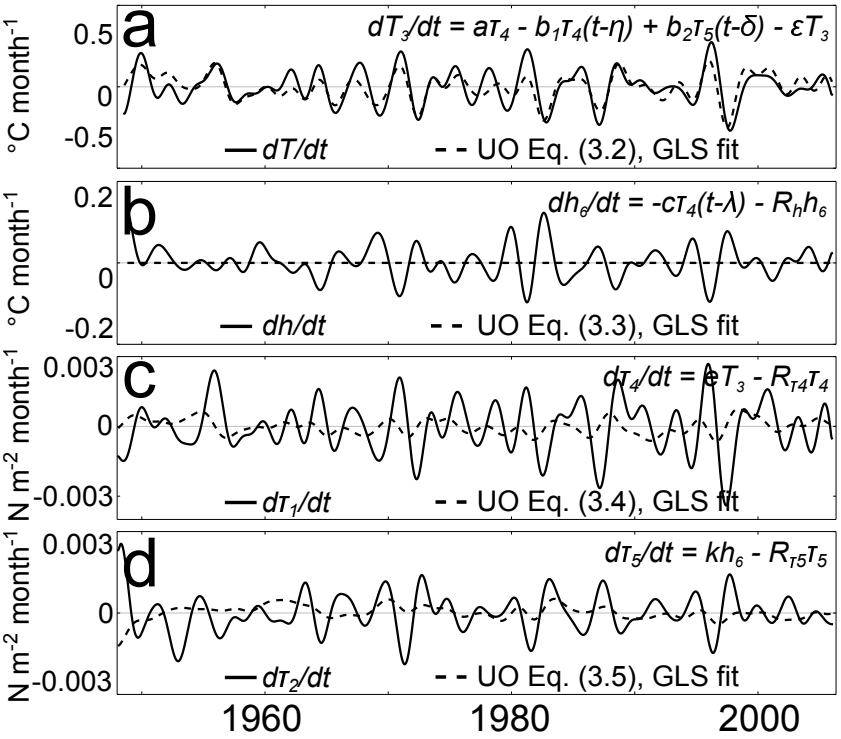

Figure 3.7: Fitted curves for the UO model using ACCESS-OM. In each panel, the solid black line is the tendency determined directly from ACCESS-OM, and the dashed line is the tendency calculated from the right-hand side of the relevant equation where the coefficients are estimated via GLS regression. All data are filtered with a 12 month Parzen filter prior to fitting. **a** The Niño-3 (5°S-5°N, 150-90°W) SST anomaly tendency dT_3/dt calculated from the UO Eq. (3.2); **b** the Niño-6* (8°S-16°N, 150-170°E) thermocline depth anomaly tendency dh_6/dt calculated from the UO Eq. (3.3); **c** the Niño-4* (5°S-5°N, 150°E-160°W) zonal wind stress anomaly tendency $d\tau_4^x/dt$ calculated from the UO Eq. (3.4); and **d** the Niño-5 (5°S-5°N, 120-140°E) zonal wind stress anomaly tendency $d\tau_5^x/dt$ calculated from the UO Eq. (3.5). Note that since the coefficients for Eq. (3.3) estimated using GLS are statistically indistinguishable from zero, the thick line is close to the origin in panel **b**.

at the 95% confidence interval ($p = 0.48$, for a two-sided t-distribution). The fit of the URO returns a value for $(a - b_1)e/R_{\tau_4^x}$ that is trivial (statistically indistinguishable from zero), leading to a fitted curve that explains essentially none of the variance in the simulated tendency. This result is obtained when ε is equal to zero; for $\varepsilon > 0$, the URO coefficient matrix is singular and unable to be fit to the simulated tendency. The poor fit of Eq. (3.10) is most likely due to the thermocline depth anomaly being defined off-

Table 3.2: Regression coefficients obtained via GLS regression of the individual balance relations Eqs. (3.25) and (3.28) in the appendix, and the derived values for the constants a, b_1, and b_2 from these individual balance relations, compared with the constants estimated directly from the UO Eq. (3.2). The explained variance (ρ^2) of the fitted curves to the model tendencies along with the corresponding rmse values are reported. Estimates for the parameter values significant at the 95% confidence interval ($p < 0.05$, estimated using a two-sided Student's t-test) are shown in bold.

Constants	Eqs. (3.25) and (3.28)	UO Eq. (3.2)
R °C (N m^{-2})$^{-1}$ month^{-1}	**15**	-
K_E month^{-1}	**0.26**	-
ρ^2 (%)	3.6	-
Rmse °C month^{-1}	0.10	
α °C (N m^{-2})$^{-1}$	**50**	-
γ °C (N m^{-2})$^{-1}$	**12**	-
β °C (N m^{-2})$^{-1}$	0	-
η months	8	-
δ months	1	-
ρ^2 (%)	72	-
Rmse °C	0.29	
$a = R + \alpha K_E$	28	8.8
$b_1 = \gamma K_E$	2.9	13
$b_2 = \beta K_E$	0	1.1

rather than on-equator, as discussed in the following subsection.

For a delay term δ of 3 months, and assuming an AR(2) error correlation structure, the UWPO coefficients found by GLS regression of Eq. (3.14) result in a fitted curve explaining 14% of the variance in the model dT_3/dt. Although this does not necessarily imply that the western Pacific oscillator negative feedback mechanism is unimportant in modeling the behavior of ENSO, we note that the UO and UARO weight the coefficient b_2 as least important in contributing to the transition of an ENSO event. It is possible that the UWPO negative feedback is incorrect, or ill-suited to the actual physical mechanism operating in ACCESS-OM.

Based on these fits we perform a quick ranking of the relative importance of each of

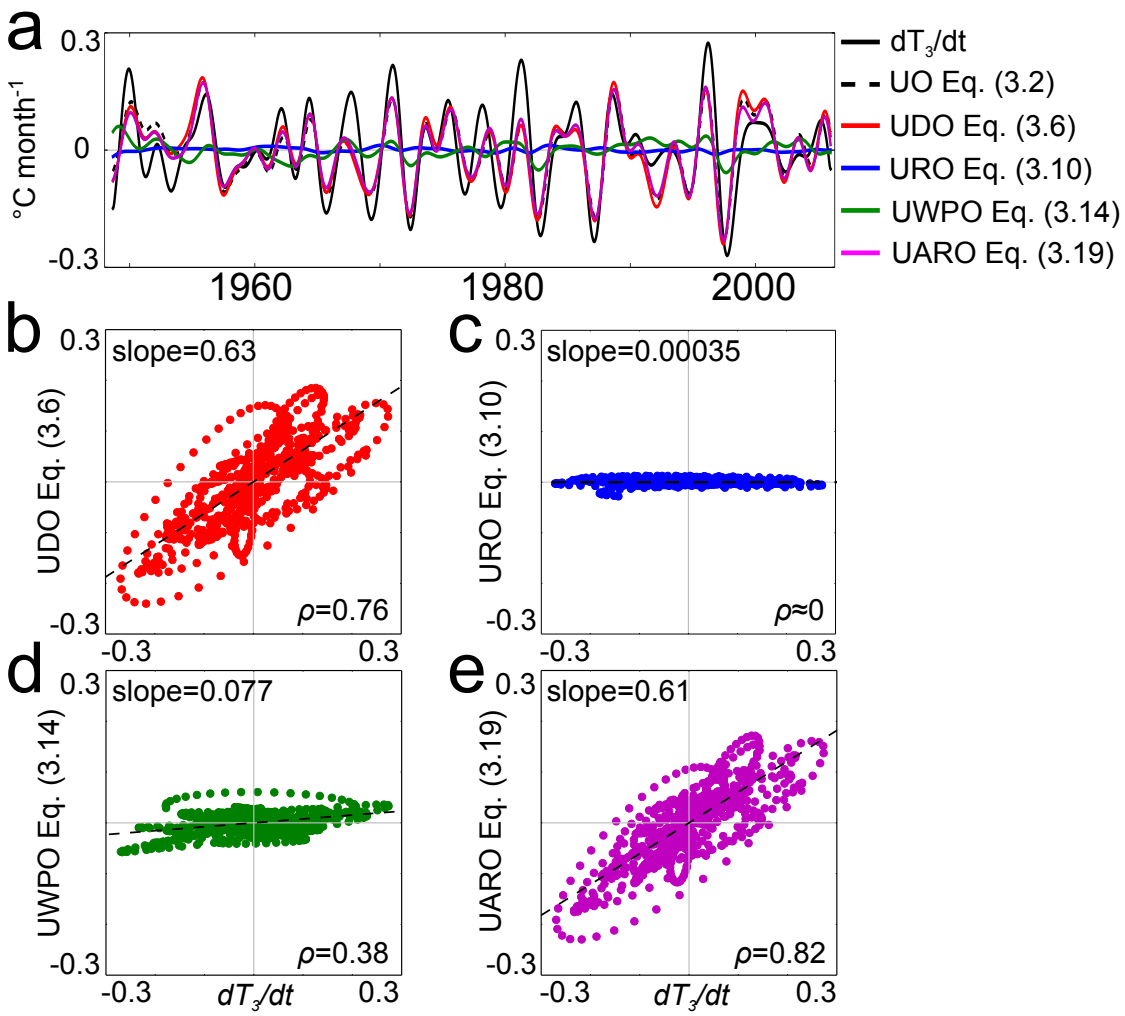

Figure 3.8: Comparison of the fits to the ACCESS-OM SST anomaly tendency dT_3/dt by each of the UO component oscillators where the coefficients are estimated using GLS regression. **a** The black line is dT_3/dt determined directly from ACCESS-OM. The red line corresponds to the right-hand side of Eq. (3.6) for the delayed oscillator (UDO), the dark blue line corresponds the right-hand side of Eq. (3.10) for the recharge oscillator (URO), the green line corresponds to the right-hand side of Eq. (3.14) for the western Pacific oscillator (UWPO), and the magenta line corresponds to the right-hand side of Eq. (3.19) for the advective-reflective oscillator (UARO). **b-e** Scatter plots of dT_3/dt (°C month^{-1}) determined directly from ACCESS-OM (x-axis) against dT_3/dt (°C month^{-1}) calculated from **b** the UDO (red); **c** the URO (dark blue); **d** the UWPO (green); and **e** the UARO (magenta). In each of panels **b-e**, ρ is the correlation coefficient between dT_3/dt determined directly from ACCESS-OM and the corresponding tendency calculated from each of the underpinning models.

the mechanisms described in the UO and its underpinning models. The UWPO term describing locally forced eastwards propagating Kelvin waves is weighted as the least important mechanism in the UO and UARO compared with the delayed and advective-reflective negative feedbacks. The inclusion of a term parameterizing the Niño-5 zonal wind stress anomalies in Eq. (3.28) used to derive the UO SST anomaly tendency equation is not a significant improvement over the relation with this term omitted. A similar result is found by comparing the fits of the UO and UDO equations for the SST anomaly tendencies. We conclude, then, that the UWPO mechanism for ENSO decay is the least important in describing the ENSO behaviors simulated by ACCESS-OM. With a delay term of $\eta = 2$ or 3 months, the UDO Eq. (3.6) can be used to assess the accuracy of the UARO mechanism describing the importance of local mean and anomalous zonal advection at the edge of the western Pacific warm pool. GLS fitting using values for the delay term equal to 2 and 3 months, respectively, is unable to return values for the damping term ε that are statistically distinguishable from zero. Furthermore, the rmses of the fitted curves to both values of the delay term are higher than those for $\eta = 7$ (rmse= 0.066°C month^{-1}, for $\eta = 2$; rmse= 0.064°C month^{-1}, for $\eta = 3$). Hence, we conclude that the UDO feedback mechanism in the UO and its underpinning models is the most important in contributing to ENSO growth and decay, followed by the UARO feedback mechanism and the UWPO feedback mechanism.

The original models

The original delayed oscillator Eq. (3.8) provides a very close fit to the simulated tendency estimated directly from ACCESS-OM. The rmse - calculated using cross-validation - is minimized for $\eta = 1$ months, leading to the fitted curve explaining 99% of the variance of the modeled dT_3/dt. This value for the delay term, $\eta = 1$ month, is smaller than the values given in Battisti and Hirst (1989), of $\eta = 6$ months, and W01, of $\eta = 5$ months. When a delay value of $\eta = 5$ (consistent with W01) is used to fit the original delayed oscillator, the resulting fitted curve explains 94% of the variance in dT_3/dt calculated directly from ACCESS-OM (the cross-validated rmse is 0.052 °C month^{-1}). It is not surprising that the delayed oscillator Eq. (3.8) provides such a close estimate

of the modeled dT_3/dt; indeed, the tendency term on the left-hand side of Eq. (3.8) is directly proportional to the right-hand side, regardless of the value of the delay parameter η. When Eq. (3.8) is refit to the simulated dT_3/dt with τ_4^x substituted for T_3 on the right-hand side of the equation, the result is poorer than that of the delayed oscillator Eq. (3.8) (rmse= 0.054 °C month^{-1}, $\rho^2 = 71\%$, for $\eta = 3$ months), which indicates that the relation $\tau_4^x \propto T_3$ is incomplete, as discussed in section 3.5.3, below.

The values of the recharge oscillator coefficients estimated via GLS regression are similar to those of previous studies (e.g. Mechoso et al., 2003). However, the fitted curve here explains only 35% of the variance in the model dT_3/dt, for an rmse of 0.076°C month^{-1} (figure 3.9a). The original recharge oscillator SST equation performs considerably better than the URO, the difference being due to the averaging regions for the thermocline depth anomalies and the omission of an explicit damping term in the original equation.

The recharge oscillator equation for dT_3/dt has particularly poor closure during the period 1990-95, as previously shown by Graham et al. (2014). However, the years 1990-95 in ACCESS-OM are marked by central Pacific ENSO events, the mechanisms of which are not well described by the recharge oscillator model (Kug et al., 2010; Yeh et al., 2014). That is, the recharge oscillator assumes that the primary development and decay dynamics of ENSO are related to the shoaling and deepening of the equatorial thermocline, which is not necessarily the case for central Pacific ENSO events (Singh and Delcroix, 2013; Yeh et al., 2014). It is for this reason that the variances explained by the recharge model fitted curves for dT_3/dt (and dh_W/dt in the following subsection) are relatively low.

Note that our results do not imply that the delayed oscillator is a superior diagnostic than the recharge oscillator. For example, the decay of El Niño events, rather than their growth, might be better described in the delayed oscillator (Li and Clarke, 1994; Mantua and Battisti, 1994), which may be partly due to the omission of noise forcing that is important in the excitation of ENSO events (Vecchi et al., 2006). Differences between our results and those of previous studies (e.g., Mechoso et al., 2003) might also arise due to differences in data used (Mechoso et al. (2003) used a CGCM, whereas we used a "realistic" flux-forced ocean model), or differences in filtering techniques (Mechoso

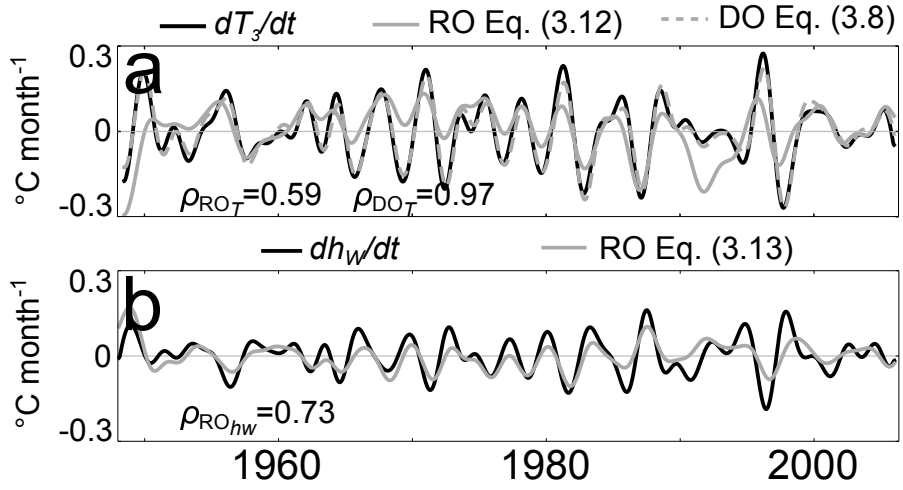

Figure 3.9: Fitted curves for the original delayed and recharge oscillator models using ACCESS-OM. **a** The solid black line is dT_3/dt determined directly from ACCESS-OM. The dashed grey line corresponds to the tendency calculated from the right-hand side of the original delayed oscillator equation for T_3, namely Eq. (3.8), with a delay η of five months and where the coefficients are estimated using GLS regression (column 2, table 3.1). The solid grey line corresponds to the tendency calculated from the right-hand side of the original recharge oscillator equation for T_3, namely Eq. (3.12), where the coefficients are estimated using GLS regression (column 5, table 3.1). **b** The solid black line is dh_W/dt determined directly from ACCESS-OM. The solid grey line corresponds to the tendency calculated from the right-hand side of the original recharge oscillator equation for h_W, namely Eq. (3.13), where the coefficients are estimated using GLS regression (column 5, table 3.1). In each panel, the correlation coefficients (ρ) between the delayed and recharge oscillator tendency equations and the corresponding tendencies calculated directly from ACCESS-OM are reported.

et al. (2003) extracted and analyzed only the ENSO cycle - removing high and low frequency variability from the timeseries of SST, thermocline depth, and zonal wind stress anomalies).

A study by Bettio (2007) examined the skill of the delayed and recharge oscillator frameworks in diagnosing the ENSO behavior of the Australian Bureau of Meteorology's Research Centre (BMRC) CGCM (Power et al., 2006) compared with observations. Bettio (2007) found that the delayed oscillator demonstrated superior skill over the recharge oscillator in capturing ENSO behavior when applied to the BMRC CGCM. Bettio (2007) argues that eastern equatorial upwelling processes (here represented in the coefficient

R_h) are less efficient at explaining the majority of the variability in eastern equatorial SST anomalies in their model compared with observations. A similar result is possible here for the ACCESS-OM data, particularly given the presence of a cold tongue bias in the central-eastern equatorial Pacific (figure 3.2), which can develop due to biases in upwelling that result from excessively strong trade winds (Vannière et al., 2013). For this reason, it is difficult to determine from the analysis here which of the delayed and recharge oscillator mechanisms for negative feedback is more realistic.

3.5.2 Thermocline tendency equations

Unified oscillator and underpinning models

We next consider the extent to which the UO prognostic equation for thermocline depth anomaly Eq. (3.3) captures the behavior of dh_6/dt calculated directly from the ACCESS-OM data. W01 defined the thermocline depth using the 20°C isotherm, while here we use the depth averaged temperature above 300m. Hence, to evaluate the skill of the W01 curve, using the W01 coefficients, Eq. (3.3) (and term 1 on the right-hand side of Eq. (3.5)) is divided by 20°C m^{-1} (i.e., the regression coefficient estimated in section 3.3 relating the depth averaged temperature above 300m to the 20°C isotherm depth). The W01 coefficients are also converted to units of months. The W01 curve poorly emulates the behavior of the simulated tendency dh_6/dt (rmse = 0.16°C month^{-1}, $\rho^2 = 0.11\%$).

The GLS regression fit of Eq. (3.3) to the ACCESS-OM dh_6/dt (identical to the UWPO and UARO thermocline equations) returns trivial values for the coefficient c when $\lambda = 0, 1, ..., 10$ months, leading to a fitted curve that explains essentially none of the variance in the model dh_6/dt. When the URO thermocline depth anomaly tendency Eq. (3.11) is fit to the simulated dh_6/dt, a similar result to that of the UO Eq. (3.3) is obtained (rmse = 0.040°C month^{-1}, $\rho^2 = 4.6\%$).

While in W01 the UO Eq. (3.2) for dT_3/dt is derived using a series of balance relations, Eq. (3.3) for dh_6/dt is inferred directly from the off-equatorial vorticity equation (appendix). As such, a similar procedure of fitting the individual balance relations as in the previous subsection for the UO equation for dT_3/dt is not applicable here.

The original models

For the original recharge oscillator thermocline depth anomaly tendency, the fitted curve explains 54% of the variance in the model dh_W/dt, and the rmse is 0.043°C month^{-1} (figure 3.9b). Hence, the original recharge oscillator prognostic thermocline depth anomaly equation provides a considerably better fit to the simulated tendency than both the UO and the URO. Comparing Eqs. (3.11) and (3.13), we observe that the better fit for the original model is primarily the result of a more appropriate averaging region for the thermocline depth anomaly. In the original recharge oscillator, h_W represents equatorial western Pacific thermocline depth anomalies, whereas h_6 in the URO represents off-equatorial western Pacific thermocline depth anomalies. W01 argues that since the maximum interannual variability in the thermocline depth anomaly is in the off-equatorial western Pacific region, the variable h_6 in the UO equations should be averaged over the Niño-6* region, rather than over the equatorial western Pacific. However, the mechanism governing ENSO growth and transition in the recharge oscillator requires the discharge and recharge of *equatorial* heat content, which is consistent with observations (e.g. Meinen and McPhaden, 2000), implying that the thermocline depth anomaly in the western Pacific is more appropriately averaged on, rather than off, the equator.

In the original western Pacific oscillator, there are two prognostic equations for thermocline depth: one for the Niño-3 (i.e. equatorial) thermocline depth anomaly, Eq. (3.15), and the other for the Niño-6* thermocline depth anomaly, Eq. (3.16), which is identical to the UO Eq. (3.3). The right-hand side of Eq. (3.15) is fit to the ACCESS-OM output, finding that the coefficients a^h and ε^h are statistically indistinguishable from zero. The GLS regression fit of Eq. (3.15) to the simulated dh_3/dt is consistent with the poor fits of the UWPO's prognostic equation for the SST anomaly tendency, Eq. (3.14), and the western Pacific negative feedback mechanism in Eq. (3.2).

3.5.3 Niño-4* zonal wind stress tendency equations

There are three versions of equations for τ_4^x among the UO, its underpinning models, and the original versions of these models: a prognostic version, as in the UO, in terms of T_3 and τ_4^x; a diagnostic version that relates τ_4^x directly to T_3, as in the recharge oscillator

and the original delayed oscillator; and a prognostic version in terms of h_6 and τ_4^x, as in the original western Pacific oscillator.

We first consider the prognostic UO Eq. (3.4) for the Niño-4* zonal wind stress anomaly tendency. Applying the W01 parameter values as coefficients to this equation results in a curve that is unable to replicate $d\tau_4^x/dt$ calculated from ACCESS-OM. The GLS regression analysis applied to Eq. (3.4) does not improve the fit, returning a trivial value for e (rmse= 1.0×10^{-3} N m^{-2} month^{-1}, $\rho^2 = 1.3 \times 10^{-4}$%; figure 3.7c). We hypothesize that the tendency term in Eq. (3.4) is unnecessary, and that the dominant balance is simply between the Niño-4* zonal wind stress anomaly and the Niño-3 SST anomaly. To test this hypothesis we rearrange Eq. (3.4) as follows

$$\tau_4^x = \frac{e}{R_{\tau_4^x}} T_3 - \frac{1}{R_{\tau_4^x}} \frac{d\tau_4^x}{dt}, \tag{3.20}$$

and apply GLS regression analysis. We find that the coefficient $1/R_{\tau_4^x}$ in front of the tendency term is statistically indistinguishable from zero, which indicates that it is not linearly correlated with the model state and can be treated as noise. The dominant balances in Eq. (3.20) are illustrated in figure 3.10a. The fit for Eq. (3.9) between τ_4^x and T_3 produces similar results to that of Eq. (3.20) (rmse = 0.0059 N m^{-2} month^{-1}, $\rho^2 = 58\%$). However, there is clear structure in the residual of Eqs. (3.9) and (3.20) when the tendency term is omitted (i.e., $\tau_4^x - eT_3/R_{\tau_4^x}$), with coherent peaks and troughs corresponding to El Niño and La Niña years, which is indicative of nonlinearity in the dependence of τ_4^x on T_3.

Given the importance of atmospheric nonlinearities in parameterizing processes such as westerly wind bursts and the Madden-Julian Oscillation as well as the super El Niño events of 1982-83 and 1997-98 (Vecchi et al., 2006; Levine and Jin, 2010; Choi et al., 2013), the inclusion of nonlinearity in Eq. (3.9) may improve the fit. A suitable candidate is a piecewise nonlinearity, which has been found to aid in replicating the asymmetries in ENSO amplitude, sequencing, and timing (Choi et al., 2013). We note that previous studies have also extended the simple steady state atmospheric model above to include time-dependence between τ_4^x and T_3, since wind stress anomalies have been demonstrated to adjust to SST on the order of a month or so (Neelin et al., 2000; Syu and Neelin, 2000; Mechoso et al., 2003). While such a time-dependent relationship has been found

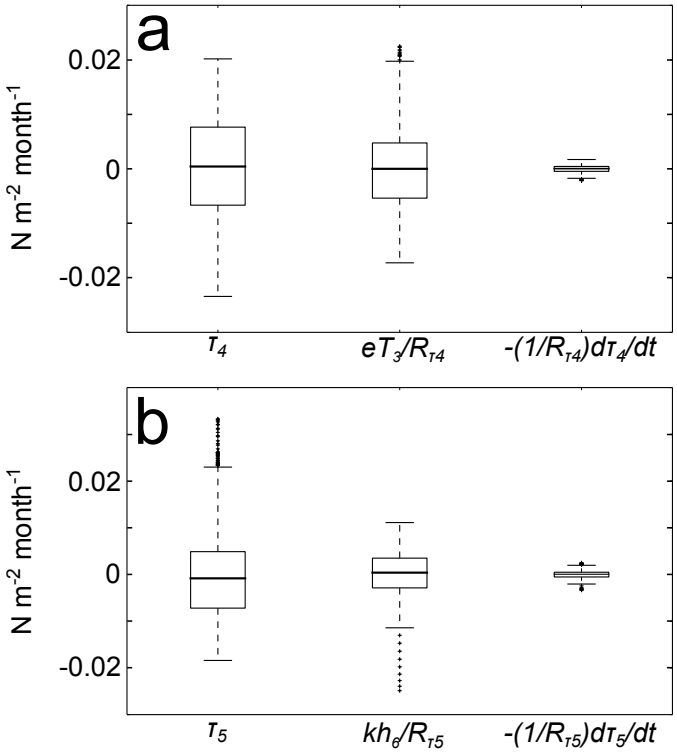

Figure 3.10: The dominant balances of terms in the zonal wind stress anomaly Eqs. (3.20) and (3.21) (i.e., Eqs. (3.4) and (3.5) rearranged to have the tendency terms on the right-hand side and the damping terms on the left). In each box plot, the bold horizontal line represents the median value of the term (i.e., median value through time), the lower horizontal line of the box represents the 25th percentile and the upper horizontal line represents the 75th percentile, the whiskers extend to the most extreme data points that are not considered outliers and the crosses represent outlier data (i.e. outside the 99th percentile). **a** The terms in the Niño-4* (5°S-5°N, 150°E-160°W) zonal wind stress anomaly equation, where the parameter values are estimated by GLS regression. **b** The terms in the Niño-5 (5°S-5°N, 120-140°E) zonal wind stress anomaly equation, where the parameter values are estimated by GLS regression.

to improve the relationship between τ_4^x and T_3, we emphasize that this is not the case when a simple wind stress anomaly tendency term is included, as in the UO Eq. (3.4).

Finally, the original western Pacific oscillator equation for the Niño-4* zonal wind stress anomaly tendency, Eq. (3.17), is fit to the simulated tendency using GLS regression analysis, yielding a fitted curve that explains essentially none of the variance in $d\tau_4^x/dt$ estimated directly from ACCESS-OM (rmse= 0.0012 N m^{-2} month^{-1}, $\rho^2 = 1.0\%$).

3.5.4 Niño-5 zonal wind stress tendency equations

There are only two versions of equations for τ_5^x among the UO, its underpinning models, and the original versions of these models: a prognostic version, as in the UO, and a diagnostic version that relates τ_5^x directly to h_6, as in the URO.

First, the prognostic UO Eq. (3.5) for Niño-5 zonal wind stress anomaly is considered. The curve calculated using the W01 parameters explains essentially none of the variance in $d\tau_5^x/dt$ (figure 3.7d). When the right-hand side of Eq. (3.5) is fit to the model $d\tau_5^x/dt$, the correlation coefficient between the fitted curve and $d\tau_5^x/dt$ is 3.6×10^{-3}. Hence, as for Eq. (3.4), we argue that the derivative formulation here is inappropriate. We rearrange Eq. (3.5) as for Eq. (3.4), with the tendency terms on the right-hand side and the damping terms on the left, obtaining

$$\tau_5^x = \frac{k}{R_{\tau_5^x}} h_6 - \frac{1}{R_{\tau_5^x}} \frac{d\tau_5^x}{dt}, \tag{3.21}$$

Performing the same dominant balance analysis on a rearranged Eq. (3.5) as in the previous section for Eq. (3.20), we find that the tendency term $d\tau_5^x/dt$ is also uncorrelated with the model state and can be treated as noise. Unlike with Eq. (3.20), there is no coherent structure in the residual (i.e., $\tau_5^x - kh_6/R_{\tau_5^x}$), although this might be due to the fact that τ_5^x depends on h_6 through the parameterization of local SST anomalies, which are not represented in Eq. (3.5).

Second, the URO equation for the Niño-5 region zonal wind stress anomaly - which assumes a simple linear relationship between τ_5^x and h_6 - is fit to the simulated $d\tau_5^x/dt$ and is not a considerable improvement over the fit of the UO equation: the linear relation explains only 3.5% of the variance in the model τ_5^x. As mentioned previously, other factors, such as SST and nonlinear processes, play a role in changing the Niño-5 zonal wind stress anomaly and their explicit parameterization in Eq. (3.9) might improve the description of τ_5^x.

3.6 Does the fitted UO produce an oscillation?

3.6.1 The UO and its underpinning models

To investigate whether the UO and its component models produce a realistic periodicity using the GLS fitted values, each of the systems of equations outlined in section 3.4 is solved numerically using the R statistical computing package Rdesolve (Soetaert et al., 2010). We find that the numerical solutions of the UO, UDO, URO, UWPO, and UARO do not oscillate in the absence of stochastic forcing. This result is not surprising given the poor fits of the equations for thermocline depth and zonal wind stress anomalies in each framework.

3.6.2 The original conceptual model formulations

We next investigate whether the original delayed, recharge, and western Pacific oscillators produce oscillations when solved using the GLS fitted values for the parameter values. Both the delayed and the recharge oscillators are found to produce oscillatory solutions, the period of which can be calculated analytically. Assuming solutions to the delayed oscillator of the form $\exp(i\sigma t)$, the dispersion relation is given by Mechoso et al. (2003) as:

$$\left(i\sigma - \frac{ae}{R_{\tau_4^x}}\right) = -\frac{b_1 e}{R_{\tau_4^x}} \exp(-i\sigma\eta), \tag{3.22}$$

yielding a period of 4.2 years using the values of the coefficients estimated by GLS regression. In the case of the recharge oscillator, the period can be calculated with the following expression by Mechoso et al. (2003)

$$P = 2\pi \left\{ \left(\frac{b_2 k R_h}{R_{\tau_5^x}}\right) - \left[\left(\frac{ae - b_1 e}{R_{\tau_4^x}}\right)^2 + \left(\frac{ce}{R_{\tau_4^x}}\right)^2 \right] \right\}^{-1/2}. \tag{3.23}$$

Using the GLS estimated coefficients for the original recharge oscillator from table 3.1, the period is 5.2 years. However, as for the UO and its underpinning models, the numerical solution of the original western Pacific oscillator using the GLS fitted values is not oscillatory.

Mechoso et al. (2003) investigate the realism of the original delayed and recharge oscillator conceptual models in diagnosing ENSO behaviors using two fitting methods: the

first fit the conceptual models directly to CGCM data, and the second fit each of the individual balance relations that were employed in the derivation of the two conceptual models. Using fitting method 1, Mechoso et al. (2003) find that the simple models appear to reproduce a realistic ENSO period, but when the implied parameters estimated by this method are substituted into the individual balance relations, they result in erroneous estimates of amplitude and phase. Fitting method 2 results in more robust estimates for the parameter values, although it yields smaller ENSO periods for the delayed and recharge oscillators than estimated by the CGCM, which Mechoso et al. (2003) attribute to multiple scales of time dependence in the CGCM wind stress-SST anomaly relationship. [Although, we note that such a time-dependent relationship is not adequately represented through the inclusion of a wind stress anomaly tendency term, as in the UO Eqs. (3.4) and (3.5).] The same procedure outlined in Mechoso et al. (2003) is not carried out here; however, we can expect a similar result to with respect to the differences between the fitting methods for the original delayed and recharge oscillators.

3.7 Discussion and conclusion

The unified oscillator (UO) is often cited as a concise description of ENSO that incorporates several existing paradigms of ENSO dynamics, such as the recharge oscillator, delayed oscillator, western Pacific oscillator, and advective-reflective oscillator. We have investigated this claim, but find that the unified oscillator is no more effective at diagnosing ENSO behavior in the flux-forced Australian Community Climate and Earth System Ocean Model (ACCESS-OM) than the delayed oscillator formulation that the unified oscillator incorporates.

In the original formulation of the UO, W01 suggests suitable parameter values based on their capacity to produce oscillations on interannual timescales in the coupled system of delay differential equations. When applied to the relevant equations, we find these values to be ineffective in capturing the associated ACCESS-OM tendencies of SST, ocean heat content, and zonal surface wind stress anomalies. As an alternative, and in order to assess the fidelity of the UO equations with respect to the simulated ENSO behavior in ACCESS-OM, we use generalized least squares regression analysis to find more ap-

propriate parameter estimates. While the fitted curve of the UO SST anomaly equation replicates the model dT_3/dt reasonably well, the remaining equations for thermocline depth and zonal wind stress anomalies capture essentially none of the variance in the ACCESS-OM tendencies, and as a result, the estimated coefficient values substituted into the UO and its underpinning model equations fail to produce oscillatory solutions. This can be attributed to two key factors.

First, the inclusion of the derivative terms in the UO prognostic Eqs. (3.4) - (3.5) for zonal wind stress anomalies is inappropriate. An examination of the dominant balances in each of these equations indicates that simple steady-state equations, in which the zonal wind stresses change linearly with the predictors, are more appropriate than the derivative formulations. However, this does not imply that linear relationships between zonal wind stress anomalies and the corresponding predictors are sufficient.

Second, the averaging region of the thermocline depth anomaly defined in the UO is mismatched to the formulation. W01 argues that since observations show that the maximum interannual thermocline depth and sea level variations are in the off-equatorial region, the discharge and recharge of the equatorial Pacific is best modeled using Niño-6* (8-16°N, 150-170°E) thermocline depth anomalies. This conflicts with the arguments of Jin (1997a) and a study by Meinen and McPhaden (2000) who show that the discharge and recharge of *equatorial* heat content - i.e. averaged in the western equatorial Pacific and the Niño-3 (5°S-5°N, 150-90°W) regions, respectively, rather than off-equatorial heat content - play an important role in the growth and decay of an ENSO event. Our results agree with these earlier studies; we find that when the heat content is averaged in the equatorial western Pacific the variance explained in the ACCESS-OM thermocline depth anomaly tendency is considerably higher than when the thermocline depth anomaly is averaged in the off-equatorial western Pacific.

We find that the inclusion of the western Pacific oscillator feedback mechanism in the UO does not substantially improve the fit of this equation to the ACCESS-OM dT_3/dt, as evidenced by comparing the SST anomaly equation from the UO and the delayed oscillator. Furthermore, both the original and the W01 versions of the western Pacific oscillator model capture very little of the variance in the SST, thermocline depth, and

zonal wind stress anomaly tendencies that they describe. It is important to recognize that our results do not establish whether or not the dominant negative feedback described by the western Pacific oscillator is a physical mechanism - previous studies have found evidence for the western Pacific oscillator operating in nature, and particularly during large ENSO events (Boulanger and Menkes, 2001; Boulanger et al., 2003). Rather, our results imply that the inclusion of the western Pacific oscillator in the UO in its present form is not necessary or sufficient for replicating the ENSO tendencies produced by the ACCESS-OM simulation.

A notable weakness of the UO theory is in combining mechanisms that are not necessarily independent. For example, the discharge of equatorial heat content in the recharge oscillator implicitly takes into account the Kelvin wave processes explained by the delayed oscillator negative feedback mechanism (Jin, 1997a). That is, the time-integrated effect of eastwards propagating upwelling Kelvin waves initiated by the reflection of Rossby wave pairs at the western boundary of the Pacific (from the delayed oscillator) partly contribute to the ocean mass adjustment (from the recharge oscillator) that leaves the thermocline anomalously shallow following an El Niño event. While it may be true that the evolution of ENSO is the result of multiple negative feedback mechanisms acting in concert, the UO in its current form is unable to adequately incorporate and delineate the different mechanisms in operation.

With these factors in mind, and by comparing the UO equations with the corresponding equations from the original conceptual models it incorporates, we suggest a number of improvements to the UO, namely:

(1) define the averaging region for the thermocline depth anomaly in the western Pacific on-, rather than off-, equator, based on model sensitivity and/or the location of maximum interannual variability;

(2) remove the tendency term in the Niño-4* (5°S-5°N, 150°E-160°W) zonal wind stress equation;

(3) remove the tendency term in the Niño-5 (5°S-5°N, 120-140°E) zonal wind stress equation [The description of τ_5^x from Eq. (3.5) might be further improved via the

inclusion of an explicit SST term, although evaluation of the most appropriate parameterization of this term requires further investigation.]; and

(4) include stochastic wind forcing in each of the zonal wind stress anomaly tendency equations, to energize the fluctuations in the face of dissipation, as has been done for the recharge oscillator recently by Levine and Jin (2010).

Nevertheless, even with these modifications, it would be difficult for an improved unified model to significantly surpass the performance of the simple delayed oscillator equation in capturing the ENSO behavior of the ACCESS-OM simulation. For frequencies of 12 months or greater, and parameter values of $ae/R_{\tau_4^x} = 0.16$ month^{-1} and $b_1 e/R_{\tau_4^x} = 0.20$ month^{-1}, we find that the delayed oscillator Niño-3 SST anomaly tendency equation explains 94% of the variance in the corresponding tendency calculated directly from the ACCESS-OM data. Hence, we recommend the delayed oscillator model as a starting point for further research and improvement, which is summarized as follows:

$$\frac{dT_3(t)}{dt} = \frac{ae}{R_{\tau_4^x}}\tau_4^x(t) - \frac{b_1 e}{R_{\tau_4^x}}\tau_4^x(t-\eta), \tag{3.24a}$$

$$\text{for } \tau_4^x(t) = \frac{e}{R_{\tau_4^x}}T_3(t) + \alpha N(t)G(t), \tag{3.24b}$$

$$\frac{dN(t)}{dt} = -\omega N(t) + w(t), \tag{3.24c}$$

where we have introduced a multiplicative (state-dependent) noise variable, $N(t)$, representing red noise, $w(t)$ is white noise with a Gaussian distribution, $G = 1 + BT$, and α, ω, and B are constants. These additions to the delayed oscillator are based on modifications to the original recharge oscillator by Levine and Jin (2010), who demonstrated that multiplicative noise influenced ENSO stability and asymmetry, and confirmed previous findings that the low-frequency component of noise forcing is critical in the excitation of El Niño events (Vecchi et al., 2006; Gebbie et al., 2007; Zavala-Garay et al., 2008). We also note that multiplicative, rather than simply additive, noise is most appropriate, as it allows for the inter-dependence between high frequency stochastic forcing events such as the Madden Julian Oscillation or westerly wind bursts, which are not independent of the background state of ENSO (Kessler and Kleeman, 2000; Vecchi and Harrison, 2000; Eisenman et al., 2005; Gebbie et al., 2007; Tziperman and Yu, 2007). Additional

improvement might be found in the delayed oscillator by including a nonlinearity in the atmospheric response to SST, as per Choi et al. (2013), an addition which resulted in a model better able to reproduce key ENSO asymmetries.

One limitation of the UO formulation, and of linear conceptual models in general, is the estimation of constant parameter values, when in reality ENSO is a nonlinear system with temporally evolving dynamics and spatial flavors (Yeh et al., 2014). Furthermore, these ENSO dynamics and spatial flavors are highly dependent on a mean state that is expected to warm into the future (e.g. Yeh et al., 2009; Kug et al., 2009; Wittenberg, 2009; Collins et al., 2010; Vecchi and Wittenberg, 2010; Santoso et al., 2013; Kim et al., 2014a; Wittenberg et al., 2014; Capotondi et al., 2015). For example, the delay terms in Eqs. (3.2) and (3.3) depend on Kelvin and Rossby wave speeds and the location where the waves are generated, which are not necessarily stationary in time. The parameter values may also be influenced by the meridional breadth, duration and location of wind forcing (Wittenberg, 2002; Vecchi and Harrison, 2003; Capotondi et al., 2006; Kim et al., 2008), which are not the same from one event to another.

Importantly, we are not arguing that the parameter values obtained from the application of generalized least squares regression analysis to the ACCESS-OM simulation are the "best" parameter values for any model. Indeed, it is expected that the application of the same analysis for a different model, or time period, will result in a different set of parameter values than those found here for the ACCESS-OM simulation. However, reanalysis products, such as SODA v2.2.4 and ERSST v3b, are forced by similar atmospheric fluxes to those used to force the ACCESS-OM simulation (Griffies et al., 2012), resulting in similar reproductions of SST, thermocline depth, and wind stress anomalies, despite the fact that while reanalysis data are corrected to observations, the ACCESS-OM OGCM is not (figure 3.4). Therefore, replication of the analysis performed here on ACCESS-OM using reanalysis data is unlikely to produce a markedly different set of *conclusions* to those presented here.

Linear conceptual models have played, and will most likely continue to play, an important role in our understanding of ENSO behavior. Nevertheless, differences in ENSO flavors and variability in space and time, and the potential complexities associated with

changes in ENSO behavior under climate change, predicate the need for a more complete consideration of the role and importance of nonlinearities in the climate system when making conclusions about modeled behaviors.

3.8 Appendix: derivation of the unified oscillator

The equations that W01 used to derive the UO model are briefly introduced in this section.

As for the delayed oscillator model (Battisti and Hirst, 1989), W01 assumes that the SST, vertical velocity, and zonal current velocity anomalies described in the Lamont model for SST anomaly tendencies (Zebiak and Cane, 1987) are linearly related to zonal wind stress anomalies in the eastern equatorial Pacific, yielding

$$\frac{dT_3}{dt} = R\tau_4^x + K_E h_3, \tag{3.25}$$

where T_3 is the Niño-3 (5°S-5°N, 150-90°W) SST anomaly, τ_4^x is the Niño-4* (5°S-5°N, 150°E-160°W) zonal wind stress anomaly, h_3 is the Niño-3 thermocline depth anomaly, and R and K_E are constants. Battisti and Hirst (1989) used Eq. (3.25) to directly derive the delayed oscillator by assuming that τ_4^x is proportional to the SST anomaly averaged in the eastern equatorial Pacific and that the zonal tilt in the equatorial thermocline depth is proportional to the zonal wind stress anomalies ($h_3 \propto h_W + \tau_4^x$). However, W01 argues that Eq. (3.25) on its own overlooks the importance of the western equatorial Pacific zonal wind stress anomalies that are important in forcing an upwelling Kelvin wave that contributes to ENSO decay. Hence to derive the UO, W01 considers Eq. (3.25) and an equation describing the balance between the zonal tilt in the equatorial thermocline depth and zonal wind stresses (from the reduced gravity model)

$$g' \frac{\partial H}{\partial x} = \frac{\tau^x}{\rho_0 H}, \tag{3.26}$$

where g' is the reduced gravity, H is the mean thermocline depth, ρ_0 is a constant for the seawater density, and τ^x is the zonal wind stress. W01 integrates Eq. (3.26) over the equatorial box from east to west and considers only the anomalous terms, obtaining

$$h_3 = h_W + \alpha\tau_4^x + \beta\tau_5^x, \tag{3.27}$$

where, as before, τ_4^x is the Niño-4* zonal wind stress anomaly, τ_5^x is the Niño-5 (5°S-5°N, 120-140°E) zonal wind stress anomaly, h_3 is the Niño-3 thermocline depth anomaly, h_W is the western equatorial thermocline depth anomaly, and α and β are constants.

In the delayed oscillator, wave dynamics are responsible for modulating h_W on ENSO-timescales, hence h_W is assumed to be proportional to $-\tau_4^x(t-\eta)$. The third term on the right-hand side of Eq. (3.27), $\beta\tau_5^x$, which does not appear in the delayed or recharge oscillators, describes the effect of Niño-5 zonal wind stress anomalies in forcing an upwelling Kelvin wave that acts to damp eastern equatorial Pacific SST anomalies (from the western Pacific oscillator, Weisberg and Wang, 1997). This term is assumed to be proportional to $\tau_5^x(t-\delta)$, where δ represents the delay in the propagation of the Kelvin wave from west to east. Substitution of these terms into Eq. (3.27) yields the following equation

$$h_3 = \alpha\tau_4^x - \gamma\tau_4^x(t-\eta) + \beta\tau_5^x(t-\delta), \tag{3.28}$$

which can then be substituted into Eq. (3.25) to yield the UO equation for the Niño-3 SST anomaly tendency, namely

$$\frac{dT_3}{dt} = a\tau_4^x - b_1\tau_4^x(t-\eta) + b_2\tau_5^x(t-\delta), \tag{3.29}$$

where

$$a = R + \alpha K_E, \qquad b_1 = \gamma K_E, \qquad b_2 = \beta K_E. \tag{3.30}$$

W01 further added a cubic damping term to Eq. (3.29), $\varepsilon {T_3}^3$, to limit growth.

To derive the UO equation for the Niño-6* (8-16°N, 150-170°E) thermocline depth anomaly tendency, Eq. (3.3), W01 starts from the vorticity equation describing the generation of *off-equatorial* Rossby waves

$$\frac{\partial h_6}{\partial t} - c_r\frac{\partial h_6}{\partial x} + Rh = \nabla \times \left[\frac{\tau}{\rho_0 f}\right], \tag{3.31}$$

where f is the Coriolis parameter, c_r is the long Rossby wave speed, and R is a damping term. W01 argues that it takes time (e.g., λ months) for the off-equatorial Rossby waves to propagate west from the forcing region in the central-eastern equatorial Pacific, hence introduces a delay term into Eq. (3.31) to obtain the UO Eq. (3.3), namely

$$\frac{dh_6}{dt} = -c\tau_4^x(t-\lambda) - R_h h_6, \tag{3.32}$$

where the thermocline depth anomalies are averaged in the Niño-6* region and the zonal wind stress term is averaged in the Niño-4* region.

Finally, W01 derives the UO equations for the Niño-4* and Niño-5 zonal wind stress anomalies from a reduced gravity atmospheric model, e.g.

$$\frac{\partial U}{\partial t} - ByV = -\frac{\partial P}{\partial x} - GU, \tag{3.33}$$

$$ByU = -\frac{\partial P}{\partial y}, \tag{3.34}$$

$$\frac{\partial P}{\partial t} + c_a^2 \left(\frac{\partial U}{\partial x} + \frac{\partial V}{\partial y} \right) = -Q - GP, \tag{3.35}$$

where U, and V are the zonal and meridional wind anomalies, P is the atmospheric pressure anomaly, c_a is the atmospheric Kelvin wave speed, and G is an atmospheric damping term. This system is combined into one third-order partial differential equation, then, averaging from the eastern to the central equatorial Pacific, and assuming that Q is proportional to T_3, the UO Eqs. (3.4) and (3.5) are directly obtained

$$\frac{d\tau_4^x}{dt} = eT_3 - R_{\tau_4^x}\tau_4^x, \tag{3.36}$$

$$\frac{d\tau_5^x}{dt} = kh_6 - R_{\tau_5^x}\tau_5^x. \tag{3.37}$$

Chapter 4

Effectiveness of the Bjerknes stability index in representing ocean dynamics

In this chapter, the Bjerknes stability index (originally proposed by Jin et al. (2006), and now widely used to understand ENSO feedbacks, growth, and stability under past, present, and future climates) is evaluated for its efficacy in capturing the key ocean feedbacks contributing to ENSO growth and stability. This chapter contributes to the overall thesis aims by addressing the following specific objectives:

1. How well does the Bjerknes stability index reproduce the main ocean feedbacks contributing to ENSO evolution compared with the corresponding formulations from the tropical Pacific heat budget equation?

2. In light of the findings relating to question 1), how useful is the Bjerknes index in the context of model intercomparisons?

Here, the Bjerknes stability index is calculated using the same flux-forced ACCESS-OM data analysed in chapter 3. The phase, magnitude, and sign of the ENSO ocean feedbacks represented by the Bjerknes stability are compared with the corresponding terms from the heat budget.

Contributions

The main text of this chapter is a paper published in *Climate Dynamics*, with the following citation: Graham, F. S., J. N. Brown, C. Langlais, S. J. Marsland, A. T. Wittenberg, and N. J. Holbrook, 2014: Effectiveness of the Bjerknes stability index in

representing ocean dynamics. *Climate Dynamics*, **43**, 2399-2414, doi:10.1007/s00382-014-2062-3.

The experimental design and analysis methods were discussed between Dr Jaclyn N. Brown, Dr Clothilde Langlais, Dr Andrew T. Wittenberg, Assoc. Prof. Neil J. Holbrook and myself. The ACCESS-OM simulation data was supplied by Dr Simon J. Marsland, who provided technical assistance. I performed the necessary coding to calculate the Bjerknes stability index and terms from the heat budget equation in the ACCESS-OM data, and carried out all the data analysis. All sections of the coauthored paper and the review process were led by myself under the guidance of the coauthors.

4.1 Abstract

The El Niño-Southern Oscillation (ENSO) is a naturally occurring coupled phenomenon originating in the tropical Pacific Ocean that relies on ocean-atmosphere feedbacks. The Bjerknes stability index (BJ index), derived from the mixed-layer heat budget, aims to quantify the ENSO feedback process in order to explore the linear stability properties of ENSO. More recently, the BJ index has been used for model intercomparisons, particularly for the CMIP3 and CMIP5 models. This study investigates the effectiveness of the BJ index in representing the key ENSO ocean feedbacks - namely the thermocline, zonal advective, and Ekman feedbacks - by evaluating the amplitudes and phases of the BJ index terms against the corresponding heat budget terms from which they were derived. The output from ACCESS-OM (a global ocean/sea ice flux-forced model) is used to calculate the heat budget in the equatorial Pacific. Through the model evaluation process, the robustness of the BJ index terms are tested. We find that the BJ index overestimates the relative importance of the thermocline feedback to the zonal advective feedback when compared with the corresponding terms from the heat budget equation. The assumption of linearity between variables in the BJ index formulation is the primary reason for these differences. Our results imply that a model intercomparison relying on the BJ index to explain ENSO behavior is not necessarily an accurate quantification of dynamical differences between models that are inherently nonlinear. For these reasons, the BJ index may not fully explain underpinning changes in ENSO under global warming scenarios.

4.2 Introduction

Since Bjerknes (1969) first introduced the notion that El Niño-Southern Oscillation (ENSO) resulted from coupled ocean-atmosphere interactions in the equatorial Pacific, great advances have been made in understanding the dynamics of this phenomenon (Wyrtki, 1975; Cane and Zebiak, 1985; Zebiak and Cane, 1987; Battisti, 1988; Battisti and Hirst, 1989; Philander, 1990; Picaut et al., 1996; Jin, 1997a). Nonetheless, there are a diverse range of ENSO behaviors both within and between coupled general circulation models (CGCMs), including differences in the frequency and amplitude of the coupled

ENSO mode, in the asymmetry of ENSO events, and in the behavior and type of dynamics that play a role (Wittenberg, 2009; Vecchi and Wittenberg, 2010; Collins et al., 2010; Watanabe et al., 2012; Choi et al., 2013).

Previous studies have argued that diversity between CGCMs can be attributed to variations in the modeled background ocean-atmosphere state of the equatorial Pacific, which alter the coupled instability (Philander et al., 1984; Neelin and Jin, 1993; Fedorov and Philander, 2001). In keeping with this theory, Jin et al. (2006) derived a coupled ENSO stability index, called the Bjerknes stability index (BJ index), from the mixed layer heat budget equation with the aim of (i) depicting the growth rate of the leading coupled ENSO-like mode, and (ii) understanding and quantifying ENSO diversity in CGCMs based on a variety of mean states. The BJ index is given by the constant R, which represents the Bjerknes positive feedback. This index quantifies the key processes involved in equatorial Pacific ocean-atmosphere dynamics - namely advection by mean currents, thermodynamic damping, the thermocline feedback, the zonal advective feedback, and the Ekman feedback. The metric R is derived from the coupled system of equations that collectively describe the recharge oscillator model (Jin, 1997a,b), that is

$$\left\langle \frac{\partial T}{\partial t} \right\rangle_E = R\langle T \rangle_E + F\langle h \rangle_W, \tag{4.1}$$

$$\left\langle \frac{\partial h}{\partial t} \right\rangle_E = -\epsilon\langle h \rangle_W - \tilde{F}[\tau^x], \tag{4.2}$$

where $\langle T \rangle_E$ is the volume averaged temperature from the sea surface to the depth of the mixed layer in the central-eastern equatorial Pacific (5°S-5°N, 175°E-80°W), $\langle h \rangle_W$ is the thermocline depth averaged in the western equatorial Pacific (5°S-5°N, 120-175°E), and $[\tau^x]$ is the zonal wind stress anomaly averaged across the entire equatorial Pacific basin (5°S-5°N, 120°E-80°W) and is related to $\langle T \rangle_E$ by $[\tau^x] = \lambda\langle T \rangle_E$, where λ can be estimated via regression analysis. F and $\tilde{F}$ are constants representing the frequency of the interannual oscillation of the system and Sverdrup transport across the equatorial Pacific basin, respectively. Finally, ϵ is the damping rate of ocean adjustment. Angle brackets denote volume averaged quantities and square brackets denote variables that have been averaged across the full equatorial Pacific basin.

The BJ index has many useful applications and has aided understanding of the dynamics

of the climate system. The BJ index is in good agreement with the linear growth rates of intermediate-complexity models and more complex CGCMs under changing background states, demonstrating its potential usefulness in evaluating the stability of coupled models (Jin et al., 2006; Kim and Jin, 2011a). Lübbecke and McPhaden (2013) used the BJ index to compare coupled instabilities in the Pacific and Atlantic ENSO-like modes, which allowed them to demonstrate that the Atlantic was overall more damped than the Pacific, most likely due to a weaker thermocline feedback. The BJ index has also been used in model intercomparison studies to assess changes in ENSO stability under historical and future climatic conditions. Kim and Jin (2011b) compared the BJ index estimated from 12 CGCMs among the Coupled Model Intercomparison Project phase 3 (CMIP3) in both historical and increased CO_2 climates, finding that the positive ocean feedbacks were likely to grow under global warming. However, the CGCMs were diverse in their representation of ENSO characteristics, which limited the reliability of this conclusion. More recently, Kim et al. (2014b) applied the BJ index to a suite of CMIP5 models and compared the estimated growth rates with observations. They argue that, due to the cold tongue bias, the majority of CMIP5 models underestimate the magnitude of the positive ocean feedback terms compared with observations.

It is well known that CGCMs suffer biases in the tropical Pacific, such as the cold tongue bias, and biases in the seasonal cycle and the western Pacific warm pool edge, that affect the frequency, amplitude, and dynamics of the simulated ENSO (Guilyardi et al., 2009; Brown et al., 2012). While the BJ index attempts to account for such diversity between CGCMs through quantification of the mean state, by the use of averaging regions that are fixed in space the BJ index is limited in the extent to which it can account for the diversity in location and spread of ENSO events, both within and across CGCMs. A further difficulty with using the BJ index to compare CGCMs is in choosing an appropriate time period over which to calculate the BJ index. That is, internal variability within models leads to a range of spatial "flavors" of ENSO in which local and remote ENSO dynamics dominate to varying degrees (Ashok et al., 2007; Kug et al., 2010; Karnauskas, 2013). Comparing CGCMs over time periods characterized by different spatial "flavors" of ENSO may lead to conflicting results from the BJ index, even when

the underlying dynamics are not necessarily markedly different. This is a particularly important consideration when applying the BJ index to CGCM simulations of future climate scenarios.

Studies applying the BJ index to observations or reanalysis products have found that the thermocline feedback is at least twice the magnitude of the zonal advective feedback (Lübbecke and McPhaden, 2013; Kim et al., 2014b). This result conflicts with that of Jin and An (1999), who used a simple model to compare the roles of the thermocline and zonal advective feedbacks in the Niño-3 region (5°S-5°N, 150-90°W) and found that the two feedbacks made similar contributions to changes in the temperature tendency. Results from mixed layer heat budget analyses of the National Center for Environmental Prediction coupled model support the finding that the zonal advective feedback and the thermocline feedback are of a similar magnitude (Huang et al., 2010, 2011). However, Dewitte et al. (2013) highlight the difficulty in determining the importance of the thermocline feedback over the zonal advective feedback, due to changes in the relative strength of each feedback over time. In particular, since 1976 the thermocline feedback has become more effective at influencing the sea surface temperature (SST) in the Niño-4 region (5°S-5°N, 160°E-150°W) than the zonal advective feedback due to an increase in vertical stratification. Nevertheless, causes for the overestimation of the thermocline feedback with respect to the zonal advective feedback in the BJ index have not been identified.

The BJ index describes the climate system using linear equations. However, studies of atmospheric forcing in the equatorial Pacific have demonstrated that a phase nonlinearity exists in the observed and modeled relationship between the shortwave component of the heat flux and the SST (Lloyd et al., 2012; Bellenger et al., 2014). As a result, the assumption of linearity in the calculation of the BJ index thermodynamic damping coefficient may mask the extent of this nonlinearity. Whether the assumption of linearity in the ocean components of the BJ index is robust is yet to be established.

Given that the BJ index has been used to understand climate dynamics, climate change, and to assess model performance, we examine whether the formulation of the BJ index is effective in capturing the key ocean dynamics important to ENSO. Using a global

ocean/sea ice model simulation of the period 1980-2007, we contrast the magnitudes and phases of the feedback terms calculated from the model using the BJ index with the corresponding heat budget feedbacks that the BJ index approximates. As the BJ index terms are derived as simplifications of the heat budget terms, we explore how well they still capture the underlying ocean dynamics. The robustness of the assumption of linearity in the individual balance equations used to derive the ocean feedbacks is analyzed. Where the assumption of linearity is inappropriate, we consider the implications on the reliability and accuracy of the BJ index. We demonstrate that the BJ index may not accurately quantify the underlying ocean dynamics of the model, which has implications for studies that rely on the BJ index to measure model performance, to perform model intercomparisons, and to assess how global warming affects ENSO dynamics.

Section 4.3 describes the climate model run used in this study, the method used to calculate the mixed layer heat budget in the equatorial Pacific, and the BJ index calculation. In section 4.4, the positive ocean feedbacks from the BJ index are compared with the respective terms from the heat budget. Sections 4.5 and 4.6 provide a discussion and summary of the results.

4.3 Data and methods

In this study, the output from a global ocean/sea ice model simulation was analyzed. We choose to analyze the output from a flux-forced ocean/sea ice model rather than from a coupled ocean/atmosphere/sea ice model so that our calculations of the mixed layer heat budget and BJ index are not confounded by the errors that arise in the latter due to model biases. Furthermore, using an ocean/sea ice model is advantageous as the SST (mean state and variability) from flux-forced ocean/sea ice models is constrained to agree with observational products from which many of the underlying assumptions of the BJ index are derived. An alternative would be to use reanalysis data; however, this may introduce further complications in that the data is not dynamically consistent (Oke et al., 2013). Further, the goal of this study is to provide an example of how the BJ index can be misleading when studying model intercomparisons of ENSO dynamics, not to accurately evaluate the BJ index terms. To this end, the use of ocean model data is

most appropriate and adequate for our demonstration purposes. In the following section, the mixed-layer heat budget is defined and calculated, and the BJ index is introduced.

We note also that, by definition, the BJ index characterizes the coupled feedbacks in ENSO dynamics, which are not explicit in flux-forced ocean/sea ice models. As a consequence, the coupled feedback terminology employed in studies applying the BJ index to coupled models is not directly applicable in the context of a flux-forced model, such as the one analyzed in this study. In a flux-forced ocean model experiment, the origin of the flux forcings are not necessarily constrained. It is possible that the wind stresses and heat fluxes are physically unrelated to SST anomalies, although they could be statistically related - for instance, we could envisage scenarios where the flux forcings are stochastically generated, or are driven by factors external to the tropical Pacific region studied. Hence, what are referred to, in the coupled feedback terminology of the BJ index, as "feedbacks" should be denoted "sensitivities" in the flux-forced ocean model framework. Furthermore, the BJ index for a strongly coupled system - e.g., a CGCM - and a weakly coupled system - such as the flux-forced ocean model analyzed here - will be different, and in the latter framework, we cannot determine whether ENSO is stable or unstable.

Keeping in mind the implications of using a flux-forced ocean model when interpreting what are essentially coupled feedbacks, a substantial gap remains in the testing of the BJ index: we have yet to understand the accuracy of the BJ index representation of ENSO feedbacks in the context of "realistic" data (i.e. data that suffer from as few biases as possible and that are strongly representative of historical observations of the tropical Pacific Ocean). This current work seeks to close this gap, by comparing the BJ index representation of ENSO feedbacks with their heat budget counterparts. To be consistent with previous studies of the BJ index, in what follows, we refer to coupled phenomenon as "feedbacks", with the understanding that they are not actually the result of coupled processes in this flux-forced ocean experiment, but are essentially "sensitivities".

4.3.1 ACCESS-OM

Monthly means from the Australian Community Climate and Earth System Simulator Ocean Model (ACCESS-OM; Bi et al., 2013a), that couples the NOAA/GFDL ocean model MOM4p1 (Griffies, 2009) and the LANL sea ice model CICE4.1 (Hunke and Lipscomb, 2010), are calculated and analyzed. In general, ACCESS-OM has a horizontal resolution of 1° with the following three refinements: a tripolar grid (Murray, 1996) north of 65°N; a cosine dependent meridional grid spacing in the Southern Ocean; and a meridional resolution of 1/3° between 10°S and 10°N, gradually extending to 1° between 10°S (°N) and 20°S (°N). The vertical discretization uses a z* coordinate (Adcroft and Campin, 2004) and there are 50 vertical levels with a resolution extending from 10m in the upper 200m to approximately 333m in the deep ocean. The model run is forced with surface heat, freshwater, and momentum fluxes derived from the forcing and bulk-formulae of Large and Yeager (2009). The simulation uses the protocols of the CLIVAR Working Group on Ocean Model Development Coordinated Ocean-Ice Reference Experiments version 2 (CORE-v2) as described in Griffies et al. (2012) and first utilized in Danabasoglu et al. (2014).

The mixing scheme in ACCESS-OM combines three different parameterizations: (i) the K profile parameterization (KPP) for the surface mixed layer (Large et al., 1994); (ii) a tidal mixing parameterization for the abyssal ocean (Simmons et al., 2004) and coastal oceans (Lee et al., 2006); and (iii) a constant background diffusivity of 1.0×10^{-5} m^2 s^{-2} elsewhere. A linear sea surface salinity (SSS) restoring with a timescale of 60 days is used in the upper model layer. Water mass fluxes instead of virtual salt fluxes are employed in the upper boundary and water volume is conserved using a global ocean water flux correction.

In general, the ACCESS-OM simulation of the tropical Pacific compares well with observations (figures 3.2 - 3.5; Bi et al., 2013a). However, the thermocline is slightly shallower than the observations in the eastern equatorial Pacific, which gives rise to zonal currents that are stronger than observed in the eastern equatorial Pacific.

We applied a low-pass filter to the data to remove variability with frequencies shorter than 90 days. This 90 day cutoff period was chosen to separate seasonal and interannual

variability from phenomena with shorter timescales, such as Tropical Instability Waves (TIWs), oceanic Kelvin waves, the Madden-Julian oscillation (MJO) and westerly wind bursts (WWB), consistent with other studies (e.g. Kessler et al., 1998).

4.3.2 Mixed layer depth definition

The mixed layer depth (MLD) was defined according to a constant density threshold; the depth at which a density difference of 0.125 kg m^{-3} compared to the surface was first reached. As demonstrated by Huang et al. (2010), this is an appropriate criterion to calculate the MLD in the equatorial region, and the results of the heat budget analysis should not be sensitive to the choice of criterion.

The MLD estimated from ACCESS-OM using this density criterion was compared with the corresponding estimates from the UK Met Office subsurface ocean temperature and salinity data (UKMO), which combines eXbendable BathyThermograph (XBT) and hydrographic profiles, data from moored buoys, profiling floats, and altimeters of the global ocean (Ingleby and Huddleston, 2007). Figure 4.1a-d illustrates the differences in the seasonal MLD of ACCESS-OM and UKMO. In general, the climatological equatorial Pacific MLD is deeper in UKM than in ACCESS-OM, except in the eastern Pacific, from 140-80°W and 5-20°S. There is reasonably strong agreement between the interannual MLD anomalies of ACCESS-OM and UKMO (figure 4.1e); however, the UKMO MLD anomalies show more marked interannual deepening than those of ACCESS-OM.

The efficiency of the thermocline feedback during El Niño events is modulated by the deepening of the MLD, even in the absence of strong winds. Here, we compare the thermocline efficiency in ACCESS-OM and the UKMO dataset by regressing the thermocline depth anomalies and temperature anomalies directly below the mixed layer - the thermocline efficiency factor, denoted f_H - as per An and Jin (2000, 2001); Thual et al. (2011). [We note that while this method is valid in the eastern equatorial Pacific, where the thermocline is relatively shallow, it neglects the important role of stratification in modulating the thermocline feedback efficiency in the western-central Pacific (Dewitte et al., 2013). However, as we are predominantly interested in the thermocline efficiency in the eastern equatorial Pacific, this regression method suffices for our purposes.] The

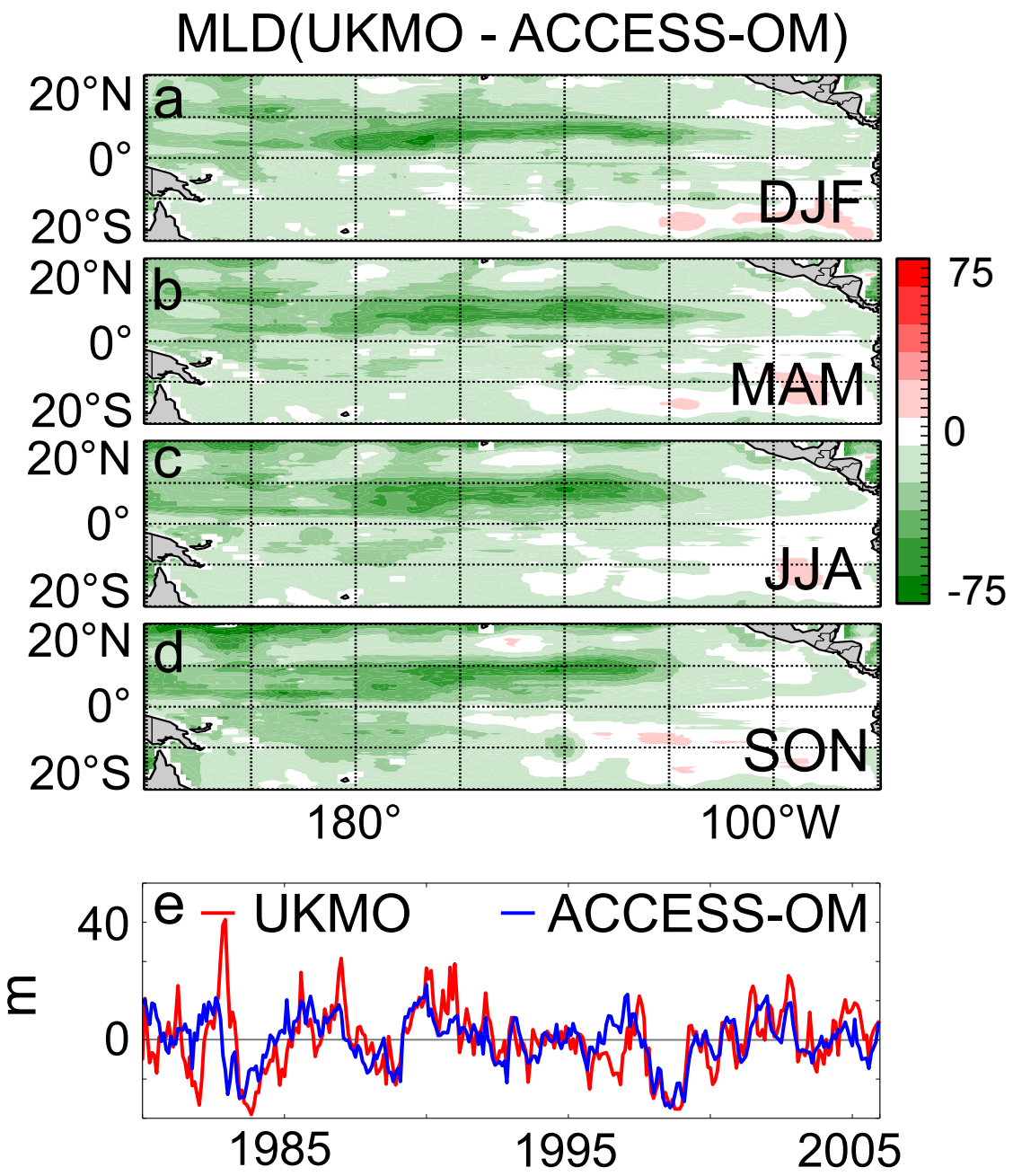

Figure 4.1: Comparison of mixed layer depth estimates in ACCESS-OM and UKMO using a density criterion. Panels **a-d** illustrate the seasonal differences between the two data, averaged over the period 1980-2005. The color interval is 10 m. Panel **e** illustrates the interannual variability in the mixed layer depth anomalies in ACCESS-OM (blue line) and UKMO (red line).

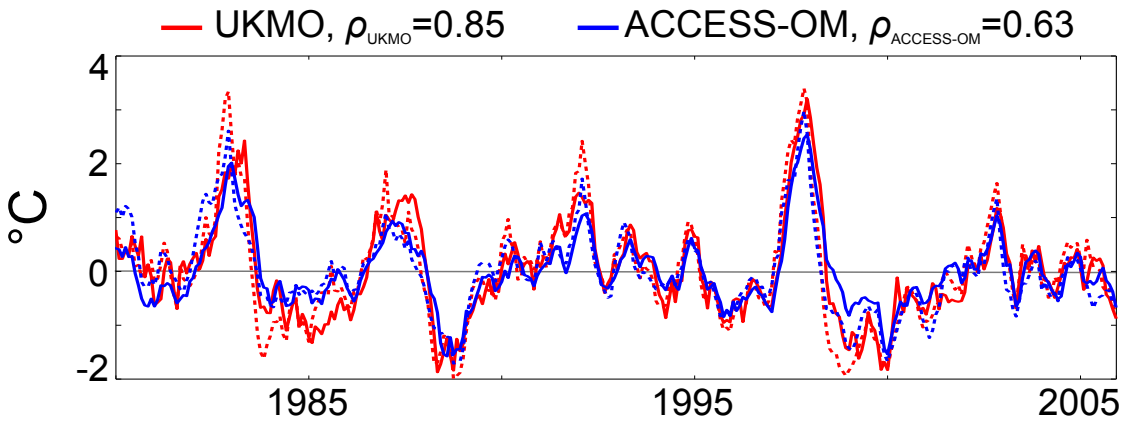

Figure 4.2: The thermocline efficiencies of the ACCESS-OM simulation (blue) and the UKMO reanalysis data (red). The dashed lines represent thermocline depth anomalies and the solid lines represent the multiplication of the temperature anomalies taken directly below the mixed layer and the corresponding thermocline efficiency factors f_H, estimated via least squares regression of the equation $\langle h \rangle_E = f_H \langle T_H \rangle_E$.

thermocline efficiency in ACCESS-OM is slightly reduced ($f_H = 0.63$, $R^2 = 0.77$) compared with the observations ($f_H = 0.85$, $R^2 = 0.82$; figure 4.2). In ACCESS-OM there tends to be poorer agreement between the thermocline depth anomalies and temperature anomalies directly below the MLD in the early part of the observational period (1980-1985), which may be linked to a greater degree of uncertainty in the radiative forcings during this period. When the MLD is assumed to be fixed at 50 m, the thermocline efficiency factor for the UKMO and ACCESS-OM data reduces to $f_H = 0.63$ and $f_H = 0.53$, respectively. This suggests that a time varying, rather than constant, MLD allows for an improved representation of the thermocline feedback efficiency in modulating SST on interannual timescales, and is more appropriate for our purposes.

4.3.3 Mixed layer heat budget

The equation for the mixed layer heat budget can be written

$$\frac{\partial T}{\partial t} = Q_q - \mathbf{u} \cdot \nabla T - w_e \frac{T - T_H}{H_{HB}} + Res, \tag{4.3}$$

(e.g. Qu, 2003; Santoso et al., 2010; Schiller and Ridgway, 2013). Here, $\frac{\partial T}{\partial t}$ is the potential temperature tendency averaged in the mixed layer, Q_q is the net downward surface heat flux, which combines the shortwave, longwave, sensible, and latent heat fluxes at the

surface omitting the amount of shortwave heat that penetrates through the base of the mixed layer, $\mathbf{u}$ is the two dimensional vertically averaged horizontal velocity vector, and the term $\mathbf{u}\cdot\nabla T$ represents horizontal advection of heat. The residual term Res represents unresolved processes, including high frequency eddies, vertical and lateral diffusion, and any spurious numerical diffusion. The second to last term on the right hand side of Eq. (4.3) represents vertical advection into the mixed layer, where w_e is the vertical entrainment velocity and the term multiplied by w_e is a parameterization of the vertical temperature gradient calculated via the difference between the mixed layer temperature T and the temperature at the grid point just below the mixed layer T_H, divided by the temporally and spatially varying MLD (H_{HB}). The vertical entrainment velocity is given by

$$w_e = \frac{\partial H_{HB}}{\partial t} + \mathbf{u}_H \cdot \nabla H_{HB} + w_H, \tag{4.4}$$

where $\mathbf{u}_H \cdot \nabla H_{HB}$ is the horizontal velocity vector at the base of the mixed layer $\mathbf{u}_H$ multiplied by the corresponding horizontal gradient of the MLD ∇H_{HB}. The vertical velocity at the base of the mixed layer is given by w_H. Since from below only mean entrainment into the mixed layer affects the mixed layer temperature, we introduce the Heaviside step function notation, $H(\overline{w_e})$, where

$$H(x) = \begin{cases} 1, & x > 0 \\ 0, & \text{otherwise,} \end{cases}$$

to denote that the vertical entrainment velocity must be positive definite.

Eq. (4.3) is decomposed into seasonal climatologies (denoted by an overbar) and anomalies (denoted by a prime), yielding the following mixed layer anomalous heat budget equation

$$\begin{aligned} \frac{\partial T'}{\partial t} &= {Q_q}' - \mathbf{u}' \cdot \nabla \overline{T} - \overline{\mathbf{u}} \cdot \nabla T' - \mathbf{u}' \cdot \nabla T' + \overline{\mathbf{u}' \cdot \nabla T'} \\ &\quad - H(\overline{w_e}) w_e' \frac{\overline{T} - \overline{T_H}}{H_{HB}} - H(\overline{w_e}) \overline{w_e} \frac{T' - T_H'}{H_{HB}} - H(\overline{w_e}) w_e' \frac{T' - T_H'}{H_{HB}} + \overline{H(\overline{w_e}) w_e' \frac{T' - T_H'}{H_{HB}}} + Res', \\ &= S' + Res'. \end{aligned} \tag{4.5}$$

Note that we apply the Heaviside step function to the climatological vertical entrainment velocity in each case. This is for consistency with the BJ index calculation below and

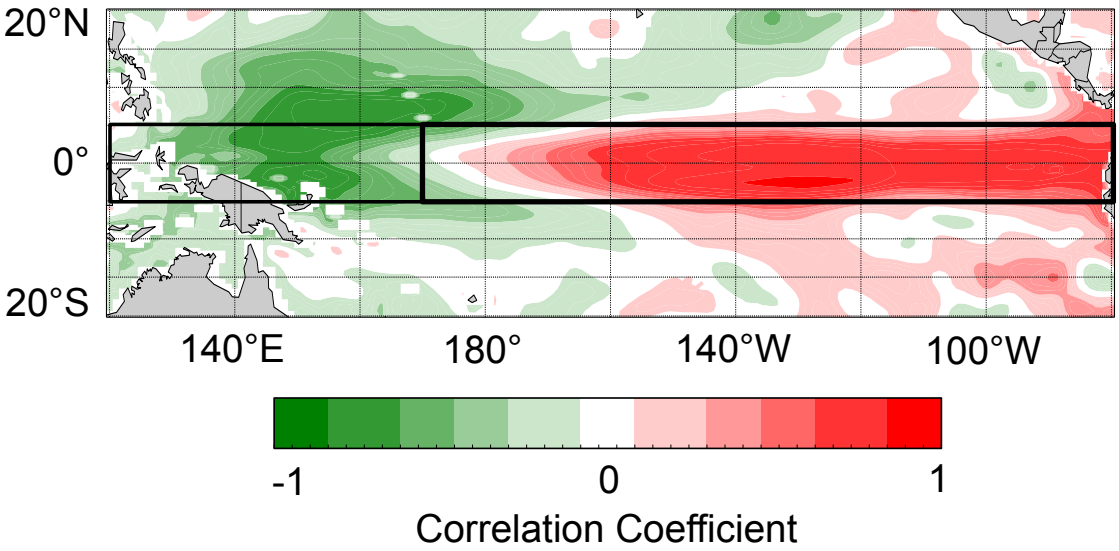

Figure 4.3: The correlation field of the leading EOF mode of upper ocean heat content anomalies in the equatorial Pacific. The boxes delineate the western Pacific region from the central-eastern Pacific region for the purposes of our study.

with Kim and Jin (2011a), and yields a better approximation to the linear relation in Eq. (4.15). The temperature tendency $\partial T'/\partial t$ and S' are volume averaged in the central-eastern equatorial Pacific (5°S-5°N, 175°E-80°W; figure 4.3) and denoted $\langle \partial T/\partial t \rangle_E$ and $\langle S \rangle_E$, respectively (note that here, and in what follows, the prime notation used to denote an anomaly has been dropped). Figure 4.4a shows the time evolution of $\langle \partial T/\partial t \rangle_E$ and $\langle S \rangle_E$ over the period 1980-2007. The curves $\langle \partial T/\partial t \rangle_E$ and $\langle S \rangle_E$ correlate well ($\rho = 0.83$), indicating that the right-hand side of Eq. (4.5), even when the residual terms are omitted, is a good approximation to the mixed layer temperature tendency of the equatorial Pacific. The main discrepancies between $\langle \partial T/\partial t \rangle_E$ and $\langle S \rangle_E$ arise during large ENSO events, for instance 1982-83 and 1997-98, when there were notable changes to TIW behavior. It is expected that there would be better agreement between the two curves with the addition of vertical diffusion terms, which play an important role in ENSO events (e.g. Zhang and McPhaden, 2010).

In the derivation of the BJ index, the nonlinear terms from the heat budget are neglected.

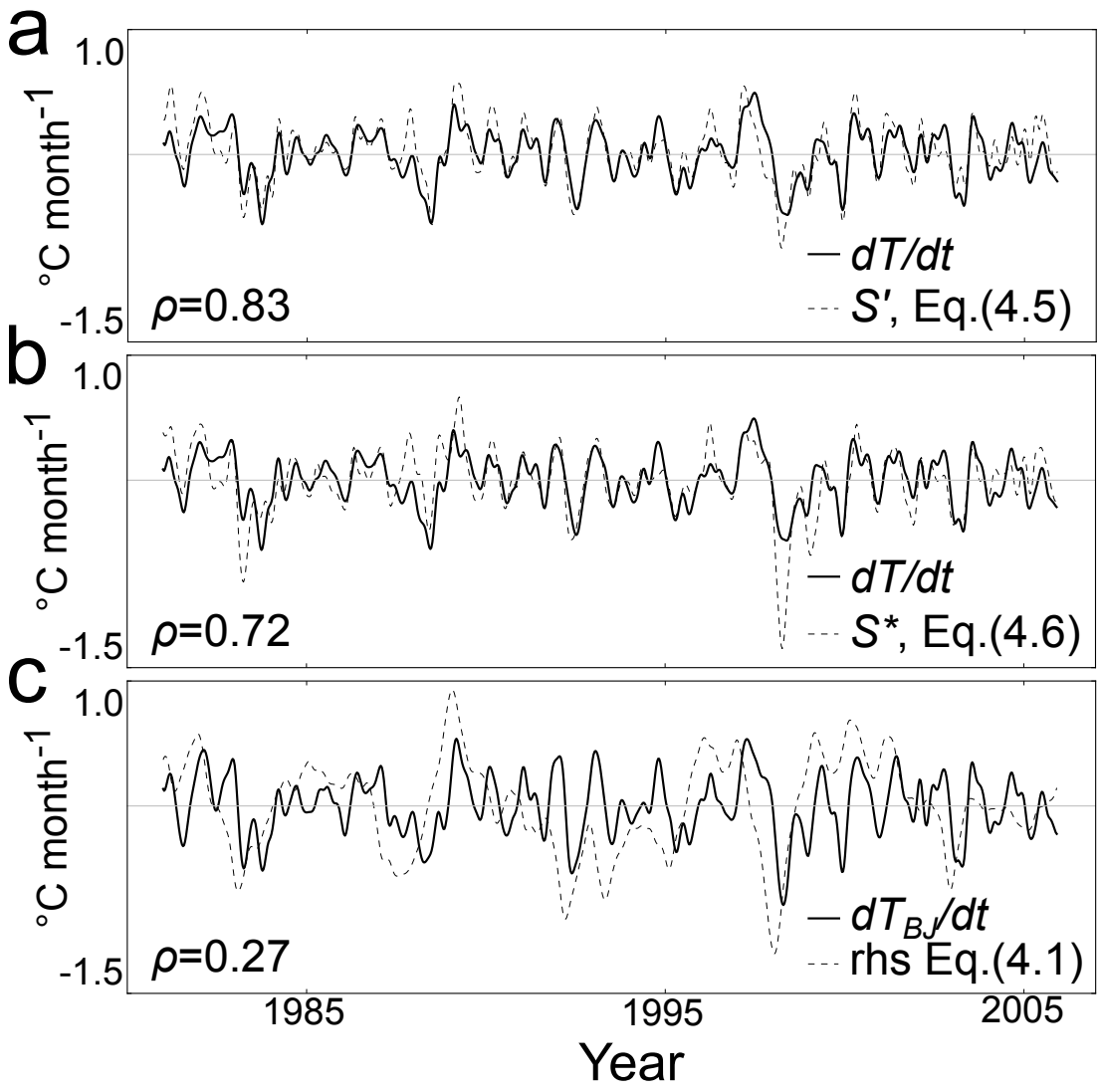

Figure 4.4: Closure of the temperature tendency. **a** is the anomalous heat budget equation in Eq. (4.5); **b** is the anomalous heat budget equation including only the terms corresponding to those in the BJ index, that is Eq. (4.6); and **c** is the BJ index formulation of the recharge oscillator temperature equation, Eq. (4.1). In each, the solid line is the anomalous temperature tendency, $\langle \partial T/\partial t \rangle_E$, and the dashed line is the right-hand side of the corresponding equations. Note that the temperature tendency in **c** differs from the upper panels due to the constant rather than variable MLD in the BJ index formulation. The correlation coefficients between the two timeseries in each panel are reported (ρ values). A low-pass filter to remove variability of 90 days and less was applied to each of the timeseries. The mean of each timeseries in the three panels is close to zero.

The heat budget, now containing only the features considered by the BJ index, is

$$\begin{aligned}\left\langle \frac{\partial T}{\partial t} \right\rangle_E &= \underbrace{-\left(\langle \overline{u} \rangle_E \left\langle \frac{\partial T}{\partial x} \right\rangle_E + \langle \overline{v} \rangle_E \left\langle \frac{\partial T}{\partial y} \right\rangle_E \right)}_{(1)} + \underbrace{\langle Q_q \rangle_E}_{(2)} \\ &\quad + \underbrace{\langle H(\overline{w_e}) \overline{w_e} \rangle_E \left\langle \frac{\partial T}{\partial z} \right\rangle_E}_{(3)} - \underbrace{\langle u \rangle_E \left\langle \frac{\partial \overline{T}}{\partial x} \right\rangle_E}_{(4)} + \underbrace{\langle H(\overline{w_e}) w_e \rangle_E \left\langle \frac{\partial \overline{T}}{\partial z} \right\rangle_E}_{(5)}, \\ &= \langle S^* \rangle_E, \end{aligned} \tag{4.6}$$

where $\langle \partial T/\partial z \rangle_E = \langle -(T - T_H)/H_{HB} \rangle_E$, and the terms on the right-hand side of the equation represent (1) advection due to mean zonal and meridional currents, (2) thermodynamic damping, (3) the thermocline feedback, (4) the zonal advective feedback, and (5) the Ekman feedback, respectively. Note the neglect of the spatial eddy terms in Eq. (4.5). As above, the angle brackets denote volume averaged variables and the subscript E denotes averaging in the central-eastern box. The two sides of Eq. (4.6) are plotted in figure 4.4b. The correlation coefficient between the left- and right-hand sides is 0.72.

Comparison of figures 4.4a and 4.4b illustrates the effect of removing the nonlinear terms on the closure of the heat budget. As expected, there is poorer closure during the large ENSO events of 1982-83 and 1997-98. There is also poor closure during the 1988-89 La Niña event. In this case, that the preceding 1986-87 El Niño event was not phase locked to the seasonal cycle may have given rise to nonlinearities that were not present during other events.

4.3.4 The BJ index

The BJ index is derived from the mixed layer heat budget equation, with the nonlinear terms omitted (Eq. (4.6)), and a series of linear balance relations obtained from approximations to the ENSO ocean-atmosphere coupled dynamics (c.f. Battisti and Hirst, 1989; Jin, 1997a; Jin and An, 1999; An and Jin, 2001; Jin et al., 2006). An outline of the BJ index derivation is provided in the appendix. The BJ index is a constant number

evaluated as R, where

$$R = \underbrace{-\left(\frac{\langle\overline{u}\rangle_E}{L_x} + \frac{\langle -2y\overline{v}\rangle_E}{L_y^2} + \frac{\langle\overline{w}\rangle_E}{H_{BJ}}\right)}_{(1)} \underbrace{-\alpha}_{(2)}$$
$$+ \underbrace{a_h\beta_h\mu\left\langle\frac{\overline{w}}{H_{BJ}}\right\rangle_E}_{(3)} + \underbrace{\beta_u\mu\left\langle-\frac{\partial\overline{T}}{\partial x}\right\rangle_E}_{(4)} + \underbrace{\beta_w\mu\left\langle-\frac{\partial\overline{T}}{\partial z}\right\rangle_E}_{(5)}. \tag{4.7}$$

The terms on the right-hand side of Eq. (4.7) are (1) advection by mean currents, (2) thermodynamic damping, (3) the thermocline feedback, (4) the zonal advective feedback, and (5) the Ekman feedback, and can be related to the corresponding terms in Eq. (4.6). The constant coefficients β_h, β_u, β_w measure the sensitivity of the response of different oceanic variables (i.e. $\langle h\rangle_E - \langle h\rangle_W$, $\langle u\rangle_E$, and $\langle w\rangle_E$) to wind stress forcing at the surface, the coefficient μ is the air-sea coupling coefficient, and the coefficient a_h measures the sensitivity of the mixed layer temperature response to changes in the thermocline depth. The constants a_1 and a_2 are obtained via regression of the volume averaged temperature anomalies in the central-eastern Pacific box with volume averaged temperature anomalies averaged zonally and meridionally, respectively, at the boundaries of the central-eastern box. We note that the terms in Eq. (4.7) are only the components of the heat budget that contribute to growth R as described in Eq. (4.1). The components of the heat budget that contribute to frequency F are

$$F = \beta_{uh}\left\langle-\frac{\partial\overline{T}}{\partial x}\right\rangle_E + a_h\left\langle\frac{\overline{w}}{H_{BJ}}\right\rangle_E. \tag{4.8}$$

Details of how the terms in Eqs. (4.7) and (4.8) are derived from Eq. (4.6) are given in the appendix.

Consistent with previous studies (Jin et al., 2006; Kim and Jin, 2011a), the BJ index is calculated by estimation of the sensitivity coefficients in Eq. (4.7) from linear least squares regression, where in each case the intercept is constrained to be zero. Error bounds for the 95% confidence levels are also calculated. The spatial boxes for averaging the feedbacks in the BJ index are determined using empirical orthogonal function (EOF) analysis of upper ocean heat content anomalies (defined as the volume averaged temperature in the uppermost 300m of the equatorial ocean). Here, the upper ocean

heat content is used as a proxy for thermocline depth (the depth of the 20°C isotherm), which is a good approximation in the equatorial ocean (e.g. Rebert et al., 1985), for ease of comparison with previous studies. The results of the EOF analysis for the full equatorial Pacific between 15°S-15°N and from 120°E-80°W are shown in figure 4.3. The 175°E line is identified as delineating the western box (5°S-5°N and 120-175°E) from the central-eastern box (5°S-5°N and 175°E-80°W). The temperature anomaly $\langle T \rangle_E$ and the net downward surface heat flux anomaly $\langle Q \rangle_E$ are both averaged in the central-eastern box; the upper ocean heat content anomaly is averaged in the central-eastern box $\langle h \rangle_E$ and the western box $\langle h \rangle_W$; and the zonal wind stress anomalies are averaged collectively over the western and central-eastern boxes $[\tau^x]$. In the boxed regions, $[\tau^x]$ and $\langle Q \rangle_E$ are area averaged and the remaining variables are volume averaged between the surface and a constant MLD of H_{BJ}=50m. The assumption of a constant MLD in the BJ index introduces an error in the estimation of the feedback terms of a similar order to the feedbacks themselves, and is also investigated. The parameterization of $\left\langle \frac{\partial T}{\partial z} \right\rangle_E$ in the mixed layer heat budget definition is $\left\langle \frac{\partial T}{\partial z} \right\rangle_E \approx \langle -(T - T_H)/H_{HB} \rangle_E$. In the BJ index, this term is split into two components: the first component $\langle -T/H_{BJ} \rangle_E$ contributes to advection by mean currents; the second, denoted $\left\langle \frac{\partial T}{\partial z} \right\rangle_E \approx \langle T_H/H_{BJ} \rangle_E$, contributes to the thermocline feedback.

4.4 Analysis of the BJ index

The feedback terms in the BJ index are calculated and compared with the corresponding terms calculated from the mixed layer heat budget equation, Eq. (4.5). A more detailed derivation of the BJ index from the heat budget appears in the appendix.

4.4.1 The recharge oscillator using the BJ index

First, we address how well the recharge oscillator description of ENSO reproduces the volume averaged temperature anomaly tendency with the BJ index definition of R and F. The terms in Eq. (4.1), which appear in more detail in Eq. (4.20) from the appendix, were calculated and the left- and right-hand sides of this equation plotted in figure 4.4c. The BJ index formulation of the temperature tendency - the right-hand side of Eq.

(4.1) - does a poor job of modeling the true temperature tendency in the ACCESS-OM output; the correlation coefficient between the two curves is 0.27 (table 4.1). The BJ formulation of the temperature tendency appears to capture the low frequency variability of the temperature tendency. Hence, as expected, the correlation coefficient for the same two timeseries when a 12-month filter is applied is slightly higher ($\rho = 0.38$). There is poor budget closure during the periods 1992-95 and 1999-2003. However, central Pacific El Niño events (i.e., events that occur near the western Pacific warm pool region), which are characterized by a less strong recharge mechanism than eastern Pacific El Niño events (Ren and Jin, 2013), occurred during these two periods (Singh et al., 2011). Thus, given that the right-hand side of Eq. (4.1) assumes a robust recharge mechanism, it is perhaps not surprising that poorer closure is observed in 1992-95 and 1999-2003.

We investigate whether the lack of agreement between the left- and right-hand sides of Eq. (4.1) is due to (a) omitting the nonlinear terms from the heat budget Eq. (4.5), or (b) a poor representation of the terms in the BJ index. To determine this, we compare the terms from the heat budget that correspond to the BJ index temperature tendency formulation, that is, figures 4.4b and 4.4c. If these are similar, then the error in the recharge oscillator is due to omitting the nonlinear terms from the heat budget Eq. (4.5); otherwise, it is due to poor approximations of the heat budget terms it does contain. The heat budget formulation more accurately captures the shape and variability of the temperature tendency and explains a higher proportion of the variance in the temperature tendency ($\rho = 0.72$; $\rho^2 = 0.52$) compared with the BJ index formulation ($\rho = 0.27$; $\rho^2 = 0.073$). Hence, we conclude that at least some of the assumptions underlying the BJ index formulation are either incorrect or inadequate in explaining ENSO dynamics, rather than there being a problem with the omission of terms. Next, we investigate the three ocean feedback terms separately to explore how and why the BJ index does not represent the ocean dynamics correctly over this period.

4.4.2 Thermocline feedback

The BJ index form of the thermocline feedback is given by

$$a_h \beta_h \mu \left\langle \frac{\overline{w}}{H_{BJ}} \right\rangle_E ,$$

Table 4.1: Correlation coefficients between each of the ocean feedbacks described by the Bjerknes stability index and the corresponding feedbacks calculated from the heat budget equation

	Eq.	ρ
Full anomalous heat budget, $\frac{d\langle T\rangle_E}{dt} = \langle S\rangle_E$	(4.5)	0.83
Heat budget equivalent to BJ index, $\frac{d\langle T\rangle_E}{dt} = \langle S^*\rangle_E$	(4.6)	0.72
BJ index temperature tendency, $\frac{d\langle T\rangle_E}{dt} = R\langle T\rangle_E + F\langle h\rangle_W$	(4.1)	0.27
Thermocline feedback		
$-\langle H(\overline{w_e})\overline{w_e}\rangle_E \left\langle \frac{\partial T}{\partial z}\right\rangle_E = a_h\beta_h\mu\left\langle \frac{\overline{w}}{H_{BJ}}\right\rangle_E \langle T\rangle_E$		0.60
(i) $\langle H(\overline{w})T_H\rangle_E = a_h\langle h\rangle_E$,	(4.9)	0.91
(ii) $\langle h\rangle_E - \langle h\rangle_W = \beta_h[\tau^x]$,	(4.10)	0.86
(iii) $[\tau^x] = \mu\langle T\rangle_E$,	(4.11)	0.84
Full thermocline feedback		
$-\langle H(\overline{w_e})\overline{w_e}\rangle_E \left\langle \frac{\partial T}{\partial z}\right\rangle_E = a_h\beta_h\mu\left\langle \frac{\overline{w}}{H_{BJ}}\right\rangle_E \langle T\rangle_E + a_h\left\langle \frac{\overline{w}}{H}\right\rangle_E \langle h\rangle_W$	(4.12)	0.51
Zonal advective feedback		
$-\langle u\rangle_E \left\langle \frac{\partial \overline{T}}{\partial x}\right\rangle_E = \beta_u\mu\left\langle -\frac{\partial \overline{T}}{\partial x}\right\rangle_E \langle T\rangle_E$		0.45
(i) $\langle u\rangle_E = \beta_u[\tau^x] + \beta_{uh}\langle h\rangle_W$,	(4.13)	0.68
Full zonal advective feedback		
$-\langle u\rangle_E \left\langle \frac{\partial \overline{T}}{\partial x}\right\rangle_E = \beta_u\mu\left\langle -\frac{\partial \overline{T}}{\partial x}\right\rangle_E \langle T\rangle_E + \beta_{uh}\left\langle -\frac{\partial \overline{T}}{\partial x}\right\rangle_E \langle h\rangle_W$	(4.14)	0.58
Ekman feedback		
$-\langle w_e\rangle_E \left\langle \frac{\partial \overline{T}}{\partial z}\right\rangle_E = \beta_w\mu\left\langle -\frac{\partial \overline{T}}{\partial z}\right\rangle_E \langle T\rangle_E$		0.14
(i) $\langle H(\overline{w})w\rangle_E = -\beta_w[\tau^x]$,	(4.15)	0.82
Thermodynamic damping $\alpha\langle T\rangle_E$		
(i) $\langle Q\rangle_E = -\alpha\langle T\rangle_E$,	(4.17)	0.90

which is an approximation to the full thermocline feedback from the heat budget, namely $\overline{w}\langle\frac{\partial T}{\partial z}\rangle_E$. The thermocline feedback accounts for the effect of wind stress forcing on the slope of the thermocline, which in turn generates subsurface and surface temperature anomalies. The BJ index approximates $\langle\frac{\partial T}{\partial z}\rangle_E$ in the thermocline feedback by $\langle T_H/H_{BJ}\rangle_E$. Following this, there are three more approximations made in stepping from the heat budget to the BJ index formulation of the thermocline feedback in Jin et al. (2006).

The first coefficient in the thermocline feedback, a_h, can be estimated via regression of the subsurface temperature anomaly $\langle T_H\rangle_E$ against the central-eastern averaged thermocline depth anomaly $\langle h\rangle_E$:

$$\langle H(\overline{w})T_H\rangle_E = a_h\langle h\rangle_E. \tag{4.9}$$

This relation was defined only for the scenario when $\overline{w} > 0$. The term $H(\overline{w})$ is the Heaviside step function that ensures only vertical motion into the mixed layer affects the mixed layer temperature. The scatter plot and timeseries of this relation are illustrated in figure 4.5a. In ACCESS-OM, the corresponding regression slope is 2.0 ± 0.1, and the correlation coefficient between $\langle H(\overline{w})T_H\rangle_E$ and $\langle h\rangle_E$ is 0.91 (table 4.1), which indicates that the explained variance is 83%. This estimate for a_h is consistent with Kim and Jin (2011a).

Secondly, the coefficient β_h can be estimated via regression of the difference in thermocline slope across the equatorial Pacific against the wind stress forcing, namely

$$\langle h\rangle_E - \langle h\rangle_W = \beta_h[\tau^x]. \tag{4.10}$$

Figure 4.5b shows the scatter plot and timeseries of this relationship, yielding a β_h value of $16 \times 10 \pm 11$ °C Pa^{-1}, again consistent with the estimate of Kim and Jin (2011a). The variable $[\tau^x]$ explains 74% of the variance in the thermocline slope.

Finally, the coefficient representing the sensitivity of the wind response to temperature forcing μ, a component of each of the oceanic feedback terms, can be estimated via regression of the zonal wind stress anomalies onto the temperature anomalies, that is

$$[\tau^x] = \mu\langle T\rangle_E. \tag{4.11}$$

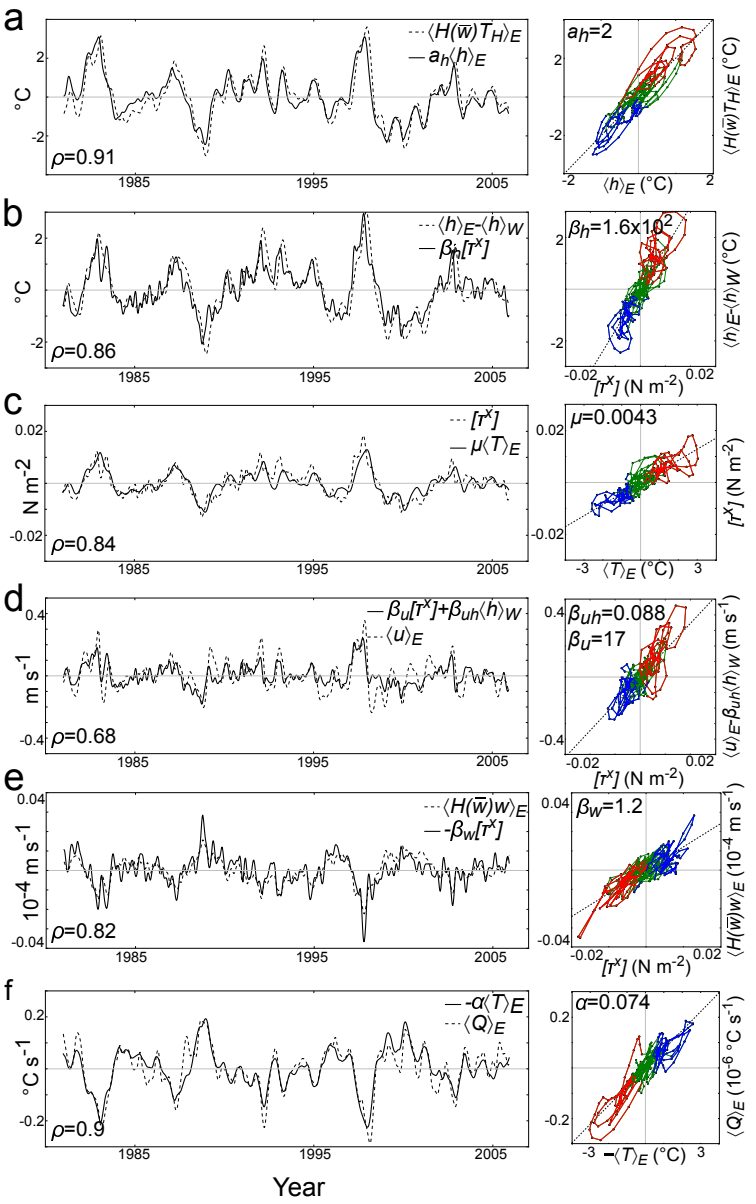

Figure 4.5: Timeseries and scatter plots from the balance equations used to derive the BJ index. The scatter plots are colored by El Niño years (red dots), La Niña years (blue dots), and neutral years (green dots). The correlation coefficients between the two timeseries (post-fitting) in each panel are reported (ρ values). **a** The left panel shows the timeseries of $a_h\langle h\rangle_E$ (solid line) and $\langle H(\overline{w})T_H\rangle_E$ (dashed line) and the right panel shows the scatter plot of these two same variables where the black dotted slope line represents the value of the coefficient a_h as estimated from least squares regression of the balance relation $\langle H(\overline{w})T_H\rangle_E = a_h\langle h\rangle_E$, Eq. (4.9). **b** As in panel **a** except for the balance relation in Eq. (4.10). Here, the solid line in the left panel is $\beta_h[\tau^x]$ and the dashed line is $\langle h\rangle_E - \langle h\rangle_W$. **c** As in panel **a** except for the balance relation in Eq. (4.11). Here, the solid line in the left panel is $\mu\langle T\rangle_E$ and the dashed line is $[\tau^x]$. **d** As in panel **a** except for the balance relation in Eq. (4.13). Here, the solid line in the left panel is $\beta_u[\tau^x] + \beta_{uh}\langle h\rangle_W$ and the dashed line is $\langle u\rangle_E$. **e** As in panel **a** except for the balance relation in Eq. (4.15). Here, the solid line in the left panel is $-\beta_w[\tau^x]$ and the dashed line is $\langle H(\overline{w})w\rangle_E$. **f** As in panel **a** except for the balance relation in Eq. (4.17). Here, the solid line in the left panel is $-\alpha\langle T\rangle_E$ and the dashed line is $\langle Q\rangle_E$.

The scatter plot and timeseries of this relation are shown in figure 4.5c. The regression slope is $0.43 \pm 0.03 \times 10^{-2}$ Pa $^{\circ}$C^{-1} and the correlation coefficient between $[\tau^x]$ and $\langle T \rangle_E$ is 0.84. This estimate for μ agrees with those from similar studies (Kim and Jin, 2011a; Lübbecke and McPhaden, 2013).

Previous studies (e.g. Frauen and Dommenget, 2010; Choi et al., 2013) have argued that on ENSO-like timescales there is a nonlinear relationship, rather than a linear one, between zonal wind stress and SST, which gives rise to an asymmetry between El Niño and La Niña events. We find that for the ACCESS-OM run, and using the basin-wide averaged zonal mean wind stress $[\tau^x]$ and central-eastern volume-averaged temperature $\langle T \rangle_E$, there is an approximately 33% difference in slope between warm events and cool events for the relation in Eq. (4.11), which indicates that the assumption of linearity is not sufficient. This value for the difference in slope is higher than observed, but is less than the value estimated from the GFDL coupled ocean/atmosphere/land/sea ice model CM2.1 (Choi et al., 2013). However, it should be noted that our value is not directly comparable with the values estimated in Choi et al. (2013) for two primary reasons: (i) we regress the basin-wide average of $[\tau^x]$ with the volume-averaged temperature, rather than the Niño-4 averaged zonal wind stress with the Niño-3.4 averaged SST; and (ii) the model data used in this study is an ocean-only run forced by $[\tau^x]$, not a coupled run.

Combining Eqs. (4.9) - (4.11), the BJ index thermocline feedback approximation of the heat budget thermocline feedback is:

$$\langle H(\overline{w})\overline{w} \rangle_E \left\langle \frac{\partial T}{\partial z} \right\rangle_E = a_h \beta_h \mu \left\langle \frac{\overline{w}}{H_{BJ}} \right\rangle_E \langle T \rangle_E + a_h \left\langle \frac{\overline{w}}{H_{BJ}} \right\rangle_E \langle h \rangle_W, \tag{4.12}$$

where the coefficient that is multiplied by $\langle T \rangle_E$ on the right-hand side of Eq. (4.12) is the BJ index thermocline feedback that contributes to the growth of an ENSO event R in Eq. (4.1), and the coefficient that is multiplied by $\langle h \rangle_W$ is a component of the frequency term F in Eq. (4.1).

The total BJ index thermocline feedback, term (3) in Eq. (4.7), is 2.9 $[-0.5, +0.6]$ year^{-1}, which is larger than the values estimated by Kim and Jin (2011a) and Lübbecke and McPhaden (2013). The larger thermocline feedback in our case is likely due to a larger value of $\langle \overline{w} \rangle_E$ obtained here than in previous studies; however, this is to be expected

due to physical and dynamical differences in the models used. For example, the term a_h is sensitive to the model data used and contributes to uncertainty in the value of the thermocline feedback since (i) a_h is a function of the mean ocean stratification, which varies considerably from model to model (e.g. Yeh et al., 2010; Lengaigne et al., 2011); and (ii) a_h cannot be fully determined by simple linear regression between $\langle h \rangle_E$ and $\langle T_H \rangle_E$ since the strength of the thermocline feedback depends on the balance between the contributions of zonal and vertical advection to the temperature anomaly tendency (Dewitte et al., 2013).

When multiplied by $\langle T \rangle_E$, as in the first term on the right-hand side of Eq. (4.12), the thermocline feedback can be compared with the heat budget thermocline feedback, term (3) in Eq. (4.6) (figure 4.6a). The correlation coefficient between the two curves is 0.60. The BJ index thermocline feedback overestimates the heat budget thermocline feedback due to two key reasons. Firstly, the magnitude of the BJ index thermocline feedback is determined by the magnitude of the coefficient $a_h \beta_h \mu \left\langle \frac{\overline{w}}{H_{BJ}} \right\rangle_E$, which multiplies the $\langle T \rangle_E$ term in Eq. (4.12). It is possible that this coefficient is too large, due to an overestimation of the regression coefficients in Eqs. (4.9) - (4.11), or an overestimation of the mean upwelling $\langle \overline{w} \rangle_E$. Secondly, the BJ index thermocline feedback captures the main features of the low-frequency variability of the heat budget thermocline feedback, which means it may miss some ENSO events when multiple events of the same sign occur in succession. It follows that there are points in time where the BJ index thermocline feedback is large and positive or large and negative, although the heat budget thermocline feedback is near zero.

In order to make a complete comparison of the BJ index thermocline feedback with that of the heat budget, it is necessary to include the components of the thermocline feedback contributing to both growth and frequency, that is, both terms on the right-hand side of Eq. (4.12). These components are combined and plotted against the heat budget thermocline feedback in figure 4.6b. Although the magnitude of the combined BJ index thermocline feedback is more similar to the heat budget thermocline feedback than the component contributing to growth alone, the correlation between the two timeseries is slightly smaller (ρ=0.51). The biggest discrepancies between the combined BJ index

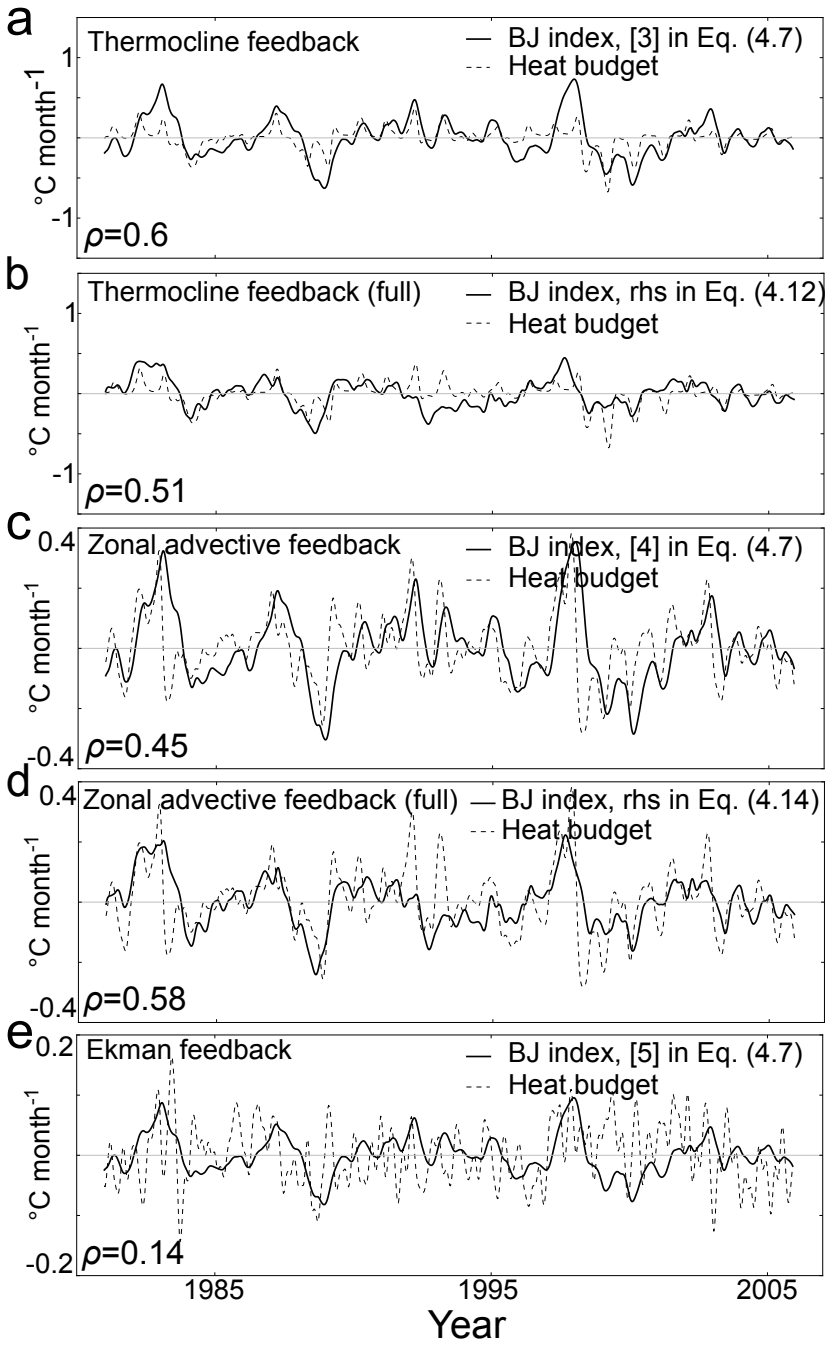

Figure 4.6: Oceanic feedbacks from the BJ index (solid lines) and their corresponding representation in the heat budget (dashed lines). The panels show: **a** the thermocline feedback contributing to growth in the BJ index, that is term (3) in Eq. (4.7); **b** the full thermocline feedback, including both growth and frequency contributions from Eq. (4.12); **c** the zonal advective feedback contributing to growth in the BJ index, that is term (4) in Eq. (4.7); **d** the full zonal advective feedback, including both growth and frequency contributions from Eq. (4.14); and **e** the Ekman feedback contributing to growth in the BJ index, that is term (5) in Eq. (4.7). Note the different scales on the y-axes.

thermocline feedback and the heat budget thermocline feedback occur during central Pacific ENSO events (e.g., 1992-95 and 1999-2003), which have a less robust recharge mechanism than eastern Pacific events.

4.4.3 Zonal advective feedback

The zonal advective feedback contribution to the BJ index is

$$\beta_u \mu \left\langle -\frac{\partial \overline{T}}{\partial x} \right\rangle_E,$$

which represents the change in the mixed layer temperature tendency due to the action of anomalous zonal currents on the mean zonal temperature gradient, namely the term $\langle u \rangle_E \left\langle -\frac{\partial \overline{T}}{\partial x} \right\rangle_E$ in the heat budget.

The term β_u can be estimated via multiple linear regression from an equation relating the anomalous zonal currents $\langle u \rangle_E$ to forcing by the local anomalous zonal wind stress $[\tau^x]$ and the geostrophic adjustment to the thermocline depth gradient $\langle h \rangle_W$, given by (Jin, 1997b)

$$\langle u \rangle_E = \beta_u [\tau^x] + \beta_{uh} \langle h \rangle_W. \tag{4.13}$$

In the ACCESS-OM run, β_u is 17 ± 2 m s^{-1} Pa^{-1} and β_{uh} is 0.088 ± 0.02 m s^{-1} °C^{-1}. The value for β_u is higher than the value estimated by Lübbecke and McPhaden (2013) for the equatorial Atlantic ocean, although our estimate of β_{uh} is comparable. The scatter plot and timeseries of the relation in Eq. (4.13), including both the wind stress forcing and the geostrophic adjustment, are illustrated in figure 4.5d. The correlation coefficient is 0.68 and the explained variance is 47%, both of which are relatively low. Lübbecke and McPhaden (2013) found that this relation was also poor in the observational datasets, although they argued that this is related to the short time period of overlapping years and the poor quality of the thermocline data. However, when a 12-month filter is applied to the variables $\langle u \rangle_E$, $[\tau^x]$, and $\langle h \rangle_W$, the correlation coefficient between the left- and right-hand sides of Eq. (4.13) increases to 0.81. We note that the basin-wind average of $[\tau^x]$ may not be as appropriate for accurately estimating the sensitivity of the zonal currents to wind forcing as an average of zonal wind stress in the Niño-4 region, where $\left\langle \frac{\partial T}{\partial x} \right\rangle_E$ is strong.

Eqs. (4.11) and (4.13) are combined to yield the BJ index zonal advective feedback approximation to the heat budget zonal advective feedback, namely

$$\langle u\rangle_E\left\langle -\frac{\partial\overline{T}}{\partial x}\right\rangle_E = \beta_u\mu\left\langle -\frac{\partial\overline{T}}{\partial x}\right\rangle_E\langle T\rangle_E + \beta_{uh}\left\langle -\frac{\partial\overline{T}}{\partial x}\right\rangle_E\langle h\rangle_W, \tag{4.14}$$

where the coefficient that is multiplied by $\langle T\rangle_E$ on the right-hand side of Eq. (4.14) is the BJ index zonal advective feedback and the coefficient that is multiplied by $\langle h\rangle_W$ contributes to the frequency term in Eq. (4.1).

The zonal advective feedback from the BJ index is 1.4 ± 0.3 year^{-1}, which is greater than previous estimates (c.f. Lübbecke and McPhaden, 2013). The zonal advective feedback from the BJ index can be multiplied by $\langle T\rangle_E$, as in Eq. (4.14), and compared with the corresponding zonal advective feedback from the heat budget (figure 4.6c). The correlation coefficient between the two curves is 0.45, with the BJ index zonal advective feedback explaining 20% of the variance in the original heat budget zonal advective feedback.

When geostrophic effects are added to the zonal advective feedback from the BJ index, that is, the second term in Eq. (4.14), the correlation with the heat budget zonal advective feedback increases to 0.58; however, this modified zonal advective feedback does a poorer job of capturing the magnitude of the heat budget zonal advective feedback (figure 4.6d).

4.4.4 Ekman feedback

The Ekman feedback term in the BJ index is written

$$\beta_w\mu\left\langle -\frac{\partial\overline{T}}{\partial z}\right\rangle_E,$$

and describes the effect on the equatorial temperature tendency of the anomalous wind forced upwelling acting on the mean vertical temperature gradient. It is derived from the term $\langle H(\overline{w})w\rangle_E\left\langle\frac{\partial\overline{T}}{\partial z}\right\rangle_E$.

The coefficient β_w can be estimated by regressing the anomalous upwelling $\langle H(\overline{w})w\rangle_E$ onto the zonal wind stress anomalies $[\tau^x]$, i.e.,

$$\langle H(\overline{w})w\rangle_E = -\beta_w[\tau^x], \tag{4.15}$$

yielding a value of β_w equal to $1.2 \pm 0.09 \times 10^{-4}$ m s^{-1} Pa^{-1}, which is again consistent with the value estimated by Kim and Jin (2011a). The scatter plot and timeseries are shown in figure 4.5e. The correlation coefficient is 0.82, and the explained variance is 68%. As above for the estimation of β_u, an average of the zonal wind stress anomalies in a region where $\left\langle \frac{\partial T}{\partial z} \right\rangle_E$ is strong, rather than over the full equatorial Pacific, may be more appropriate for estimating the sensitivity of $\langle H(\overline{w})w \rangle_E$ to wind forcing.

The BJ index approximation to the heat budget Ekman feedback is found by combining Eqs. (4.11) and (4.15), yielding

$$\langle H(\overline{w})w \rangle_E \left\langle \frac{\partial \overline{T}}{\partial z} \right\rangle_E = \beta_w \mu \left\langle -\frac{\partial \overline{T}}{\partial z} \right\rangle_E \langle T \rangle_E. \tag{4.16}$$

Again, taking into account μ from section 4.4.2 above, the value of the BJ index Ekman feedback coefficient is 0.38 ± 0.06 year^{-1}. When multiplied by $\langle T \rangle_E$, the BJ index Ekman feedback can be compared with the Ekman feedback from the heat budget (figure 4.6e). The correlation coefficient between the two curves is 0.14. In particular, we note that the BJ index Ekman feedback underestimates the magnitude of the large ENSO events.

4.4.5 Evaluating the MLD

One difference between the BJ index feedbacks and the corresponding heat budget feedbacks is their definition of MLD. That is, while the BJ index terms are volume averaged in the top 50m of the equatorial Pacific, the heat budget terms are volume averaged between the surface and a variable MLD.

To investigate the difference in magnitudes of the ocean feedbacks that the definition of MLD introduces, we calculate each of the three ocean feedbacks in the mixed layer heat budget equation - the thermocline feedback, the zonal advective feedback and the Ekman feedback - for the case when the MLD varies and for the case when it is held fixed at 50m depth (figure 4.7). We find that the largest difference between the two MLD definitions arises for the thermocline feedback, where the error is of a similar order of magnitude as the feedback itself. By contrast, there is a smaller difference between the MLD definitions for the zonal advective feedback.

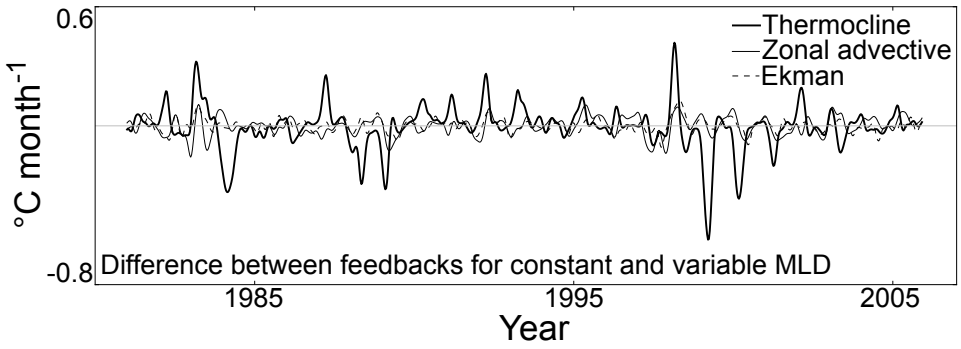

Figure 4.7: Difference between the cases when the MLD is variable and fixed at 50m for: the heat budget thermocline feedback (dark solid line), the zonal advective feedback (light solid line), and the Ekman feedback (dashed line).

Closer examination of the terms in the BJ index highlights the differences between the cases when the MLD is fixed and when it varies. Central-eastern averaged temperature $\langle T \rangle_E$, and its horizontal derivatives, as well as the zonal current $\langle u \rangle_E$ do not change significantly when averaged in a variable rather than fixed volume. There is a greater difference between the vertical and entrainment velocities, $\langle w \rangle_E$ and $\langle w_e \rangle_E$, respectively, since the latter takes into account horizontal flow at the base of the mixed layer as well as the tendency of the MLD. However, the largest difference arising from the change in MLD definitions is in the term $\left\langle \frac{\partial T}{\partial z} \right\rangle_E$, which in the BJ index is parameterized as $\langle T_H / H_{BJ} \rangle_E$. When the MLD is allowed to vary, the variance in $\langle T_H / H_{BJ} \rangle_E$ increases markedly due to the large change in H_{BJ}. It is for this reason that the thermocline and Ekman feedbacks are so noticeably different for the two MLD definitions.

4.4.6 Other BJ index terms

In the previous sections we contrast the BJ index ocean feedbacks with the corresponding terms from the heat budget. In what follows we calculate the BJ index terms that quantify thermodynamic damping and advection by mean currents.

Thermodynamic damping

The thermodynamic damping coefficient, denoted α, is calculated via linear regression of the local net downward surface heat flux anomalies onto the volume averaged temperature anomalies in the central-eastern equatorial box, namely

$$\langle Q \rangle_E = -\alpha \langle T \rangle_E. \tag{4.17}$$

Here, $\langle Q \rangle_E$ is scaled by the constants ρ =1035 kg m^{-3} and c_p = 3989.24 J kg^{-1} °C^{-1} to be of the same units as $\alpha \langle T \rangle_E$. The value of α is 2.3 ± 0.1 year^{-1} in our model run, and the scatter plot and timeseries are shown in figure 4.5f. This value is slightly higher than values reported in previous studies (e.g., Kim and Jin (2011a) and Lübbecke and McPhaden (2013) estimate α to be between 1.30 and 1.90 year^{-1}), but generally within the 95% confidence intervals of these previous estimates. The correlation coefficient between $\langle Q \rangle_E$ and $\langle T \rangle_E$ is 0.90. As the accuracy of the BJ index formulation of the thermodynamic damping term from the heat budget equation has already been studied (e.g. Lloyd et al., 2012), we do not compare it with the corresponding term from the heat budget here.

Surface heat fluxes are the largest contributor to damping in the central equatorial Pacific, and are dominated by the shortwave (Q_{SW}) and latent heat fluxes (Lloyd et al., 2011). Previous studies (e.g. Lloyd et al., 2012; Bellenger et al., 2014) argue that the cloud processes described in the shortwave feedback (i.e., the coefficient α_{SW} estimated via regression of the shortwave heat flux $\langle Q_{SW} \rangle_E$ with $\langle T \rangle_E$) are highly complex, implying that the linear relationship between $\langle Q \rangle_E$ and $\langle T \rangle_E$ described above is perhaps over simplified. Hence, it is likely that the uncertainty associated with our value of α is larger than estimated above. However, given that our focus in this study is on the representation of the ocean feedbacks important to ENSO, we do not investigate this matter further.

Advection by mean currents

The remaining terms in Eq. (4.22) from the appendix represent advection of the temperature averaged in the central-eastern equatorial box due to mean zonal, meridional,

and vertical currents, namely

$$-\left(\frac{\langle\overline{u}\rangle_E}{L_x}+\frac{\langle-2y\overline{v}\rangle_E}{L_y^2}+\frac{\langle\overline{w}\rangle_E}{H_{BJ}}\right), \tag{4.18}$$

which are collectively -1.9 year^{-1}.

4.4.7 Total BJ index

The terms in Eq. (4.7), as estimated in sections 4.4.2 - 4.4.6, are summed, yielding a BJ index of 0.49 $[-0.2, +1]$ year^{-1}, illustrated in figure 4.8. The largest contributor to the instability growth is the thermocline feedback, and the largest damping is from mean advection. The BJ index, R, is negative and as it sets the growth of the recharge oscillator model from Eq. (4.1), it is clear that the system is unstable in the ACCESS-OM simulation for the period 1980-2007. The largest uncertainty associated with the estimate of R for our model comes from the ocean feedbacks, and in particular the thermocline and zonal advective feedbacks, respectively. The error estimate associated with the total BJ index is very large, due to the cumulative uncertainties associated with the estimates of the regression coefficients. It is unlikely that the error estimate associated with the BJ index would improve if a longer, coupled model run were to be employed due to the range of ENSO behaviors in CGCMs.

4.5 Discussion

The BJ index quantifies the positive feedback (instability growth) in the recharge oscillator model, and is used to understand the stability properties of ENSO as described by that model. The BJ index is derived from a series of balance equations and approximations to the mixed layer heat budget equation. We have explored the robustness of these approximations and their implications for the representations of the ocean feedbacks important to ENSO in the BJ index. We found that the approximations did not always accurately portray the ocean dynamics they described and could be misleading for model intercomparisons.

One of the largest inconsistencies between the heat budget feedbacks and the corresponding BJ index parameterization arose due to an overestimation of the correlation

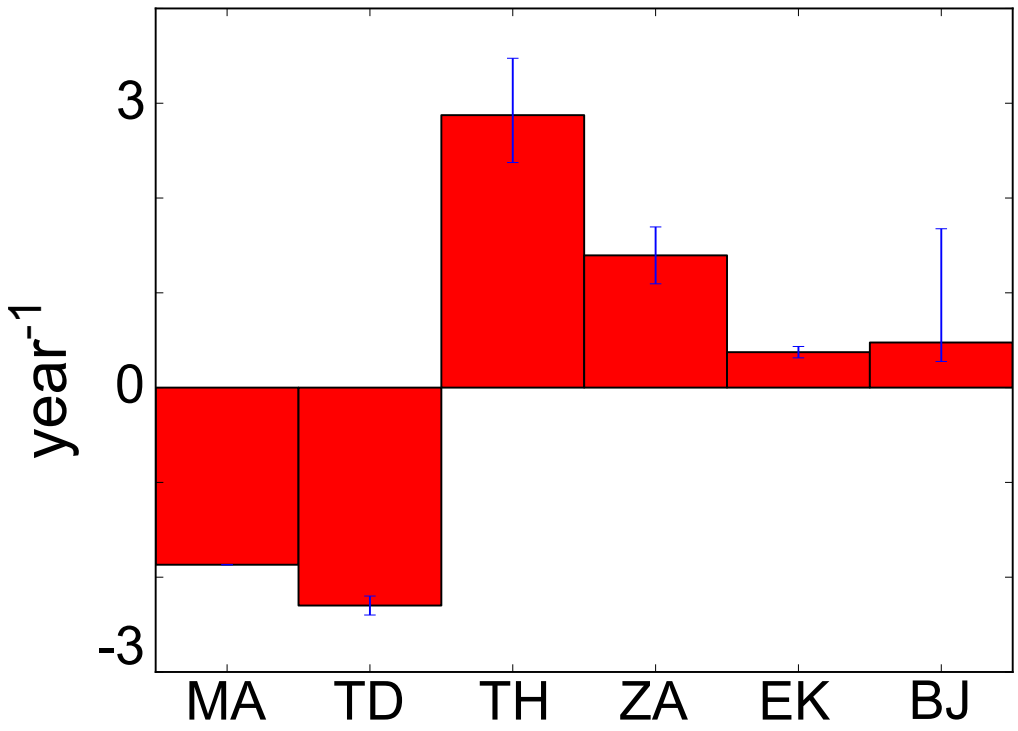

Figure 4.8: The BJ index and its contributing terms. MA represents advection by mean currents, TD is thermodynamic damping, TH is the thermocline feedback, ZA is the zonal advective feedback, EK is the Ekman feedback, and BJ is the BJ index, R.

between each. For example, noting that the correlation coefficient is the cosine of the angle between two vectors, suppose that the vectors A and B are orthogonal so that $\rho_{AB} = 0$. Now, suppose vector C bisects the right angle between A and B. Then $\rho_{AC} = \rho_{BC} = \cos(\pi/4) \approx 0.7$, such that A and B account for approximately 50% of the variance in C, despite having no variance in common. In the case of the Ekman feedback, the individual balance relations used to derive the BJ index feedback from that of the heat budget were highly correlated: the timeseries of wind stress anomalies $[\tau^x]$ and temperature anomalies $\langle T \rangle_E$ from Eq. (4.11) had a correlation coefficient of 0.84, and the timeseries of vertical velocity anomalies $\langle H(\overline{w})w \rangle_E$ and wind stress anomalies $[\tau^x]$ had a correlation coefficient of 0.82. However, the correlation coefficient between the original heat budget Ekman feedback and the BJ index Ekman feedback was only

0.14.

A second source of error in the BJ index formulation was the assumption of linearity in the balance relations Eqs. (4.9) - (4.11), (4.13), (4.15), and (4.17). It is well known that the wind stress feedback is a nonlinear function of SST (Wang and McPhaden, 2000; Jin et al., 2003; Timmermann et al., 2003; An and Jin, 2004; Gebbie et al., 2007; Brown et al., 2010) and this is highlighted by the balance relation in Eq. (4.13) where the linear approximation could only explain 47% of the variance in the zonal current anomaly. Although nonlinearities were not explicitly included in the BJ index, large ENSO events, or those events with markedly different dynamics, had an influence on the determination of the regression coefficients in the BJ index calculation. Furthermore, given the range of ENSO behaviors within a GCM with constant external forcing (Wittenberg, 2009; Kug et al., 2010; Ogata et al., 2013), it is possible that there will be periods in the future marked by different flavors of ENSO where the nonlinear terms will be more important (Vecchi et al., 2006).

A third problem that has been identified from our analysis relates to the use of regression coefficients in constructing the BJ index feedbacks. Regression coefficients do not tell us whether each of the timeseries used in the analysis are lagged, nor do they provide information on the similarities and differences between the curves. We illustrate this point with the use of a theoretical model in figure 4.9. We calculate a regression coefficient between time series R (red curve) and each of A - a timeseries of the same magnitude and shape as R, but lagged by $\pi/3$ units - and B - a timeseries with a magnitude up to 1.75 times that of R and with a different shape. Both calculations result in a regression coefficient of 0.5, suggesting that the sensitivity between R and A is the same as R and B. If we apply a similar argument to the BJ index, we conclude that the magnitude of the BJ index feedbacks may be over- or underestimated, which is clear from comparison of the BJ index thermocline feedback with the heat budget feedback in figure 4.6a. That the BJ index may over- or underestimate feedback magnitudes has implications for the usefulness of model intercomparisons.

A fourth difference between the BJ index feedbacks and the heat budget feedbacks was due to the different parameterizations of the MLD. While the heat budget ocean

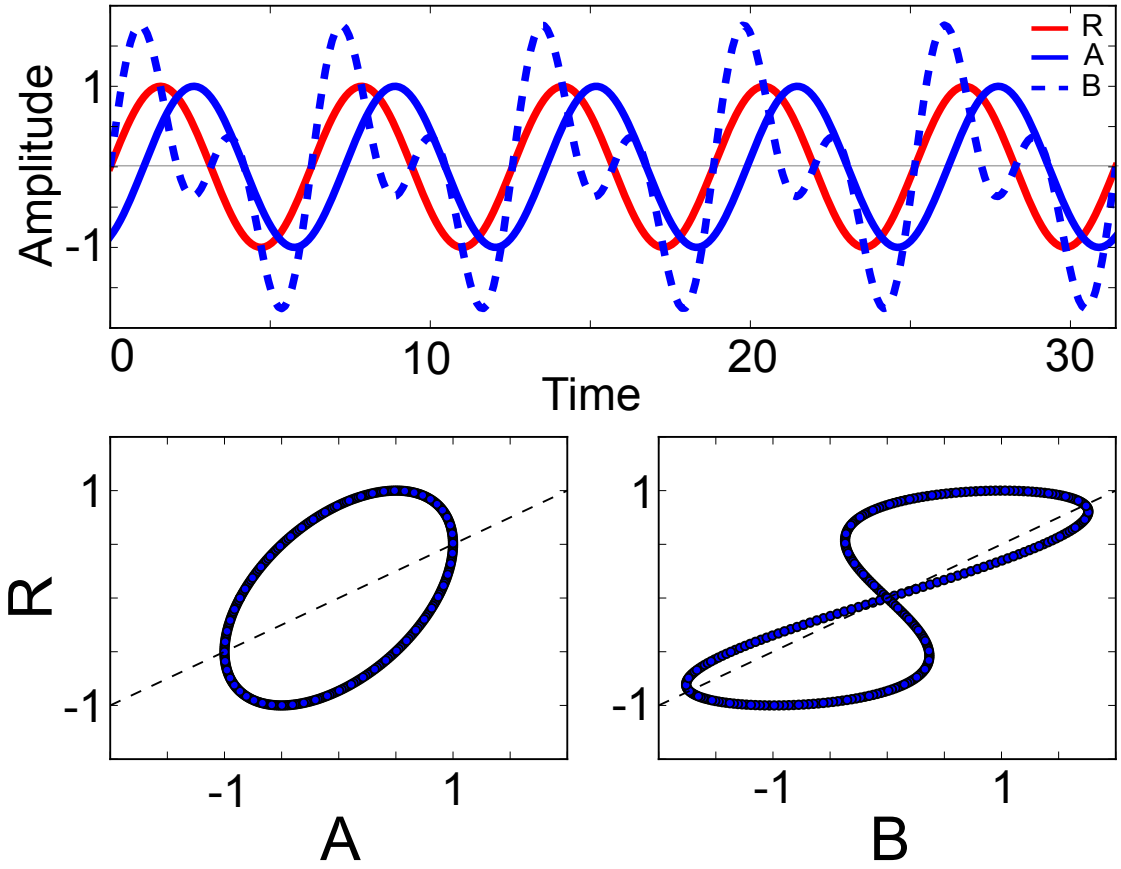

Figure 4.9: Toy model highlighting the problem with using the regression coefficient as an estimate of the similarity between feedbacks. The top panel shows the timeseries of R (red line), A (blue solid line), and B (blue dashed line). The lower left panel shows the regression between R and A; the lower right panel shows the regression between the R and B. Note that the regression coefficients, t_A and t_B, for the regressions in the lower panels are equal.

feedbacks were calculated within a temporally and spatially varying MLD, the BJ index assumed that the MLD was a constant 50m. Although 50m is close to the mean MLD across the equatorial Pacific, it is nevertheless a gross approximation to the true MLD and does not provide a realistic expression of the oceanic processes that give rise to mixed layer temperature variations. For example, a constant mixed layer depth will not capture the changes in stratification associated with a deepening thermocline during El Niño events (DiNezio et al., 2012). Given that a robust estimate of the MLD is a standard output in most models, it is not costly to include the more accurate representation of

ocean dynamics via a varying MLD rather than a fixed MLD in calculating the BJ index feedback terms.

Finally, the values of the feedbacks estimated by the BJ index will depend on the time period and region over which they are calculated. We estimated the averaging domain by EOF analysis of 28 years of heat content anomaly data, but even within this period there were different spatial "flavors" of ENSO (e.g. both canonical eastern Pacific events and central Pacific events as in Ashok et al., 2007) such that the BJ index results may be inadvertently weighted towards a particular spatial signal of ENSO.

4.6 Summary

In the original paper on the BJ index, Jin et al. (2006) used an intermediate complexity model to demonstrate that the BJ index is a good approximation to the coupled slow instability of ENSO. As a result, they argued that the BJ index can be used instead of eigenanalysis, which is not feasible in many CGCMs, to assess how the leading, linear ENSO-like mode might change under different background states of the equatorial Pacific. Since then, the BJ index has been widely used in model intercomparisons of complex, nonlinear CGCMs with variable MLDs to assess changes in ENSO feedbacks from historical periods to periods with increased CO_2 forcing (e.g. Kim and Jin, 2011a; Bellenger et al., 2014). We argue that since the BJ index misrepresents the true magnitude of the ENSO ocean feedbacks - namely the thermocline, zonal advective, and Ekman feedbacks - as calculated using the mixed layer heat budget equation for the tropical ocean, it should be used with caution as a diagnostic tool to assess model behavior and biases. Furthermore, when assessing dynamical differences between models it may be more fruitful to calculate the heat budget feedbacks directly, which explicitly account for nonlinearities that are not parameterized in the BJ index.

Our analysis was restricted to an ocean-only GCM run over a short period; however, we argue that the use of a flux-forced ocean/sea ice model (that is comparable to observational products) is preferable in this instance to a coupled ocean/atmosphere/sea ice model, which may suffer biases that can complicate the representation of ocean-atmosphere interactions in the tropical Pacific. The ACCESS-OM simulation has been

useful in understanding the workings of the BJ index formula and its shortcomings. We are hopeful that the BJ index can be improved by incorporating appropriate nonlinearities into the balance relations that underlie each of the feedbacks and by including a temporally and spatially varying MLD. However, this may be challenging given the uncertainties associated with future changes in ENSO behavior, limited observational data, and differing ENSO behavior across models.

Based on the recharge discharge oscillator model, the BJ index is a powerful tool for diagnosing the stability of the leading ENSO-like mode in coupled models; however, we have demonstrated that the BJ index does not adequately describe the dynamics of the ocean feedbacks of ENSO. As a consequence, its application in the assessment of model behavior, biases, and intercomparisons, particularly under climate change scenarios, should be conducted with caution, being fully mindful of the pitfalls and limitations described here.

4.7 Appendix: derivation of the BJ index

The BJ index is derived from the linearized anomalous temperature tendency equation, namely

$$\frac{\partial T'}{\partial t} = -\overline{u}\frac{\partial T'}{\partial x} - \overline{v}\frac{\partial T'}{\partial y} - \overline{w}\frac{\partial T'}{\partial z} - u'\frac{\partial \overline{T}}{\partial x} - v'\frac{\partial \overline{T}}{\partial y} - w'\frac{\partial \overline{T}}{\partial z} + {Q_q}', \tag{4.19}$$

where the overline notation denotes climatological fields (i.e., averaged over the full time period) and the prime denotes anomalous fields that have the seasonal cycle removed. In what follows we drop the prime notation. The terms in Eq. (4.19) are averaged vertically, from the ocean surface to the MLD, and horizontally in the central-eastern equatorial Pacific (5°S-5°N, 175°E-80°W), in which the majority of ENSO variability occurs, yielding

$$\begin{aligned}\frac{\partial \langle T\rangle_E}{\partial t} = &-\left(\frac{\langle \overline{u}\rangle_E}{L_x} + \frac{\langle -2y\overline{v}\rangle_E}{L_y^2} + \frac{\langle \overline{w}\rangle_E}{H_{BJ}}\right)\langle T\rangle_E + \langle Q\rangle_E \\ &- \left\langle \frac{\partial \overline{T}}{\partial x}\right\rangle_E \langle u\rangle_E - \left\langle \frac{\partial \overline{T}}{\partial z}\right\rangle_E \langle H(\overline{w})w\rangle_E + \left\langle \frac{\overline{w}}{H_{BJ}}\right\rangle_E \langle H(\overline{w})T_H\rangle_E,\end{aligned} \tag{4.20}$$

where L_x and L_y are the longitudinal and latitudinal extents of the central-eastern box, respectively, and the factor $-2y/L_y$ assumes that the tropical SST anomalies are Gaussian with an e-folding decay scale of L_y. The term H_{BJ} is the MLD, T_H is the temperature at the grid point just below the mixed layer, and $H(\overline{w})$ ensures that only the vertical motion into the mixed layer affects the mixed layer heat budget. Note that in deriving Eq. (4.20), the small term $-v'\partial T/\partial y$ has been omitted, consistent with Jin et al. (2006). A series of balance equations from section 4.4 (Eqs. (4.9) - (4.11), (4.13), (4.15), and (4.17)) are applied to approximate the terms in Eq. (4.20). These balance equations yield coefficients that estimate the strength of the air-sea coupling μ, the sensitivity of oceanic responses to surface winds β_h, β_u, β_w, and the magnitude of advection by mean currents and thermodynamic damping. Collectively, they enable the temperature tendency in Eq. (4.20) to be separated into growth and frequency components, expressed in the form of the recharge oscillator model (Jin, 1997a), namely,

$$\frac{\partial \langle T\rangle_E}{\partial t} = R\langle T\rangle_E + F\langle h\rangle_W. \tag{4.21}$$

Here the coefficients R and F are explicit functions of the basic state, rather than simply coefficients estimated via regression to observations or model data. R is the growth term

that underpins the BJ index, and is given by

$$R = -\left(\frac{\langle\overline{u}\rangle_E}{L_x} + \frac{\langle -2y\overline{v}\rangle_E}{L_y^2} + \frac{\langle\overline{w}\rangle_E}{H_{BJ}}\right) - \alpha + a_h\beta_h\mu\left\langle\frac{\overline{w}}{H_{BJ}}\right\rangle_E + \beta_u\mu\left\langle -\frac{\partial\overline{T}}{\partial x}\right\rangle_E + \beta_w\mu\left\langle -\frac{\partial\overline{T}}{\partial z}\right\rangle_E, \tag{4.22}$$

and the frequency term F is given by

$$F = \beta_{uh}\left\langle -\frac{\partial\overline{T}}{\partial x}\right\rangle_E + a_h\left\langle\frac{\overline{w}}{H_{BJ}}\right\rangle_E. \tag{4.23}$$

Chapter 5

How coupled models alter El Niño ocean dynamics: a case study using the ACCESS coupled model

This chapter presents an analysis of a coupled general circulation model (CGCM) - the Australian Community Climate and Earth System Simulator Coupled Model version 1.3 (ACCESS-CM1.3) - for its capability to capture the salient features of El Niño evolution. Consistent with the thesis aims (chapter 1), this chapter addresses the following specific objectives:

1. How well do the El Niño evolution heat budget dynamics in a simulation of the CGCM compare to the dynamics of a corresponding flux-forced ocean general circulation model (OGCM) simulation (where the dynamics represented in the OGCM are close to observed)?

2. Does the CGCM simulate the same spatial flavours that are present in the flux-forced OGCM simulation?

3. How similar are the El Niño evolution pathway/s of the CGCM and flux-forced OGCM?

In order to address these objectives, the heat budget equation for the tropical Pacific is calculated in both the CGCM and flux-forced OGCM. The relative contributions of each of the heat budget feedbacks to El Niño growth are evaluated. The underlying El Niño evolution pathways - that is, the dynamics instrumental in driving the patterns of

growth and variability - in the CGCM and flux-forced OGCM are further contrasted.

Contributions

The main text of this chapter is a paper submitted to *Climate Dynamics*. The experimental design and analysis methods were discussed between Dr Jaclyn N. Brown, Dr Andrew T. Wittenberg, Assoc./Prof. Neil J. Holbrook, and myself. The ACCESS-OM simulation data - the same simulation analysed in chapters 3 and 4 - were supplied by Dr Simon J. Marsland, who also provided technical assistance. The code used to calculate the heat budget terms was based on similar code written by Jaison Kurian (UCLA). All other coding and data analysis was performed by myself. All sections of the coauthored paper were led by myself with manuscript refinement provided by the coauthors, namely Dr Jaclyn N. Brown, Dr Andrew T. Wittenberg, Dr Simon J. Marsland, and Assoc./Prof. Neil J. Holbrook.

5.1 Abstract

Sea surface temperature (SST) metrics are widely used to investigate how global warming will impact El Niño-Southern Oscillation (ENSO) behavior in coupled general circulation models (CGCMs). However, SST metrics are limited in their ability to provide a clear picture of the development of ENSO anomalies, and to account for the reasons underpinning ENSO behavior, at least partly due to biases in CGCMs. The realism of El Niño evolution is evaluated in the Australian Community Climate and Earth System Simulator (ACCESS) CGCM using the mixed layer heat budget equation calculated during El Niño development and contrasted against that of the ACCESS ocean-only component (ACCESS-OM) forced with observed surface fluxes. Two types of El Niño were identified in the CGCM. The first type was a double peaked event with warming centers evolving concurrently in the eastern and western Pacific. The separation between the two peaks was attributed to the westward bias in the dynamic warm pool edge. Despite considerable differences between the evolution of SST patterns in the CGCM double peaked El Niño events and those of the OGCM, some CGCM double peaked events were erroneously categorized as central Pacific El Niños by SST metrics. The second CGCM El Niño type involved warming in the eastern Pacific that appeared to be similar to that of the corresponding OGCM events, yet displayed a distinctly different dynamical evolution.

Double peaked events were also found in several CMIP5 models, indicating that the CGCM behavior identified in this study was consistent with other leading coupled models. The results suggested that evaluation of spatial evolution pathways was a more powerful tool for diagnosing El Niño spatial flavors in CGCMs than standard SST metrics.

5.2 Introduction

Coupled General Circulation Models (CGCMs) are some of our most effective tools for investigating the dynamics of El Niño-Southern Oscillation (ENSO) and the response of ENSO to global warming (Meehl et al., 2006; Yeh et al., 2006, 2009; Collins et al., 2010; Vecchi and Wittenberg, 2010). Improvements are continually being made among models

with respect to some of the salient features of ENSO, such as its amplitude, frequency, seasonality, and stability (AchutaRao and Sperber, 2006; Deser et al., 2012; Guilyardi et al., 2012a; Bellenger et al., 2014; Kim et al., 2014b). Nevertheless, there is considerable diversity in the simulation of ENSO dynamics, both within and across CGCMs (Lloyd et al., 2009; Belmadani et al., 2010; Ham and Kug, 2012; Lloyd et al., 2012; Brown et al., 2013; Capotondi, 2013; Capotondi et al., 2015) and even more diversity in how ENSO will change under global warming (Leloup et al., 2008; Guilyardi et al., 2009; Collins et al., 2010; Boucharel et al., 2011; Kim and Jin, 2011b).

It follows that a current focus of ENSO research is in quantifying the realism of behaviors simulated by CGCMs, which requires comparison of model output with observed features such as sea surface temperature (SST), winds, rainfall, clouds, mixed layer depth (MLD), thermocline depth, and ocean currents. However, we have glimpsed only a sample of the possible ENSO behaviors and spatial flavors (or types; that is, patterns of warming and cooling) that could occur (figure 5.1). This is partly due to the fact that ENSO modulates climate on multiple timescales, demonstrating strong interannual variability as well as decadal to multidecadal variability (Allan, 2000; Allan et al., 2003; Wittenberg, 2009; Choi et al., 2012; Wittenberg et al., 2014), that may not yet be clearly distinguishable from our relatively short observational record. The framework schematized in figure 5.1 presents three of the possible scenarios for the range of ENSO dynamics evidenced in CGCMs: i) CGCMs simulate realistic dynamics, of which some may mirror the observations; ii) CGCMs are unable to reflect present-day ENSO dynamics; or iii) CGCMs capture dynamics that are qualitatively similar to those of the real world as well as some unrealistic ones. [We note that there are additional possible scenarios to these three discussed here, such as the observational or reanalysis data exhibiting biases in their representation of reality, as well as the real-world variability changing due to external radiative forcings.] Scenario i) is desirable if we are to use CGCMs to understand future externally forced ENSO events, while scenario ii) implies little faith in the ability of coupled models to perform this task. Based on results from recent studies (e.g. Wittenberg et al., 2006; Guilyardi et al., 2009; Brown et al., 2013) scenario iii) is perhaps the most likely, indicating that while CGCMs have utility, their underlying biases should be taken

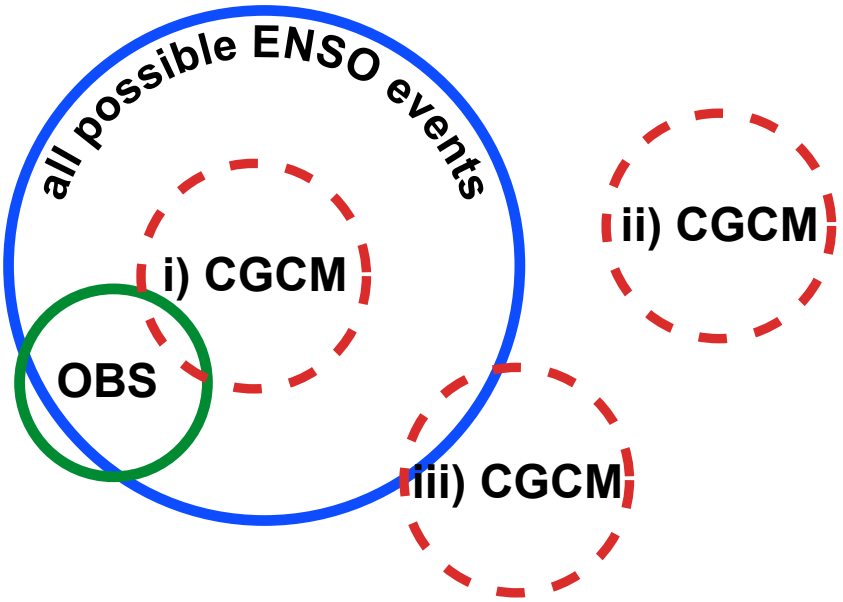

Figure 5.1: Schematic representing the possible relationships between the ENSO behaviors simulated by CGCMs (red dashed circles), the full range of possible ENSO behaviors under present-day conditions (blue circle) and the observed ENSO behaviors (green circle). The green circle extends slightly outside the blue circle to represent observational errors, such as in measurement or reconstruction. We also note that the blue circle is itself evolving on decadal to centennial timescales due to natural internal variability, as well as due to external radiative forcings.

into consideration when interpreting simulated ENSO behaviors.

Several biases in the tropical Pacific prevent models from realistically simulating ENSO behavior. For example, cooler than observed SSTs in the central-eastern equatorial Pacific alter patterns of precipitation and wind stress, impacting the strength of the thermodynamical response to SST, as well as ocean dynamics, such as the thermocline and zonal advective feedbacks (Belmadani et al., 2010; Xiang et al., 2011; Brown et al., 2012; DiNezio et al., 2012; Brown et al., 2013). Previous studies have found that a westward extension of ENSO anomaly patterns in CGCMs reduces their capacity to correctly reproduce central Pacific El Niño events and the frequency of the two types of El Niño present in observations (Wittenberg et al., 2006; Kao and Yu, 2009; Yeh et al., 2009; Ham and Kug, 2012; Taschetto et al., 2014). These biases also impact our capacity to understand the El Niño related dynamical processes operating in CGCMs and how

they might be changing.

Metrics such as the Niño-3 SST anomaly index are often used to quantify the magnitude and frequency of ENSO events for model evaluation. The majority of CGCMs can now simulate a spatially averaged SST anomaly signal that is within the range of uncertainty predicted by observations (AchutaRao and Sperber, 2006). However, evaluating the spatial flavor of CGCM El Niño events based solely on the resemblance of their spatially averaged SST anomalies to those observed may result in misleading classifications. For instance, not only do CGCMs have SST anomalies in different geographic locations to the observations (especially due to model biases), similar patterns of SST anomalies in both CGCMs and observations may be the result of different processes (although, the atmosphere directly responds to the details of the SST pattern, rather than the underlying dynamics, and the effects of the SST pattern itself can be felt remotely). Consequently, the dynamical sources of the SST anomalies are potentially more indicative of the El Niño flavor than the SST pattern alone. It follows that ENSO research has recently focused on exploring the simulation of El Niño-related temperature anomaly tendencies via first analyzing the balance of heat budget dynamics, such as the thermocline and zonal advective feedbacks (AchutaRao and Sperber, 2006; DiNezio et al., 2009; Belmadani et al., 2010; Kug et al., 2010; DiNezio et al., 2012).

In this study, we explore whether an Intergovernmental Panel on Climate Change (IPCC)-class CGCM is able to realistically reproduce the dynamics that contribute to the development of El Niño events - i.e., the dynamical "evolution pathways". This question is particularly pertinent as we interpret ENSO behavior in CGCM global warming scenarios: to accurately diagnose future changes requires a thorough understanding of the realism of simulated historical ENSO dynamics. To investigate the issue, we calculate the mixed layer averaged heat budget equation over the tropical Pacific in a simulation of the Australian Community Climate and Earth System Simulator Coupled Model version 1.3 (ACCESS-CM1.3; Bi et al., 2013b) CGCM, which contributes to the Coupled Model Intercomparison Project Phase 5 (CMIP5). The evolution pathways of the El Niño events are categorized into distinct types and compared with output from the corresponding flux-forced ocean general circulation model (OGCM) component of ACCESS-CM1.3,

namely ACCESS-OM (Bi et al., 2013a).

This paper is structured as follows. We first introduce the models and the heat budget method used to analyze them. The different El Niño evolution pathways are explored in the CGCM and contrasted with the corresponding OGCM pathways. Finally, the results are discussed and summarized.

5.3 Data and methods

5.3.1 The ACCESS model

In this study, the ENSO dynamics modeled in a 60-year simulation (1948-2007) of the Australian Community Climate and Earth System Simulator Ocean Model, ACCESS-OM, were compared with those of a 156-year simulation (1850-2005) of the corresponding fully coupled model, ACCESS-CM1.3. We chose to compare the ACCESS CGCM results with the flux-forced ACCESS component OGCM rather than in situ, or remotely sensed, observations or reanalysis data for a number of reasons. First, ACCESS-OM has been found to realistically simulate the main features of the tropical Pacific ocean (Bi et al., 2013a; Graham et al., 2014) as well as the spatial flavors of ENSO (appendix A). Second, the ENSO spatial structure, timescales, phase locking, and growth and decay rates are reasonably well simulated by the ACCESS CMIP5 historical simulations (Rashid et al., 2013). Third, in order to calculate the terms in the heat budget equation (section 5.3.2) we required high-resolution four-dimensional temperature and ocean current data, as well as reliable estimates of the MLD. Yet, prior to the commencement of the Tropical Ocean Global Atmosphere program's Tropical Atmosphere Ocean/Triangle Trans-Ocean Buoy Network (TAO/TRITON) array in 1994, subsurface observations in the tropical Pacific were relatively sparse and thus the relevant ocean subsurface observations in the equatorial wave-guide were too short in record length to adequately evaluate the decadal to multi-decadal modulation of ENSO. Fourth, an alternative was to use reanalysis data, which represent a model assimilation of observations. However, these data can suffer from dynamical inconsistencies (e.g. Oke and Griffin, 2011; Balmaseda et al., 2013; Oke et al., 2013) that are not necessarily present in ACCESS-OM. For example, data assimilation techniques used in reanalysis models involves updates of the model

state at each time step to align with observations, resulting in imbalances in fluxes of momentum, heat, and freshwater, that are not necessarily associated with specific dynamical processes (Oke et al., 2013). Finally, by using an ocean model with the same ocean configuration as the CGCM, we were more able to attribute differences in El Niño dynamics to model coupling rather than ocean parameterizations or grid definitions.

Accordingly, the ACCESS-OM and ACCESS-CM1.3 simulations analyzed here used identical ocean configurations, differing only in the surface boundary conditions. The ocean component of the ACCESS-OM and ACCESS-CM1.3 simulations was an OGCM that drew its codebase and most of its configuration from the NOAA Geophysical Fluid Dynamics Laboratory (GFDL) MOM4p1 ocean model (Griffies, 2009). The model had a zonal resolution of 1° and a meridional resolution of 1/3° between 10°S and 10°N, extending to 1° between 10°S (°N) and 20°S (°N). The vertical resolution extended from 10m in the upper 200m to approximately 333m in the deep ocean over a total of 50 vertical levels. The sea-ice component that was coupled to both ACCESS models was the Los Alamos National Laboratory CICE4.1 (Hunke and Lipscomb, 2010), which was run on the ACCESS ocean grid.

ACCESS-OM was forced with surface heat, freshwater, and momentum fluxes derived from the forcing and bulk-formulae of Large and Yeager (2009) and used the protocols of the CLIVAR Working Group on Ocean Model Development interannually-varying Coordinated Ocean-ice Reference Experiments version 2 (CORE-II; Griffies et al., 2012; Danabasoglu et al., 2014). The atmospheric component of ACCESS-CM1.3 drew its codebase from the UK Met Office Unified Model (Davies et al., 2005; Martin et al., 2006). The zonal resolution was 1.25°, the meridional resolution was 1.875°, and there were 38 vertical levels. For the ACCESS-CM1.3 simulation, coupling between the ocean/sea-ice model and the atmospheric model was provided via OASIS3.25 (Valcke, 2006). Here, we use the CSIRO-BOM ACCESS1.3 *historical* simulation (1850-2005) as submitted to the CMIP5 database. The nomenclature of the term "*historical* simulation" follows Taylor et al. (2012) and the implementation for the ACCESS models is described by Dix et al. (2014).

Monthly anomalies of oceanic variables - namely SST, MLD, depth of the 20°C isotherm

(a standard proxy for the tropical ocean thermocline depth), horizontal and vertical currents, and surface heat fluxes (shortwave, longwave, latent, and sensible heat fluxes) - were computed by subtracting the annual cycle from the monthly mean outputs. The data were smoothed using an 11-point Parzen filter to remove frequencies of sub-annual variability.

5.3.2 The mixed layer heat budget

The mixed layer heat budget equation used in this study is adapted from Vialard and Delecluse (1998) and is given by

$$\partial_t T' = A'_x + A'_y + A'_z + Q' + DER', \tag{5.1}$$

where the symbol ∂_t represents a partial derivative with respect to time, the apostrophe $'$ denotes an anomalous quantity, and T' is the anomalous potential temperature integrated over the mixed layer (figure 5.2). The term A'_x on the right-hand side represents the mixed layer averaged anomalous zonal advection defined as

$$A'_x = -\frac{1}{h}\int_{-h}^{0} \left[\overline{u^*}\partial_x T^{*\prime} + u^{*\prime}\partial_x \overline{T^*} + u^{*\prime}\partial_x T^{*\prime}\right] dz, \tag{5.2}$$

where u^* is the full, 4-dimensional zonal current, T^* is the full, 4-dimensional potential temperature, and the overline notation denotes a climatological quantity. [Note that in chapter 4 of this thesis, the climatological quantities calculated in the heat budget equations (e.g., Eq. 4.19, etc.) represented long term quantities. In this chapter, we include the annual cycle in the climatological terms for consistency with previous studies (e.g. Stevenson and Niiler, 1983; Huang et al., 2010; Schiller and Ridgway, 2013).] The terms A'_y and A'_z in Eq. (5.1) represent anomalous meridional and vertical advection, respectively, and are constructed similarly to Eq. (5.2). Q' in Eq. (5.1) is the anomalous net surface heat flux, which can be calculated by summing the surface shortwave, longwave, latent, and sensible heat fluxes and subtracting the net shortwave contribution that penetrates through the mixed layer (Q_{swout}). In the tropical Pacific, Q_{swout} calculated from ACCESS-OM, and averaged over the period 1948-2007, is maximized in the Niño-3 region (5°S-5°N, 150-90°W; the maximum value of Q_{swout} in the Niño-3 region was 8.0 W m^{-2}, approximately 3.7% of the net surface shortwave heat flux there).

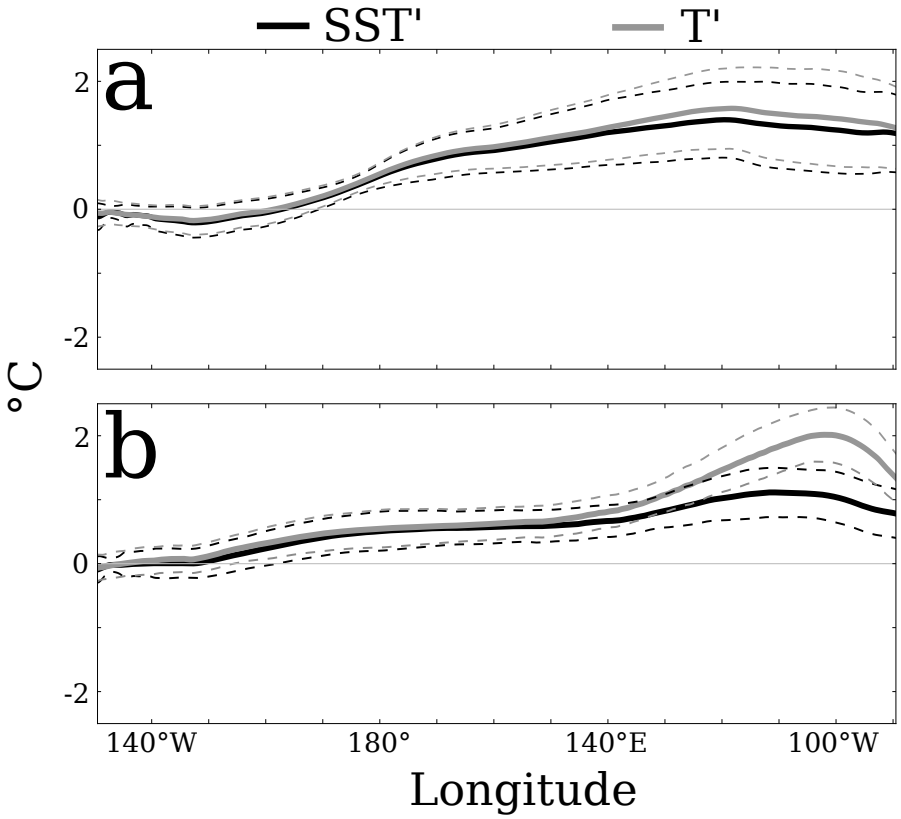

Figure 5.2: Equatorial SST' and T' (i.e., averaged between 2°S and 2°N) in ACCESS-OM (panel **a**) and ACCESS-CM1.3 (panel **b**). In each panel, the black (gray) line represents the mean of SST' (T') during the development period of all El Niño events and the dashed lines represent the standard deviations of the corresponding terms over all El Niño events averaged during the El Niño development period.

Finally, the term DER' in Eq. (5.1) represents anomalous residual processes, such as diffusion, entrainment, and turbulent heat fluxes into the mixed layer, that are not well resolved when the heat budget is calculated offline. Eq. (5.1) and its derivation are described in more detail in appendix B. In what follows, we refer to the depth-averaged (i.e., 3-dimensional, rather than the asterisked 4-dimensional) forms of the terms on the right-hand side of Eq. (5.2), and the corresponding terms for A'_y and A'_z.

The thermocline feedback, $\overline{w}\partial_z T'$ (derived from the A'_z term), is known to be a dominant term in the growth and termination of an El Niño event (An and Jin, 2001). It is defined as the action of the anomalous vertical temperature gradient on the mean upwelling.

Likewise, the zonal advective feedback, $u'\partial_x\overline{T}$ (from A'_x in Eq. (5.2)), is also important for the growth of El Niño, and is defined as the action of the anomalous zonal currents on the mean zonal temperature gradient.

5.3.3 Defining El Niño events

Due to the asymmetry in timing, duration, and amplitude between El Niño and La Niña events (Choi et al., 2013), and that the historical spatial flavors of El Niño do not necessarily have direct counterparts during La Niña episodes Yeh et al. (2014), we expect some differences in the evolutionary behavior of La Niña to that presented here for El Niño events. However, in the interests of conciseness, we choose here to focus solely on the evolution of El Niño events; the evolution pathways of La Niña events is a topic for future research.

El Niño events in the OGCM and CGCM were defined when a 5-month running mean of the unfiltered SST anomalies in the Niño-3.4 region (5°S-5°N, 170-120°W) exceeded 0.4°C for a period of at least 6 months (Trenberth, 1997). The Niño-3.4 region, along with the other regions utilized in this study, are illustrated in figure 5.3a.

Following Su et al. (2014), the El Niño development period encompassed the months from the initiation of the event, when T' in the eastern Pacific (5°S-5°N, 180-80°W) was close to zero and the $\partial_t T'$ was positive, to the point when the event reached its peak (figure 5.3b). As a first means of diagnosing the balance of terms contributing to the growth and damping of each El Niño, each of the heat budget terms was scaled by the maximum amplitude in T' during the development period, and averaged over the equator (2°S-2°N) within the longitudinal spans of the eastern Pacific (i.e., 180-80°W). This region was chosen to ensure that the location of maximum amplitude and greatest variability in the majority of the heat budget terms was captured, given the sensitivity of certain terms to the averaging region (for example, averaging in the Niño-4 region (5°S-5°N, 160°E-150°W) alone would lead to a misrepresentation of the magnitude of the thermocline and zonal advective feedbacks, which are dominant in the Niño-3 and Niño-4 regions, respectively, as illustrated in table 5.1). We choose to scale the heat budget terms during development period of each event by the maximum amplitude of T'

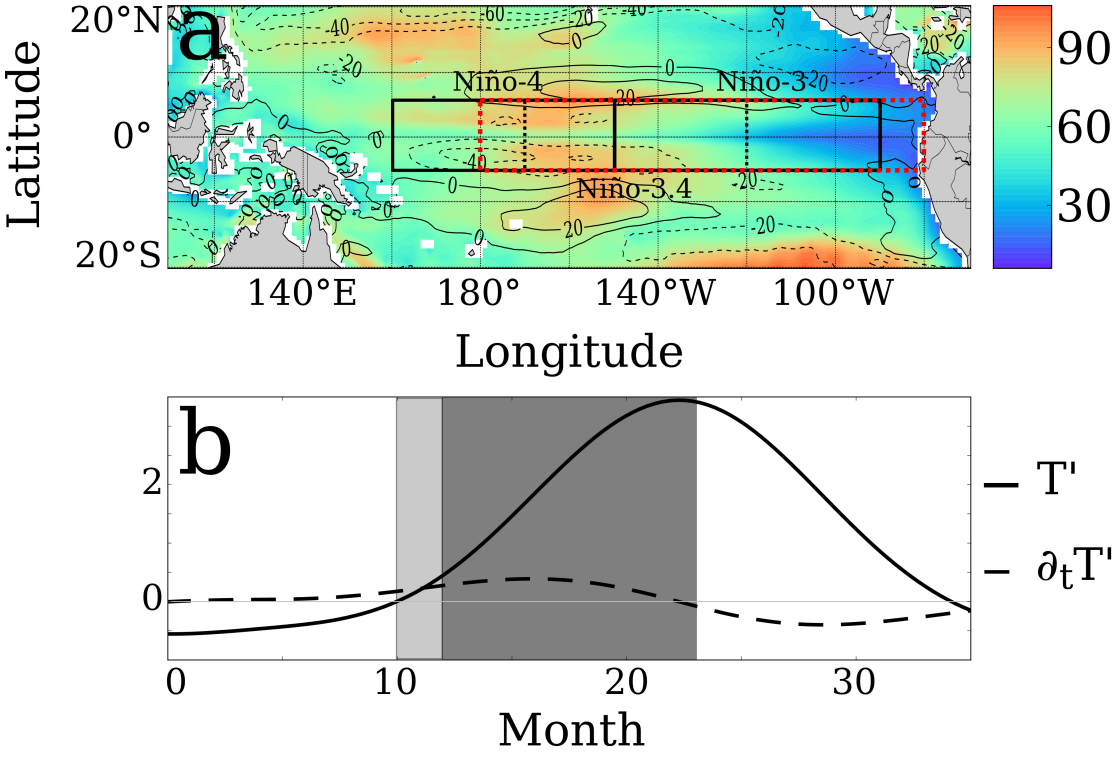

Figure 5.3: Panel **a** shows the mean MLD (m) in ACCESS-OM averaged over the period 1948-2007 (shaded) and the difference between the mean MLD in ACCESS-OM and ACCESS-CM1.3 (contours). The Niño-3 (5°S-5°N, 150 – 90°W; black), Niño-3.4 (5°S-5°N, 170 – 120°W; black dotted), Niño-4 (5°S-5°N, 160°E – 150°W; black), and eastern Pacific (5°S-5°N, 180 – 80°W; red dotted) averaging regions are also indicated. Panel **b** shows the evolution of T' (black line; units °C) and $\partial_t T'$ (dashed line; units °C per month) over the three years surrounding the 1997 EP El Niño event. The 2 month period shaded in light grey represents the initiation period of the El Niño and the 11 month period shaded in dark grey represents the development period of the El Niño.

during the development period, rather than the maximum amplitude of T' over the whole period for the following reasons: (i) one of the aims of the research is to investigate how the relative contributions of heat budget terms compare from the OGCM to the CGCM, and this is more easily demonstrated if the terms are scaled by the event maximum of T' rather than the maximum over the whole period; and (ii) due to the fact that while "super" eastern Pacific El Niño events have been observed (that is, events where SST anomalies exceed 3°C), the same extreme of temperature is not readily observed during central Pacific El Niño events (Ashok et al., 2007), such that scaling all events by the

maximum amplitude over the whole period would result in much smaller values for the heat budget terms during weak eastern Pacific and central Pacific El Niño events than those during "super" eastern Pacific El Niño events. The heat budget terms were then averaged over the development period, and their standard deviations over this same period were calculated. Consistent with previous studies (e.g. Ham and Kug, 2012; Taschetto et al., 2014), events were also classified as eastern Pacific (EP) if the SST anomaly averaged in the Niño-3 or Niño-3.4 region was greater than the SST anomaly averaged in the Niño-4 region throughout the El Niño event, or as central Pacific (CP) if the reverse occurred.

Table 5.1: Mean values and standard deviations of the heat budget terms averaged in the Niño-3 and Niño-4 regions from the development period of selected El Niño events in the ACCESS-OM and ACCESS-CM1.3 simulations. Differences in heat budget values between the Niño-3 and Niño-4 regions in each model simulation *not* significant at the 95% confidence interval (using a two-sided Student's t-test) are shown in bold.

	ACCESS-OM				**ACCESS-CM1.3**			
	1991		**1997**		**1872**		**1913**	
	Niño-3	**Niño-4**	**Niño-3**	**Niño-4**	**Niño-3**	**Niño-4**	**Niño-3**	**Niño-4**
Q'	-0.11 (0.06)	-0.17 (0.09)	**-0.15 (0.05)**	**-0.11 (0.09)**	-0.05 (0.01)	0.08 (0.04)	-0.03 (0.01)	0.04 (0.04)
$\overline{u}\partial_x T'$	-0.03 (0.03)	0.02 (0.08)	**-0.01 (0.01)**	**0.00 (0.09)**	-0.04 (0.05)	0.17 (0.06)	-0.04 (0.07)	0.02 (0.04)
$u'\partial_x \overline{T}$	0.05 (0.05)	0.15 (0.16)	0.06 (0.02)	0.22 (0.28)	0.04 (0.05)	0.38 (0.09)	0.01 (0.05)	-0.19 (0.16)
$u'\partial_x T'$	0.03 (0.02)	-0.10 (0.14)	-0.02 (0.01)	-0.26 (0.35)	0.01 (0.04)	-0.12 (0.04)	0.12 (0.02)	0.00 (0.06)
$\overline{v}\partial_y T'$	**0.04 (0.03)**	**0.03 (0.03)**	0.07 (0.02)	0.03 (0.04)	**-0.01 (0.02)**	**-0.02 (0.03)**	-0.04 (0.04)	-0.02 (0.02)
$v'\partial_y \overline{T}$	**0.01 (0.04)**	**0.01 (0.02)**	0.05 (0.02)	0.01 (0.04)	-0.01 (0.02)	-0.06 (0.03)	-0.01 (0.02)	-0.04 (0.02)
$v'\partial_y T'$	0.01 (0.01)	0.00 (0.02)	-0.03 (0.01)	0.00 (0.03)	0.05 (0.01)	0.12 (0.02)	0.05 (0.04)	0.10 (0.01)
$\overline{w}\partial_z T'$	0.07 (0.05)	0.00 (0.04)	**0.09 (0.03)**	**0.11 (0.09)**	0.19 (0.10)	0.04 (0.01)	0.08 (0.16)	0.02 (0.01)
$w'\partial_z \overline{T}$	0.01 (0.02)	0.02 (0.01)	0.02 (0.02)	-0.01 (0.04)	0.05 (0.04)	-0.04 (0.01)	0.01 (0.04)	-0.07 (0.02)
$w'\partial_z T'$	**-0.01 (0.01)**	**0.00 (0.01)**	-0.02 (0.01)	0.02 (0.03)	-0.03 (0.03)	-0.01 (0.01)	-0.03 (0.04)	0.01 (0.01)
DER'	-0.02 (0.04)	0.08 (0.04)	0.02 (0.02)	0.08 (0.07)	0.00 (0.10)	-0.14 (0.24)	0.01 (0.08)	-0.02 (0.18)

Although important for contrasting the El Niño behaviors in the OGCM and CGCM, neither of these two classification methods, which involved averaging terms over a specific region, could be relied upon to accurately identify the El Niño spatial flavor during the development period, as discussed in subsequent sections. Hence, an alternative method for classifying the El Niño type was adopted, namely the El Niño evolution pathway. The El Niño evolution pathway method took into consideration the balance of heat budget terms in each El Niño event over the full longitudinal extent of the tropical Pacific, as well as the evolution of variables such as thermocline depth and zonal wind stress.

5.4 Results

5.4.1 El Niño in ACCESS-OM

A total of 14 El Niño events were identified in the OGCM flux-forced simulation, four of which were classified as CP El Niño events. The December averages of T' for selected EP and CP events - the 1997 EP event and the 1991 CP event, respectively - are illustrated in figure 5.4. The magnitude and location of maximum warming differed for the two events, being found further west in the CP event compared with the EP event. The location of the dynamic warm pool edge (DWPE; Brown et al., 2013) was approximately 162°E ($\sigma = 5.2$°E; tracking the 29.0°C sea surface isotherm), such that the western (eastern) extent of warm (cool) SST anomalies was comparable with observations (see also appendix A). The evolution of T', $\partial_t T'$, and zonal wind stress anomalies for the 1991 CP and 1997 EP El Niño events are illustrated in figure 5.5

Figure 5.6 summarizes the relative contributions of the heat budget terms (i.e., scaled by the overall amplitude) to the growth and damping of each El Niño event during the development period and in the eastern equatorial Pacific. The thermocline feedback ($\overline{w}\partial_z T'$) and the zonal advective feedback ($u'\partial_x \overline{T}$) tended to be among the dominant terms contributing to growth for most events, as were diffusion, entrainment, and residual processes, DER'. Damping was dominated by the net surface heat flux anomaly (Q').

Variations in the patterns of relative growth and damping in the heat budget terms can be readily understood from detailed analysis of individual events. For example, a

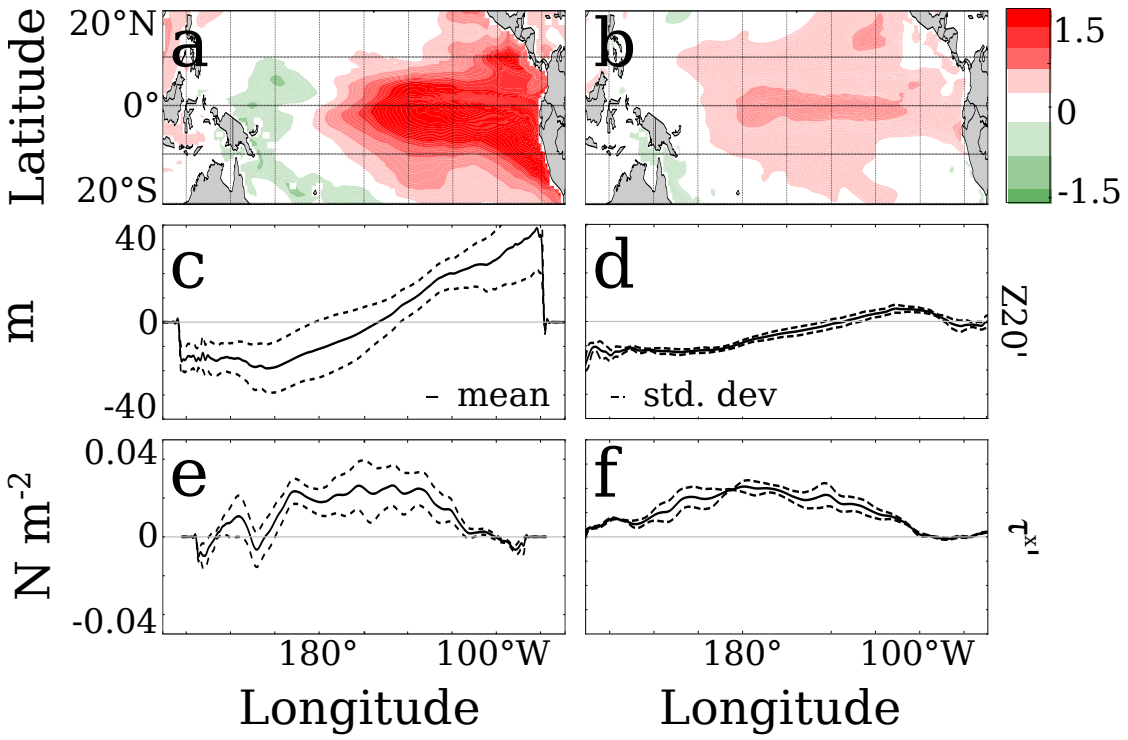

Figure 5.4: Features of selected El Niño events in ACCESS-OM. The left column shows results from the 1997 EP El Niño event and the right column shows results from the 1991 CP event. Panels **a** and **b** are the December averages of the mixed layer temperature anomaly T' (°C) for the two El Niño events; panels **c** and **d** show the equatorial thermocline depth anomalies ($Z20'$); and panels **e** and **f** show the zonal wind stress anomalies ($\tau^{x\prime}$). The dotted lines in panels **c** - **f** represent mean values and the dashed lines represent standard deviations at each longitude, both calculated over all months in the development period, and averaged over 2°S - 2°N.

greater proportion of terms contributed to damping, rather than growth, of the 1997 super El Niño event (and to a lesser extent the 1976 El Niño event) due to an increase in the relative contribution of the meridional advection terms to growth. The increase in meridional advection was partly driven by a strengthening of the anomalous meridional currents. Accelerated warming along the equator, compared with off-equatorial regions, caused a weakening in the anomalous meridional temperature gradient across the equator, which further strengthened meridional advection during the 1997 El Niño event (Cai et al., 2014). The 1982 event, which was also a super El Niño event, also exhibited a similar relative increase in the meridional advection terms, although damping during

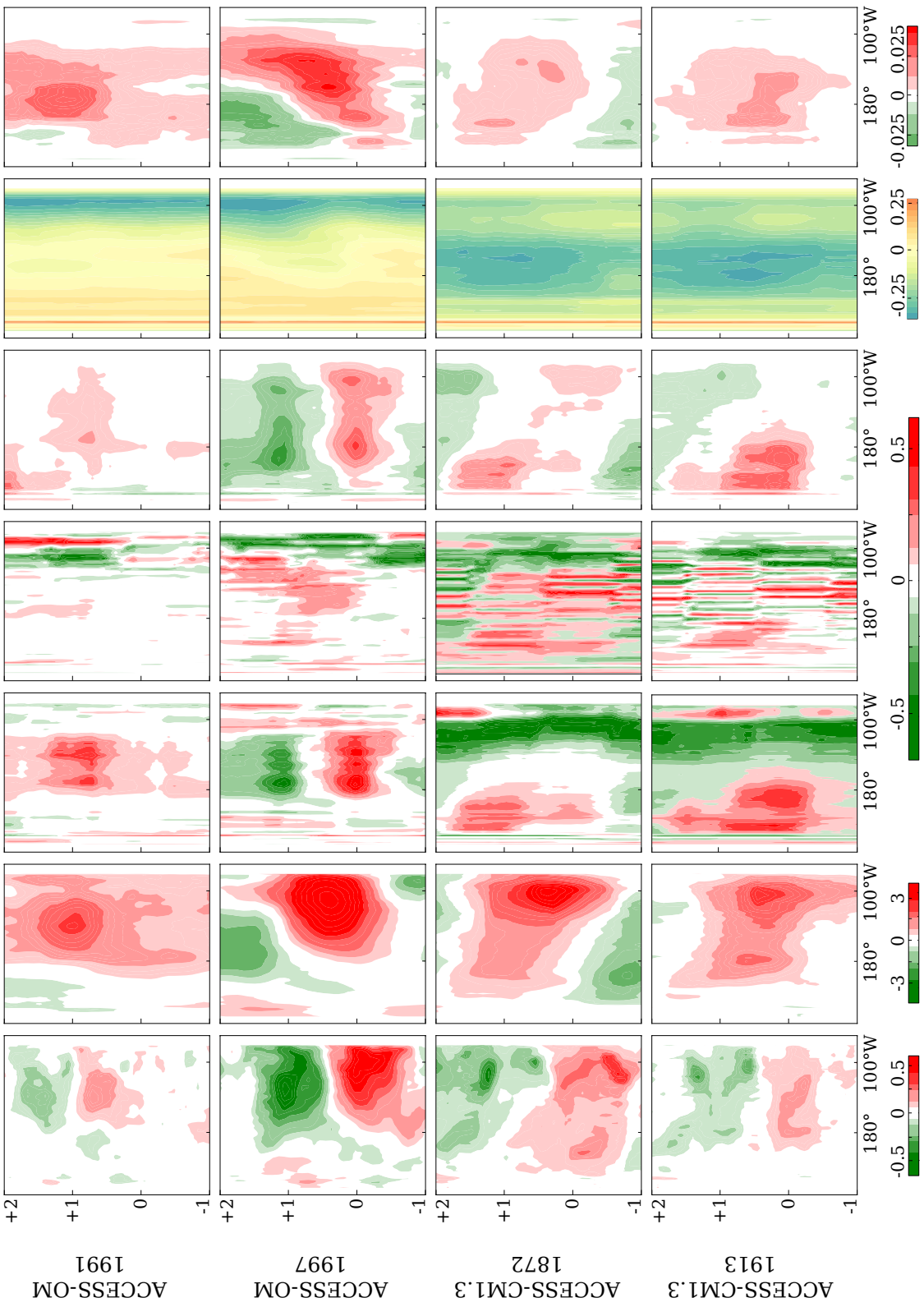

Figure 5.5: Evolution of selected variables during the 1991 CP and 1997 EP El Niño events in the ACCESS-OM simulation (top two panels, respectively) and during the 1872 eastern Pacific and 1913 double peaked El Niño events in the ACCESS-CM1.3 simulation. Variables in each column are averaged from 2°S to 2°N, and are (from left): $\partial_t T'$, T', $u'\partial_x \overline{T}$, $\overline{u}\partial_x T'$, u', $\overline{u}$, and τ_x', respectively. The color intervals and units for each variable differ as per indicated below each column.

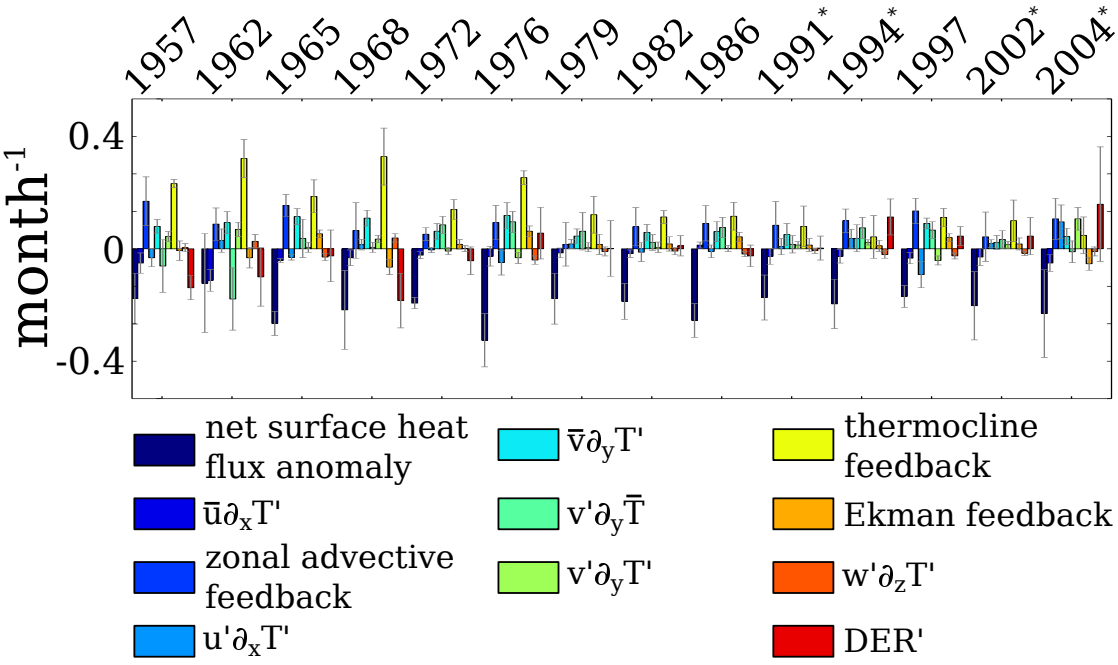

Figure 5.6: Relative contribution of the heat budget terms to growth and damping during the development period of each El Niño event in ACCESS-OM. All heat budget terms were scaled by the maximum amplitude of T' during the El Niño development period and averaged in the eastern Pacific (180-80°W), between 2°S and 2°N. The asterisk notation denotes central Pacific El Niño events; the remaining events were eastern Pacific El Niño events.

this event was led predominantly by the net surface heat fluxes.

Compared with EP El Niño events, CP events saw a slight increase in the relative contribution of the zonal advective feedback and DER' processes to growth. DER' processes were particularly large during the 1994 and 2004 CP El Niño events, both of which involved greater warming in the off-equatorial regions in the lead up to the El Niño event relative to the 1991 and 2002 events. It is possible that the monthly resolution of the ACCESS-OM data and the relatively course vertical grid resolution (10 m in the upper 200 m) led to higher values for DER' during these events than would be found for data with higher temporal and vertical resolution. Online calculation of the heat budget terms would also explicitly diagnose diffusive processes combined in this DER' term; however, such a calculation was beyond the scope of the current study. Apart from the

relatively larger DER' term during the 1994 and 2004 El Niño events, there was not a marked difference between the balance of heat budget terms during CP events to that of EP events (despite the overall magnitude of the heat budget terms being larger during EP El Niño events than during CP El Niño events).

Finally, our results for the first two decades of the simulation were associated with a higher degree of uncertainty than the later decades due to the fact that prior to 1984, the radiative forcings in the CORE-II dataset were climatological, rather than interannually-varying (Large and Yeager, 2009). In addition, the wind forcings prior to 1980 were highly uncertain (Wittenberg, 2004).

5.4.2 El Niño in ACCESS-CM1.3

Over the 156-year (i.e., 1850-2005) of the *historical* simulation of ACCESS-CM1.3, a total of 28 El Niño events were identified. Using the EP/CP metric introduced in section 5.3.3, 23 of the events were classified as EP events and the remaining five were classified as CP events.

Figure 5.7 summarizes the relative contributions of the heat budget processes to growth and damping in the CGCM El Niño events. There were a number of distinct differences between the CGCM results and those of the OGCM. First, while the zonal advective feedback was also of the most important terms contributing to growth in the OGCM, in the CGCM, this term was less important in inciting growth, and contributed to damping in the eastern Pacific during four El Niño events. Second, consistent with Rashid and Hirst (2015) Q' was generally of the smallest contributors to El Niño development in the CGCM events, and contributed to growth, rather than damping, of eleven El Niño events. Third, the balance of terms from one event to the next varied more markedly in the CGCM than in the OGCM, particularly between events of the same type (e.g., compare the 1878 and 1883 El Niño events from the CGCM in figure 5.7 with the 1997 EP and 1991 CP El Niño events in figure 5.6). The sensitivity of the sign and magnitude of the CGCM heat budget terms to the averaging region (e.g., table 5.1) highlights the problem with relying on spatially averaged quantities to infer El Niño behavior.

Based on the spatial patterns of T' evolution and equatorial thermocline depth anomalies,

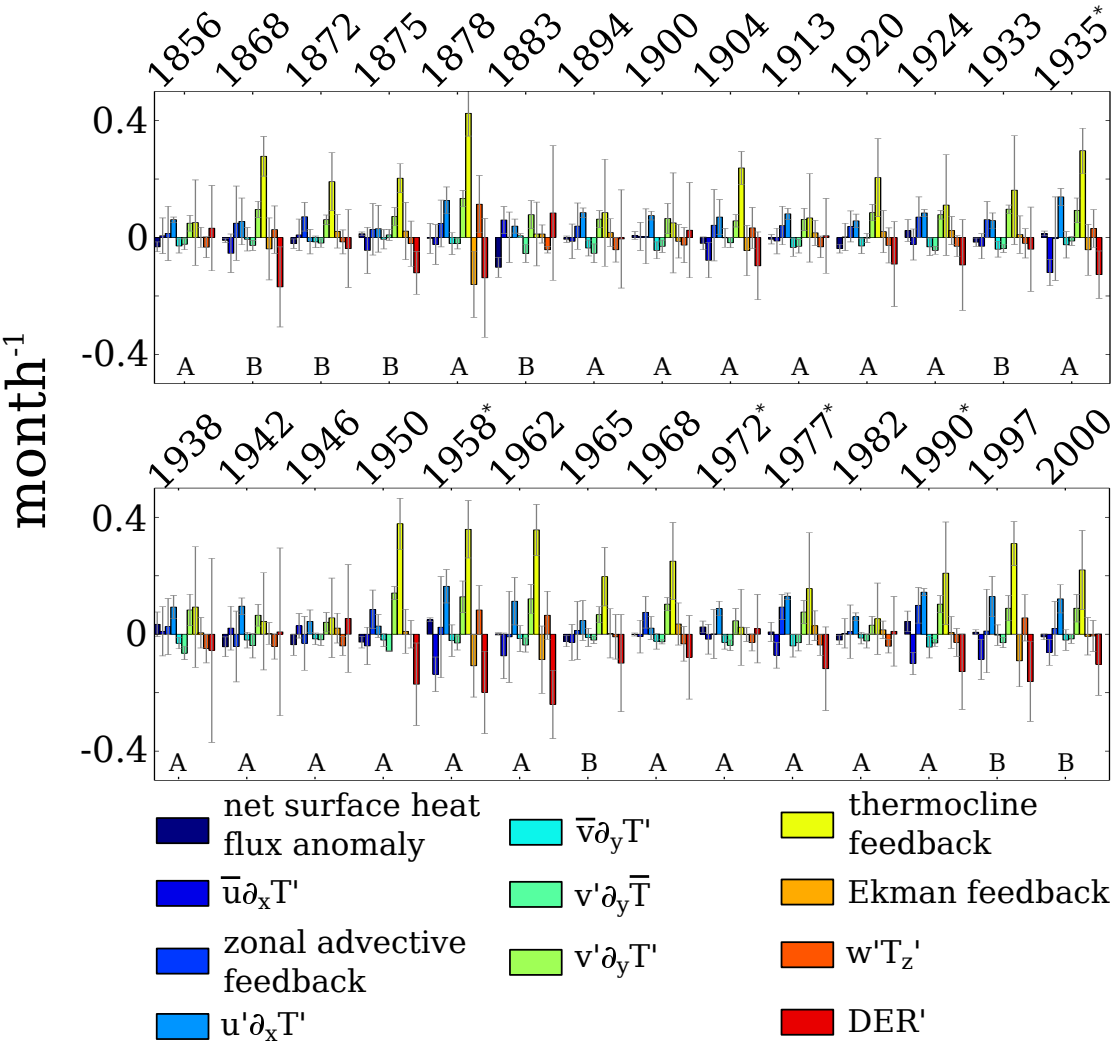

Figure 5.7: Relative contribution of the heat budget terms to growth and damping during the development period of each El Niño event in ACCESS-CM1.3. All heat budget terms were scaled by the maximum amplitude of T' during the El Niño development period and averaged in the eastern Pacific (180-80°W), between 2°S and 2°N. The asterisk notation denotes events classified as central Pacific El Niño events using the definition described in section 5.3.3. 'A' denotes type A, double peaked El Niño events, 'B' denotes type B, eastern Pacific events in the CGCM.

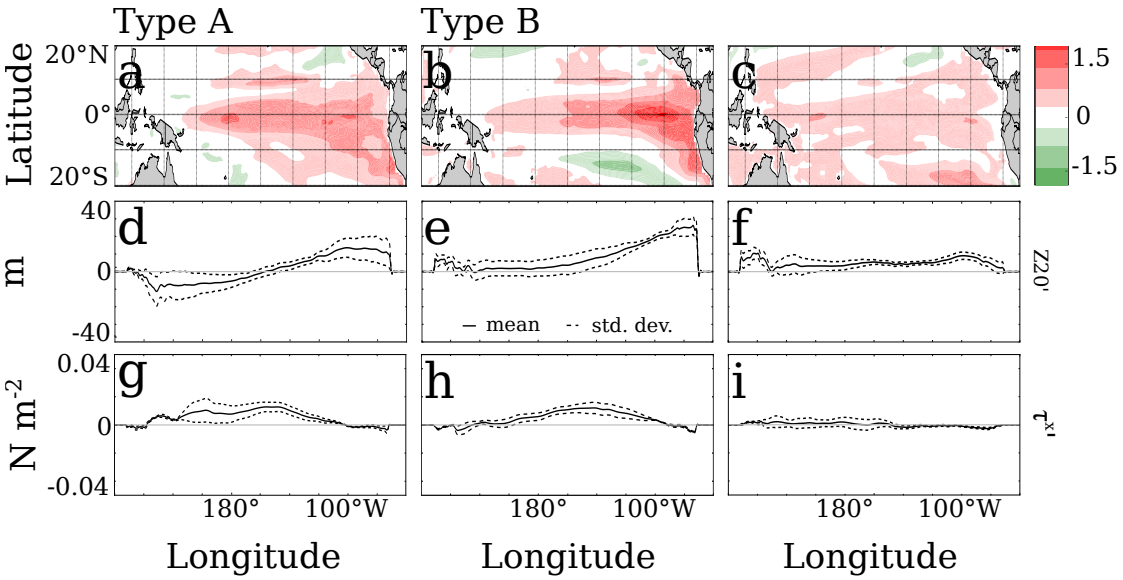

Figure 5.8: Features of selected El Niño events in ACCESS-CM1.3. Type A (left column) represents the December average of a characteristic double peaked event (the 1913 event) and type B (middle column) represents the December averaged of a characteristic EP event (the 1872 event). The right column is the June average of the 1990 event; an event with warm peaks in both the eastern and western equatorial Pacific, but with behavior in the thermocline depth anomaly ($Z20'$) and zonal wind stress anomaly ($\tau^{x\prime}$) that differs considerably from both El Niño types in the CGCM. Panels **a** - **i** are the same as in figure 5.4 for each of the three CGCM El Niño events.

two types of El Niño were identified in the CGCM: type A events involved the evolution of two distinct peaks in T', a western peak located near the dateline in the western Pacific and an eastern peak located between 120 and 100°W in the eastern Pacific (20 events in the CGCM record; figure 5.8a); and type B events were characterized by peaks in the eastern Pacific (eight events in the CGCM record; figure 5.8b). The variance/coherence of the spectra of T' averaged alternatively in the Niño-3 and Niño-4 regions is compared in figure 5.9.

Type A: the double peaked event

As compositing all of the type A events in the CGCM simulation results led to a smearing of the relevant dynamics, we chose a representative event (the 1913 CGCM event) to

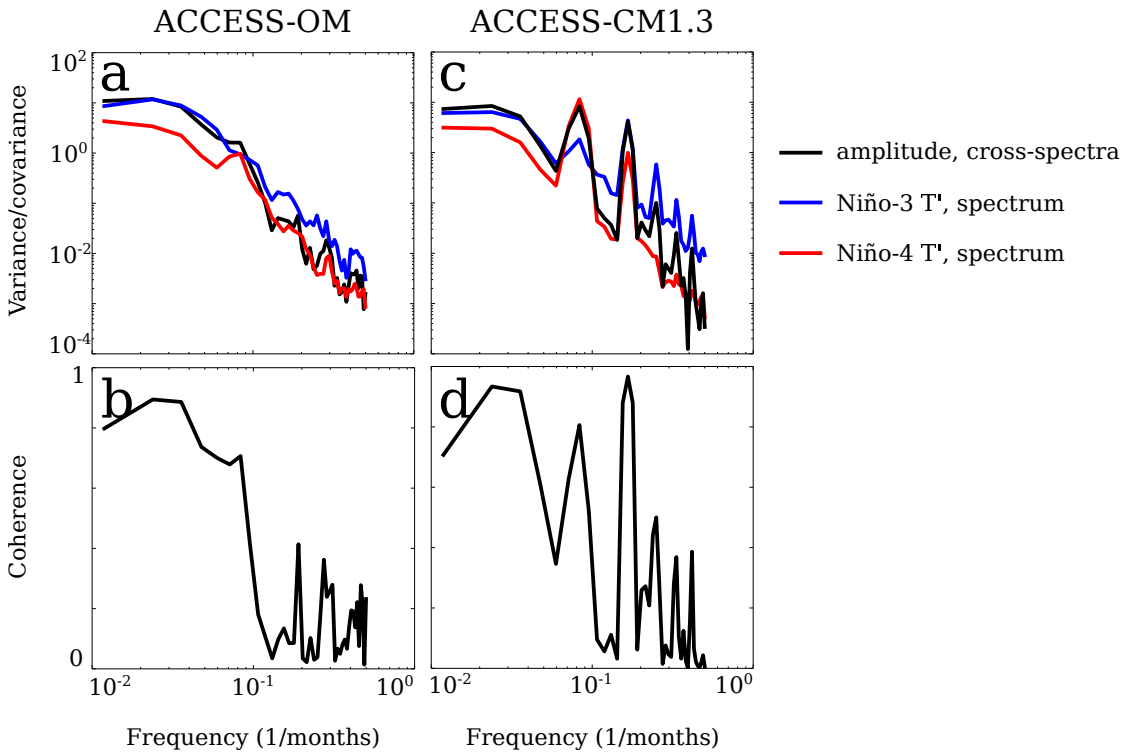

Figure 5.9: Panels **a** and **c** illustrate the variance in indices of T' averaged in the Niño-3 (blue) and Niño-4 (red) regions and their covariance (black) for the ACCESS-OM and ACCESS-CM1.3 simulations, respectively. Panels **b** and **d** illustrate the coherence of T' averaged in the eastern and western-central Pacific for the ACCESS-OM and ACCESS-CM1.3 simulations.

describe the development of type A El Niño events. This particular event was chosen based on the similarity of its spatial evolution of equatorial T' to that of a composite of T' over all type A events. However, for comparison purposes, in the figures that follow we present the individual results alongside composites of all El Niño events from both the OGCM and the CGCM.

Mixed layer temperature anomalies for the 1913 double peaked event evolved in a similar manner to a hybrid EP/CP event (figure 5.8a). Warming, led by the thermocline feedback, initiated in the eastern Pacific in February, although the anomalies extended further west than in the characteristic OGCM EP event - a well known consequence of the Pacific equatorial cold tongue bias in CGCMs. In addition to the eastern equatorial

Pacific warm peak, a separate warm peak in T' emerged during boreal summer in the western equatorial Pacific near the dateline. [This western warm peak occurred within the expected region of maximum warming during a CGCM CP El Niño given the western Pacific warm bias in most CGCMs (Taschetto et al., 2014)]. However, unlike any of the EP and CP events from the OGCM, the warm peaks in the CGCM double peaked event grew concurrently, and separately, during the El Niño development period.

To investigate what allowed the separation of the two warm peaks in the double peaked event, the heat budget terms were meridionally-averaged between 2°S and 2°N at each longitude over the development period. The thermocline feedback, zonal advective feedback, and zonal mean advection term were found to dominate the growth of T' during the CGCM 1913 event. Figure 5.10 compares these terms for a composite of all OGCM El Niño events (panel a) with the 1913 CGCM event and a composite of all CGCM El Niño events (panel b). The thermocline feedback dominated growth in the eastern Pacific for both the CGCM and the OGCM, and the sign, magnitude, and warming patterns of this term were comparable between the two models. The zonal advective feedback $u'\partial_x\overline{T}$ was of a similar magnitude for both models, although the warming was shifted west in the CGCM compared with the OGCM by approximately 50° of longitude (>5000km), and the zonal mean advection term $\overline{u}\partial_x T'$ was considerably larger in the western-central Pacific during the 1913 CGCM event (it reached a maximum of 0.3°C per month) than in the OGCM (where it was close to zero °C per month).

On closer inspection of the evolution of the zonal advection terms during the development of the 1913 event (figure not shown), the zonal advective feedback was found to have led the zonal mean advection term in warming the western Pacific due to an increase in the anomalous zonal currents there. Warming induced by the zonal advective feedback then increased the positive (negative) anomalous mixed layer temperature gradient in the western (west-central) Pacific, leading to growth (decay) of the zonal mean advection term in the western (west-central) Pacific. The climatologically westward currents of the South Equatorial Current (SEC), which were stronger than observed in the CGCM (figure not shown), further advected the western warm patch and the western-central cool patch to the west, causing sufficient cooling in the central Pacific to prevent the

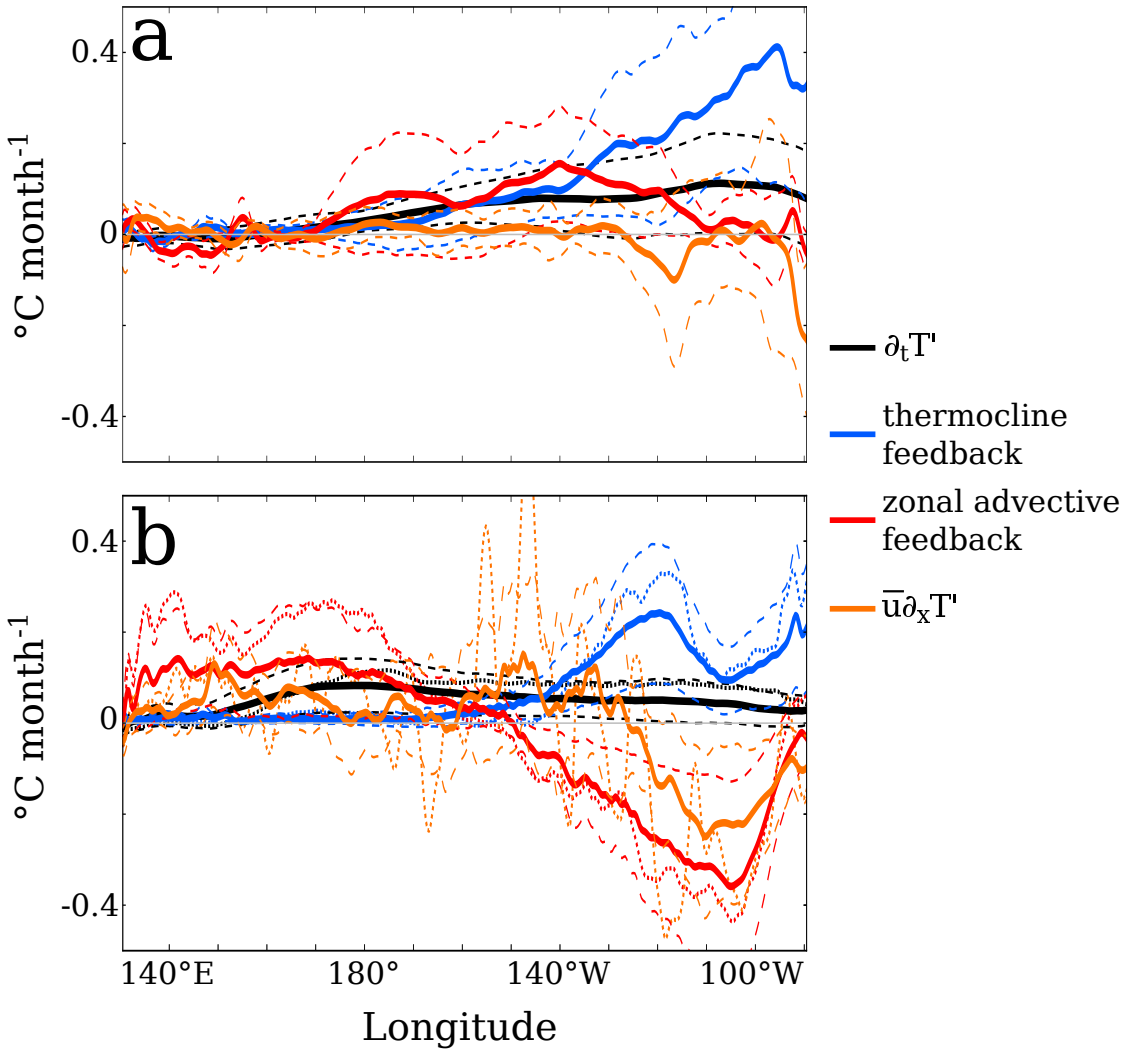

Figure 5.10: The solid (dashed) lines are the means (standard deviations) of the dominant equatorial (2°S-2°N) heat budget terms contributing to growth, averaged during the development period for a composite of all El Niño events in **a** ACCESS-OM and **b** ACCESS-CM1.3. In each panel the black line is the mixed layer averaged temperature anomaly tendency $\partial_t T'$, the blue line is the thermocline feedback $\overline{w}\partial_z T'$, the red line is the zonal advective feedback $u'\partial_x \overline{T}$, and the orange line is the zonal mean advection $\overline{u}\partial_x T'$. In panel **b**, the dotted lines represent the mean values of each of the heat budget terms for the 1913 double peaked El Niño event in ACCESS-CM1.3.

interaction of the eastern and western warm peaks. It is likely that the presence of the cold tongue bias, which shifted the thermal gradients further to the west in the CGCM, along with the stronger than observed SEC, were responsible for the double peaked events, which were not at all apparent in the OGCM.

Despite differences in the spatial patterns of T' between the CGCM type A events and the OGCM EP El Niño events, their ocean dynamics, notably the thermocline depth and zonal wind stress anomalies across the Pacific, were qualitatively similar (figures 5.4c, e and 5.8d, g). Similar patterns in the evolution of equatorial thermocline depth anomalies between the two events (albeit of a smaller magnitude in the CGCM; figure 5.11), suggested that the mechanism of discharge and recharge of equatorial heat content that was prevalent in observed ENSO events (Jin, 1997a; Meinen and McPhaden, 2000) also operated in the CGCM. These results also suggested that the traditional mechanisms for growth in the OGCM - that is, the Bjerknes feedback (Bjerknes, 1969; Lloyd et al., 2011), Kelvin and Rossby wave response (Suarez and Schopf, 1988; Battisti and Hirst, 1989; Picaut et al., 1997), and resulting zonal tilt of the thermocline (Jin, 1997a) - played a role in the development of the double peaked El Niño event. However, mean state temperature biases generated the additional unphysical warming response in the western Pacific independently of that to the east.

The presence of the secondary western Pacific warm peak led to the erroneous classification of five CGCM double peaked El Niño events as central Pacific El Niño types, despite clear evolution differences between the double peaked events of the CGCM and the OGCM central Pacific events (figures 5.4b, d, and f and 5.8a, d, and g), and considerable differences in the magnitude and sign of the heat budget terms in the eastern Pacific compared with the central and western Pacific (figure not shown). It follows that the utility of using standard ENSO metrics, such as the Niño-3 or Niño-4 indices, to classify double peaked spatial flavors of ENSO and to characterize their development is questionable.

The features of several of the CGCM double peaked events departed from the "typical" evolution pathway. Figure 5.8 panels c, f, and i, demonstrate one such example, the 1990 event, that involved weak warming across the full equatorial Pacific (although with peaks

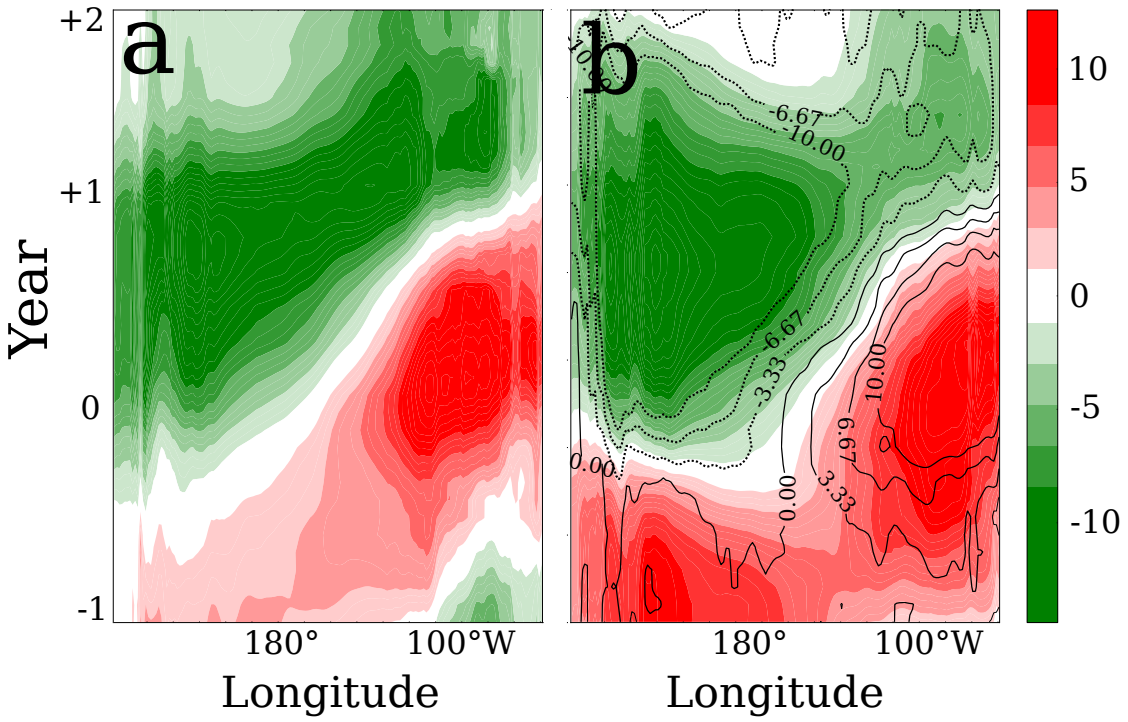

Figure 5.11: Equatorial thermocline depth anomalies (shaded; m) for a composite of all El Niño events in **a** ACCESS-OM and **b** the ACCESS-CM1.3. In both panels, thermocline depth anomalies are averaged between 2°S-2°N for the three years surrounding the composite El Niño event. The shading interval is 2.5 m. In panel **b**, the contours represent the thermocline depth anomalies for the CGCM 1913 double peaked event.

in the east and west that led to its double peaked classification) and both north and south of the equator to approximately 20° latitude. As evidenced by a weak deepening of the thermocline along the equator and almost zero equatorial zonal wind stress anomaly, the dynamical evolution of this event deviated considerably from that expected. The 1935 event displayed similar characteristics to the 1990 event, as did the 1894, 1900, and 1924 events to a lesser extent. It is possible that the warm bias in the shortwave heat flux in ACCESS-CM1.3 (Rashid and Hirst, 2015), or longer-term ENSO variability, played a role in the abnormal development of these events.

Type B: the EP event

The spatial patterns in T' during the type B event more closely resembled the flux-forced OGCM EP El Niño than did those of the CGCM double peaked El Niño event. Warm anomalies for a characteristic type B event in the CGCM - namely the 1872 event - evolved from the eastern equatorial Pacific, with a maximum located near 100°W (figure 5.8b). Compared with the flux-forced OGCM EP event, there was a warm bias along the west coast of South America in the far eastern Pacific resulting from an overly warm shortwave heat flux, and an extension of warming further west along the equatorial Pacific than observed.

The balance of the heat budget terms during the development period of CGCM type B events differed considerably from that of the flux-forced OGCM EP events. During the CGCM type B El Niño events, growth was dominated by the thermocline feedback, and in some cases followed by the nonlinear zonal advective term $u'\partial_x T'$, which arose due to a relatively large positive zonal gradient in the mean mixed layer temperature near the coast of South America, combined with negative anomalous zonal currents there. Damping in the eastern Pacific was inconsistent; during some events DER' processes dominated damping, while meridional advection played a role in damping other events. The relative contribution of Q' to damping across all type B El Niño events in the CGCM was approximately five times smaller than the contribution of Q' to damping EP El Niño events in the OGCM simulation. This was largely a result of a positive bias in the CGCM shortwave heat flux across most of the equatorial Pacific, with the longwave and sensible heat fluxes also characterized by slightly positive biases in the eastern Pacific, all of which acted to amplify T' (figure 5.12). The shortwave heat flux bias in ACCESS-CM1.3 has been attributed to unrealistic SST-cloud interactions in this CGCM (Rashid and Hirst, 2015). These unrealistic SST-cloud interactions were in part due to a climatological bias in the low cloudiness in ACCESS-CM1.3, associated with an overly strong cold tongue compared with observations, and also partly due to overly strong descending atmospheric motion (Rashid and Hirst, 2015). A similar result has been found in the GFDL-CM2p1 CGCM (Wittenberg et al., 2006).

The development of a secondary warm peak in the western Pacific, as in the CGCM type

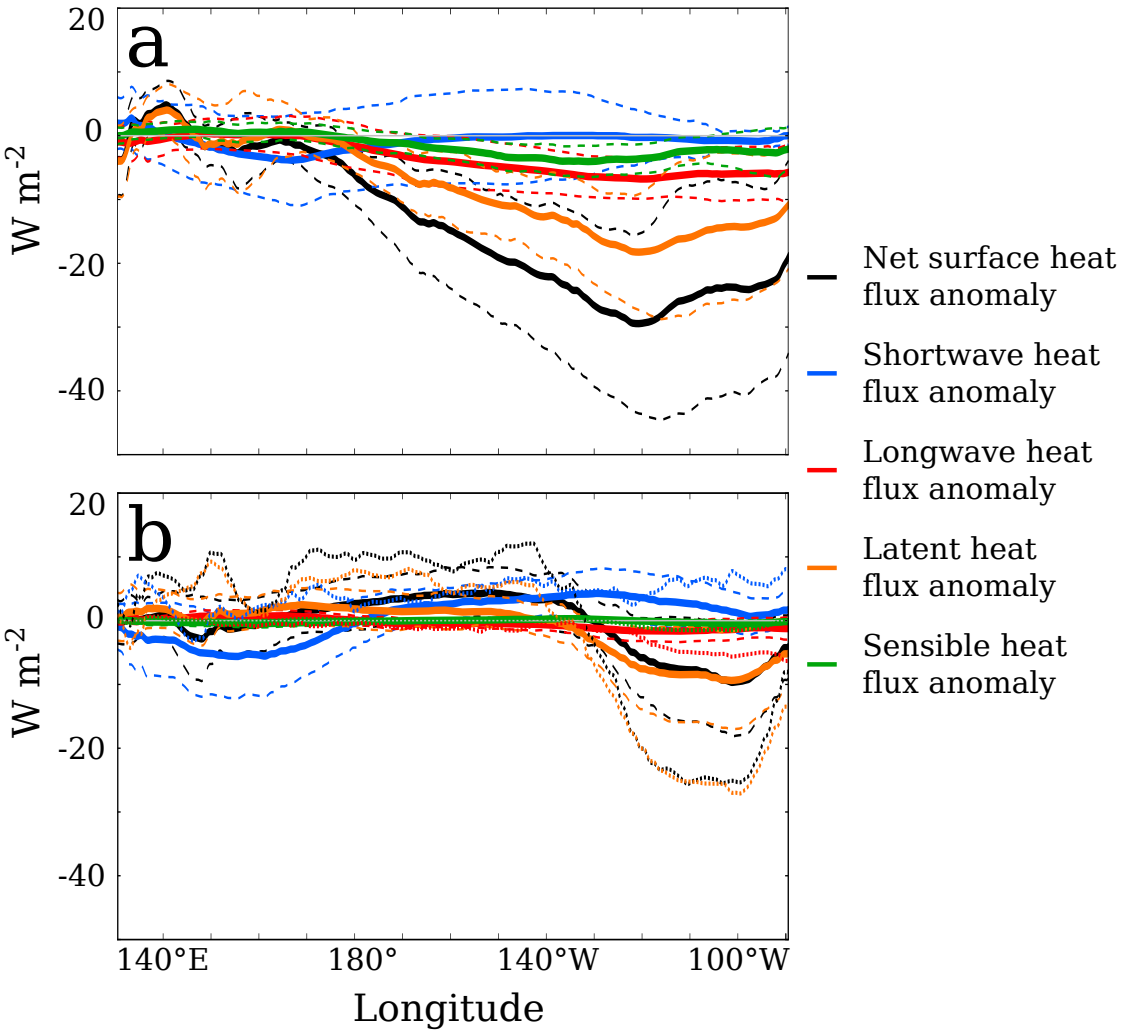

Figure 5.12: The solid (dashed) lines are the mean values (standard deviations) of the anomalous heat flux variables averaged between 2°S-2°N during the development period for a composite of all El Niño events in **a** ACCESS-OM and **b** ACCESS-CM1.3. In each panel, the black line is the net anomalous surface heat flux, the blue line is the net anomalous shortwave heat flux (total surface flux minus flux through the mixed layer), the red line is the surface anomalous longwave heat flux, the orange line is the surface anomalous latent heat flux, and the green line is the surface anomalous sensible heat flux. The dotted lines in panel **b** represent the mean values during the development period of the CGCM 1872 eastern Pacific event.

A events, was prevented in the CGCM type B events partly due to differing patterns of westerly wind stresses. During the 1872 CGCM event - and CGCM type B events more broadly - the maximum in the westerly (i.e. anomalous) equatorial zonal wind stresses was shifted further to the east (5°S-5°N, 150-120°W) than in the CGCM double peaked El Niño events (5°S-5°N, 150°E-160°W), with weakly westerly or even easterly wind stresses to the west (5°S-5°N, 180-150°W). As a consequence, u' and the zonal advective feedback were considerably smaller in the western-central Pacific during the 1872 event than during the CGCM double peaked events, preventing the development of significant warming in the western Pacific.

Is ACCESS-CM1.3 representative of other CGCMs?

To investigate whether the double peaked El Niño present in ACCESS-CM1.3 was a feature common to other coupled models, we calculated the mixed layer temperature anomaly in *historical* simulations of nine CMIP5 models and evaluated the evolution of T' during the development period of each El Niño. All of the CGCMs analyzed were found to have double peaked events in the period over which they were simulated (table 5.2). Several models exhibited more diverse spatial flavors than seen in either the flux-forced ACCESS-OM (OGCM) or ACCESS-CM1.3 simulations; for example, the CSIRO-Mk3.6.0 and GFDL-CM2.1 models were found to have El Niño events that evolved almost entirely in the western Pacific. The location of the western equatorial Pacific warm peak generally corresponded well with the location of the DWPE; models that simulated a more realistic location of the DWPE had western peaks located further to the east. This is consistent with the warming anomaly being related to the zonal advective feedback, which is largest at the DWPE (Brown et al., 2013). While details of the evolution pathways, including the full heat budget equation, were not examined here, these results give us confidence that the double peaked event from ACCESS-CM1.3 is within the range of commonly simulated behaviors by CGCMs.

Table 5.2: Summary of the El Niño spatial flavors present in nine CMIP5 models based on the evolution of T'.

Model		Reference	Years (total)	El Niños (total)	Type A events (total)	Mean location (standard deviation, σ) DWPE	western peak
CanCM4	Canadian Coupled Model v4	(Merryfield et al., 2013)	45	9	4	158°E (12°E)	173°W (14°E)
CanESM2	Canadian Earth System Model v2	(Chylek et al., 2011)	156	34	15	152°E (3.6°E)*	172°E (7.0°E)
CNRM-CM5	Centre National de Recherches Météorologiques Coupled Global Climate Model v5	(Voldoire et al., 2013)	156	33	12	167°E (2.5°E)*	179°E (12°E)
CSIRO-Mk3.6.0	Commonwealth Scientific and Industrial Research Organisation mark v3.6.0	(Collier et al., 2011)	156	27	18	150°E (0.6°E)*	156°E (7.2°E)
GFDL-CM2.1	Geophysical Fluid Dynamics Laboratory Coupled Model v2.1	(Delworth et al., 2006)	145	26	7	162°E (18°E)	169°E (14°E)
MPI-ESM-LR	Max Planck Institute Earth System Model - low resolution	(Giorgetta et al., 2013)	156	26	13	156°E (8.3°E)*	153°E (1.1°E)
MPI-ESM-P	Max Planck Institute Earth System Model	(Giorgetta et al., 2013)	156	26	14	153°E (7.5°E)	163°E (13°E)
MRI-CGCM3	Meteorological Research Institute Coupled Atmosphere-Ocean General Circulation Model v3	(Yukimoto et al., 2012)	156	28	12	165°E (1.9°E)*	179°E (12°E)
NorESM1-M	Norwegian Earth System Model v1 - intermediate resolution	(Bentsen et al., 2013)	156	37	16	172°E (1.8°E)*	170°W (12°E)

5.5 Discussion

Here, we contrasted El Niño development in a simulation of ACCESS-CM1.3 with a corresponding simulation of the flux-forced ACCESS-OM. We found that the balance of heat budget dynamics and characterization of most El Niño spatial flavors in ACCESS-CM1.3 were different to those in ACCESS-OM. With respect to the balance of heat budget terms contributing to El Niño growth and decay, there were three marked differences between the CGCM and the flux-forced OGCM: (1) the zonal advective feedback contributed to damping in the eastern Pacific during the development period of four CGCM El Niño events; (2) the net surface heat flux anomaly was a noticeably weaker contributor to damping in the CGCM than in the OGCM, and acted to reinforce the positive mixed layer temperature anomalies in the central Pacific; and (3) the balance of heat budget terms differed more markedly for different El Niño events in the CGCM than in the OGCM.

We found two types of El Niño in the CGCM with distinct evolution pathways, which we characterized as double peaked and eastern Pacific events, respectively. The separate western Pacific warm peak present in the double peaked El Niño events was not a feature of either EP or CP OGCM events and is not at all clearly apparent in recent historical observations. While the spatial pattern of warming during CGCM eastern Pacific events (type B events) was more similar to the OGCM EP events, we found that these events were less like the OGCM EP events with respect to the relative contributions of the heat budget terms to growth and damping. The differences in the CGCM giving rise to these two spatial flavors of El Niño were largely due to biases in the spatial patterns of warming, mean zonal currents, and the net surface heat flux anomaly.

Previous studies have shown that CGCMs do not faithfully simulate the spatial locations of CP El Niño events (Ham and Kug, 2012; Taschetto et al., 2014). Not only were there no CP El Niños in our *historical* simulation using ACCESS-CM1.3, this CGCM simulated another unfamiliar spatial type of El Niño, which we denoted a double peaked event. When standard EP/CP metrics were used to diagnose the spatial flavors of El Niño in the ACCESS-CM1.3 simulation, these double peaked events were alternatively classified as either EP or CP events. That is, standard EP/CP metrics were inadequate

as a classification scheme of the two concurrent warming centers for the double peaked events. We further found that the balance of heat budget terms in the eastern Pacific during the CGCM El Niño events was so distinctly different from that in the central Pacific that the use of Niño-3 and Niño-4 indices to determine El Niño pathways in the CGCM was ineffective.

A warm bias in the shortwave heat flux in ACCESS-CM1.3 compared with ACCESS-OM over the central Pacific resulted in a warmer simulation of net surface heat flux anomalies, and warmer mixed layer temperature anomalies, both of which modified the spatial distribution of anomalies during El Niño evolution. The bias in the shortwave heat flux has been previously attributed to errors in the climatological background state of the model influencing the shortwave cloud radiative forcing scheme in ACCESS-CM1.3,explained by the following negative feedback process. Cooler climatological SSTs along the equatorial Pacific in ACCESS-CM1.3 under strong climatological descending atmospheric motion cause an increase in the formation of low-level boundary-layer clouds, which act to reinforce the cooler climatological SSTs. As a consequence, during El Niño years, increases in the net surface heat flux anomalies generate ocean warming to a greater extent than could occur in a model with warmer climatological SSTs and weaker descending or ascending atmospheric motion (Rashid and Hirst, 2015). Given the uncertainty associated with the magnitude and sign of the cloud feedback on climate, the representation of cloud forcing schemes in CGCMs represents a challenging, but important, feature for improving the simulation of ENSO in CGCMs, including under historical and future climate scenarios (Solomon et al., 2007).

A number of events were identified that did not match the evolution pathways of the "typical" double peaked event. For example, the spatial pattern of warming during the evolution of the 1990 CGCM El Niño event was relatively uniform throughout much of the tropical Pacific between 10°S and 10°N. In addition, the thermocline depth and wind stress anomalies during this event were considerably weakened compared with other double peaked events. As such, the 1990 CGCM El Niño displayed characteristics that were outside the range of those observed (figure 5.1). It is possible that factors outside the scope of the current study, such as the effect of the shortwave heat flux bias or

decadal modulation of El Niño, had an influence on the development of the 1990 event and others like it.

We have argued that the heat budget evolution pathways for the majority of El Niño events in an *historical* simulation using ACCESS-CM1.3 did not match the evolution pathways of the flux-forced OGCM El Niño events. However, we cannot contend, with a high degree of certainty, that the El Niño events simulated by the ACCESS-CM1.3 CGCM are not possible. It is well known that processes governing the development of ENSO modulate on decadal to centennial timescales (Zhang and McPhaden, 2006; Wittenberg, 2009), such that to accurately characterize the state of El Niño in an OGCM requires up to 240 years of observations, and in a CGCM at least 250 years of simulation (Stevenson et al., 2010). While we were limited in this study by having only 60 years for our flux-forced OGCM simulation and 156 years for our *historical* CGCM simulation, these records are nevertheless among the longest available that also allow the calculation of terms in the heat budget equation. We do not expect that the double peaked event is a new flavor of El Niño. Rather, it seems much more reasonable that the double peaked event is the CGCM equivalent of the observed eastern Pacific El Niño that has been modified due to the westward bias in the DWPE (Brown et al., 2013) and overly strong SEC. Hence, a reasonable supposition is that the ENSO behaviors present in this ACCESS-CM1.3 simulation fit within circle iii) in figure 5.1: they display some qualitatively similar features to those observed, but also simulate some unrealistic ones.

The mixed layer temperature anomalies from *historical* simulations of an additional nine CMIP5 CGCMs were also analyzed and compared. There was diversity within and between these CGCMs: several appeared to be able to simulate eastern Pacific events, while others had warming located predominantly west of the dateline for each of the El Niño events. Importantly, each of the CGCMs analyzed exhibited a double peaked El Niño spatial flavor. The location of the western Pacific warm peaks during double peaked El Niño events was correlated with the location of the DWPE: those CGCMs with a DWPE located closer to observed tended to simulate western warm peaks that were located further to the east. That ACCESS-CM1.3 is not the only CGCM to simulate spatial flavors of El Niño that are far from observed gives us confidence that the biases

exhibited by ACCESS-CM1.3 are within the range of behaviors expected in CGCMs.

Our work has highlighted the importance of the location of and dynamical behavior at the western extent of the equatorial Pacific cold tongue region (eastern extent of the western Pacific dynamic warm pool edge) in realistically capturing El Niño evolution dynamics. With respect to the ACCESS-CM1.3 CGCM, the equatorial Pacific thermal gradient, including in the region of the western Pacific dynamic warm pool edge, might be ameliorated by improvements in the low level cloud scheme. Mechanisms to further improve the simulation of the western extent of the equatorial Pacific cold tongue region need to be investigated.

5.6 Conclusions

We have found that the evolution of El Niño in an *historical* simulation of ACCESS-CM1.3 diverged markedly from the corresponding flux-forced OGCM with respect to the spatial flavors and underlying dynamics of each event. Most notably, instead of simulating a central Pacific type El Niño spatial flavor, ACCESS-CM1.3 simulated a double peaked El Niño event, with concurrent warming centers located in the eastern and western equatorial Pacific. The western Pacific warm peak arose predominantly due to a westwards bias in the mixed layer temperature and zonal current anomalies in the CGCM. A second spatial flavor of El Niño in the CGCM presented similarly to the eastern Pacific El Niño event in the OGCM; however, its underlying evolution pathway did not resemble the observed, canonical eastern Pacific event.

A notable implication of our work concerns the use of Niño indices to diagnose changes to El Niño under global warming scenarios. We have demonstrated that it was not necessarily possible to ascertain from averaged quantities, such as the mixed layer temperature anomaly in the eastern Pacific, whether ACCESS-CM1.3 was accurately simulating the spatial flavors of El Niño or the observed dynamical evolution pathways. Therefore, to use such averaging metrics to diagnose changes under global warming scenarios may result in misleading conclusions about how El Niño will change and why. Accordingly, Niño-averaged quantities should be considered in concert with other metrics, such as spatial maps through the development period of an El Niño, to arrive at a holistic

understanding of differences between *historical* and future CGCM simulations.

5.7 Appendix A: ENSO in ACCESS-OM

We evaluated the realism of the ENSO behavior in ACCESS-OM by comparison with observational data during the 1991-92 central Pacific and 1997-98 eastern Pacific El Niño events. This analysis complemented other studies of the tropical Pacific climate simulated in ACCESS-OM (Bi et al., 2013a; Graham et al., 2014). The mean vertical thermal and zonal current structures in ACESS-OM were also evaluated due to their importance in setting the timing, location, and duration of ENSO events. We analyzed potential temperature data from the Australian Bureau of Meteorology Research Centre (BMRC) ocean analyses (Smith, 1994) - derived predominantly from TAO/TRITON mooring data and ship-of-opportunity XBT data - and zonal ocean current data from a simulation of the Simple Ocean Data Assimilation (SODA) version 2.2.4 (Carton and Giese, 2008). In general, ACCESS-OM was found to reproduce the historical behavior of El Niño well.

The evolution of equatorial SST and SST anomalies for the three years surrounding the 1991 and 1997 El Niño events in the ACCESS-OM simulation data was compared with the corresponding BMRC data (figure 5.13). The SST anomaly in ACCESS-OM was slightly cooler throughout the 1991-92 event than in the observations and the location of maximum warming during this event was shifted slightly (by up to 5°) eastwards in ACCESS-OM. The location and timing of warm SST anomalies during the 1997-98 El Niño event were comparable to the observations; however, the cool anomalies peaked earlier in the BMRC data than in the ACCESS-OM simulation during the subsequent La Niña event.

The thermocline depth and thermocline depth anomaly were averaged between 2°S and 2°N for both the ACCESS-OM and BMRC simulation data, and their behaviors during the 1991-92 and 1997-98 El Niño events were contrasted (figure 5.14). The thermocline was slightly shallower across the Pacific in ACCESS-OM than in the observations. The magnitude of the equatorial thermocline depth anomaly in ACCESS-OM was slightly reduced during the 1991-92 event compared with the observations, although the locations of maximum anomalies were similar in the two datasets. During the 1997-98 event, the extrema in the thermocline depth anomaly of the eastern equatorial Pacific in ACCESS-

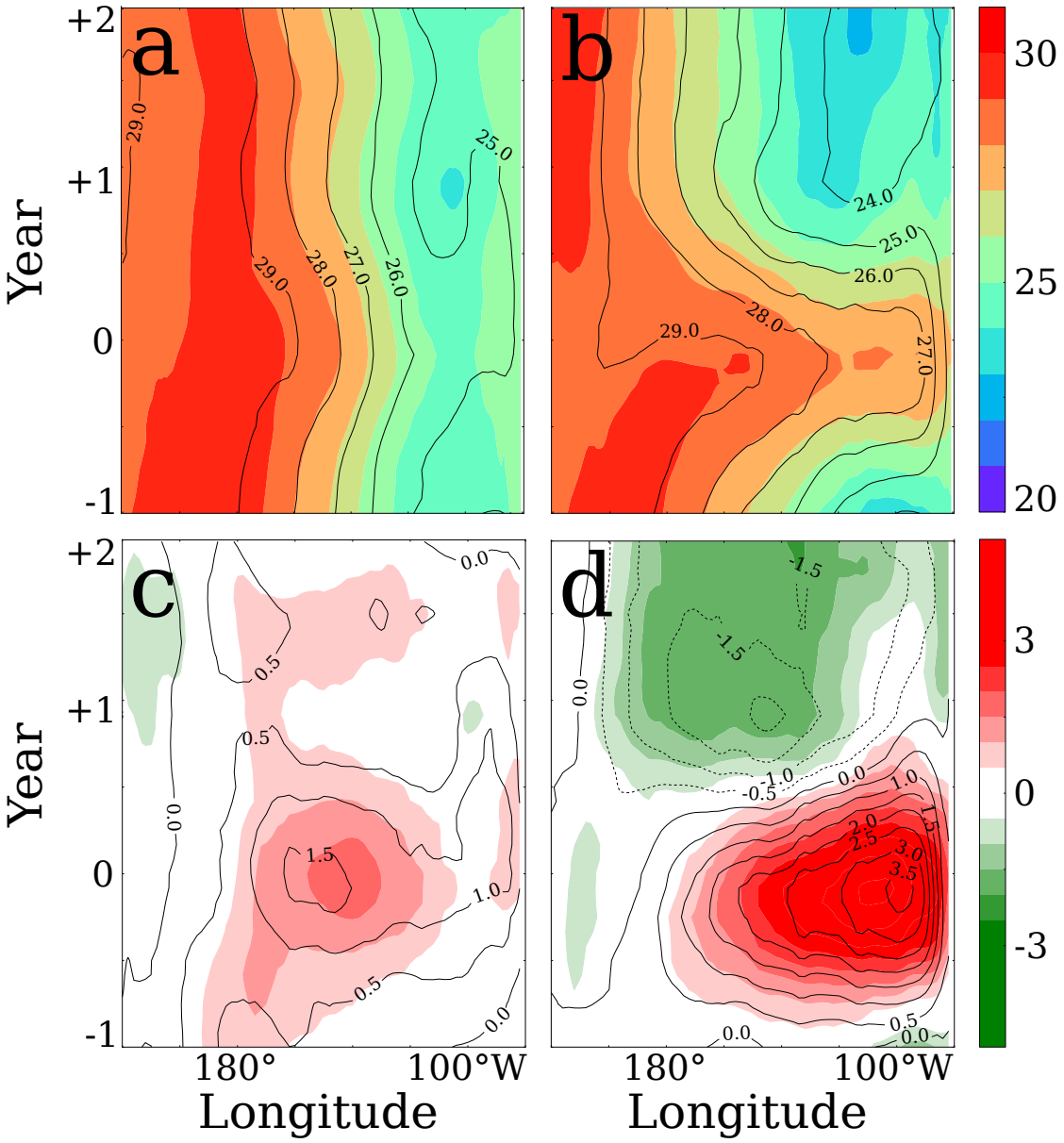

Figure 5.13: Panel **a** (**c**) shows the SST (anomaly) evolution averaged between 2°S and 2°N over the three years surrounding the 1991-92 El Niño event in ACCESS-OM (shading) and the BMRC reanalysis data (contours). Panels **b** and **d** are the same as panels **a** and **c**, but for the 1997-98 El Niño event. Data are in units of °C. The shading interval in the upper panels is 1°C and in the lower panels is 0.5°C.

OM were shifted eastwards by approximately 15° compared with the observations.

The mean vertical structure of potential temperature averaged between 2°S and 2°N and over the period 1980-2004 for the ACCESS-OM and BMRC datasets was compared (figure 5.15a). There was good agreement between the two datasets, although on average, ACCESS-OM was slightly warmer in the eastern equatorial Pacific above 200 m and in the western Pacific warm pool region above 150 m. The mean positions of the equatorial thermocline over the period 1980-2004 for the two datasets, as well as the mean positions during the 1991-92 and 1997-98 El Niño events, were also comparable.

Finally, the vertical structure of the equatorial zonal current anomalies in the ACCESS-OM dataset was contrasted with the corresponding variable from SODA (figure 5.15b), both averaged over the period 1980-2001. There was generally good agreement between the datasets, particularly with respect to the structure and location of the equatorial undercurrent (EUC), although there was a more marked weakening of the ACCESS-OM simulated EUC in the western equatorial Pacific below 100 m. The surface westwards currents along the equator were stronger in SODA by up to 0.2m s^{-1} in the western-central Pacific.

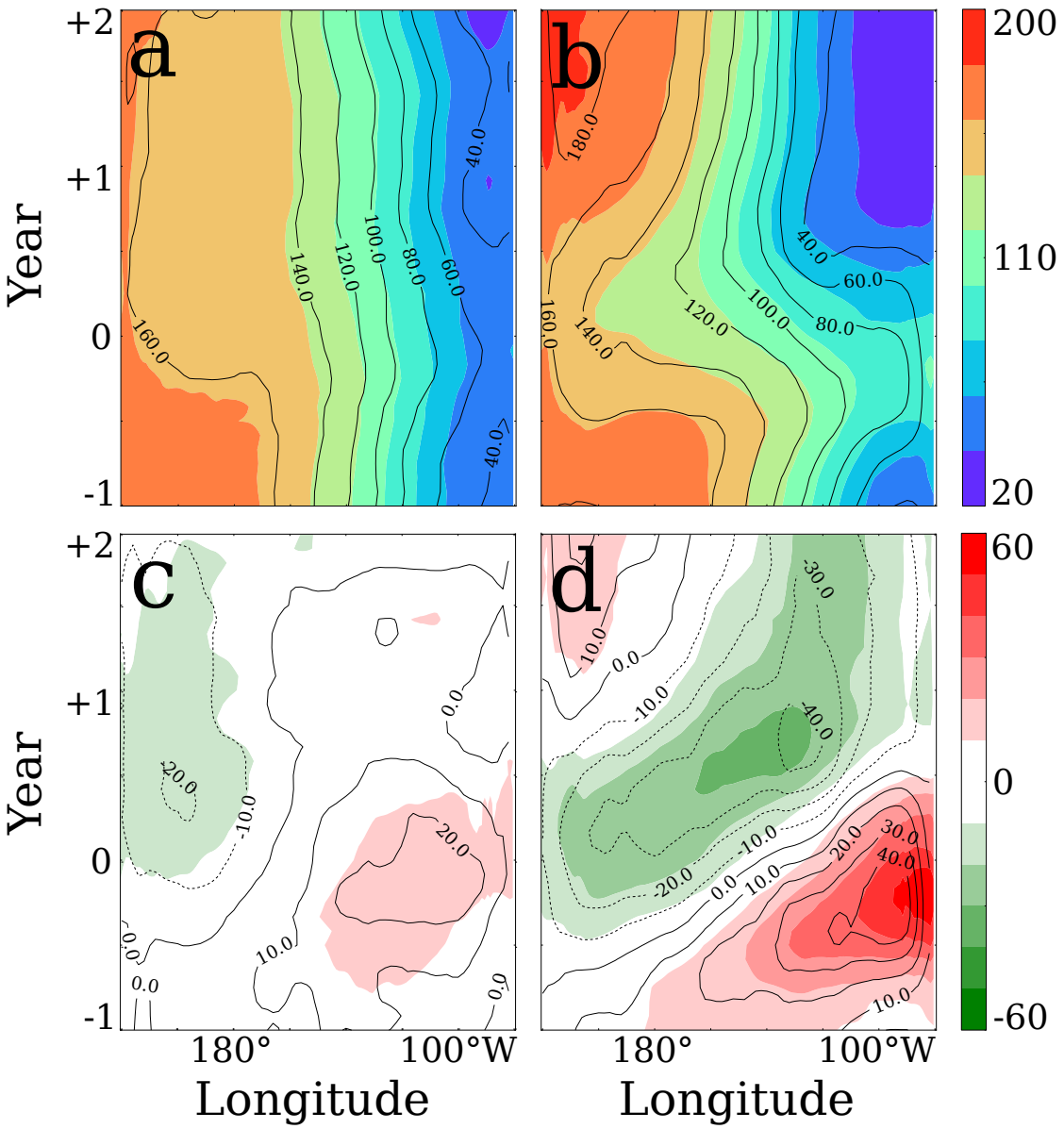

Figure 5.14: Panel **a** (**c**) shows the evolution of the 20°C isotherm depth (anomaly) averaged between 2°S and 2°N over the three years surrounding the 1991-92 El Niño event in ACCESS-OM (shading) and the BMRC reanalysis data (contours). Panels **b** and **d** are the same as panels **a** and **c**, but for the 1997-98 El Niño event. Data are in units of meters. The shading interval in each panel is 10m.

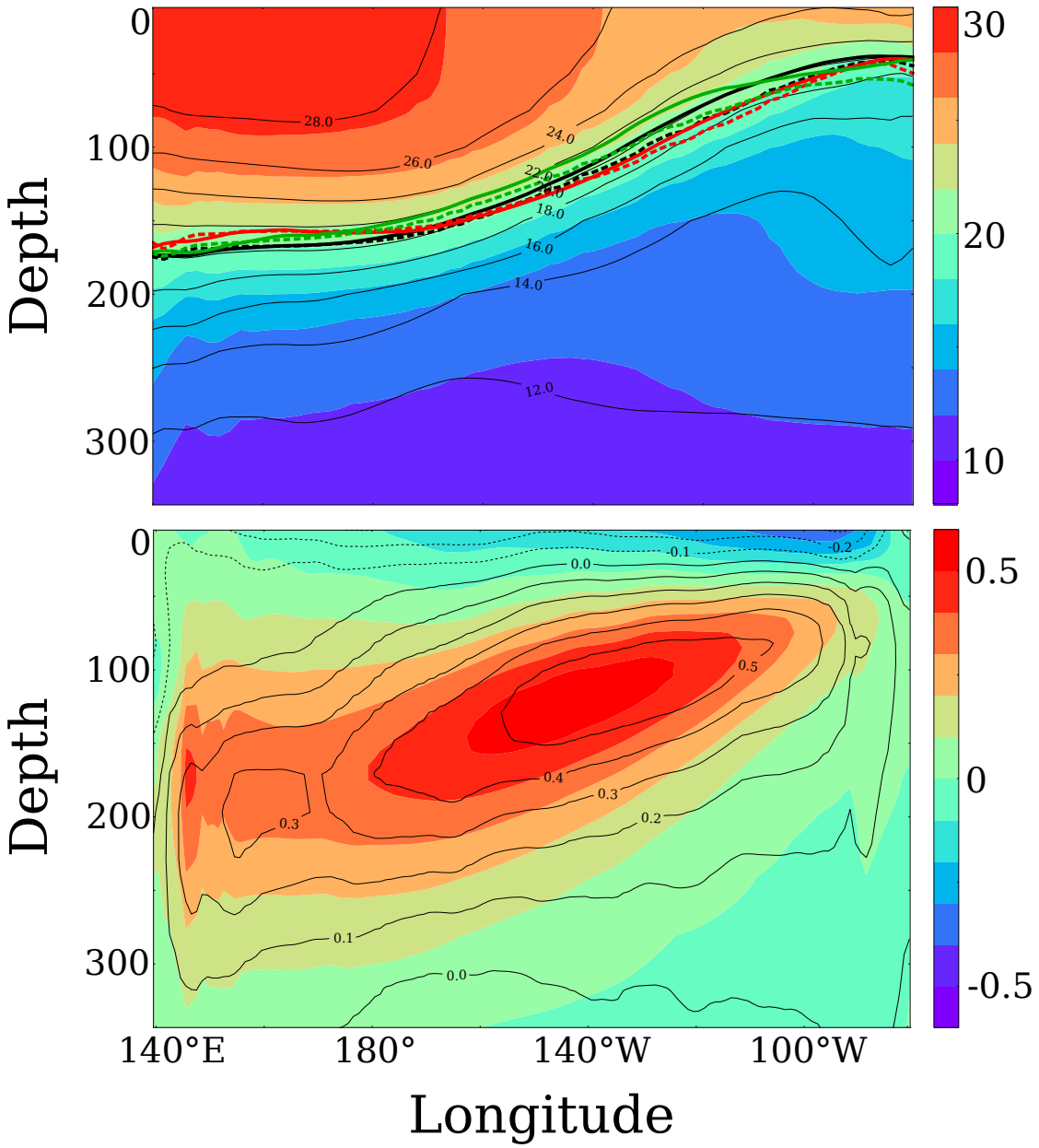

Figure 5.15: **a** Vertical potential temperature structure of the tropical Pacific Ocean averaged between 2°S and 2°N and over the period 1980-2004 from ACCESS-OM (shading) and the BMRC reanalysis data (contours). The black solid (dashed) line shows the mean position of the thermocline over the same period from BMRC (ACCESS-OM); the red solid (dashed) line shows the mean position of the thermocline for the three years surrounding the 1991-92 El Niño event from BMRC (ACCESS-OM); and the red solid (dashed) line shows the mean position of the thermocline for the three years surrounding the 1997-98 El Niño event from BMRC (ACCESS-OM). Data are in units of °C and the shading interval is 1°C. **a** Same for panel **a** but for vertical zonal current from ACCESS-OM (shading) and the SODA reanalysis data (contours). Units are in m s^{-1} and the shading interval is 0.1 m s^{-1}.

5.8 Appendix B: The heat budget equations

In order to understand dynamical differences between the ENSO events in ACCESS-OM and ACCESS-CM1.3, we consider the heat tendency budget averaged in the mixed layer adapted from Vialard and Delecluse (1998), namely

$$\partial_t T^* = -u^* \partial_x T^* - v^* \partial_y T^* - w \partial_z T^* + Q_s^* + DER^*, \tag{5.3}$$

where T^* is the potential temperature, u^* is the zonal current velocity, v^* is the meridional current velocity, w^* the vertical current velocity, and Q_s^* is the net surface heat flux penetrating through the mixed layer, which can be calculated via the sum of the net downwards shortwave, longwave, latent, and sensible heat fluxes at the sea surface. DER^* represents entrainment into and diffusion processes within the mixed layer as well as other processes that are unable to be adequately resolved in our offline calculation of the heat budget (i.e. residuals). Derivatives are computed using centered differences.

The time-varying MLD over which the terms are averaged is denoted h, and is defined in both ACCESS simulations as the depth at which the density layer σ_0 deviates from surface values by 0.125 kg m^{-3} (calculated offline). The mean MLD in the ACCESS simulations is compared in figure 5.3. In chapter 4, the thermocline efficiency factor f_H - an indicator of the effectiveness of the thermocline feedback in warming the mixed layer during El Niño - was introduced. The efficiency of the thermocline feedback in ACCESS-OM was found to be slightly worse ($f_H = 0.63$ and $R^2 = 0.77$ for $p < 0.001$ using a two-sided Student's $t-$test) than the UK Met Office subsurface ocean temperature and salinity data (UKMO) reanalysis ($f_H = 0.85$ and $R^2 = 0.82$ for $p < 0.001$ using a two-sided Student's $t-$test; Ingleby and Huddleston, 2007). The thermocline efficiency factor for the ACCESS-CM1.3 model analyzed here (for the period 1980-2005, as for the comparison between the ACCESS-OM and UKMO datasets) was $f_H = 0.52$ ($R^2 = 0.66$ for $p < 0.001$ using a two-sided Student's $t-$test), which indicates that the mean upwelling is less effective in advecting warm water into the mixed layer during El Niño events in ACCESS-CM1.3 than in the ACCESS-OM and the UKMO datasets.

We decompose each of the terms in Eq. (5.3) into the sum of their climatological ($\overline{T^*}$)

and anomalous ($T^{*\prime}$) components, for example

$$T^* = T^{*\prime} + \overline{T^*}, \tag{5.4}$$

and integrate over h, yielding

$$\partial_t T' = A'_x + A'_y + A'_z + Q' + DER', \tag{5.5}$$

where T' is the anomalous mixed layer integrated potential temperature. The mixed layer integrated anomalous advection terms in Eq. (5.5) are the zonal advection term, given by

$$A'_x = -\frac{1}{h}\int_{-h}^{0} \left[\overline{u^*}\partial_x T^{*\prime} + u^{*\prime}\partial_x \overline{T^*} + u^{*\prime}\partial_x T^{*\prime}\right] dz, \tag{5.6}$$

the meridional advection term

$$A'_y = -\frac{1}{h}\int_{-h}^{0} \left[\overline{v^*}\partial_y T^{*\prime} + v^{*\prime}\partial_y \overline{T^*} + v^{*\prime}\partial_y T^{*\prime}\right] dz, \tag{5.7}$$

and vertical advection term

$$A'_z = -\frac{1}{h}\int_{-h}^{0} \left[\overline{w^*}\partial_z T^{*\prime} + w^{*\prime}\partial_z \overline{T^*} + w^{*\prime}\partial_z T^{*\prime}\right] dz, \tag{5.8}$$

$$\approx \frac{1}{h}\left[w'_{-h}(\overline{T_{-h}} - \overline{T}) + \overline{w_{-h}}(T'_{-h} - T') + w'_{-h}(T'_{-h} - T')\right], \tag{5.9}$$

where the subscript $-h$ denotes the value of a variable at the base of the mixed layer. Continuity requires that only upwards motion in w is considered. The net anomalous heat flux (per ocean heat capacity in the equatorial region) is

$$Q' = \frac{Q'_{net} + Q'_{sw}}{h\rho_0 c_p} = \frac{Q'_{sw0} + Q'_{lw0} + Q'_{la0} + Q'_{se0} + Q'_{sw}}{h\rho_0 c_p}, \tag{5.10}$$

where Q'_{sw0}, Q'_{lw0}, Q'_{la0}, and Q'_{se0} are the anomalous shortwave, longwave, latent, and sensible heat fluxes at the sea surface, respectively, $\rho_0 = 1035$ kg m^{-3} is the constant density of seawater, and $c_p = 3989.24$ J kg^{-1} K^{-1} is the constant specific heat capacity of seawater. Q'_{sw} in Eq. (5.10) is the depth-averaged (i.e. 3-dimensional) anomalous shortwave heat flux that penetrates into the mixed layer below the surface, namely

$$Q'_{sw} = \frac{1}{h}\int_{-h}^{1} \left[Q^*_{sw}\right]. \tag{5.11}$$

Q_{sw} is calculated based on a single exponential decay rule (Morel and Antoine, 1994) to calculate ocean absorption. ACCESS-OM uses data from the Sea-viewing Wide

Field-of-view Sensor (SeaWiFS) Project dataset for the diffuse attenuation coefficient of the downwelling photosynthetically-available radiation (Cracknell et al., 2001; Bi et al., 2013a).

Chapter 6

Discussion

6.1 Aims and objectives

This thesis is an assessment of a hierarchy of theoretical frameworks for their capacity to diagnose El Niño-Southern Oscillation (ENSO) related processes and dynamics. Accordingly, this thesis provides an important step towards the identification and development of suitable process-based diagnostics to aid in the improvement of coupled general circulation model (CGCM) simulations of ENSO.

Previous studies have applied frameworks and associated metrics, such as low-order conceptual models and the linear Bjerknes stability index, to observations and CGCMs in order to understand simulated ENSO behaviours (Kessler, 1991; Picaut et al., 1996; Clarke et al., 2000; Meinen and McPhaden, 2000, 2001; Boulanger et al., 2003; Hasegawa and Hanawa, 2003; Mechoso et al., 2003; Bettio, 2007; Choi et al., 2013). These frameworks are also commonly used for model intercomparisons to understand the sensitivities of CGCMs to changes in the tropical Pacific Ocean induced by global warming (Kim and Jin, 2011a,b; Kim et al., 2014b). Yet, a systematic evaluation of the capacity of many frameworks to accurately diagnose ENSO behaviours had not previously been undertaken.

Consequently, this thesis aimed to:

I. Assess the accuracy of a hierarchy of frameworks - namely the unified oscillator conceptual model, the Bjerknes stability index, and the heat budget equation - in capturing the observed balance of processes and dynamics contributing to ENSO evolution;

II. Identify possible improvements to each framework to better their performance in diagnosing simulated ENSO behaviour; and

III. Ascertain the extent to which each framework has utility in understanding and diagnosing model behaviours and sensitivities.

To achieve these aims, a number of specific objectives were identified in chapter 1 and addressed in chapters 3-5 of this thesis. They are summarised as follows:

Chapter 3: the unified oscillator

1. To what extent did the unified oscillator faithfully represent the ENSO behaviour of a realistic flux-forced ocean general circulation model (OGCM), namely the Australian Community Climate and Earth System Simulator Ocean Model (ACCESS-OM)? This relates to aim I above.

2. Did the unified oscillator offer superior functionality in capturing ENSO behaviour than the simpler conceptual models that it combines (aim I)?

3. How was the formulation of the unified oscillator modified to improve its simulation of ENSO events (aim II)?

Chapter 4: the Bjerknes stability index index/heat budget

4. How faithfully did the Bjerknes stability index reproduce the key ocean dynamics important to ENSO evolution compared with the corresponding heat budget equation that it simplifies (aim I)?

5. How useful is the Bjerknes stability index in the context of model intercomparisons (aim III)?

Chapter 5: classification of CGCM ENSO behaviours using the heat budget equation

6. How realistically did the ACCESS CGCM (ACCESS-CM1.3) simulate the heat budget dynamics during El Niño evolution compared with the corresponding flux-forced simulation of ACCESS-OM (aim III)?

7. Were the spatial flavours present in the flux-forced ACCESS-OM simulation faithfully replicated in the ACCESS-CM1.3 simulation (aim III)?

8. How did the El Niño evolution pathways of the ACCESS-CM1.3 simulation compare to those of the flux-forced ACCESS-OM simulation (aim III)?

In what follows, the key results from chapters 3-5 are discussed, with reference to the overarching thesis objectives outlined above. A discussion of the nature of ENSO revealed by this work, and of future research directions, is also provided.

6.2 Key findings and implications

6.2.1 Unified oscillator

Chapter 3 represents the first systematic evaluation of the ability of the unified oscillator to realistically replicate key features of the ENSO cycle. The unified oscillator was found to poorly replicate the magnitude, phase, and structure of ENSO-related anomalies. The results suggest that in its current form, the unified oscillator is not an appropriate framework for diagnosing ENSO behaviours in CGCMs. However, this does not necessarily imply that there is no utility in conceptual models that combine multiple mechanisms to describe ENSO development and transition. Rather, further work on such unified oscillators should be undertaken before they are considered to be sufficiently versatile in capturing a full range of ENSO behaviours.

The accuracy of the unified oscillator in representing the main features of the ENSO cycle was first addressed via comparison of the unified oscillator equations for the sea surface temperature (SST) anomaly, thermocline depth anomaly, and wind stress anomaly tendencies with the corresponding simulated tendencies estimated directly from ACCESS-OM (objective 1). The parameter values in the unified oscillator equations were taken directly from Wang (2001) - the predicted values - and alternatively estimated via generalised least squares (GLS) regression analysis - the fitted values. In the case of the SST anomaly tendency equation, the predicted curve overestimated the magnitude of the corresponding simulated tendency, explaining only 14% of the variance in the simulated tendency, compared with 61% explained by the fitted curve. The predicted and fitted

curves for the unified oscillator thermocline depth and zonal wind stress anomaly tendencies were unable to replicate the phase and variability of the corresponding simulated tendencies, explaining essentially none of their variances.

A further objective of chapter 3 was to compare the performance of the unified oscillator with those of the individual component models that it combines - the delayed, advective-reflective, western Pacific, and recharge oscillators (objective 2). Overall, the original delayed oscillator model provided the most accurate diagnostic of ENSO behaviour, predominantly due to the assumption of a diagnostic relation between the Niño-4 zonal wind stress anomaly and Niño-3 SST anomaly. The results from the unified oscillator formulations of the delayed and advective-reflective oscillators, which included prognostic zonal wind stress equations, were comparable to that of the unified oscillator.

The western Pacific oscillator equations - the original versions and those derived from the unified oscillator - were neither necessary nor sufficient in modelling the ENSO behaviour simulated in ACCESS-OM. This was partly due to the western Pacific thermocline depth anomaly being averaged off- rather than on-equator. However, it is possible that the main negative feedback mechanism described by the western Pacific oscillator was inappropriately parameterised, or did not operate, either at all or in concert with other mechanisms, during every ENSO event in the ACCESS-OM simulation.

The original delayed oscillator equation for the SST anomaly tendency provided a closer fit to the simulated tendency than did the corresponding equation from the original recharge oscillator. In particular, the fitted recharge oscillator curve poorly emulated the magnitude, phase, and sign of the simulated tendency during periods marked by central Pacific El Niños. This result does not imply that the delayed oscillator was a better descriptor of ENSO than the recharge oscillator, particularly given the limitations of the delayed oscillator in inciting ENSO growth (Li and Clarke, 1994; Mantua and Battisti, 1994; Kessler and McPhaden, 1995). Rather, it may imply that the recharge oscillator equations are missing dynamics important to central Pacific El Niño events (Kug et al., 2010).

Based on the findings of chapter 3, modifications to the unified oscillator model were proposed (objective 3). These included adopting a diagnostic, rather than prognostic,

equation relating the Niño-4 zonal wind stress and SST anomalies, as well as modifying the averaging region for the thermocline depth anomaly to be on- rather than off-equator in the western Pacific. Ultimately, however, due to the superior performance of the original delayed oscillator in capturing ENSO-related variability, this model was suggested as a most appropriate starting point from which to modify and improve conceptual models.

While only a few modifications to the unified oscillator were considered in this thesis, recent studies have highlighted a number of additional considerations that may further enhance the ability of unified conceptual models to capture a range of ENSO behaviours. For example, asymmetries in the duration, magnitude, and timing of ENSO events have been effectively replicated through the inclusion of nonlinearities in the relationship between SST and zonal wind stress anomalies (Frauen and Dommenget, 2010; Choi et al., 2013). Accounting for a southwards shift in the westerly wind stress anomalies may improve modelling of the transition from El Niño to La Niña (Harrison, 1987; Vecchi and Harrison, 2003). Explicitly including features such as the seasonal cycle (Tziperman et al., 1995), stochastic forcings (e.g. westerly wind bursts or the Madden-Julian Oscillation; Vecchi et al., 2006), and the mean state of the tropical Pacific (Guilyardi, 2006) may aid in the ability of conceptual models to capture ENSO diversity.

Even with the incorporation of the additional mechanisms described above, further considerations should be taken into account when low-order unified conceptual models are used to evaluate ENSO behaviours in CGCMs. For example, variables included in conceptual models are averaged over fixed spatial regions that do not necessarily enclose the locations of maximum heating (or cooling) for both observed spatial flavours of ENSO. Given the diversity in ENSO types already observed, and the potential for more marked spatial variability on decadal to centennial timescales (Wittenberg, 2009; Wittenberg et al., 2014; Capotondi et al., 2015), spatial averaging regions should be mindfully chosen to ensure their relevance to the analysed data. On a similar note, the mechanisms leading to ENSO growth and decay vary from event to event, despite the fact that the parameter values weighting each of these mechanisms remain constant in time.

Finally, it is important to recognise that low-order conceptual models are derived based on observed features of the tropical Pacific that are not necessarily well replicated in

CGCMs (Delecluse et al., 1998; Guilyardi et al., 2003; AchutaRao and Sperber, 2006; Belmadani et al., 2010; Collins et al., 2010; Capotondi and Wittenberg, 2013; Capotondi et al., 2015). For example, many CGCMs simulate net surface heat fluxes that are not phase locked to the seasonal cycle due to biases in the shortwave heat flux, which in turn alters the behaviour and variability of ENSO-related anomalies (Rashid and Hirst, 2015). Consequently, it is possible to imagine a scenario where the balance of parameter values obtained by the application of a unified conceptual model to a CGCM does not reflect the true dynamical behaviour of the CGCM (e.g. Mechoso et al., 2003). In fact, this highlights a significant challenge in the development of effective process-based diagnostics: while they are formulated to account for different behaviours and sensitivities of CGCMs, to be truly effective, their construction must be flexible enough to accurately distinguish between realistic and biased dynamics simulated by the CGCMs. It follows that the results of the application of conceptual models to CGCMs should be interpreted in light of the underlying dynamics of the dataset analysed, as it is possible to get the "right" result for the wrong reason.

6.2.2 Bjerknes stability index

Chapter 4 comprises a study that assessed the accuracy of the representation of ENSO ocean dynamics by the Bjerknes stability index, a simplified metric that quantifies the contribution of the linear heat budget feedbacks to the growth of ENSO (Jin et al., 2006). The Bjerknes stability index was found to misrepresent the magnitude, variability, and structure of the key ENSO ocean feedbacks in ACCESS-OM. As such, in its current linear form, the Bjerknes stability index cannot necessarily be relied upon to accurately portray the balance of dynamics leading to ENSO evolution in CGCMs, and hence has limited utility in model intercomparisons. Indeed, while two models may have similar values for the Bjerknes stability index feedbacks, the corresponding magnitudes and behaviours of the heat budget dynamics may be considerably different.

An objective of this thesis was to evaluate how effectively the Bjerknes stability index represented the ocean dynamics contributing to the growth and termination of ENSO (objective 4). In chapter 4, the Bjerknes stability index feedbacks were calculated using

output from the ACCESS-OM simulation and compared with the corresponding heat budget feedbacks that the Bjerknes stability index feedbacks are intended to represent. The following factors were found to impact on the ability of the Bjerknes stability index to accurately capture the magnitude, variability, and structure of the key ocean feedbacks:

(i) In the derivation of each feedback, multiple balance relations between ENSO-related variables were employed. However, an incorrect assumption was made that strong correlations between the variables in each balance relation implied a strong correlation between the original and derived feedbacks. In reality, that A is correlated with B, and B with C, does not imply that A is correlated with C, a feature apparent in the results of chapter 4: the original heat budget feedbacks were found to be generally poorly correlated with their counterparts in the Bjerknes stability index formulation.

(ii) Linearity in each of the balance relations was assumed, when nonlinearities may actually be important (Frauen and Dommenget, 2010; Lloyd et al., 2012; Choi et al., 2013). In addition, the nonlinear dynamical heating terms, which have been found to play a substantial role in some ENSO events (An and Jin, 2004), were omitted.

(iii) An over-simplification of the magnitude and structure of the feedbacks occurred due to the application of regression analysis to each of the balance relations. As regression analysis was relatively uninformative regarding the nature of the similarities between two timeseries, for example if they were lagged or in phase, the accuracy of the magnitude of each of the regression coefficients was not to be trusted.

(iv) Finally, the use of a constant mixed layer depth, rather than a more accurate temporally and spatially varying one, may have impacted on the strength of the relationships between variables in the balance relations.

The Bjerknes stability index parameterises the growth term in the recharge oscillator coupled system of equations, where the nonlinear terms from the heat budget equation

are excluded. Hence, to test the diagnostic power of the Bjerknes stability index in the recharge oscillator equations, these equations were compared with the heat budget equation, which was reduced to contain only the terms calculated in the Bjerknes stability index (that is, the linear terms). Theoretically, if the Bjerknes stability index is indeed a true simplification of the heat budget, these two methods should have been strongly correlated. Instead, the recharge oscillator equations for the SST and thermocline depth anomalies were found to provide a considerably poorer fit to the ACCESS-OM simulation tendencies than the linear heat budget equation. It is likely that missing mechanisms from the recharge oscillator equations, such as mechanisms important to central Pacific events, as well as inaccuracies in the calculation of the Bjerknes stability index that also led to the parameterisations made in the recharge oscillator equations, influenced the fit.

Another objective of this thesis was to evaluate the usefulness of the Bjerknes stability index in the context of model intercomparisons (objective 5). Compared with the unified oscillator, the Bjerknes stability index has the potential to be a powerful diagnostic tool in understanding ENSO behaviours in CGCMs: it is computationally inexpensive to calculate, accounts for the major dynamics influencing ENSO growth and transition, and it reduces a highly-complex ocean-atmosphere coupled system into a few parameters whose sensitivities to changes in the mean state, for example, due to global warming or longer term internal variability (i.e. decadal to centennial timescales), can be readily calculated. However, as for the unified oscillator, in its current form, the Bjerknes stability index has limited capacity as a tool for model intercomparisons due to its potential to misrepresent the ocean feedbacks important to ENSO. That is, the Bjerknes stability index cannot be relied upon to accurately account for the true balance between ENSO processes simulated by a CGCM, and hence is limited in its ability to diagnose model sensitivities and behaviours. In particular, the Bjerknes stability index has the potential to yield similar values of the heat budget feedbacks for two very different models. It follows that in its current form, the Bjerknes stability index has little utility as a framework to accelerate CGCM improvement.

A number of modifications to the Bjerknes stability index were suggested, including

the use of temporally- and spatially-varying mixed layer depths - as opposed to using a constant mixed layer depth - and the inclusion of nonlinearities, both in the balance relations that are employed in the Bjerknes stability index derivation, and in the recharge oscillator equations.

The results from chapter 4 highlight a key limitation of low-order diagnostic frameworks: it is understandable, and not surprising, that the highly complex nature of ENSO events - the varying development characteristics and diversity in spatial flavours from one event to the next - cannot be wholly understood from a small set of parameters. It is therefore a recommendation of this thesis that the Bjerknes stability index would be better used in concert with more comprehensive diagnoses, such as the original heat budget equation, when characterising CGCM ENSO behaviours.

6.2.3 Diagnosis of CGCM ENSO behaviours using the heat budget equation

Chapter 5 of this thesis focused on evaluating the realism of simulated El Niño evolution dynamics in a leading CGCM (i.e., ACCESS-CM1.3) in comparison with an equivalent flux-forced OGCM simulation that represented a baseline of ENSO dynamics. This was undertaken to explore the effect of coupling on El Niño behaviours.

A first objective of chapter 5 was to assess the realism of the heat budget dynamics simulated by the fully coupled ACCESS-CM1.3 during El Niño development with respect to the corresponding dynamics in the flux-forced ocean-only ACCESS-OM (objective 6). Three major differences in the balance of heat budget dynamics contributing to El Niño development were identified. First, the net surface heat flux anomaly was up to three times smaller during El Niño development in the CGCM than in the OGCM, and acted to reinforce, rather than damp, the positive mixed layer temperature anomaly during many CGCM El Niño events. Second, consistent with the OGCM results, the thermocline feedback was generally the most important term contributing to growth in the eastern Pacific for the majority of the El Niño events in the CGCM. However, the thermocline feedback was negative in the central Pacific during some of El Niño events in the CGCM, which was not the case in any of the OGCM El Niño events. Third,

the zonal advective feedback contributed to damping, rather than growth, of the mixed layer temperature anomalies in the eastern Pacific during a number of CGCM El Niño events. Other notable differences between the balance of heat budget dynamics in the CGCM and OGCM were the relative increases in the nonlinear zonal advective term to growth, and diffusion and residual terms to damping.

The spatial flavours simulated by the CGCM were evaluated and compared with the eastern and central Pacific El Niño spatial flavours from the OGCM (objective 7). The CGCM was unable to capture central Pacific spatial flavours of El Niño, instead simulating an unrealistic double peaked El Niño event, with concurrent warming centres in both the eastern and western Pacific. The other spatial flavour of El Niño simulated by the CGCM involved patterns of warming similar to the eastern Pacific spatial flavour of El Niño, although shifted further west at the edge of the warm pool due to the cold tongue bias, and west along the west coast of South America due to a warm bias in the shortwave heat flux arising from a bias in the low level cloud scheme. The spatial patterns of El Niño were analysed in nine additional CMIP5 CGCMs and the double peaked El Niño event was a feature common to each.

Examination of the evolution pathways, that is, the dynamics giving rise to the patterns of warming during El Niño evolution, revealed the cause of the double peaked spatial flavour of El Niño (objective 8). As in the flux-forced OGCM simulation, the evolution pathway of the eastern peak of warming was dominated by the thermocline feedback. By contrast, anomalous zonal advection led the development of the secondary warm peak in the western Pacific warm pool. Its evolution can be described as follows.

The anomalously westwards position of the dynamic warm pool edge in the CGCM allowed warm mixed layer temperature anomalies to extend further to the west than in the OGCM, also shifting the eastwards anomalous zonal currents and mean zonal mixed layer temperature gradient to the west (this behaviour is consistent with the well documented cold tongue bias in CGCMs). As a result, the maximum in the zonal advective feedback was located further to the west in the CGCM than in the OGCM, leading to warming in the western Pacific. As the western warm peak developed, a positive (negative) anomalous zonal mixed layer temperature gradient to the west (east) of the warm

peak increased (decreased) the zonal mean advection term. A stronger than observed South Equatorial Current in the CGCM advected warm water further to the west, ultimately preventing interaction between the eastern and western peaks. Interestingly, the east-west tilt of the thermocline depth and location of maximum westerly wind stress anomalies during the double peaked event were qualitatively similar to, although smaller in magnitude than, those of the eastern Pacific event in the OGCM. The results supported the presence of the recharge oscillator mechanism of transition during the double peaked events by the discharge of warm water volume.

The evolution pathway of the CGCM eastern Pacific El Niño spatial flavour was also examined (objective 8). Similar to the double peaked event, warming in the eastern Pacific was attributed to the thermocline feedback and the western extent of warming expanded into the western Pacific warm pool region. By contrast with the CGCM double peaked event, the location of peak westerly wind stress anomalies during this event was shifted to the east, causing an eastwards shift in the zonal advection term that prevented the development of a secondary western Pacific warm peak.

A notable result from chapter 5 was that a metric relying on spatial averages of El Niño temperature anomalies typically used to diagnose spatial flavours of ENSO in observations failed to detect the CGCM double peaked El Niño event and sometimes misdiagnosed it as a westwards shifted central Pacific El Niño. This finding highlights the importance of examining full spatial patterns of warming during El Niño evolution in concert with averaged diagnostic tools to explore the full range of simulated ENSO behaviours.

6.3 Overview

6.3.1 Summary of findings

This thesis focused on a number of ENSO theoretical frameworks to determine the extent to which they could be used as process-based metrics to understand simulated CGCM ENSO behaviours. There was a specific focus on the unified oscillator conceptual model, the Bjerknes stability index, and the heat budget equation for the tropical Pacific.

The heat budget equation was further applied to an IPCC-class CGCM (the ACCESS model) to explore the realism of the simulated El Niño evolution dynamics. Here the main findings with respect to the research objectives outlined in sections 1.2.2 and 1.2.3 (reiterated in section 6.1) are summarised.

1. When using the parameter values suggested by Wang (2001), as well as those estimated by generalised least squares regression (the fitted values), the unified oscillator equations for SST anomaly, thermocline depth anomaly, and zonal wind stress anomaly tendencies failed to capture the magnitude, phase, and structure of the corresponding tendencies simulated by ACCESS-OM; their numerical solutions using the fitted parameter values also failed to produce an oscillation. These results suggested that the unified oscillator was not a faithful representation of the ACCESS-OM ENSO behaviour.

2. The unified oscillator was significantly outperformed by the original formulation of the delayed oscillator conceptual model in replicating the simulated SST anomaly tendency. The original recharge oscillator parameterisation of the thermocline depth anomaly tendency also surpassed that of the unified oscillator. The performance of the unified oscillator formulations of the delayed, recharge, advective-reflective, and western Pacific oscillators were on par with, or worse than, that of the unified oscillator.

3. Modifications to the unified oscillator were proposed, including using a diagnostic relationship between zonal wind stress and SST, and calculating the thermocline depth anomaly on-, rather than off-, equator.

4. The Bjerknes stability index feedbacks misrepresented the magnitude, phase, and structure of the corresponding heat budget dynamics that they were supposed to represent. The poorer performance of the Bjerknes stability index feedbacks was predominantly due to the simplifying assumptions in its derivation and the presumption of linearity between key ENSO variables.

5. Given that the Bjerknes stability index alternately over- and under-estimated the importance of different feedbacks to the leading growth rate of ENSO, and omitted

other feedbacks such as the nonlinear dynamical heating terms, it cannot be relied upon as an accurate diagnostic tool for use in model intercomparisons.

6. The heat budget dynamics simulated by the ACCESS CGCM during El Niño evolution displayed some qualitative similarities to the corresponding OGCM dynamics. However, coupling biases, including a westward extension of the mixed layer temperature anomalies and positive shortwave heat flux anomaly, led to differences in the locations, magnitudes, timing, and signs of the CGCM heat budget dynamics compared with their OGCM counterparts. In particular, the simulation of the net surface heat flux anomalies in the eastern Pacific, thermocline feedback in the central Pacific, and zonal advective feedback in the western Pacific were particularly unrealistic in the CGCM, and often of the wrong sign.

7. The CGCM failed to capture the central Pacific spatial flavour of El Niño, instead simulating a double peaked event that was characterised by warming centres in both the eastern and western Pacific. The CGCM also simulated an El Niño flavour whose patterns of temperature anomalies averaged in the mixed layer matched those of the eastern Pacific El Niño in the OGCM.

8. In the case of the CGCM double peaked El Niño event, the evolution pathway of the eastern peak was led by the thermocline feedback, and the evolution pathway of the western Pacific warm peak was characterised by strong zonal advection. The westward extension of the dynamic warm pool edge in the CGCM, and overly strong South Equatorial Current, prevented the interaction of the two peaks. Simple eastern Pacific/central Pacific El Niño metrics sometimes inadvertently categorised the doubled peaked event as a central Pacific event. The east-west tilt mode of the thermocline depth that operated in the OGCM was also present in the CGCM, resulting in a similar discharge of warm water volume, albeit of a smaller magnitude than in the OGCM. The evolution pathway of the OGCM eastern Pacific event was comparable to that of the *eastern peak alone* in the CGCM double peaked El Niño event.

6.3.2 Lessons learnt and future directions

This thesis has reviewed a number of frameworks for understanding ENSO behaviours, finding that many of them - particularly low-order conceptual models and the Bjerknes stability index - are insufficient in accurately diagnosing the salient features of ENSO, such as their amplitude, period, and dynamics. This is at least in part due to the assumption of linearity between ENSO-related variables in these frameworks, their inflexibility in modelling behaviours that evolve in space and time - on interannual to centennial timescales - and the simplifying assumptions in their derivation.

One particular issue highlighted here relates to the difficulty in identifying metrics that are sufficiently advanced, as to describe the salient features of ENSO, and sufficiently flexible, as to account for variations in the simulation of these features in CGCMs. Some metrics used in ENSO research - such as balance equations underlying the Bjerknes stability index - are constructed based on observed phenomena, that are not necessarily well replicated in CGCMs. The investigation of spatial flavours simulated in ACCESS-CM1.3 revealed that the standard Niño metrics used to diagnose El Niño types were inapplicable for many El Niño events simulated by this CGCM. Importantly, this highlights the need for a range of metrics as well as diagnostic tools to interpret ENSO behaviours.

A pertinent question to be addressed is which frameworks or diagnostics should be used to understand ENSO behaviours simulated in CGCMs, beyond the low-order models of ENSO analysed in this thesis? One potentially suitable candidate for assessing CGCM ENSO behaviours, that was not analysed here, is the linear inverse model (LIM; Penland and Sardeshmukh, 1995). LIMs are linear, dynamical evolution operators that characterise the state, and interactions, of variables in a stochastically-forced system. In the case of ENSO, a LIM may identify patterns of variability in different tropical oceanic processes, including SST, thermocline depth, and zonal wind stress anomalies, diagnosed from observational data (Newman et al., 2011a) or coupled models (Penland and Sardeshmukh, 1995). LIMs also have power in elucidating the relationships between ENSO variables, and their relative contributions to ENSO growth and decay (Newman et al., 2011a,b). As a result, LIMs have potential utility in characterising ENSO diversity within and between CGCMs, and identifying biases in CGCM simulations of the

tropical Pacific that give rise to this diversity, and thus may be better suited to progress our understanding of the sensitivities of CGCMs to climate change.

The heat budget equation also has utility in characterising ENSO diversity and biases in CGCMs. In this thesis, the heat budget equation facilitated identification and classification of El Niño spatial flavours present in a CGCM, and gave insight into the biases that altered the El Niño behaviours simulated in the CGCM from those of the OGCM. In particular, the heat budget analysis emphasised the importance of the location of and dynamical behaviour at the eastern extent of the western Pacific dynamic warm pool edge in realistically capturing El Niño evolution dynamics and spatial flavours. It follows that improvements in the CGCM representation of this region may lead to marked improvements in the overall simulation of ENSO by CGCMs.

With respect to the ACCESS-CM1.3 CGCM, a more broad improvement in the simulation of the equatorial Pacific might be achieved by amelioration of the low level cloud scheme, and subsequent representation of the shortwave heat flux. This is particularly important in the central Pacific region, where the shortwave heat flux tended to reinforce, rather than damp, mixed layer temperature anomalies. Mechanisms to further improve the realism of CGCM simulations of the tropical Pacific, and particularly the western extent of the equatorial Pacific cold tongue region, need to be investigated.

This thesis makes a contribution to reviewing current ENSO frameworks with the aim of developing process-based metrics to better account for the range of ENSO behaviours in CGCMs. The evolution pathways approach adopted in chapter 5 of this thesis was found to be a suitable diagnostic of El Niño spatial flavours and behaviours, and consequently has utility in exploring the sensitivities of and diversity within and between CGCMs, including in model intercomparison studies. However, spatial evolution pathways that incorporate the heat budget equation feedbacks are complex and can be computationally expensive. It follows that considerable work remains in moulding a diagnostic tool that enables us to more accurately understand and quantify the salient features of simulated ENSO events, such as their development characteristics, and relationship to the mean state and seasonal cycle, while still being simple and computationally inexpensive to calculate in a CGCM.

Appendix A

List of Acronyms

ACCESS-CM1.3	Australian Community Climate and Earth System Simulator Coupled Model
ACCESS-OM	Australian Community Climate and Earth System Simulator Ocean Model
ACF	autocorrelation function
AR	autoregressive model
ARC	Australian Research Council
BJ	Bjerknes
BMRC	British Oceanographic Data Centre
CARS	CSIRO atlas of regional seas
CGCM	coupled general circulation model
CICE4.1	sea-ice model version 4.1
CLIVAR	Climate Variability and Predictability
CM	GFDL Coupled Model (versions 2.0, 2.1, 3, 2.5)
CMIP3	Coupled Model Intercomparison Project phase 3
CMIP5	Coupled Model Intercomparison Project phase 5
CO_2	carbon dioxide
CORE	Coordinated Ocean-ice Reference Experiments
CP	central Pacific
CSIRO	Commonwealth Scientific and Industrial Research Organisation
DER	diffusion, entrainment, and residual processes
DWPE	dynamic warm pool edge
ENSO	El Niño-Southern Oscillation
EOF	empirical orthogonal function
EP	eastern Pacific
ESRL	Earth System Research Laboratory
FLOR	forecast-oriented low ocean resolution

ERSST	Extended Reconstructed Sea Surface Temperature
EUC	equatorial undercurrent
GFDL	Geophysical Fluid Dynamics Laboratory
GLS	generalised least squares
IMAS	Institute for Marine and Antarctic Studies
IPCC	Intergovernmental Panel on Climate Change
ITCZ	Intertropical Convergence Zone
KPP	K profile parameterisation
LANL	Los Alamos National Laboratory
LIM	Linear Inverse Model
MLD	mixed layer depth
MOM4p1	Modular Ocean Model version 4.1
NOAA	National Oceanic and Atmospheric Administration
OAR	Oceanic & Atmospheric Research
OLS	ordinary least squares
OGCM	ocean general circulation model
OSCAR	Ocean Surface Current Analysis Real-time
PACF	partial autocorrelation function
PMEL	Pacific Marine Environmental Laboratory
PSD	Physical Sciences Division
SEC	south equatorial current
SODA	Simple Ocean Data Assimilation
SOI	Southern Oscillation index
SSS	sea surface salinity
SST	sea surface temperature
SWM	Shallow Water Model
TAO	Tropical Atmosphere-Ocean
TOGA	Tropical Ocean Global Atmosphere
TRITON	Triangle Trans-Ocean Buoy Network
UCLA	University of California, Los Angeles
UO	unified oscillator
UARO	advective-reflective oscillator, unified oscillator version
UDO	delayed oscillator, unified oscillator version
UM	unified model
URO	recharge oscillator, unified oscillator version
UWPO	western Pacific oscillator, unified oscillator version
UTAS	University of Tasmania
VOS	voluntary observing ship
WHOI	Woods Hole Oceanographic Institute
W01	Wang (2001)
XBT	expendable bathythermograph

References

AchutaRao, K., and K. R. Sperber, 2006: ENSO simulation in coupled ocean-atmosphere models: are the current models better? *Climate Dynamics*, **27**, 1–15, doi:10.1007/s00382-006-0119-7.

Adcroft, A., and J.-M. Campin, 2004: Rescaled height coordinates for accurate representation of free-surface flows in ocean circulation models. *Ocean Modelling*, **7**, 269–284.

Allan, R., 2000: *El Niño and the Southern Oscillation: multiscale variability, global and regional impacts*, 356. Cambridge University Press, UK.

Allan, R. J., C. J. C. Reason, J. A. Lindesay, and T. J. Ansell, 2003: Protracted ENSO episodes and their impacts in the Indian Ocean region. *Deep Sea Research II: Topical Studies in Oceanography*, **50 (12-13)**, 2331–2347, doi:10.1016/S0967-0645(03)00059-6.

An, S.-I., and F.-F. Jin, 2000: An eigen analysis of the interdecadal changes in the structure and frequency of the ENSO mode. *Geophysical Research Letters*, **27**, 1573–1576.

An, S.-I., and F.-F. Jin, 2001: Collective role of thermocline and zonal advective feedbacks in the ENSO mode. *Journal of Climate*, **14**, 3421–3432.

An, S.-I., and F.-F. Jin, 2004: Nonlinearity and asymmetry of ENSO. *Journal of Climate*, **17**, 2399–2412.

An, S.-I., F.-F. Jin, and I.-S. Kang, 1999: The role of zonal advection feedback in phase transition and growth of ENSO in the Cane-Zebiak model. *Journal of the Meteorological Society of Japan*, **77 (6)**, 1151–1160.

An, S.-I., and B. Wang, 2000: Interdecadal change of the structure of the ENSO mode and its impact on the ENSO frequency. *Journal of Climate*, **13**, 2044–2055.

Andrews, E. D., R. C. Antweiler, P. J. Neiman, and F. M. Ralph, 2004: Influence of ENSO on flood frequency along the California coast. *Journal of Climate*, **17**, 337–348.

Ashok, K., S. K. Behera, S. A. Rao, H. Weng, and T. Yamagata, 2007: El Niño Modoki and its possible teleconnection. *Journal of Geophysical Research*, **112 (C11)**, 1–27, doi:10.1029/2006JC003798.

Balmaseda, M. A., K. Mogensen, and A. J. Weaver, 2013: Evaluation of the ECAMWF ocean reanalysis system ORAS4. *Quarterly Journal of the Royal Meteorological Society*, **139**, 1132–1161, doi:10.1002/jq.2063.

Barnett, T. P., 1977: An attempt to verify some theories of El Niño. *Journal of Physical Oceanography*, **7 (5)**, 633–647.

Battisti, D. S., 1988: The dynamics and thermodynamics of a warming event in a coupled tropical atmosphere/ocean model. *Journal of the Atmospheric Sciences*, **45**, 2889–2919.

Battisti, D. S., and A. C. Hirst, 1989: Interannual variability in a tropical atmosphere-ocean model: Influence of the basic state, ocean geometry and nonlinearity. *Journal of the Atmospheric Sciences*, **46 (12)**, 1687–1712.

Bellenger, H., E. Guilyardi, J. Leloup, M. Lengaigne, and J. Vialard, 2014: ENSO representation in climate models: from CMIP3 to CMIP5. *Climate Dynamics*, **42 (7-8)**, 1999–2018, doi:10.1007/s00382-013-1783-z.

Belmadani, A., B. Dewitte, and S.-I. An, 2010: ENSO feedbacks and associated time scales of variability in a mulitmodel ensemble. *Journal of Climate*, **23 (12)**, doi:10.1175/2010JCLI2830.1.

Bentsen, M., and Coauthors, 2013: The Norwegian Earth System Model, NorESM1-M – part 1: Description and basic evaluation of the physical climate. *Geoscientific Model Development*, **6 (3)**, 687–720, doi:10.5194/GMD-6-687-2013.

Bettio, L., 2007: On the character, dynamics, and predictability of ENSO in the observations and a coupled GCM. Ph.D. thesis, School of Earth Sciences, University of Melbourne, 314 pp.

Bi, D., and Coauthors, 2013a: ACCESS-OM: the ocean and sea ice core of the ACCESS coupled model. *Australian Meteorological and Oceanographic Journal*, **63 (1)**, 213–232.

Bi, D., and Coauthors, 2013b: The ACCESS coupled model: description, control climate and evaluation. *Australian Meteorological and Oceanographic Journal*, **63**, 41–64.

Bjerknes, J., 1966: A possible response of the atmospheric Hadley Circulation to equatorial anomalies of ocean temperature. *Tellus*, **18 (4)**, 820–829.

Bjerknes, J., 1969: Atmospheric teleconnections from the equatorial Pacific. *Monthly Weather Review*, **97 (3)**, 163–172.

Boucharel, J., B. Dewitte, Y. Penhoat, B. Garel, S.-W. Yeh, and J.-S. Kug, 2011: ENSO nonlinearity in a warming climate. *Climate Dynamics*, **37 (9-10)**, 2045–2065, doi:10.1007/s00382-011-1119-9.

Boulanger, J.-P., S. Cravatte, and C. Menkes, 2003: Reflected and locally wind-forced interannual equatorial Kelvin waves in the western Pacific Ocean. *Journal of Geophysical Research*, **108 (C10)**, 3311, doi:10.1029/2002JC001760.

Boulanger, J.-P., and C. Menkes, 1999: Long equatorial wave reflection in the Pacific Ocean from TOPEX/POSEIDON data during the 1992-1998 period. *Climate Dynamics*, **15 (3)**, 205–225, doi:10.1007/s003820050277.

Boulanger, J.-P., and C. Menkes, 2001: The TRIDENT Pacific model. Part II: The thermodynamical model and the role of long equatorial wave reflection during the 1993-1998 TOPEX/POSEIDON period. *Climate Dynamics*, **17**, 175–186.

Boulanger, J.-P., C. Menkes, and M. Lengaigne, 2004: Role of high- and low-frequency winds and wave reflection in the onset, growth and termination of the 1997-1998 El Niño. *Climate Dynamics*, **22 (2-3)**, 267–280, doi:10.1007/s00382-003-0383-8.

Brown, J. N., and A. V. Fedorov, 2010: Estimating the diapycnal transport contribution to warm water volume variations in the tropical Pacific Ocean. *Journal of Climate*, **23**, 221–237, doi:10.1175/2009JCLI2347.1.

Brown, J. N., J. S. Godfrey, and S. E. Wijffels, 2010: Nonlinear effects of tropical instability waves on the equatorial Pacific circulation. *Journal of Physical Oceanography*, **40 (2)**, 381–393, doi:10.1175/2009JPO3963.1.

Brown, J. N., C. Langlais, and C. Maes, 2013: Zonal structure and variability of the western Pacific dynamic warm pool edge in CMIP5. *Climate Dynamics*, **42**, 3061–3076, doi:10.1007/s00382-013-1931-5.

Brown, J. N., P. C. McIntosh, M. J. Pook, and J. S. Risbey, 2009: An investigation of the links between ENSO flavors and rainfall processes in southeastern Australia. *Monthly Weather Review*, **137 (11)**, 3786–3795, doi:10.1175/2009MWR3066.1.

Brown, J. N., and Coauthors, 2012: Implications of CMIP3 model biases and uncertainties for climate projections in the western Tropical Pacific. *Climatic Change*, **119 (1)**, 147–161, doi:10.1007/s10584-012-0603-5.

Cai, W., and Coauthors, 2014: Increasing frequency of extreme El Niño events due to greenhouse warming. *Nature Climate Change*, **4**, 111–116, doi:10.1038/NCLIMATE2100.

Cai, W., and Coauthors, 2015: Increased frequency of extreme La Nina events under greenhouse warming. *Nature Climate Change*, **5 (2)**, 132–137, doi:10.1038/NCLIMATE2492.

Cane, M. A., and S. E. Zebiak, 1985: A theory for El Nino and the Southern Oscillation. *Science (New York, N.Y.)*, **228 (4703)**, 1085–7, doi:10.1126/science.228.4703.1085.

Cane, M. A., S. E. Zebiak, and S. C. Dolan, 1986: Experimental forecasts of El Niño. *Nature*, **321**, 827–832.

Capotondi, A., 2013: ENSO diversity in the NCAR CCSM4 climate model. *Journal of Geophysical Research*, **118**, 1–16, doi:10.1002/jgrc.20335.

Capotondi, A., and A. T. Wittenberg, 2013: ENSO diversity in climate models. *US CLIVAR Variations*, **11 (2)**, 10–14.

Capotondi, A., A. T. Wittenberg, and S. Masina, 2006: Spatial and temporal structure of Tropical Pacific interannual variability in 20th century coupled simulations. *Ocean Modelling*, **15**, 274–298, doi:10.1016/j.ocemod.2006.02.004.

Capotondi, A., and Coauthors, 2015: Understanding ENSO diversity. *Bulletin of the American Meteorological Society*, in press.

Carton, J. A., and B. S. Giese, 2008: A reanalysis of ocean climate using Simple Ocean Data Assimilation (SODA). *Monthly Weather Review*, **136 (8)**, 2999–3017, doi:10.1175/2007MWR1978.1.

Chen, G., and C.-Y. Tam, 2010: Different impacts of two kinds of Pacific Ocean warming on tropical cyclone frequency over the western North Pacific. *Geophysical Research Letters*, **37 (1)**, L01 803, doi:10.1029/2009GL041708.

Choi, J., S.-I. An, and S.-W. Yeh, 2012: Decadal amplitude modulation of two types of ENSO and its relationship with the mean state. *Climate Dynamics*, **38 (11-12)**, 2631–2644, doi:10.1007/s00382-011-1186-y.

Choi, K., G. A. Vecchi, and A. T. Wittenberg, 2013: ENSO transition, duration and amplitude asymmetries: role of the nonlinear wind stress coupling in a conceptual model. *Journal of Climate*, **26**, 9462–9476, doi:10.1175/JCLI-D-13-00045.1.

Chylek, P., J. Li, M. K. Dubey, M. Wang, and G. Lesins, 2011: Observed and model simulated 20th century Arctic temperature variability: Canadian earth system model CanESM2. *Atmospheric Chemistry and Physics Discussion*, **11**, 22 893–22 907, doi:10.5194/acpd-11-22893-2011.

Clarke, A. J., S. Van Gorder, and G. Colantuono, 2007: Wind stress curl and ENSO discharge/recharge in the equatorial Pacific. *Journal of Physical Oceanography*, **37**, 1077–1091, doi:10.1175/JPO3035.1.

Clarke, A. J., J. Wang, and S. Van Gorder, 2000: A simple warm-pool displacement ENSO model. *Journal of Physical Oceanography*, **30**, 1679–1691.

Collier, M., and Coauthors, 2011: The CSIRO-Mk3.6.0 atmosphere-ocean GCM: participation in CMIP5 and data publication. 19th International Congress on Modelling and Simulation.

Collins, M., and Coauthors, 2010: The impact of global warming on the tropical Pacific Ocean and El Niño. *Nature Geoscience*, **3**, 391–397.

Cracknell, A. P., S. K. Newcombe, A. F. Black, and N. E. Kirby, 2001: The ABDMAP (Algal Bloom Detection, Monitoring, and Prediction) concerted action. *Journal of Remote Sensing*, **22**, 205–247.

Dai, A., and T. M. L. Wigley, 2000: Global patterns of ENSO-induced precipitation. *Geophysical Research Letters*, **27 (9)**, 1283–1286.

Danabasoglu, G., and Coauthors, 2014: North Atlantic simulations in coordinated ocean-ice reference experiments phase II (CORE-II). Part I: Mean states. *Ocean Modelling*, **73**, 76–107, doi:10.1016/j.ocemod.2013.10.005.

Davies, T., M. J. P. Cullen, A. J. Malcolm, M. H. Mawson, A. Staniforth, A. A. White, and N. Wood, 2005: A new dynamical core for the Met Office's global and regional modelling of the atmosphere. *Quarterly Journal of the Royal Meteorological Society*, **131**, 1759–1782.

Delecluse, P., M. Davey, Y. Kitamura, S. G. H. Philander, M. J. Suarez, and L. Bengtsson, 1998: TOGA review paper: coupled general circulation modeling of the Tropical Pacific. *Journal of Geophysical Research*, **103**, 14 357–14 373.

Delworth, T. L., and Coauthors, 2006: GFDL's CM2 global coupled climate models. Part I: Formulation and simulation characteristics. *Journal of Climate*, **19 (5)**, 643–674, doi:10.1175/JCLI3629.1.

Delworth, T. L., and Coauthors, 2012: Simulated climate and climate change in the GFDL CM2.5 high-resolution coupled climate model. *Journal of Climate*, **25**, 2755–2781, doi:10.1175/JCLI-D-11-00316.1.

Deser, C., and Coauthors, 2012: ENSO and Pacific decadal variability in the Community Climate System Model Version 4. *Journal of Climate*, **25**, 2622–2651, doi:10.1175/JCLI-D-11-00301.1.

Dewitte, B., S.-W. Yeh, and S. Thual, 2013: Reinterpreting the thermocline feedback in the western-central equatorial Pacific and its relationship with the ENSO modulation. *Climate Dynamics*, **41**, 819–830, doi:10.1007/s00382-012-1504-z.

DiNezio, P. N., A. C. Clement, G. A. Vecchi, B. J. Soden, B. P. Kirtman, and S.-K. Lee, 2009: Climate response of the equatorial Pacific to global warming. *Journal of Climate*, **22**, 4873–4892, doi:10.1175/2009JCLI2982.1.

DiNezio, P. N., B. P. Kirtman, A. C. Clement, S.-K. Lee, G. A. Vecchi, and A. T. Wittenberg, 2012: Mean climate controls on the simulated response of ENSO to increasing greenhouse gases. *Journal of Climate*, **25**, 7399–7420, doi:10.1175/JCLI-D-11-00494.1.

Dix, M., and Coauthors, 2014: The ACCESS coupled model: Documentation of core CMIP5 simulations and initial results. *Australian Meteorological and Oceanographic Journal*, **63**, 83–99.

Dong, L., T. J. Vogelsang, and S. J. Colucci, 2008: Interdecadal trend and ENSO-related interannual variability in Southern Hemisphere blocking. *Journal of Climate*, **21 (12)**, 3068–3077, doi:10.1175/2007JCLI1593.1.

Duan, W., Y. Yu, and P. Zhao, 2013: Behaviors of nonlinearities modulating the El Niño events induced by optimal precursory disturbances. *Climate Dynamics*, **40 (5-6)**, 1399–1413, doi:10.1007/s00382-012-1557-z.

Dunne, J. P., and Coauthors, 2012: GFDL's ESM2 global coupled climate–carbon earth system models. Part I: Physical formulation and baseline simulation characteristics. *Journal of Climate*, **25 (19)**, 6646–6665, doi:10.1175/JCLI-D-11-00560.1.

Eisenman, I., L. Yu, and E. Tziperman, 2005: Westerly wind bursts: ENSO's tail rather than the dog? *Journal of Climate*, **18**, 5224–5238.

Evans, J. P., and I. Boyer-Souchet, 2012: Local sea surface temperatures add to extreme precipitation in northeast Australia during La Niña. *Geophysical Research Letters*, **39 (10)**, doi:10.1029/2012GL052014.

Fedorov, A. V., and S. G. Philander, 2001: A stability analysis of tropical ocean-atmosphere interactions: Bridging measurements and theory for El Niño. *Journal of Climate*, **14 (1998)**, 3086–3101.

Fradedrich, K., 1994: An ENSO impact on Europe? *Tellus*, 541–552.

Frauen, C., and D. Dommenget, 2010: El Niño and La Niña amplitude asymmetry caused by atmospheric feedbacks. *Geophysical Research Letters*, **37 (18)**, L18 801, doi:10.1029/2010GL044444.

Gebbie, G., I. Eisenman, A. T. Wittenberg, and E. Tziperman, 2007: Modulation of westerly wind bursts by sea surface temperature: A semistochastic feedback for ENSO. *Journal of the Atmospheric Sciences*, **64**, 3281–3295, doi:10.1175/JAS4029.1.

Giese, B. S., G. P. Compo, N. C. Slowey, P. D. Sardeshmukh, J. A. Carton, S. Ray, and J. S. Whitaker, 2010: The 1918/19 El Niño. *Bulletin of the American Meteorological Society*, **91 (2)**, 177–183, doi:10.1175/2009BAMS2903.1.

Giorgetta, M. A., and Coauthors, 2013: Climate and carbon cycle changes from 1850 to 2100 in MPI-ESM simulations for the Coupled Model Intercomparison Project phase 5. *Journal of Advances in Modeling Earth Systems*, **5 (3)**, 572–597, doi:10.1002/jame.20038.

Gnanadesikan, A., and Coauthors, 2006: GFDL's CM2.1 global coupled climate models. Part II: the baseline ocean simulation. *Journal of Climate*, **19 (5)**, 675–697, doi:10.1175/JCLI3630.1.

Graham, F. S., J. N. Brown, C. Langlais, S. J. Marsland, A. T. Wittenberg, and N. J. Holbrook, 2014: Effectiveness of the Bjerknes stability index in representing ocean dynamics. *Climate Dynamics*, **43**, 2399–2414, doi:10.1007/s00382-014-2062-3.

Graham, N., and W. White, 1988: The El Niño cycle: a natural oscillator of the Pacific ocean-atmosphere system. *Science*, **240**, 1293–1302.

Griffies, S. M., 2009: *Elements of MOM4p1: GFDL Ocean Group Tech. Rep. 6.* NOAA/Geophysical Fluid Dynamics Laboratory.

Griffies, S. M., M. Winton, B. L. Samuels, G. Danabasoglu, S. G. Yeager, S. J. Marsland, H. Drange., and M. Bentsen, 2012: *Datasets and Protocol for the CLIVAR WGOMD Coordinated Ocean-Sea Ice Reference Experiments (COREs).* WCRP Report No. 21/2012, pp. 21.

Griffies, S. M., and Coauthors, 2011: The GFDL CM3 coupled climate model: characteristics of the ocean and sea ice simulations. *Journal of Climate*, **24 (13)**, 3520–3544, doi:10.1175/2077JCLI3964.1.

Guilyardi, E., 2006: El Niño-mean state-seasonal cycle interactions in a multi-model ensemble. *Climate Dynamics*, **26**, 329–348.

Guilyardi, E., H. Bellenger, M. Collins, S. Ferrett, W. Cai, and A. T. Wittenberg, 2012a: A first look at ENSO in CMIP5. *Clivar Exchanges*, **17 (58)**, 29–32.

Guilyardi, E., W. Cai, M. Collins, A. V. Fedorov, F.-F. Jin, A. Kumar, D.-Z. Sun, and A. T. Wittenberg, 2012b: New strategies for evaluating ENSO processes in climate models. *Bulletin of the American Meteorological Society*, 235–238, doi:10.1175/BAMS-D-11-00106.1.

Guilyardi, E., P. Delecluse, S. Gualdi, and A. Navarra, 2003: Mechanisms for ENSO Phase Change in a Coupled GCM. *Journal of Climate*, **16**, 1141–1158.

Guilyardi, E., A. T. Wittenberg, A. V. Fedorov, M. Collins, C. Wang, A. Capotondi, G. J. van Oldenborgh, and T. Stockdale, 2009: Understanding El Niño in ocean-atmosphere general circulation models: progress and understanding. *Bulletin of the American Meteorological Society*, **March**, 325–340.

Guilyardi, E., and Coauthors, 2004: Representing El Niño in coupled ocean-atmosphere GCMs: the dominant role of the atmospheric component. *Journal of Climate*, **17**, 4623–4629, doi:10.1175/JCLI-3260.1.

Halpert, M. S., and C. F. Ropelewski, 1992: Surface temperature patterns associated with the Southern Oscillation. *Journal of Climate*, **5 (577-593)**.

Ham, Y.-G., and J.-S. Kug, 2012: How well do current climate models simulate two types of El Niño? *Climate Dynamics*, **39**, 383–398, doi:10.1007/s00382-011-1157-3.

Harrison, D. E., 1987: Monthly mean island surface winds in the central Tropical Pacific and El Niño events. *Monthly Weather Review*, **115 (12)**, 3133–3145, doi:10.1175/1520-0493(1987)115⟨3133:MMISWI⟩2.0.CO;2.

Harrison, D. E., and N. K. Larkin, 1998: El Niño-Southern Oscillation sea surface temperature and wind anomalies, 1946-1993. *Reviews of Geophysics*, **36 (3)**, 353–399.

Harrison, D. E., and G. A. Vecchi, 1999: On the termination of El Niño. *Geophysical Research Letters*, **26 (11)**, 1593–1596.

Hasegawa, T., and K. Hanawa, 2003: Heat content variability related to ENSO events in the Pacific. *Journal of Physical Oceanography*, **33 (2)**, 407–421, doi:10.1175/1520-0485(2003)033⟨0407:HCVRTE⟩2.0.CO;2.

Hastie, T., R. Tibshirani, and J. Friedman, 2001: *The elements of statistical learning*. Springer, 533 pp.

Hirst, A. C., 1986: Unstable and damped equatorial modes in simple coupled ocean-atmosphere models. *Journal of the Atmospheric Sciences*, **43**, 606–630.

Horel, J. D., 1982: On the annual cycle of the tropical Pacific atmosphere and ocean. *Monthly Weather Review*, **110**, 1863–1878.

Horel, J. D., and J. M. Wallace, 1981: Planetary-scale atmospheric phenomena associated with the Southern Oscillation. *Monthly Weather Review*, **109**, 813–829.

Huang, B., Y. Xue, H. Wang, W. Wang, and A. Kumar, 2011: Mixed Layer Heat Budget of the El Niño in NCEP Climate Forecast System. *Climate Dynamics*, **39 (1-2)**, 365–381, doi:10.1007/s00382-011-1111-4.

Huang, B., Y. Xue, D. Zhang, A. Kumar, and M. J. McPhaden, 2010: The NCEP GODAS ocean analysis of the Tropical Pacific mixed layer heat budget on seasonal to interannual time scales. *Journal of Climate*, **23 (18)**, 4901–4925, doi:10.1175/2010JCLI3373.1.

Hunke, E. C., and W. H. Lipscomb, 2010: *CICE: the Los Alamos Sea Ice Model Documentation and Software User's Manual*. New Mexico, Los Alamos National Laboratory, LA-CC-06-012 Tech. Rep. ed.

Ingleby, B., and M. Huddleston, 2007: Quality control of ocean temperature and salinity profiles - historical and real-time data. *Journal of Marine Systems*, **65**, 158–175, doi:10.1016/J.JMARSYS.2005.11.019.

Jia, L., and Coauthors, 2015: Improved seasonal prediction of temperature and precipitation over land in a high-resolution GFDL climate model. *Journal of Climate*, in press.

Jin, F.-F., 1997a: An equatorial ocean recharge paradigm for ENSO. Part I: Conceptual model. *Journal of the Atmospheric Sciences*, **54**, 811–829.

Jin, F.-F., 1997b: An equatorial ocean recharge paradigm for ENSO. Part II: A stripped-down coupled model. *Journal of the Atmospheric Sciences*, **54**, 830–847.

Jin, F.-F., and S.-I. An, 1999: Thermocline and zonal advective feedbacks within the equatorial ocean recharge oscillator model for ENSO. *Geophysical Research Letters*, **26 (19)**, 2289–2992, doi:10.1029/1999GL002297.

Jin, F.-F., S.-I. An, A. Timmermann, and J. Zhao, 2003: Strong El Niño Events and Nonlinear Dynamical Heating. *Geophysical Research Letters*, **30 (3)**, 1120, doi:10.1029/2002GL016356.

Jin, F.-F., S. T. Kim, and L. Bejarano, 2006: A coupled-stability index for ENSO. *Geophysical Research Letters*, **33 (23)**, L23 708, doi:10.1029/2006GL027221.

Johnson, N. P. A. S., and J. Mueller, 2002: Updating the accounts: global mortality of the 1918-1920 "Spanish" influenza pandemic. *Bulletin of the History of Medicine*, **76 (1)**, 105–15.

Kang, I.-S., S.-I. An, and F.-F. Jin, 2001: Why the properties of El Niño changed during the late 1970s. *Journal of the Meteorological Society of Japan*, **79 (1)**, 1–10.

Kao, H.-Y., and J.-Y. Yu, 2009: Contrasting eastern-pacific and central-pacific types of ENSO. *Journal of Climate*, **22 (3)**, 615–632, doi:10.1175/2008JCLI2309.1.

Karnauskas, K. B., 2013: Can we distinguish canonical El Niño from Modoki? *Geophysical Research Letters*, **40**, 5246–5251, doi:10.1002/grl.51007.

Kessler, W. S., 1990: Observations of long Rossby waves in the northern Tropical Pacific. *Journal of Geophysical Research*, **95**, 5183–5219.

Kessler, W. S., 1991: Can reflected extra-equatorial Rossby waves drive ENSO. *Journal of Physical Oceanography*, **21**, 444–452.

Kessler, W. S., 2002: Is ENSO a cycle or a series of events. *Geophysical Research Letters*, **29 (23)**, doi:10.1029/2002GL015924.

Kessler, W. S., and R. Kleeman, 2000: Rectification of the Madden-Julian Oscillation into the ENSO cycle. *Journal of Climate*, **13**, 3560–3575.

Kessler, W. S., and M. J. McPhaden, 1995: Oceanic equatorial waves and the 1991-1993 El Niño. *Journal of Climate*, **8**, 1757–1774.

Kessler, W. S., L. M. Rothstein, and D. Chen, 1998: The annual cycle of sst in the eastern Tropical Pacific, diagnosed in an ocean GCM. *Journal of Climate*, **11**, 777–799.

Kim, D., J.-S. Kug, I.-S. Kang, F.-F. Jin, and A. T. Wittenberg, 2008: Tropical Pacific impacts of convective momentum transport in the SNU coupled GCM. *Climate Dynamics*, **31**, 213–226, doi:10.1007/s00382-007-0348-4.

Kim, S. T., W. Cai, F.-F. Jin, A. Santoso, L. Wu, E. Guilyardi, and S.-I. An, 2014a: Response of El Niño sea surface temperature variability to greenhouse warming. *Nature Climate Change*, **4**, 786–790, doi:10.1038/nclimate2326.

Kim, S. T., W. Cai, F.-F. Jin, and J.-Y. Yu, 2014b: ENSO stability in coupled climate models and its association with mean state. *Climate Dynamics*, **42 (11-12)**, 331303 321, doi:10.1007/s00382-013-1833-6.

Kim, S. T., and F.-F. Jin, 2011a: An ENSO stability analysis. Part I: Results from a hybrid coupled model. *Climate Dynamics*, **36 (7-8)**, 1593–1607, doi:10.1007/s00382-010-0796-0.

Kim, S. T., and F.-F. Jin, 2011b: An ENSO stability analysis. Part II: Results from the twentieth and twenty-first century simulations of the CMIP3 models. *Climate Dynamics*, **36 (7-8)**, 1609–1627, doi:10.1007/s00382-010-0872-5.

Kug, J.-S., J. Choi, S.-I. An, F.-F. Jin, and A. T. Wittenberg, 2010: Warm pool and cold tongue El Niño events as simulated by the GFDL 2.1 coupled GCM. *Journal of Climate*, **23**, 1226–1239, doi:10.1175/2009JCLI3293.1.

Kug, J.-S., Y.-G. Ham, J.-Y. Lee, and F.-F. Jin, 2012: Improved simulation of two types of El Niño in CMIP5 models. *Environmental Research Letters*, **7 (034002)**, doi:10.1088/1748-9326/7/3/034002.

Kug, J.-S., F.-F. Jin, and S.-I. An, 2009: Two types of El Niño events: Cold tongue El Niño and warm pool El Niño. *Journal of Climate*, **22 (6)**, 1499–1515, doi:10.1175/2008JCLI2624.1.

Large, W., J. McWilliams, and S. Doney, 1994: Oceanic Vertical Mixing: A Review and a Model with a Nonlocal Boundary Layer Parameterization. *Reviews in Geophysics*, **32 (4)**, 363–403.

Large, W. G., and S. G. Yeager, 2009: The global climatology of an interannually varying air-sea flux data set. *Climate Dynamics*, **33**, 341–364, doi:10.1007/s00382-008-0441-3.

Larkin, N. K., and D. E. Harrison, 2002: ENSO warm (El Niño) and cold (La Niña) event life cycles: ocean surface anomaly patterns, their symmetries, asymmetries and implications. *Journal of Climate*, **15**, 1118–1140.

Latif, M., J. Biercamp, and H. von Storch, 1988: The response of a coupled ocean-atmosphere general circulation model to wind bursts. *Journal of the Atmospheric Sciences*, **45 (6)**, 964–979.

Latif, M., and Coauthors, 2001: ENSIP: the El Niño simulation intercomparison project. *Climate Dynamics*, **18 (3-4)**, 255–276.

Lee, H.-C., A. Rosati, and M. Spelman, 2006: Barotropic Tidal Mixing Effects in a Coupled Climate Model: Oceanic Conditions in the Northern Atlantic. *Ocean Modelling*, **3 (4)**, 464–477.

Leloup, J., M. Lengaigne, and J.-P. Boulanger, 2008: Twentieth century ENSO characteristics in the IPCC database. *Climate Dynamics*, **30**, 277–291.

Lengaigne, M., E. Guilyardi, J.-P. Boulanger, C. Menkes, P. Delecluse, P. Inness, J. Cole, and J. Slingo, 2004: Triggering of El Niño by westerly wind events in a coupled general circulation model. *Climate Dynamics*, **23 (6)**, 601–620, doi:10.1007/s00382-004-0457-2.

Lengaigne, M., U. Hausmann, G. Madec, C. E. Menkes, J. Vialard, and J. M. Molines, 2011: Mechanisms controlling warm water volume interannual variations in the equatorial Pacific: diabatic versus adiabatic processes. *Climate Dynamics*, **38 (5-6)**, 1031–1046, doi:10.1007/s00382-011-1051-z.

Levine, A. F. Z., and F.-F. Jin, 2010: Noise-induced instability in the ENSO recharge oscillator. *Journal of the Atmospheric Sciences*, **67**, 529–542, doi:10.1175/2009JAS3213.1.

Li, B., and A. J. Clarke, 1994: An examination of some ENSO mechanisms using interannual sea level at the eastern and western equatorial boundaries and the zonally averaged equatorial wind. *Journal of Physical Oceanography*, **24**, 681–690.

Lima, C. H. R., U. Lall, T. Jebara, and A. G. Barnston, 2009: Statistical prediction of ENSO from subsurface sea temperature using a nonlienar dimensionality reduction. *Journal of Climate*, **22**, 4501–4519, doi:10.1175/2009JCLI2524.1.

Lloyd, J., E. Guilyardi, and H. Weller, 2011: The role of atmosphere feedbacks during ENSO in the CMIP3 models. Part II: using AMIP runs to understand the heat flux feedback mechanisms. *Climate Dynamics*, **37 (7-8)**, 1271–1292, doi:10.1007/s00382-010-0895-y.

Lloyd, J., E. Guilyardi, and H. Weller, 2012: The role of atmosphere feedbacks during ENSO in the CMIP3 models. Part III: the shortwave flux feedback. *Journal of Climate*, **25 (12)**, 4275–4293, doi:10.1175/JCLI-D-11-00178.1.

Lloyd, J., E. Guilyardi, H. Weller, and J. Slingo, 2009: The role of atmosphere feedbacks during ENSO in the CMIP3 models. *Atmospheric Science Letters*, **10**, 170–176, doi:10.1002/asl.

Lübbecke, J. F., and M. J. McPhaden, 2013: A comparative stability analysis of Atlantic and Pacific Niño modes. *Journal of Climate*, **26**, 5965–5980, doi:10.1175/JCLI-D-12-00758.1.

Luo, J.-J., S. Masson, E. Roeckner, G. Madec, and T. Yamagata, 2005: Reducing climatology bias in an ocean-atmosphere CGCM with improved coupling physics. *Journal of Climate*, **18**, 2344–2360, doi:10.1175/JCLI3404.1.

Luther, D. S., D. E. Harrison, and R. A. Knox, 1983: Zonal winds in the central equatorial Pacific and El Niño. *Science*, **222 (October)**, 327–330.

Mantua, N. J., and D. S. Battisti, 1994: Evidence of the delayed oscillator mechanism for ENSO: the "observed" oceanic Kelvin mode in the far western Pacific. *Journal of Physical Oceanography*, **24**, 691–699.

Martin, G. M., M. A. Ringer, V. D. Pope, A. Jones, C. Dearden, and T. J. Hinton, 2006: The physical properties of the atmosphere in the new Hadley Centre Global Environment Model, HadGEM1. Part I: Model description and global climatology. *Journal of Climate*, **19**, 1274–1301.

McBride, J. L., and N. Nicholls, 1983: Seasonal relationship between Australian rainfall and the Southern Oscillation. *Monthly Weather Review*, **111**, 1998–2004.

McCreary, J., 1983: A model of tropical ocean-atmosphere interaction. *Monthly Weather Review*, **111**, 370–387.

McCreary, J. P., and D. Anderson, 1984: A simple model of El Niño and the Southern Oscillation. *Monthly Weather Review*, **112**, 934–946.

McIntosh, P. C., M. J. Pook, J. S. Risbey, S. N. Lisson, and M. Rebbeck, 2007: Seasonal climate forecasts for agriculture: Towards better understanding and value. *Field Crops Research*, **104 (1-3)**, 130–138, doi:10.1016/j.fcr.2007.03.019.

McPhaden, M. J., 2003: Tropical Pacific Ocean heat content variations and ENSO persistence barriers. *Geophysical Research Letters*, **30 (9)**, 1995–1998, doi:10.1029/2003GL016872.

McPhaden, M. J., 2004: Evolution of the 2002/03 El Niño. *Bulletin of the American Meteorological Society*, **85 (5)**, 677–695, doi:10.1175/BAMS-85-5-677.

McPhaden, M. J., 2012: A 21st century shift in the relationship betwen ENSO SST and warm water volume anomalies. *Geophysical Research Letters*, **39 (L09706)**, doi:10.1029/2012GL051826.

McPhaden, M. J., and X. Yu, 1999: Equatorial waves and the 1997-98 El Niño. *Geophysical Research Letters*, **26 (19)**, 2961–2964.

McPhaden, M. J., X. Zhang, H. H. Hendon, and M. C. Wheeler, 2006: Large scale dynamics and MJO forcing of ENSO variability. *Geophysical Research Letters*, **33 (16)**, L16 702, doi: 10.1029/2006GL026786.

Mechoso, C. R., J. D. Neelin, and J.-Y. Yu, 2003: Testing simple models of ENSO. *Journal of the Atmospheric Sciences*, **60**, 305–318.

Meehl, G. A., H. Teng, and G. Branstator, 2006: Future changes of El Niño in two coupled climate models. *Climate Dynamics*, **26 (6)**, 549–566, doi:10.1007/s00382-005-0098-0.

Meinen, C. S., and M. J. McPhaden, 2000: Observations of warm water volume changes in the equatorial Pacific and their relationship to El Niño and La Niña. *Journal of Climate*, **13**, 3551–3559.

Meinen, C. S., and M. J. McPhaden, 2001: Interannual variability in warm water volume transport in the equatorial Pacific during 1993-99. *Journal of Physical Oceanography*, **31**, 1324–1345.

Merryfield, W. J., W.-S. Lee, G. J. Boer, V. V. Kharin, J. F. Scinocca, G. M. Flato, R. S. Ajayamohan, and J. C. Fyfe, 2013: The Canadian seasonal to interannual prediction system. Part I: models and initialization. *Monthly Weather Review*, **141**, 2910–2945, doi:10.1175/MWR-D-12-00216.1.

Meyers, G., 1979: On the annual Rossby wave in the tropical North Pacific Ocean. *Journal of Physical Oceanography*, **9**, 663–674.

Meyers, G., P. McIntosh, L. Pigot, and M. Pook, 2007: The years of El Niño, La Niña, and interactions with the tropical Indian Ocean. *Journal of Climate*, **20 (13)**, 2872–2880, doi: 10.1175/JCLI4152.1.

Meyers, G., H. Phillips, N. Smith, and J. Sprintall, 1991: Space and time scales for optimal interpolation of temperature - tropical Pacific Ocean. *Progress in Oceanography*, **28**, 189–218.

Morel, A., and D. Antoine, 1994: Heating rate within the upper ocean in relation to its bio-optical state. *Journal of Physical Oceanography*, **24**, 1652–1665.

Munich Re, 1999: Weather-related natural disasters 1998. Tech. rep., Munich Re, Munich, Germany.

Murray, R., 1996: Explicit Generation of Orthogonal Grids for Ocean Models. *Journal of Computational Physics*, **126 (2)**, 251–275, doi:10.1006/jcph.1996.0136.

Neelin, J. D., D. S. Battisti, A. C. Hirst, F.-F. Jin, Y. Wakata, T. Yamagata, and S. E. Zebiak, 1998: ENSO theory. *Journal of Geophysical Research*, **103 (C7)**, 14 261–14 290.

Neelin, J. D., and F.-F. Jin, 1993: Modes of interannual tropical ocean-atmosphere interactions - a unified view. Part II: Analytical results in the weak-coupling limit. *Journal of the Atmospheric Sciences*, **50 (21)**, 3504–3522.

Neelin, J. D., F.-F. Jin, and H.-H. Syu, 2000: Variations in ENSO phase-locking. *Journal of Climate*, **13**, 2570–2590.

Newman, M., M. A. Alexander, and J. D. Scott, 2011a: An empirical model of tropical ocean dynamics. *Climate Dynamics*, **37**, 1823–1841, doi:10.1007/s00382-011-1034-0.

Newman, M., S.-I. Shin, and M. A. Alexander, 2011b: Natural variation in ENSO flavors. *Geophysical Research Letters*, **38 (L14705)**, 1–7, doi:10.1029/2011GL047658.

Nicholls, N., 1985: Predictability of interannual variations of Australian seasonal tropical cyclone activity. *Monthly Weather Review*, **113**, 1144–1149.

Nicholls, N., 1992: *El Niño/Southern Oscillation variability in the Australian region. El Niño, historical and paleoclimatic aspects of the Southern Oscillation*, 151–174. Cambridge University Press, Cambridge, UK.

Ogata, T., S.-P. Xie, A. T. Wittenberg, and D.-Z. Sun, 2013: Interdecadal amplitude modulation of El Niño/Southern Oscillation and its impacts on tropical Pacific decadal variability. *Journal of Climate*, doi:10.1175/JCLI-D-12-00415.1.

Oke, P. R., and D. A. Griffin, 2011: The cold-core eddy and strong upwelling off the coast of New South Wales in early 2007. *Deep Sea Research II*, **58**, 574–591, doi:10.1016/j.dsr2.2010.06.006.

Oke, P. R., and Coauthors, 2013: Towards a dynamically balanced eddy-resolving ocean reanalysis: BRAN3. *Ocean Modelling*, **67**, 52–70, doi:10.1016/j.ocemod.2013.03.008.

Penland, C., and P. D. Sardeshmukh, 1995: The optimal growth of tropical sea surface temperature anomalies. *Journal of Climate*, **8**, 1999–2024.

Philander, S. G., 1990: *El Niño, La Niña, and the Southern Oscillation*. Academic Press: San Diego.

Philander, S. G. H., T. Yamagata, and R. C. Pacanowski, 1984: Unstable air-sea interactions in the tropics. *Journal of the Atmospheric Sciences*, **41 (4)**, 604–613.

Picaut, J., and T. Delcroix, 1995: Equatorial wave sequence associated with warm pool displacements during the 1986-1989 El Niño-La Niña. *Journal of Geophysical Research*, **100 (C9)**, 18 393–18 408, doi:10.1029/95JC01358.

Picaut, J., M. Ioualalen, C. Menkes, T. Delcroix, and M. J. McPhaden, 1996: Mechanism of the zonal displacements of the Pacific warm pool: Implications for ENSO. *Science*, **274 (5292)**, 1486–9.

Picaut, J., F. Masia, and Y. du Penhoat, 1997: An advective-reflective conceptual model for the oscillatory nature of the ENSO. *Science*, **277 (5326)**, 663–666, doi:10.1126/science.277.5326.663.

Power, S., F. Delage, C. Chung, G. Kociuba, and K. Keay, 2013: Robust twenty-first-century projections of El Niño and related precipitation variability. *Nature*, **502 (7472)**, 541–545, doi:10.1038/nature12580.

Power, S., M. Haylock, R. A. Colman, and X. Wang, 2006: The predictability of interdecadal changes in ENSO activity and ENSO teleconnections. *Journal of Climate*, **19**, 4755–4771.

Qu, T., 2003: Mixed layer heat balance in the western North Pacific. *Journal of Geophysical Research*, **108 (C7)**, 3242, doi:10.1029/2002JC001536.

Queensland Government, 2011: Queensland floods commission of inquiry: Interim report. Tech. rep., Queensland Government, Brisbane, Queensland, Australia.

R Development Core Team, 2008: *R: A Language and Environment for Statistical Computing*. Vienna, Austria, R Foundation for Statistical Computing, URL http://www.R-project.org, ISBN 3-900051-07-0.

Rashid, H. A., and A. C. Hirst, 2015: Investigating the mechanisms of seasonal ENSO phase locking bias in the ACCESS coupled model, submitted.

Rashid, H. A., A. Sullivan, A. C. Hirst, D. Bi, and S. J. Marsland, 2013: Evaluation of El Niño-Southern Oscillation in the ACCESS coupled model simulations for CMIP5. *Australian Meteorological and Oceanographic Journal*, **63 (1)**, 161–180.

Rasmusson, E., and T. H. Carpenter, 1982: Variations in tropical sea surface temperature and surface wind fields associated with the Southern Oscillation/El Niño. *Monthly Weather Review*, **110**, 354–384.

Rebert, J., J. Donguy, and G. Eldin, 1985: Relations between sea level, thermocline depth, heat content, and dynamic height in the tropical Pacific Ocean. *Journal of Geophysical Research*, **90 (C6)**, 11 719–11 725.

Ren, H.-L., and F.-F. Jin, 2013: Recharge oscillator mechanisms in two types of ENSO. *Journal of Climate*, doi:10.1175/JCLI-D-12-00601.1.

Roberts, M. J., and Coauthors, 2009: Impact of resolution on the Tropical Pacific circulation in a matrix of coupled models. *Journal of Climate*, **22**, 2541–2256, doi:10.1175/2008JCLI2537.1.

Ropelewski, C. F., and M. S. Halpert, 1987: Global and regional scale precipitation patterns associated with the El Niño/Southern Oscillation. *Monthly Weather Review*, **115**, 1606–1626.

Ropelewski, C. F., and M. S. Halpert, 1989: Precipitation patterns associated with the high index phase of the Southern Oscillation. *Journal of Climate*, **2**, 268–284.

Santoso, A., S. McGregor, F.-F. Jin, W. Cai, M. H. England, S.-I. An, M. J. McPhaden, and E. Guilyardi, 2013: Late-twentieth-century emergence of the El Niño propagation asymmetry and future projections. *Nature*, **504 (7478)**, 126–130, doi:10.1038/nature12683.

Santoso, A., A. Sen Gupta, and M. H. England, 2010: Genesis of Indian Ocean mixed layer temperature anomalies: A heat budget analysis. *Journal of Climate*, **23 (20)**, 5375–5403, doi:10.1175/2010JCLI3072.1.

Schiller, A., and K. R. Ridgway, 2013: Seasonal mixed layer dynamics in an eddy-resolving ocean circulation model. *Journal of Geophysical Research*, **118**, 1–19, doi:10.1002/jgrc.20250.

Schneider, E. K., Z. X. Zhu, B. S. Giese, B. H. Huang, B. P. Kirtman, J. Shukla, and J. A. Carton, 1997: Annual cycle and ENSO in a coupled ocean-atmosphere general circulation model. *Monthly Weather Review*, **125**, 680–702.

Schopf, P. S., and M. J. Suarez, 1988: Vacillations in a coupled ocean-atmosphere model. *Journal of the Atmospheric Sciences*, **45 (3)**, 549–566.

Shaman, J., and M. Lipsitch, 2013: The El Niño-Southern Oscillation (ENSO)-pandemic influenza connection: coincident or causal? *Proceedings of the National Academy of Sciences of the United States of America*, **110 Suppl 1**, 3689–91, doi:10.1073/pnas.1107485109.

Shu, L., and A. J. Clarke, 2002: Using an ocean model to examine ENSO dynamics. *Journal of Physical Oceanography*, **32**, 903–923.

Simmons, H., S. Jayne, L. Laurent, and A. Weaver, 2004: Tidally driven mixing in a numerical model of the ocean general circulation. *Ocean Modelling*, **6**, 245–263.

Singh, A., and T. Delcroix, 2013: Eastern and central Pacific ENSO and their relationships to the recharge/discharge oscillator paradigm. *Deep Sea Research I: Oceanographic Research Papers*, **82**, 32–43, doi:10.1016/j.dsr.2013.08.002.

Singh, A., T. Delcroix, and S. Cravatte, 2011: Contrasting the flavors of El Niño-Southern Oscillation using sea surface salinity observations. *Journal of Geophysical Research*, **116 (C06016)**, doi:10.1029/2010JC006862.

Smith, N. R., 1991: Objective quality control and performance diagnostics of an oceanic subsurface thermal analysis scheme. *Journal of Geophysical Research*, **96**, 3279–3287.

Smith, N. R., 1994: An improved system for tropical ocean subsurface temperature analyses. *Journal of Atmospheric and Oceanic Technology*, **12**, 850–870.

Smith, N. R., 1995: The BMRC ocean thermal analysis system. *Australian Meteorological Magazine*, **44**, 93–110.

Smith, N. R., J. E. Blomley, and G. Meyers, 1991: A univariate statistical interpolation scheme for subsurface thermal analyses in the tropical oceans. *Progress in Oceanography*, **28**, 219–256.

Soetaert, K., T. Petzoldt, and R. W. Setzer, 2010: Solving differential equations in R: Package desolve. *Journal of Statistical Software*, **33 (9)**, 1–25, URL http://www.jstatsoft.org/v33/i09.

Solomon, S., D. Qin, M. Manning, Z. Chen, M. Marquis, K. B. Avery, M. Tignor, and H. L. Miller, Eds., 2007: *Climate Change 2007: the Physical Science Basis*. Cambridge University Press.

Stevenson, J. W., and P. P. Niiler, 1983: Upper ocean heat budget during the Hawaii-to-Tahiti shuttle experiment. *Journal of Physical Oceanography*, **13**, 1894–1907.

Stevenson, S., B. Fox-Kemper, M. Jochum, B. Rajagopalan, and S. G. Yeager, 2010: ENSO model validation using wavelet probability analysis. *Journal of Climate*, **23**, 5540–5547, doi:10.1175/2010JCLI3609.1.

Su, J., T. Li, and R. Zhang, 2014: The initiation and developing mechanisms of Central Pacific El Niños. *Journal of Climate*, **27**, 4473–4485, doi:10.1175/JCLI-D-13-00640.1.

Suarez, M. J., and P. S. Schopf, 1988: A delayed action oscillator for ENSO. *Journal of the Atmospheric Sciences*, **45 (21)**, 3283–3287.

Syu, H.-H., and J. D. Neelin, 2000: ENSO in a hybrid coupled model. Part I: sensitivity to physical parameterizations. *Climate Dynamics*, **16**, 19–34.

Taschetto, A. S., and M. H. England, 2009: El Niño Modoki impacts on Australian rainfall. *Journal of Climate*, **22**, 3167–3174, doi:10.1175/2008JCLI2589.1.

Taschetto, A. S., A. Sen Gupta, N. C. Jourdain, A. Santoso, C. C. Ummenhofer, and M. H. England, 2014: Cold Tongue and Warm Pool ENSO events in CMIP5: mean state and future projections. *Journal of Climate*, **27**, 2861–2885, doi:10.1175/JCLI-D-13-00437.1.

Taylor, K. E., R. J. Stouffer, and G. A. Meehl, 2012: Overview of CMIP5 and the experiment design. *Bulletin of the American Meteorological Society*, **93**, 485–498, doi:http://dx.doi.org/10.1175/BAMS-D-11-00094.1.

Thual, S., B. Dewitte, S.-I. An, and N. Ayoub, 2011: Sensitivity of ENSO to stratification in a recharge-discharge conceptual model. *Journal of Climate*, **24 (16)**, 4332–4349.

Timmermann, A., F.-F. Jin, and J. Abshagen, 2003: A nonlinear theory for El Niño bursting. *Journal of the Atmospheric Sciences*, **60**, 152–165.

Trenberth, K. E., 1997: The definition of El Niño. *Bulletin of the American Meteorological Society*, **78 (12)**, 2771–2777.

Trenberth, K. E., 1999: The extreme weather events of 1997 and 1998. *Consequences*, **5 (1)**, 3–15.

Tziperman, E., M. A. Cane, and S. E. Zebiak, 1995: Irregularity and locking to the seasonal cycle in an ENSO prediction model as explained by the quasi-periodicity route to chaos. *Journal of the Atmospheric Sciences*, **52 (3)**, 293–306, doi:10.1175/1520-0469(1995)052⟨0293:IALTTS⟩2.0.CO;2.

Tziperman, E., and L. Yu, 2007: Quantifying the dependence of westerly wind bursts on the large-scale tropical Pacific SST. *Journal of Climate*, **20**, 2760–2768.

Valcke, S., 2006: *OASIS3 User Guide (prism 2-5)*. PRISM support initiative, no. 3 ed.

van Oldenborgh, G. J., S. Y. Philip, and M. Collins, 2005: El Niño in a changing climate: a multi-model study. *Ocean Science*, **1**, 81–95.

Vannière, B., E. Guilyardi, G. Madec, F. J. Doblas-Reyes, and S. Woolnough, 2013: Using seasonal hindcasts to understand the origin of the equatorial cold tongue bias in CGCMs and its impact on ENSO. *Climate Dynamics*, **40**, 963–981, doi:10.1007/s00382-012-1429-6.

Vecchi, G. A., and D. E. Harrison, 2000: Tropical Pacific sea surface temperature anomalies, El Niño, and equatorial westerly wind events. *Journal of Climate*, **13**, 1814–1830.

Vecchi, G. A., and D. E. Harrison, 2003: On the termination of the 2002-03 El Niño event. *Geophysical Research Letters*, **30 (18)**, 1964, doi:10.1029/2003GL017564.

Vecchi, G. A., and A. T. Wittenberg, 2010: El Niño and our future climate: where do we stand? *Wiley Interdisciplinary Reviews: Climate Change*, **1**, 260–270, doi:10.1002/wcc.33.

Vecchi, G. A., A. T. Wittenberg, and A. Rosati, 2006: Reassessing the role of stochastic forcing in the 1997-8 El Niño. *Geophysical Research Letters*, **33**, L01 706, doi:10.1029/2005GL024738.

Vecchi, G. A., and Coauthors, 2014: On the seasonal forecasting of regional tropical cyclone activity. *Journal of Climate*, **27**, 7994–8016, doi:10.1175/JCLI-D-14-00158.1.

Vialard, J., and P. Delecluse, 1998: An OGCM study for the TOGA decade. Part I: role of salinity in the physics of the western Pacific fresh pool. *Journal of Physical Oceanography*, **28**, 1071–1088.

Voldoire, A., and Coauthors, 2013: The CNRM-CM5.1 global climate model: description and basic evaluation. *Climate Dynamics*, **40**, 2091–2121, doi:10.1007/s00382-011-1259-y.

von Storch, H., and F. W. Zwiers, 1999: *Statistical analysis in climate research*. Cambridge University Press, 484 pp.

Wang, B., and S.-I. An, 2001: Why the properties of El Niño changed during the late 1970s. *Geophysical Research Letters*, **28 (19)**, 3709–3712.

Wang, C., 2001: A unified oscillator model for the El Niño-Southern Oscillation. *Journal of Climate*, **14**, 98–115.

Wang, C., and J. Picaut, 2004: Understanding ENSO physics - a review. *Earth's Climate: The Ocean-Atmosphere Interaction*, Vol. 147, American Geophysical Union, 21–48.

Wang, W., and M. J. McPhaden, 2000: The surface-layer heat balance in the equatorial Pacific Ocean. Part II: Interannual variability. *Journal of Physical Oceanography*, **30**, 2989–3008.

Wang, W., S. Saha, H.-L. Pan, S. Nadiga, and G. White, 2005: Simulation of ENSO in the new NCEP Coupled Forecast System Model (CFS03). *Monthly Weather Review*, **133**, 1574–1593.

Wang, X., 1994: The coupling of the annual cycle and ENSO over the tropical Pacific. *Journal of the Atmospheric Sciences*, **51**, 1115–1136.

Watanabe, M., J.-S. Kug, F.-F. Jin, M. Collins, M. Ohba, and A. T. Wittenberg, 2012: Uncertainty in the ENSO amplitude change from the past to the future. *Geophysical Research Letters*, **39 (20)**, 1–6, doi:10.1029/2012GL053305.

Webster, P. J., and S. Yang, 1992: Monsoon and ENSO: selectively interactive systems. *Quarterly Journal of the Royal Meteorological Society*, **118**, 877–926.

Weisberg, R. H., and C. Wang, 1997: A western Pacific oscillator paradigm for the El Niño-Southern Oscillation. *Geophysical Research Letters*, **24 (7)**, 779–782.

Wittenberg, A. T., 2002: ENSO response to altered climates. Ph.D. thesis, Princeton University, available from http://www.gfdl.noaa.gov/∼atw/research/thesis.

Wittenberg, A. T., 2004: Extended wind stress analyses for ENSO. *Journal of Climate*, **17**, 2526–2540, doi:10.1175/1520-0442(2004)017⟨2526:EWSAFE⟩2.0.CO;2.

Wittenberg, A. T., 2009: Are historical records sufficient to constrain ENSO simulations? *Geophysical Research Letters*, **36 (12)**, L12 702, doi:10.1029/2009GL038710.

Wittenberg, A. T., A. Rosati, T. L. Delworth, G. A. Vecchi, and F. Zeng, 2014: ENSO modulation: Is it decadally predictable? *Journal of Climate*, **27**, 2667–2681, doi:10.1175/JCLI-D-13-00577.1.

Wittenberg, A. T., A. Rosati, N.-C. Lau, and J. J. Ploshay, 2006: GFDL's CM2 global coupled climate models. Part III: Tropical Pacific climate and ENSO. *Journal of Climate*, **19**, 698–722, doi:10.1175/JCLI3631.1.

Wu, G., and N.-C. Lau, 1992: A GCM simulation of the relationship between tropical-storm formation and ENSO. *Monthly Weather Review*, **120**, 958–977, doi:10.1175/1520-0493(1992)120⟨0958:AGSOTR⟩2.0.CO;2.

Wyrtki, K., 1975: El Niño - the dynamic response of the equatorial Pacific Ocean to atmospheric forcing. *Journal of Physical Oceanography*, **5**, 572–584.

Wyrtki, K., 1985: Water displacements in the Pacific and the genesis of El Niño cycles. *Journal of Geophysical Research*, **90 (5)**, 7129–7132.

Xiang, B., B. Wang, Q. Ding, F.-F. Jin, X. Fu, and H.-J. Kim, 2011: Reduction of the thermocline feedback associated with mean SST bias in ENSO simulation. *Climate Dynamics*, **39 (6)**, 1413–1430, doi:10.1007/s00382-011-1164-4.

Yeh, S.-W., B. Dewitte, B. Y. Yim, and Y. Noh, 2010: Role of the upper ocean structure in the response of ENSO-like SST variability to global warming. *Climate Dynamics*, **35**, 355–369, doi:10.1007/s00382-010-0849-4.

Yeh, S.-W., J.-S. Kug, and S.-I. An, 2014: Recent progress on two types of El Niño: observations, dynamics, and future changes. *Asia-Pacific Journal of Atmospheric Sciences*, **51 (1)**, 69–81, doi:10.1007/s13143-014-0028-3.

Yeh, S.-W., J.-S. Kug, B. Dewitte, M.-H. Kwon, B. P. Kirtman, and F.-F. Jin, 2009: El Niño in a changing climate. *Nature*, **461**, 511–514, doi:10.1038/nature08316.

Yeh, S.-W., Y.-G. Park, and B. P. Kirtman, 2006: ENSO amplitude changes in climate change commitment to atmospheric CO_2 doubling. *Geophysical Research Letters*, **33 (L13711)**, doi:10.1029/2005GL025653.

Yukimoto, S., and Coauthors, 2012: A new global climate model of the Meterological Research Institute: MRI-CGCM3. *Journal of the Meteorological Society of Japan*, **90A**, 23–64, doi:10.2151/jmsj.2012-A02.

Zavala-Garay, J., C. Zhang, A. M. Moore, A. T. Wittenberg, M. J. Harrison, A. Rosati, J. Vialard, and R. Kleeman, 2008: Sensitivity of hybrid ENSO models to unresolved atmospheric variability. *Journal of Climate*, **21**, 3704–3721, doi:10.1175/2007JCLI1188.1.

Zebiak, S. E., 1989: Ocean heat content variability and El Niño cycles. *Journal of Physical Oceanography*, **19**, 475–486.

Zebiak, S. E., and M. A. Cane, 1987: A model El Niño-Southern Oscillation. *Monthly Weather Review*, **115**, 2262–2278.

Zhang, X., and M. J. McPhaden, 2006: Wind stress variations and interannual sea surface temperature anomalies in the eastern equatorial Pacific. *Journal of Climate*, **19**, 226–241.

Zhang, X., and M. J. McPhaden, 2010: Surface Layer Heat Balance in the Eastern Equatorial Pacific Ocean on Interannual Time Scales: Influence of Local versus Remote Wind Forcing. *Journal of Climate*, **23 (16)**, 4375–4394, doi:10.1175/2010JCLI3469.1.

Zhang, X.-G., and T. M. Casey, 1992: Long-term variations in the Southern Oscillation and relationships with Australian rainfall. *Australian Meteorological Magazine*, **40**, 211–225.